INFORMATION TO USERS

This manuscript has been reproduced from the microfilm master. UMI films the text directly from the original or copy submitted. Thus, some thesis and dissertation copies are in typewriter face, while others may be from any type of computer printer.

The quality of this reproduction is dependent upon the quality of the copy submitted. Broken or indistinct print, colored or poor quality illustrations and photographs, print bleedthrough, substandard margins, and improper alignment can adversely affect reproduction.

In the unlikely event that the author did not send UMI a complete manuscript and there are missing pages, these will be noted. Also, if unauthorized copyright material had to be removed, a note will indicate the deletion.

Oversize materials (e.g., maps, drawings, charts) are reproduced by sectioning the original, beginning at the upper left-hand corner and continuing from left to right in equal sections with small overlaps.

Photographs included in the original manuscript have been reproduced xerographically in this copy. Higher quality 6" x 9" black and white photographic prints are available for any photographs or illustrations appearing in this copy for an additional charge. Contact UMI directly to order.

Bell & Howell Information and Learning
300 North Zeeb Road, Ann Arbor, MI 48106-1346 USA

UMI®
800-521-0600

AN EXPERIMENTAL AND THEORETICAL STUDY OF FLUIDELASTIC INSTABILITY IN CROSS FLOW MULTI-SPAN HEAT EXCHANGER TUBE ARRAYS

by

MING LI B.Eng., M.Eng.

A Thesis Submitted to the School of Graduate Studies

in Partial Fulfilment of the Requirements

for the Degree

Doctor of Philosophy

McMaster University

EXPERIMENTAL AND THEORETICAL FLUIDELASTIC INSTABILITY STUDY

DOCTOR OF PHILOSOPHY (1997) McMASTER UNIVERSITY

(Mechanical Engineering) Hamilton, Ontario

TITLE: An Experimental and Theoretical Study of Fluidelastic Instability in Cross Flow Multi-Span Heat Exchanger Tube Arrays

AUTHOR: Ming Li

B.Eng., M.Eng. (Southeast University, P.R. China)

M.Eng. (McMaster University)

SUPERVISOR: Dr. D. S. Weaver

NUMBER OF PAGES: 211

TO MY MOTHERLAND

ABSTRACT

An experimental study was conducted to investigate fluidelastic instability in multi-span heat exchanger tube arrays. This work is in support of nuclear steam generator design, especially with regard to the U-bend and inlet regions, where tubes are subjected to non-uniform cross flow. The design guidelines defined in the current ASME codes and other recommended semi-empirical formulas for fluidelastic instability have been based on the extension of experimental results from single span tube bundles. In this study, a specially designed multi-span tube array test rig was used to investigate the effects of partial flow admission. Using this test rig, the water flow can pass across any location along the tube span. Various end supports were used in the different experimental set-ups. Therefore, not only the first mode but also the higher vibration modes can be excited, depending on the location of the flow and tube-support configurations. It was been found that vibration modes higher than the third mode do not have significant vibration displacement. The experiments show that the fluid energy is additive along the span, regardless of the tube mode shape. Response peaks were observed prior to the ultimate fluidelastic instability. By analyzing the corresponding Strouhal numbers, it was found that both vortex shedding and secondary instability mechanisms exist. These two different phenomena may interact and enhance each other. Therefore, high amplitude displacement can be reached even before the ultimate fluidelastic instability. The previous and present experimental data suggest that the energy fraction is a representative parameter in the analysis of the flow induced vibration caused by nonuniform flow velocity distribution. However, existing design guidelines do not always give conservative predictions for the critical velocity. This research reveals that a single correlation of reduced velocity versus mass damping ratio does not follow the same trend in air and liquid flows. An improved design guideline is suggested, which gives consistent

conservative flow velocity predictions in multi-span tube arrays.

In parallel, an analytical model was developed for the prediction of fluidelastic instability in cross flow multi-span heat exchanger tube arrays. The model is based on concepts developed by Lever and Weaver, as well as Yetisir and Weaver, but is extended to include some crucial factors. Velocity and pressure fluctuations, caused by tube vibration were obtained by using continuity and momentum equations in curvilinear coordinates. Rather than the nonlinear function previously used, a linear area perturbation decay function was introduced to account for the decay of disturbances away from an oscillating tube. Thus, an analytical solution could be obtained. The resulting explicit instability expression is a more convenient tool to analyze effects of various design parameters. The difference between the linear and nonlinear decay functions was found to have a negligible effect on the stability threshold. Critical velocity in both streamwise and transverse directions was calculated, and the latter is lower in the high mass damping ratio range. Therefore, only the instability in the transverse direction needs to be analyzed in that range. On the other hand, there is no clear trend in the low mass damping ratio range, which agrees with many previous research results. This model is a multiple flexible tube model. Tubes directly two rows upstream and downstream of a central tube, neglected in the Yetisir and Weaver model, but are included in the present model. Significant improvement is obtained for the parallel triangular tube arrays. In contrast, little improvement is achieved on the other tube patterns due to the reduced influence of the upstream tube wake. The velocity distribution and mode shape along the tube span were introduced into the model. This is made possible because of the explicit instability equation. Therefore, the present model, in which fluid flow in two-dimensional, but considering tube mode shape in the third dimension, can be used to calculate the fluidelastic instability for multi-span tube arrays. The comparison between the theory and experimental data agrees well.

ACKNOWLEDGMENTS

The author would like to express his sincere gratitude to Dr. D.S.Weaver. His extensive knowledge in FIV and his competent assistance were invaluable throughout the entire period of this research.

The kind help and advice from the Departmental technicians, Mr. Dave Schick, Ron Lodewyks, Joe Verhaeghe and Jim McLaren are gratefully acknowledged.

The author is also grateful for the supervisory committee members, Dr. Judd, Dr. Tso and Dr. Spence, for their advice.

Thanks also to the FIV group members: Paul Feenstra, Michael Morgenroth, Vaidas Jakubauskas, Alejandro Gidi and Tony Wu, as well as friends who graduated from the department: Giridhar Chulkkapalli, Radovan Zdero, Alex Chen and many more.

The financial support provided by the Natural Science and Engineering Research Council is also gratefully acknowledged.

TABLE OF CONTENTS

LIST OF FIGURES

LIST OF TABLES

NOMENCLATURE

A, B, C, D	constants
AR	area ratio of the contraction section
A_0	minimum gap area
$A(f_i)$	displacement measured by HP analyzer
A(s,t)	stream area function
a(s,t), $a(U_r, t)$	fluctuating stream area function
a_2	constant area function
Cr	contraction ratio of the contraction section
$C_{(...)}$	fluid force coefficients
$C_i(U_r)$	function of reduced velocity in the fluid force function
C_{pi}, C_{pe}	coefficients in contraction section design
c	damping
d	tube diameter
d_c	honeycomb diameter
F	force
F_i, F_e	coefficients in contraction section design
F_n	generalized force
f	frequency
f_n	natural frequency of the tube
Δf	frequency band width
{F}	force array
f(s)	decay function
H_1, H_2	inlet and outlet height of the contraction section
k	stiffness
K	constant
K_s	pressure drop coefficient of the screen
L	length

l	wire space of the screen
l_0	$=2s_1$, and cell length of the honeycomb
M_n	generalized mass
m	mass of the tube per unit length including added mass
MDE	mass damping energy fraction
N_{row}	upstream rows within the influence of the pressure disturbance.
P	array pitch
PAF	partial admission factor
P_r	P/d, pitch ratio
P_0	mean pressure
P(s,t), p(s,t)	steady and unsteady pressure function
p(s, U_r)	pressure function
Re	Reynolds number
S_i	energy fraction
S_t	Strouhal number
U(s,t), u(s,t)	steady and unsteady velocity function
U_r	$U_\infty / l_0\omega_n$, reduced velocity
U_f	V_p/f_nd, reduced velocity based on pitch velocity
u(s, U_r)	velocity function
V	critical velocity
V_0	mean velocity
V_e	equivalent uniform velocity
V_∞	free stream velocity
V_p	pitch velocity
s	curvilinear coordinate
s_1	pressure disturbance length
s_a	attachment point
s_m	position of minimum gap
s_s	separation point

t	time
X	contour shape parameter, maximum displacement in the streamwise direction
Y	maximum displacement in the transverse direction

Greek

α	exponent of semi-empirical critical velocity' equation, pitch angle, screen deflection coefficient
β	exponent of semi-empirical critical velocity' equation, open area ratio of the screen
δ	logarithmic decrement of damping
δ_s	$m\delta/\rho d^2$, mass damping parameter
ζ	damping ratio
η	screen efficiency
θ	half angle of the diffuser
ρ	fluid density
$\phi(s)$	phase function
$\phi(x)$	mode shape function
$\psi(x)$	velocity distribution
ω	vibration frequency
ω_n	natural frequency
ω_r	ω/ω_n, frequency ratio

Subscripts

a	in air
i	mode number
I	imaginary part
R	real part
w	in water
x	streamwise direction

y	transverse direction

Superscripts

*	dimensionless parameter

CHAPTER 1

INTRODUCTION

Flow-induced vibration has been a serious concern in the design and operation of shell and tube type heat exchangers, such as steam generators, condensers, and coolers. In shell and tube type heat exchangers, one fluid flows inside the tubes while another fluid flows through the shell and across the outside of the tubes. With increased attention to performance and economics, larger scale heat exchangers are being designed with higher mass flow rates and larger thermal gradients. It is thus desirable to use small diameter tubes and large distances between the tube supports to increase the heat transfer area and reduce shell side pressure drops. These systems have, therefore, become more flexible and prone to flow-induced vibration damage in the form of fretting wear and fatigue failure at the tube-supports as well as impacting at the tube middle-span; there have even been leakage failures shortly after start-up [Paidoussis,1980].

In heat exchangers, there are four types of flow configuration generally classified as: cross-flow, internal axial flow, external axial flow and annular or leakage flow. Among these flow types, cross-flow induced vibration has been found to be the most destructive in many industrial applications.

As a result of these problems, a great deal of theoretical and experimental research has been conducted on cross-flow induced vibration of heat exchanger tube arrays. Four mechanisms are currently identified [Weaver & Fitzpatrick, 1988]:

(1). turbulent buffeting (forced vibration)

(2). fluidelastic instability (self-excited vibration)

(3). Strouhal periodicity (self-controlled vibration)

(4). acoustic resonance (mixed problems)

Turbulent buffeting and vortex shedding in general cause small amplitude vibrations which in turn may cause long term fretting wear at the tube-supports. On the other hand, fluidelastic instability may quickly result in tube failure due to its large vibration amplitude characteristics. Because of its destructive nature, the mechanism of fluid elasticity has been a subject of extensive research and development over the past two decades.

Experimental studies usually use a small scale physical tube array model which is designed to retain both geometric and dynamic similarity with the prototype. Initially, only the simplest cases of a single tube or a tube row in single phase cross flow were investigated, but as the understanding of the mechanism grew, so did the scope of the research. Now, studies cover many aspects of the subject, including, various tube array patterns, a wide range of tube natural frequencies, the mass damping ratio, and all types of flow, such as single phase air or liquid flow, two phase flow such as air-water, steam-water, and refrigerant R-11.

In the case of single phase flow, significant efforts have been made and the state of knowledge is fairly well developed for predicting the critical instability velocity for a tube array at a given mass damping ratio. Empirical stability diagrams, based on the experimental results from uniform cross flow in single span tube test apparatuses, have been developed to predict the onset of fluidelastic instability. These are given in Weaver & Fitzpatrick [1988], Pettigrew et al [1991], Paidoussis [1982] and Chen [1984].

However, in most types of tube and shell heat exchangers, for example, CANDU steam generators, multi-span tube configurations have been used, and the incoming cross flow is by no means uniform. This type of tube-flow configuration requires special consideration since the vibration mode shape and flow distribution have been found to have significant effects on the onset of the instability. As a result, a number of research projects have been undertaken in the

last few years to study the mode shape and flow distribution effects, mostly in order to develop a more comprehensive guideline for steam generator and fuel bundle design.

Furthermore, in the last decade, the development of theoretical models for fluidelastic instability has also been undertaken, often with the help of the improved understanding afforded by experimental studies. The advantages of a theoretical solution should offset the disadvantages of experimental study, which include the high cost of experimental set-up, the measurement difficulties of strongly coupled motions, the complicated interactions involved in fluidelastic instability and periodic vortex shedding. However, because of the difficulty in modeling the flow field, a completely satisfactory theoretical solution has not yet been obtained. A proper theoretical solution of the flow field would require solution of the 3-D Navier-Stokes equations in a tube bank, with conditions of moving boundaries, unsteady flow due to tube motion, and high turbulence intensity. Such a solution of the flow field in a tube array is unlikely to be successful in the near future. A numerical solution in the practical operating velocity range, which may be more realistic than the analytical solution, has been attempted, but with limited success given the existing numerical techniques and computer power. The most important step of the theoretical solution is to obtain the fluid forces acting on vibrating tubes. Attempts have been made to measure all the unsteady force coefficients [Tanaka & Takahara, 1980, Chen 1983]. Consequently, the theory using this data predicts the instability velocity quite well. However, the large number of measurements necessary for each tube array geometry make it a rather impractical design tool. In addition, effects such as the consequences of changing the pitch ratio cannot be obtained due to the lack of experimental data. Potential flow theory [Chen 1978], Paidoussis et al. [1984] has been proven inadequate. Quasi-steady theory [Price & Paidoussis, 1994] shows much better promise, although this also requires experimental input. A thorough review of theoretical models has been given by Price [1995]. A simple unsteady

model [Lever & Weaver 1986, Yetisir & Weaver 1993] requires few experimental measurements and shows reasonable agreement with experimental results. Thus, an extension of this model could be made to include the effects of multi-span tube and nonuniform flow distribution.

This thesis presents both an empirical and a theoretical study of cross flow fluidelastic instability in multi-span tube bundles, and attempts to more realistically represent the flow induced vibration in the U-bend and feed water inlet regions of nuclear steam generators. The specific objectives of the research are to:

(1). Design and build a test rig to conduct multi-span tube bundle tests.

(2). Identify and characterize the excitation mechanisms in the multi-span tube arrays, and compare them with the single span results.

(3). Investigate the effects of partial flow location, and tube mode shape function.

(4). Investigate the secondary instability phenomenon reported in the literature and study the interaction between the vortex shedding and the fluidelasticity instability mechanisms

(5). Contribute new data to the fluidelastical stability diagram and verify or modify the existing design guidelines.

(6). Modify and extend Yetisir & Weaver's theoretical model to include the effects of nonuniform flow distribution and multi-span tube configurations.

The above objectives have been accomplished, and their delineation is the subject of the present thesis. A literature review, summarizing previous experimental and theoretical studies, is given in Chapter 2.

In Chapter 3, an analytical solution of the mode shape and natural frequency of multi-span tubes is derived. This solution provides a basic and useful tool for the multi-span tube experimental design and analysis. The effect of flow location on the single span tube with

various support configurations is investigated theoretically, and later is to be compared with the experimental data. In addition, the higher mode excitation is also studied.

The design and construction of the water tunnel is presented in Chapter 4. Chapter 5 outlines the details of the equipment and procedures. The preliminary added mass and damping tests are also given in this chapter.

The results of the experiments are presented in Chapter 6, which includes those of the single span full admission tests, single span partial admission tests, two-span tests, and three-span tests. In some cases, both single flexible and full flexible tube arrays are used for the comparison. This chapter also contains a detailed discussion of the present results, including their comparison with the existing experimental data and empirical design guidelines.

The theoretical study is the subject of Chapter 7. Attempts have been made to improve the existing model. The comparison between the theoretical predictions and the experimental results are made. Finally, Chapter 8 gives concluding remarks about the present work as well as recommendations for future work.

CHAPTER 2

LITERATURE REVIEW

2.1 Introduction

Flow induced vibration of structures involves interactions between the inertial and elastic forces of the structure and the fluid forces. The exact determination of the nature of the interaction and the magnitude of the fluid forces is often difficult, since the phenomena of flow induced vibrations are complex and diverse. Very often, an individual excitation mechanism is not well understood, let alone a combination of mechanisms which accounts for many of the practical cases. Prior to the 1960's, flow induced vibration problems were rarely mentioned except in the aerospace industry. However, in recent years, significant developments in this field have been made, and its applications can be found in many other industries, including steam generators, high rise buildings, power transmission cables, ocean structures, etc.

Four basic tube array geometries of heat exchangers are shown in Figure 2.1. In general, there are four kinds of flow induced vibration mechanism, as mentioned in Chapter 1. Those mechanisms can be divided into three basic categories which are mathematically distinct: forced vibrations, self-excited vibrations and self-controlled vibrations. These are equilibrium, eigenvalue and mixed problems, respectively, and correspond to steady state response, stability and resonance phenomena [Weaver, 1992]. The idealized response of a flexible cylinder in a tube array subjected to cross flow is shown in Figure 2.2. There are three flow excitation mechanisms involved in the total range of the cross flow velocity: turbulence buffeting (forced vibration), vortex shedding periodicity (self-controlled) and fluidelastic instability (self-excited). A tube response spectrum at a liquid flow velocity where the tube is excited by

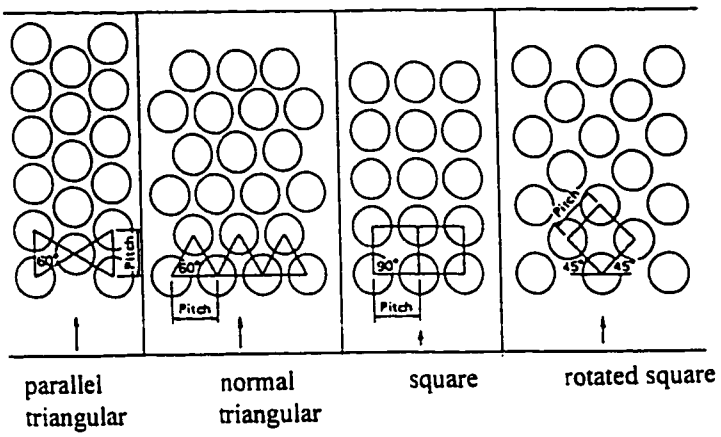

Figure 2.1 Four basic tube array geometries of heat exchangers

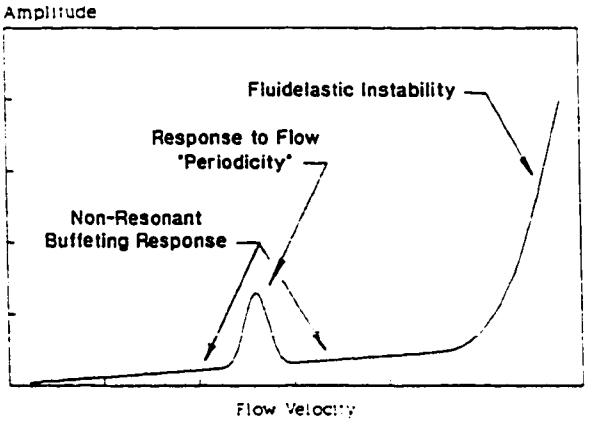

Figure 2.2 Typical amplitude response of a tube array to liquid cross flow

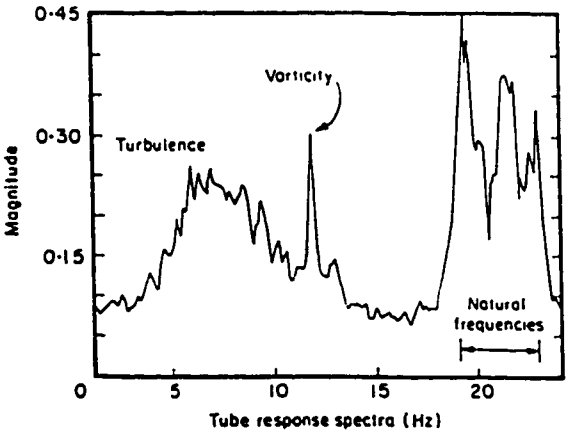

Figure 2.3 Frequency spectrum of an oscillating tube in cross flow

[Weaver & Fitzpatrick, 1988]

broadband turbulence is shown in Figure 2.3.

Forced vibrations occur when the fluid forces are a function of time only, independent of structural motion. An example is turbulent buffeting, which is caused by broad band turbulent fluctuations in the flow. The nature of the oscillation is random, and its amplitude is usually smaller than those caused by other mechanisms. Failure from fretting wear may occur only after years of service. Their modeling solutions rely on the use of statistical techniques to determine the force field and response spectra.

In self-controlled vibrations, the flow periodicity exists in the flow in the absence of structural oscillation. If the frequency of the periodicity is well removed from the natural frequencies of the structure, the vibration is a simple forced response with no interaction between fluid forces and the structural displacement. However, when the flow periodicity frequency coincides with one of the structural natural frequencies, resonance occurs. If the response amplitude becomes sufficiently large, the structural response controls the fluid excitation. Strouhal periodicity resonance is caused by a periodic flow phenomenon such as vortex shedding or shear layer instability. It was debated for a long time whether the vortex shedding mechanism exists in tube arrays. This was a period of confusion, in which the broad band turbulence and discrete excitation tended to be treated as one mechanism. However, it is now known that vortex shedding exists in staggered arrays, and shear layer instability in in-line arrays [Weaver, 1992]. This mechanism can cause vibration with significant amplitudes when the Strouhal frequency coincides with the natural frequency of the tubes. Such a phenomenon is called "lock-in". Nevertheless, "lock-in" only occurs in the early rows of the tubes subjected to liquid crossflow.

Similarly, acoustic resonance in gas flow occurs when the frequency of a periodic flow phenomenon (turbulence, vortex shedding, or shear layer instability) coincides with the natural

frequency of an acoustic standing wave in the duct. The standing waves are generally at a right angle to both the tubes and the mean flow direction. Although not necessarily strong enough to force the tubes to vibrate, acoustic resonance, up to 160 dB sound pressure, can cause severe damage and destruction to the ductworks within a short period of time. In addition, excessive noise level may be intolerable to nearby workers.

2.2 Historical Development of Cross Flow Fluidelastic Instability

Fluidelastic instability is a self-excited vibration problem, and is the most destructive excitation mechanism. In self-excited vibration, the fluid force is a function of structural displacement. Physically, it is a problem of stability, and is responsible for most short term tube failures [Paidoussis,1980]. Comprehensive reviews have been given [Pettigrew et al. 1978, Paidoussis 1983, Weaver & Fitzpatrick 1988]. The instability can cause violent tube oscillation. Most severe damage is associated with fretting wear at the tube support plates or even tube-to-tube clashing in the U-bends [Yu 1986]. Due to the fact of its being a self-excitation mechanism, the amplitude of the vibration will continue to grow with increasing flow velocity once a critical instability velocity is exceeded. The fluidelastic instability arises from the interaction between fluid forces and the elastic and inertial forces of the structure. At and above a critical flow velocity, a feedback mechanism exists between the vibrating tubes and the surrounding fluid such that energy from the flow is continuously transferred to the tubes. As a result, the amplitude of vibration increases exponentially to unacceptable levels. Typically, the design approach is to keep the natural frequency of tube arrays high enough, so that the design cross flow velocity is well below the critical velocity. However, this approach may result in overconservative designs of heat exchangers at the expense of thermal efficiency and higher capital cost. On the other hand, tube failures still remain as an operational problem due to

incomplete understanding of the mechanism. Extensive theoretical and experimental research has been conducted to obtain a better understanding of the excitation mechanism and to find methods to correctly predict the threshold velocity.

Robert [1966] found that jets formed behind a single row of cylinders. He attributed the instability to the time lag between the tube displacement and fluid force. He proposed a "jet switching" mechanism which is synchronized with adjacent tube motions. The synchronization can extract energy from the flow in excess of the system dissipation capability and potentially result in large displacement oscillations.

The research by Connors [1970], also for a single row of tubes, is regarded as the first to establish the nature of the fluidelastic mechanism. He proposed that the instability is the result of displacement-induced forces generated by interaction between adjacent tubes. But Yeung & Weaver [1983] found that a single flexible tube could become unstable in a rigid square tube array with a pitch to diameter ratio Pr = 1.5. This phenomenon suggests that both Connors' displacement mechanism and Robert's time-lag mechanism may be operative and that a simple model is not sufficient to explain all aspects of the instability.

Connors [1970] measured the static force coefficients for a row of cylinders and developed a semi-empirical model to predict fluidelastic instability.

$$\frac{V_p}{f_n d} = K\left(\frac{m\delta}{\rho d^2}\right)^{\alpha} \qquad (2\text{-}1)$$

where V_p is the critical pitch velocity, $V_p = V_\infty \cdot P_r / (P_r - 1)$, V_∞ is the freestream velocity,

$P_r = P/d$ is the tube pitch ratio, Pis the tube pitch distance, d is the tube diameter,

$V_r = V_p/f_n d$ is the reduced velocity,

f_n is the tube vibrating frequency,

δ is logarithmic decrement of damping (in water or in air),

m is the mass of the tube per unit length (including added mass),

ρ is the density of the surrounding fluid,

$\delta_s = m\delta/\rho d^2$ is the mass damping parameter,

K is an instability constant.

In Connors' equation, the exponent α in Equation (2-1) is defined as 0.5. Initially, K was defined as 9.9. Later Pettigrew et al. [1978] and [1991] modified this coefficient to be 3.3 and 3.0 respectively, while the ASME non-mandatory code recommends a value of 4.0 [Au-Yang et al., 1991]. However, other experimental studies showed that K is array dependent and the exponent may be different than 0.5. Weaver and Grover [1978] showed that grouping the damping, δ, and the mass ratio, $m/\rho d^2$, into a mass-damping parameter, $m\delta/\rho d^2$, may be incorrect. Theoretical studies by Chen [1983], Weaver & Yetsir [1993] showed that Connors' equation is valid only at a high value of δ_s. The effects of damping δ [Weaver & Grover, 1978], mass ratio $m/\rho d^2$ [Weaver & El-Kashlan, 1981], tube mass m [Weaver & Yeung, 1984], fluid density ρ [Gibert et al., 1977], approach flow direction [Yeung & Weaver, 1983], and upstream velocity [Gorman, 1980] on fluidelasticity have been studied. Results are sometimes contradictory. For example, the data of Franklin and Soper [1977] show that the turbulence level reduces the critical velocity, while the data of Southworth and Zdravkovich [1975] show that turbulence increases the critical velocity. The inconsistency in defining related parameters and critical velocity largely contributes to the significant scatter in the data bank. Paidoussis [1983] and Chen [1989] addressed such problems. For example, for the tube natural frequency and damping, some researchers use in-vacuo values, some use quiescent fluid values, and some others use observed values at the instability threshold. In addition, the critical velocity may not be easily determined from the plot of amplitude (or acceleration) vs pitch velocity, particularly

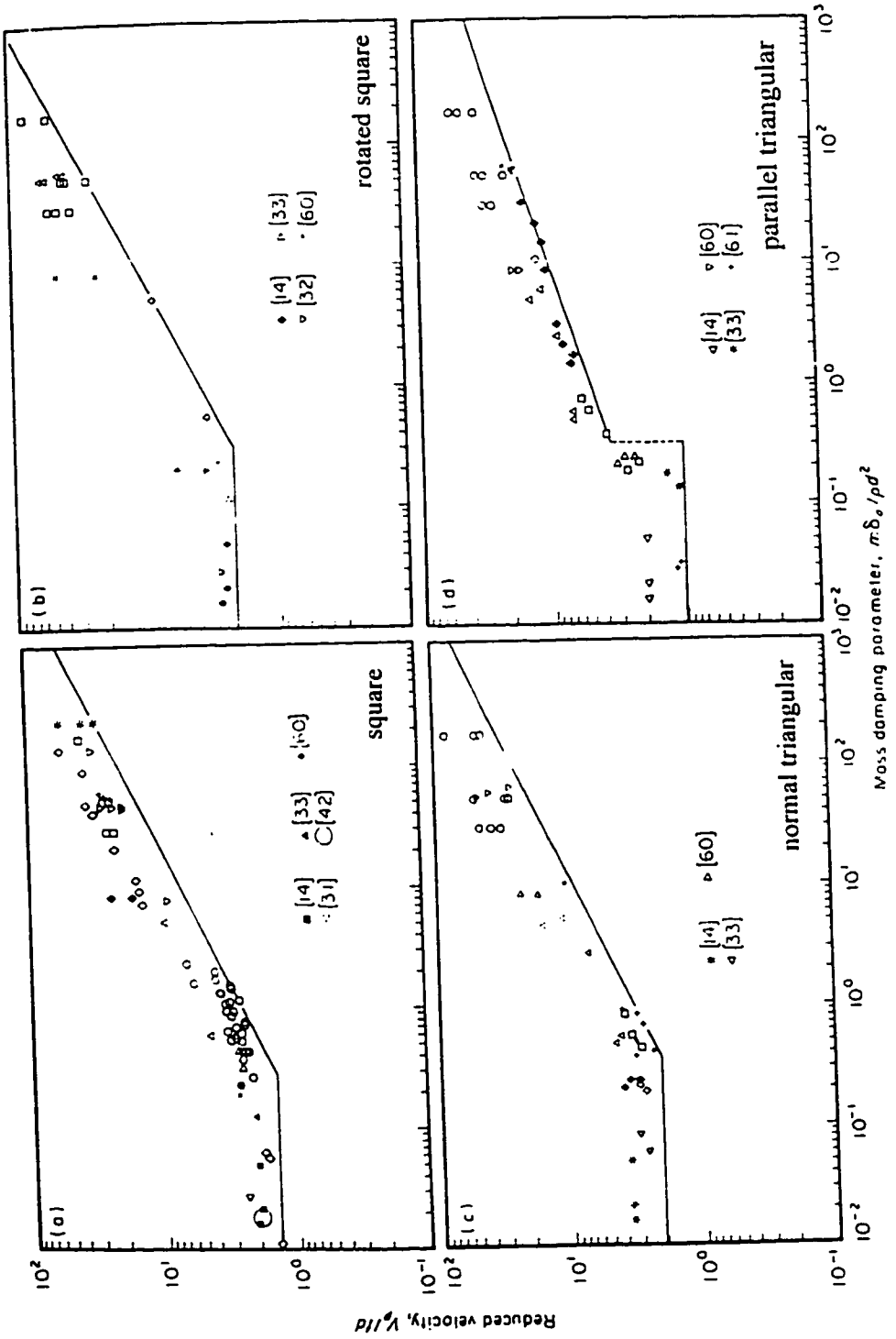

Figure 2.4 Critical reduced velocity of fluidelastic instability [Weaver & Fitzpatrick, 1988]

Table 2.1 Summary of fluidelastic instability design guidelines

Fluidelastic Instability Model	Author	Suggested coefficients K	α	β	Applicability $m\delta/\rho d^2$	Tube pattern
$K(m\delta/\rho d^2)^{\alpha}$	Pettigrew & et al. [1978]	3.3	0.5		All	All
	Pettigrew & Taylor [1991]	3.0	0.5		All	All
	Au-Yang [1991]	4.0	0.5		All	All
	Chen [1984]	2.35	0.5		> 0.7	90
		2.80	0.5		> 1.0	60
		2.10	0.15		< 0.7	90
		2.80	0.17		< 1.0	60
	Weaver & Fitzpatrick [1988]	2.5	0.48		> 0.3	90
		4.0	0.48		> 0.3	45
		3.2	0.40		> 0.3	30
		4.8	0.30		> 0.3	60
		1.4	0		< 0.3	90
		2.2	0		< 0.3	45
		2.0	0		< 0.3	30
		1.0	0		< 0.3	60
	Blevins [1977]	2.4	0.5		> 0.7	90
		3.5	0.5		> 0.7	45
		2.8	0.5		> 0.7	30
		2.3	0.5		> 0.7	60
		2.7	0.21		< 0.7	All
$K\,\delta^{\alpha}(m/\rho d^2)^{\beta}$	Weaver & El-Kashlan [1981]	4.6	0.29	0.21	air	60
$K\,\delta^{\alpha}(m/\rho d^2)^{\beta}(Pr-1)$	Paidoussis [1981]	5.8	0.4	0.4		

in liquid flow. In general, there is not a simple correlation between V_r and δ_s. A more general form than equation (2-1) was proposed by Paidoussis [1983], Weaver & El-Kashlan [1981]:

$$\frac{V_p}{f\,d} = K\left(\frac{m}{\rho d^2}\right)^{\alpha}\delta^{\beta} \qquad (2\text{-}2)$$

Weaver & Fitzpatrick [1988] provides stability boundaries based on experimental data for the four basic tube array patterns, shown in Figure 2.4. Meanwhile, there are several widely accepted design guidelines [Au-Yang, 1990], which are listed in Table 2.1.

2.3 Different Correlations for Low and High Mass Damping Parameters

Chen [1989], Yetisir & Weaver [1993] proposed that two different types of instability mechanisms exist in high δ_s (gas flow) and low δ_s (liquid flow). In gas flow, the fluidelastic instability is dominated by the fluid stiffness force, while in liquid flow, the damping force dominates the instability. In the low δ_s range, several theoretical models, Lever & Weaver [1982], Chen [1983], Price & Paidoussis [1984], and Yetisir & Weaver [1993], predicted multiple instability regions. Chen & Jendrzejcyk [1983] showed multiple unstable reduced velocity regions obtained from tests on a single row of tubes subjected to water flow. However, the available experimental data on liquid cross flow is relatively sparse and the instability threshold is usually not well defined, compared with that in air flow.

As suggested by Weaver & Yeung [1984], Weaver & Fitzpatrick [1988], the correlation of V_r and δ_s in liquid flow has a very different form than that in air flow. The authors argued V_r is independent of δ_s when the latter has a value less than 0.3. On the other hand, Pettigrew & Taylor [1991] recommended that the exponent α in equation (1-1) remains the same value of 0.5 regardless of the range of δ_s. Chen [1984, 1989] and Blevins [1984] suggested different values of α used in liquid flow. Those coefficients are also shown in Table 2.1.

2.4 The Effects of Non-Uniform Flow Distribution and Partial Flow Admission

The correlations mentioned above were based on experimental data from single span

tubes with uniform cross flow. In many heat exchanger configurations, the flow velocity along the tube span may not be uniform as assumed in equations (2-1) or (2-2). A Babcock & Wilcox CANDU steam generator is shown in Figure 2.5. The cross flow at the U-bend region is highly nonuniform, while at the flow entrance, only part of the tubes are subjected to the cross flow. In order to adapt the design formula to real heat exchangers which mostly have multi-span, non-uniform flow distribution configurations, equations (2-1) and (2-2) have to be modified and extended to account for the non-uniform velocity distribution and tube oscillation mode shape.

The effective velocity or equivalent uniform velocity V_e has been introduced to compute the effects of the nonuniform flow.

$$V_e = V_p \left[\frac{\int_0^{L_x} \psi^2(x)\phi_i^2(x)dx}{\int_0^{L} \phi_i^2(x)dx}\right]^{0.5} \qquad (2\text{-}3)$$

where $V_p(x) = V_p \psi(x)$, $\psi(x)$ is flow velocity distribution along the tube axial direction x,

$\phi_i(x)$ is *ith* mode shape function of the tube vibration,

L is the total length of the tube, L_x is the length of the tube subjected to cross flow.

Unlike the semi-empirical correlation of (2-1), equation (2-3) is derived theoretically. This relation was proposed by several investigators [Franklin & Soper 1977, Connors 1978, Pettigrew 1978] and has been used in practical applications. A different derivation is given in Appendix C.

The stability threshold for the *i*th mode of a N span tube array with velocity distribution $V_p\psi(x)$ may be written as a generalization of equation (2-1), provided that the tube mass per

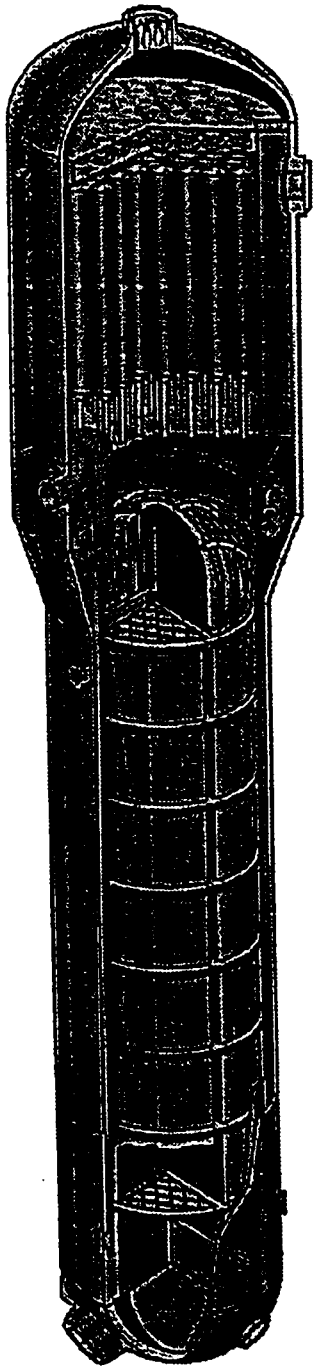

Figure 2.5 A Babcock & Wilcox steam generator

unit length, m, is constant along the tube span x

$$\frac{V_{pi}}{f_i\, d} = K\left(\frac{m\delta}{\rho d^2}\right)^{0.5} \left[\frac{\int_0^{L} \phi_i^2(x)dx}{L_x \int_0^{} \psi^2(x)\phi_i^2(x)dx}\right]^{0.5} \qquad (2\text{-}4)$$

where subscript *i* refers to parameters associated with the *ith* mode and $\phi_i(x)$ is the tube vibration mode shape for the *ith* mode of vibration. The effective pitch velocity V_{pi} is taken as the critical velocity for instability for each mode.

Several investigations have been conducted to verify equation (2-4) [Franklin & Soper 1977, Waring & Weaver 1988, Weaver & Goyder 1990, Weaver & Parrondo 1991, Parrondo et al. 1995]. In all these tests, except the last one, tubes in normal or parallel triangular array patterns were subjected to uniform air flow with partial admission, i.e., flow only cross part of the tube length. Franklin & Soper's test showed that Connor's equation may give conservative or nonconservative results, depending upon the location of the flow and the percentage of the tube subjected to cross flow, i.e., the admission ratio. Weaver et al. found that results from theoretical predictions based on equation (2-4) with the exponent of $\alpha = 0.5$ do not agree with the experimental data from a parallel triangular tube array, but agree better when $\alpha = 0.30$.

A substantial number of data in the literature shows that the design equation (2-4) is not always valid. The quadratic form of the mode shape in the numerator is the result of the linear viscous damping assumption, while the quadratic form of the velocity and mode shape functions in the denominator are the result of the assumption that the fluid force is proportional to the dynamic head (velocity squared). As we already know, the flow-structure interaction is dominated by different mechanisms at low and high mass damping parameter ranges. In

addition, the non-linearity in the flow may cause significant discrepancy between prediction and reality.

The effects of velocity distribution and mode shape were included in the last term on the right hand side of equation (2-4). When the entire tube length of a span, r, from support l_1 to l_2 is subjected to an uniform flow velocity, the velocity distribution function $\psi(x)$ is equal to unity from l_1 to l_2 and zero elsewhere, and L is the entire length of a multi-span tube. Such simplifications permit the integrals in equation (2-4) to be written in the following form, which has a clear physical interpretation

$$S_i = \frac{\int_{l_1}^{l_2} \varphi^2{}_i(x)\, dx}{\int_0^L \varphi^2{}_i(x)\, dx} \qquad (2\text{-}5)$$

S_i is called the energy fraction since it represents the fraction of the total kinetic energy in the *ith* mode contributed by the *rth* span (l_1 - l_2), which is exposed to the flow. The same procedure can also be applied to a single span tube of length L which is partially subjected to an uniform flow at the length of $l_1 < x < l_2$. The term, partial admission factor, PAF, was also used by some researchers [Waring & Weaver, 1988]

$$PAF_i = \left[\frac{\int_0^l \varphi^2{}_i(x)\, dx}{\int_{l_1}^{l_2} \varphi^2{}_i(x)\, dx}\right]^{0.5} = \left(\frac{1}{S_i}\right)^{0.5} \qquad (2\text{-}6)$$

which is simply another form of S_i. However, we will not use this term in this thesis because

it assumes the exponent α to be 0.5.

The same authors [Waring & Weaver, 1988] suggested that PAF_i can be obtained experimentally by comparing the partial admission and full admission cases. But this formula is only valid for the fundamental mode because only the fundamental mode can become unstable in the full flow admission.

$$PAF_1 = \frac{\{\frac{V_p}{f_1 d}\}_{Partial\ admission}}{\{\frac{V_p}{f_1 d}\}_{Datum\ case}} \tag{2-7}$$

where the full admission configuration is defined as the datum case. The comparison can be made between the theoretical calculation of equation (2-6) and the experimental result from equation (2-7). However, equation (2-7) is obtained by assuming that the damping value in various span configurations does not change substantially. This was found to be true for a single span experiment with average damping values in air [Waring & Weaver, 1988].

2.5 Summary of Previous Partial Flow Admission Results

A modified form of equation (2-4) for multiple span tubes has been proposed which appears to fit the experimental data better [Weaver & Parrondo, 1991]

$$\frac{V_{pi}}{f_i d} = K(\frac{m}{S_i \rho d^2})^{\alpha} \delta_i^{\beta} \tag{2-8}$$

Previous experimental results are summarized in this section. The different exponents α, β and constant K used in the semi-empirical correlation models are listed in Table 2.2 and these models are defined as I, II, III or the purpose of the following discussion.

Table 2.2 Constants for equations (2-8)

Source	K	α	β
Pettigrew et al. [1991] (I)	3.0	0.5	0.5
Weaver-Fitzpatrick [1988] (II)	4.8 ($m\delta/S_i\rho d^2$	0.3	0.3
	>0.3)	0.0	0.0
Weaver-ElKashlan [1981] (III)	4.6	0.29	0.21

The experiments of Waring & Weaver [1988] were conducted in a wind tunnel with uniform cross flow 33 to 100% of the length of the single span tubes, which were in a parallel triangular pattern with P/d = 1.47. The tubes were pinned at both ends. The flow location was varied from the center of the span to the end of the span. Tests were also conducted with uniform flow over one span in two-span or three-span tube arrays with equal span lengths. The following conclusions were drawn by the authors:

1. For admission ratios greater than 30% on single-span, simply supported tubes, the theory is conservative when the flow is centered on the span. However, the model (I) is non-conservative when flow is located towards the tube supports, especially for the lower percent admission ratios.

2. The model (I) does not appear to work well for multiple span tubes with flow over only one span. In the 2 and 3-span cases tested, the theory was substantially non-conservative. A failure to predict the correct mode was also observed.

The experiments of Weaver & Parrondo [1991] were done on the same test rig and the identical tube array configuration. Unequal span lengths were adopted for the 3-span tubes. In addition, cases with a free support condition at one end were tested. The significant phenomena observed were:

1. All three models listed in Table 2.2 give reasonable, conservative estimates of the

stability behavior of the single span array with the entire span subjected to uniform cross flow.

2. All three models give reasonable engineering predictions of the instability mode and threshold of flow when there is partial admission at one non-center span with intermediate simple supports, and the other end is set free. Interestingly, the instability mode is higher than the *1*st mode.

3. The Connors' type model of Pettigrew et al. (I) fails to predict the correct mode of instability, and non-conservatively estimates the threshold velocity, for the cases of partial admission over the entire central span. On the other hand, the other two models listed in Table 2.2 both predict the correct instability mode and provide a conservative estimate of the threshold velocity.

The experiments of Weaver & Goyder [1990] were conducted in a wind tunnel for a tube array of normal triangular geometry with Pr = 1.4. Three spans at most were used in the test. One significant difference between this experiment and Waring & Weaver [1988], Weaver & Parrondo [1991] is that turning vanes were used to guide the uniform flow past one, two or three tube spans. This is a case of multi-span with full admission with uniform flow distribution (direction changes, but magnitude remains the same). The agreement between this experiment and a Connors' type prediction was found to be reasonably good. The authors addressed this agreement by saying that it may be related to the relationship of $(m\delta/\rho d^2)^{\alpha}$ with different tube geometries. As suggested in Table 2.1, $\alpha = 0.4$ of normal triangular arrays is closer to Connors' 0.5 than that of 0.3 for parallel triangular arrays.

Parrondo et al. [1995] conducted two-span partial flow admission tests in a water tunnel. Tubes were clamped at one end, free at the another end. The intermediate support was moveable so that different flow configurations could be tested. Multiple instability regions were observed, while only the 1st and 2nd instability modes displayed significant vibration amplitudes. Model

(I) was somewhat nonconservative for many data points, while model (II) fitted the data quite well. Thus Parrondo et al. recommended model (II) for design purposes.

2.6 Damping in Multi-Span Heat Exchangers

Damping is a very complicated subject in the study of flow induced vibration in heat exchangers, especially in the presence of multiple supports. Unfortunately in many cases, damping can be given physical interpretations but cannot be measured precisely. In this section, a brief review is presented which is later helpful in understanding and interpreting the measurement results.

The mechanism which dissipates energy during vibration is called damping. In fluid flow, oscillating structures are subjected to several forms of damping which operate at the same time. Fluid damping is caused by energy transfer from an oscillating structure to the surrounding fluid and is due to the action of viscosity. Structural damping is caused by the internal friction in solid material as it deforms during vibration. In the presence of support plates, damping is also caused by the interaction between tube and support. Pettigrew et al. [1986] listed several possible forms of fluid and structure damping:

- internal or material damping,
- viscous damping between tube and fluid,
- squeeze-film damping in the clearance between tubes and tube supports,
- flow dependent damping due to fluid flow around the tube,
- damping due to friction at the tube supports,
- damping dissipated by tube impact on the support and by the resulting traveling waves.

Flow dependent damping is difficult to study because it is impossible to separate energy dissipating fluid forces from hydrodynamic forces. Usually such a mechanism is taken into

account by the fluidelastic instability phenomenon itself since instability is caused by the combined effects of those fluid forces. At the onset of instability, the total system damping must be negative in order for vibration amplitude to increase.

Goyder [1982] identified two principal types of tube motion at the tube support: rocking and lateral motion, as shown in Figure 2.6. Rocking type motion is predominant in the lower modes, whereas higher mode vibration tends to be lateral motion with small amplitude. Damping due to rocking motion is likely to be less pronounced than lateral motion. The actual motion at a given support may be a combination of rocking and lateral motion.

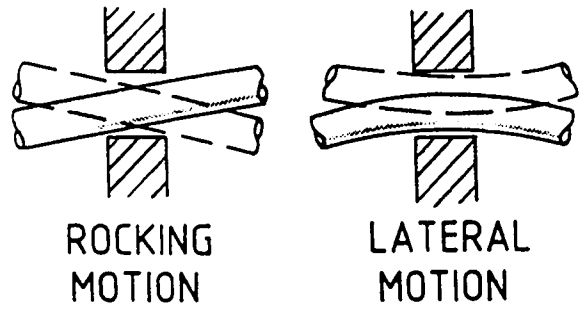

Figure 2.6 Type of tube motion at support location [referred by Pettigrew et al., 1986]

Three principal types of dynamic interaction exist between the tube and tube-supports, namely, sliding, impacting and scuffing. The latter involves impacting at an angle followed by sliding. They are shown in Figure 2.7. The energy dissipated by sliding is due to friction and is related to the product of contact force and displacement. The energy dissipated by impact is due to the local deformation of the support, followed by stress wave propagation in the support and local deformation followed by high frequency traveling waves in the tube. In practice, the interaction between tube and tube-supports may be a combination of the above. Several

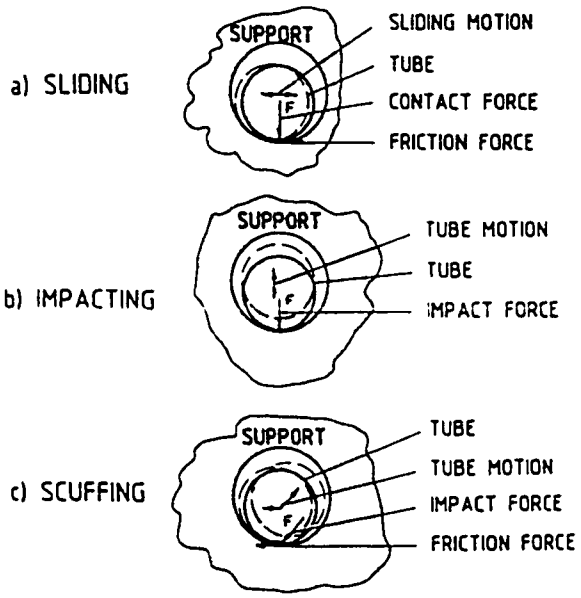

Figure 2.7 Type of dynamic interaction between tube and tube support [Pettigrew et al., 1986a]

important parameters were discussed by Pettigrew et al. [1986a,b], including:

• *Number of supports:* Assuming that span length and other tube parameters are kept constant, damping by friction at the supports increases with the number of supports.

• *Vibration frequency:* There is no apparent relationship between damping (except viscous damping) and frequency.

•*Vibration amplitude:* Damping may decrease with vibration amplitude. For sliding type damping, friction damping does not increase with amplitude as would be expected from linear damping. On the other hand, damping may increase with amplitude. At low amplitude, the tube is in contact with the support and sliding dominates. At a higher amplitude, the tube starts rattling within the tube-support. This type of motion may cause impacting type interaction and its corresponding non-linearity which would tend to increase damping. Therefore, no definite

trend of damping as a function of amplitude has been established.

• *Tube diameter or mass:* Since friction force, energy dissipated and potential energy all are proportional to tube size or mass, damping is independent of tube size or mass.

• *Side loads:* Misalignment of tube-supports or fluid drag force changes side loads. Small side loads may prevent impacting and thus, reduce damping, whereas moderate side loads may increase damping by increasing friction. Very large side loads reduce sliding and damping.

• *Higher modes:* Since higher modes involve relatively less interaction between the tube and tube-support, damping tends to decrease with mode order for mode orders higher than the number of spans.

• *Support thickness:* Damping is roughly proportional to support thickness up to 15 mm. Beyond 15 mm, it is not certain that thickness increases damping.

• *Clearance:* The tube would normally touch most supports on one side or the other. Thus, the dynamic interaction between tube and support is taking place near one side and is not much affected by the proximity of the opposite side, depending on the diameteral clearance. This is true in most cases except when the amplitude is very large or the clearance is very small, thus leading to greater damping.

In general, friction (coulomb) and impacting damping are the most important energy dissipating mechanisms in gas flow. On the other hand, tube-to-fluid damping, squeeze-film damping and friction damping are the most important mechanisms in liquid flow. Impact damping in liquids may be much less than in gases. Impact force may be attenuated and contact time lengthened by squeeze-film forces. This would tend to eliminate higher frequency traveling waves.

In conclusion, the dynamics between the tube and the tube-supports is inherently a non-linear phenomenon. Efforts have been made [Pettigrew et al., 1986] to develop a semi-

empirical model to predict interaction damping. Computer programs, such as VIBIC [Ko & Rogers, 1981], have been developed to calculate fretting-wear and squeeze-film damping. However, direct measurement is still the most reliable method of addressing total damping, especially under laboratory conditions.

CHAPTER 3

NATURAL FREQUENCIES, MODE SHAPES AND PARTIAL ADMISSION EFFECTS OF MULTI-SPAN BEAMS

3.1 Analytical Derivation

The natural frequencies and mode shapes for multi-span tubes with unequal span length are determined analytically in this chapter. The results are used with an analysis of partial admission effects in order to establish theoretical predictions and to obtain physical insights into the tube response behaviors.

3.1.1 Free Vibration of N Span Beams Simply Supported at the Ends

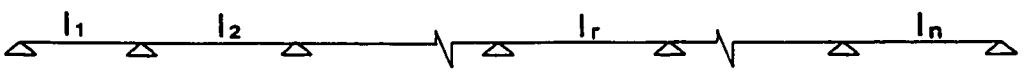

Figure 3.1 Multi-span beam with simple supports

Consider the case of a continuous beam with N spans simply supported at the two ends and at (N - 1) intermediate supports, as shown in Figure 3.1. Assume l_1, l_2, ···, l_n to be the lengths of consecutive spans, the stiffness of the beam being the same for all spans. Taking the origin of the coordinate at the left end of each span, based on the Euler-Bernoulli equation, the lateral deflection is governed by

$$EI\frac{\partial^4 u}{\partial x^4} + m\frac{\partial^2 u}{\partial t^2} = 0$$

the general solution of each span can be written in the form as [Timoshenko et al. 1955]

$$u(x) = a \sin kx + b \cos kx + c \sinh kx + d \cosh kx \tag{3-1}$$

where

$$f = \frac{k^2\lambda}{2\pi}, \quad \lambda = \sqrt{\frac{EI}{m}}$$

in which a, b, c, and d are constants to be determined by the end conditions of the beam, f is the natural frequency, E, I, and m are defined as Young's modulus, moment of inertia of the cross section, and mass per unit length, respectively. Equation (3-1) can be used to determine the shape of the deflection curve during vibration. Considering span *r* and observing that the deflection at the left end (x=0) is equal to zero, the normal function for the span *r* will be

$$u_r = a_r(\cos kx - \cosh kx) + c_r \sin kx + d_r \sinh kx \tag{3-2}$$

in which a_r, c_r and d_r are end condition constants. At a simply supported end, the displacement and bending moment are zero, i.e., u = 0, and $d^2u/d^2x = 0$. The consecutive derivatives of (3-2) with respect to x will be

$$u'_r = -a_r k(\sin kx + \sinh kx) + c_r k \cos kx + d_r k \cosh kx \tag{3-3}$$

$$u''_r = -a_r k^2(\cos kx + \cosh kx - c_r k^2 \sin kx + d_r k \sinh kx \tag{3-4}$$

Substituting x = 0 in equations (3-3) and (3-4) we obtain

$$(u'_r)_{x=0} = k(c_r + d_r), \quad (u''_r)_{x=0} = -2k^2 a_r \tag{3-5}$$

From the conditions at the simply supported ends of the beam, it can now be concluded that $a_1 = a_{n+1} = 0$.

Considering the conditions at the right end of the span r we have

$$(u_r)_{x=l_r} = 0, \quad (u'_r)_{x=l_r} = (u'_{r+1})_{x=0}, \quad (u''_r)_{x=l_r} = (u''_{r-1})_{x=0} \tag{3-6}$$

or by using eqs. (3-2), (3-3) and (3-4),

$$a_r(\cos kl_r - \cosh kl_r) + c_r \sin kl_r + d_r \sinh kl_r = 0 \tag{3-7}$$

$$-a_r(\sin kl_r + \sinh kl_r) + c_r \cos kl_r + d_r \cosh kl_r = c_{r+1} + d_{r+1} \tag{3-8}$$

$$a_r(\cos kl_r + \cosh kl_r) + c_r \sin kl_r - d_r \sinh kl_r = 2a_{r+1} \tag{3-9}$$

Adding and subtracting (3-7) and (3-9) we obtain

$$a_r \cos kl_r + c_r \sin kl_r = a_{r+1}, \qquad a_r \cosh kl_r - d_r \sinh kl_r = a_{r+1}$$

from which , provided sin kl_r is not zero,

$$c_r = \frac{a_{r+1} - a_r \cos kl_r}{\sin kl_r}, \quad d_r = \frac{-a_{r+1} + a_r \cosh kl_r}{\sinh kl_r} \tag{3-10}$$

and

$$c_r + d_r = a_r(\coth kl_r - \cot kl_r) - a_{r+1}(\operatorname{cosech} kl_r - \operatorname{cosec} kl_r) \tag{3-11}$$

Using the notations:

$$\begin{aligned} \coth kl_r - \cot kl_r &= g_r, \\ cosech\ kl_r - \operatorname{cosec} kl_r &= h_r, \end{aligned} \tag{3-12}$$

we obtain

$$c_r + d_r = a_r g_r - a_{r+1} h_r$$

In the same manner for the span $r + 1$,

$$c_{r+1} + d_{r+1} = a_{r+1} g_{r+1} - a_{r+2} h_{r+1} \tag{3-13}$$

Substituting (3-10) and (3-13) into (3-8) we obtain:

$$a_r h_r - a_{r+1}(g_r + g_{r+1}) + a_{r+2} h_{r+1} = 0 \tag{3-14}$$

Writing an analogous equation for each intermediate support, the following system of (n-1) equations will be obtained:

$$\begin{aligned} - a_2(g_1 + g_2) + a_3 h_2 &= 0 \\ a_2 h_2 - a_3(g_2 + g_3) + a_4 h_3 &= 0 \\ \cdots\cdots\cdots\cdots\cdots\cdots\cdots\cdots \\ \cdots\cdots\cdots\cdots\cdots\cdots\cdots\cdots \\ a_{n-1} h_{n-1} - a_n(g_{n-1} + g_n) &= 0 \end{aligned}$$

By putting the determinant of these equations to zero, the frequency equation for the vibration of continuous beams will be obtained.

$$\Delta_n \equiv \Delta(l_1, l_2, \cdots l_n) \equiv \begin{vmatrix} g_1+g_2, & h_2, & 0 & & \\ h_2, & g_2+g_3, & h_3 & & \\ 0, & h_3, & g_3+g_4 & & \\ \cdots & \cdots & \cdots & \cdots & \cdots \\ & & & g_{n-3}+g_{n-2}, & h_{n-2}, & 0 \\ & & & h_{n-2}, & g_{n-2}+g_{n-1}, & h_{n-1} \\ & & & 0, & h_{n-1}, & g_{n-1}+g_n \end{vmatrix}$$

which can be evaluated by the formula

$$\Delta_n - (g_{n-1} + g_n)\Delta_{n-1} + h^2_{n-1}\Delta_{n-2} = 0$$

Particular cases:

- Two spans:

$$g_1 + g_2 = 0$$

- Three spans:

$$(g_1+g_2)(g_2+g_3)-h^2_2=0 \qquad (3\text{-}15)$$

- Four spans:

$$(g_1+g_2)(g_2+g_3)(g_3+g_4)-h^2_2(g_3+g_4)-h^2_3(g_1+g_2)=0$$

3.1.2 The Free End at the Last Span

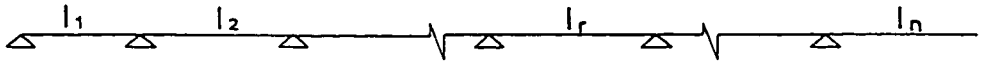

Figure 3.2 Multi-span beam with one end free

In this case, the general solution can be modified as:

$$a_1(\cos kl_1 + \cosh kl_1) + c_1(\sin kl_1 + \sinh kl_1) = 0$$

At the right free end, the bending moment and the shear are zero, i.e., $d^2u/d^2x = 0$, $d^3u/d^3x = 0$.

The conditions at the junction of the first two spans are:

$$\begin{aligned} &a_1(\cos kl_1 + \cosh kl_1) + c_1(\sin kl_1 + \sinh kl_1) = 0 \\ &a_1(-\sin kl_1 + \sinh kl_1) + c_1(\cos kl_1 + \cosh kl_1) = c_2 + d_2 \\ &a_1(\cos kl_1 + \cosh kl_1) + c_1(\sin kl_1 + \sinh kl_1) = 2a_2 \end{aligned}$$

hence

$$(c_2 + d_2)g_1 = a_2\left\{\frac{2(1 + \cosh kl_1 \cos kl_1)}{\sinh kl_1 \sin kl_1}\right\} = a_2\chi_1$$

But

$$c_2 + d_2 = a_2g_2 - a_3h_2$$

hence

$$a_2\left(\frac{\chi_1}{g_1} + g_2\right) - a_3 h_2 = 0 \qquad (3\text{-}16)$$

The calculation of the determinant can be performed in a manner similar to that of the simply supported ends except that ϕ_1 must be replaced by $-\chi_1/\phi_1$. In the case of two free ends, the replacement of ϕ_n by $-\chi_n/\phi_n$ is again necessary.

3.1.3 One or Both Ends Fixed

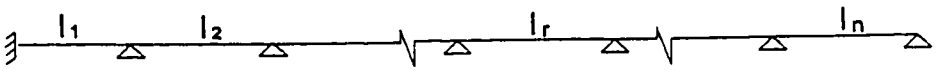

Figure 3.3 Multi-span beam with one end fixed

At a fixed end, the displacement and slope are zero, i.e., u = 0, and du/dx = 0. Therefore if both ends are so fixed, the equation is

$$\Delta_n \equiv \Delta(l_1, l_2, \cdots l_n) \equiv \begin{vmatrix} g_1, & h_1, & 0 & & \\ h_1, & g_1+g_2, & h_2 & & \\ 0, & h_2, & g_2+g_3 & & \\ \cdots & \cdots & \cdots & \cdots & \cdots \\ & & & g_{n-2}+g_{n-1}, & h_{n-1}, & 0 \\ & & & h_{n-1}, & g_{n-1}+g_n, & h_n \\ & & & 0, & h_n, & g_n \end{vmatrix}$$

Particular cases:

■ Two spans with both ends fixed

$$\Delta_2 = \begin{vmatrix} g_1, & h_1, & 0 \\ h_1, & g_1+g_2, & h_2 \\ 0, & h_2, & g_2 \end{vmatrix}$$

■ Three spans with left end fixed, right end simply supported

$$\Delta_3 = \begin{vmatrix} g_1, & h_1, & 0 \\ h_1, & g_1+g_2, & h_2 \\ 0, & h_2, & g_2+g_3 \end{vmatrix}$$

■ Three spans with left end fixed, right end free

$$\Delta_3 = \begin{vmatrix} g_1, & h_1, & 0 \\ h_1, & g_1+g_2, & h_2 \\ 0, & h_2, & g_2+g_3' \end{vmatrix} \qquad \textit{here} \qquad g_3' = \frac{\chi_3}{g_3}$$

3.2 The Procedure and Verification of the Current Method

An analytical solution is available for vibration of multi-span beams with equal span lengths [Blevins, 1979]. For unequal span beams, the finite element method is usually taken as the solution approach. However, the derivation in section 3.1 does not require the lengths of l_r for each span to be equal. Natural frequencies can be found by solving the determinant equations. Once k_r for different modes have been obtained, mode shapes can be obtained by solving the deflection equations for constants a_r, b_r, c_r and d_r at each span. A software program called MathCAD® was used as an equation solver, and was found satisfactory. The case #2 which appeared in Weaver & Parrondo [1991] was taken for comparison purposes. In order to clearly demonstrate the present computation procedure, the calculation is shown as follows:

Tube material is admiralty brass, $E = 1.1\text{x}10^{11}$ Pa, $\rho = 8500$ kg/m^3, $D_o = 12.6$ mm, $t = 0.25$ mm. The details of support arrangements and span lengths are shown in Figure 3.4. For the reason of using equations already derived in section 2.2, the coordinate origin in the figure is located at the right end of the beam. i. e. $l_1 = 0.622$ m, $l_2 = 0.305$ m, $l_3 = 0.623$ m. Using equations (3-15) and (3-16)

$$\left[\frac{-\chi_1(k_i)}{g_1(k_i)} + g_2(k_i)\right]\left[g_2(k_i) + g_3(k_i)\right] - h^2{}_2(k_i) = 0$$

here

$$g_1(k_i) = \coth(k_i l_1) - \cot(k_i l_1)$$
$$g_2(k_i) = \coth(k_i l_2) - \cot(k_i l_2)$$
$$g_3(k_i) = \coth(k_i l_3) - \cot(k_i l_3)$$
$$h_2(k_i) = \mathit{cosech}(k_i l_2) - \operatorname{cosec}(k_i l_2)$$
$$\chi_1(k_i) = \frac{2[1 + \cosh(k_i l_1)\cos(k_i l_1)]}{\sinh(k_i l_1)\sin(k_i l_1)}$$

The first three roots are: $k_1 = 2.673$, $k_2 = 5.740$, $k_3 = 6.969$. Therefore from

$$f_i = \frac{k_i^2 \lambda}{2 \pi}$$

the first three natural frequencies are: $f_1 = 17.59$ Hz, $f_2 = 80.94$ Hz, $f_3 = 118.96$ Hz. Then substituting k_i into the following equations to solve the constants of the deflection equations, we obtain the mode shape

$$\begin{aligned}
&a_1[\cos(k_i l_1) + \cosh(k_i l_1)] + c_1[\sin(k_i l_1) + \sinh(k_i l_1)] = 0 \\
&a_1[-\sin(k_i l_1] + \sinh(k_i l_1)] + c_1[\cos(k_i l_1) + \cosh(k_i l_1)] = c_2 + d_2 \\
&a_1[\cos(k_i l_1) - \cosh(k_i l_1)] + c_1[\sin(k_i l_1) - \sinh(k_i l_1)] = 2a_2 \\
&a_2[\cos(k_i l_2) - \cosh(k_i l_2)] + c_2\sin(k_i l_2) + d_2\sinh(k_i l_2) = 0 \\
&-a_2[\sin(k_i l_2) + \sinh(k_{i l_2})] + c_2\cos(k_i l_2) + d_2\cosh(k_i l_2) = c_3 + d_3 \\
&a_2[\cos(k_i l_2) + \cosh(k_i l_2)] + c_2\sin(k_i l_2) - d_2\sinh(k_i l_2) = 2a_3 \\
&a_3[\cos(k_i l_3) - \cosh(k_i l_3)] + c_3\sin(k_i l_3) + d_3\sinh(k_i l_3) = 0 \\
&a_3[\cos(k_i l_3) + \cosh(k_i l_3)] + c_3\sin(k_i l_3) - d_3\sinh(k_i l_3) = 0
\end{aligned}$$

The eigenvalue of the first mode is: $(a_1, c_1, a_2, c_2, d_2, a_3, b_3, d_3) = (1, -7.49, 8.36, 9.69, 13.89, -1.337, -0.129, 1.431)$. For easy comparison, the maximum displacement of each mode is assigned a value of unity. Thus, the mode shapes for each span are calculated by:

$$u_{i1}(x) = a_1[\cos(k_i x) + \cosh(k_i x)] + c_1[\sin(k_i x) + \sinh(k_i x)], \quad 0 \le x \le l_1$$

$$u_{i2}(x) = a_2[\cos(k_i x) - \cosh(k_i x)] + c_2\sin(k_i x) + d_2 \sinh(k_i x), \quad 0 \le x \le l_2$$

$$u_{i3}(x) = a_3[\cos(k_i x) - \cosh(k_i x)] + c_3\sin(k_i x) + d_3 \sinh(k_i x), \quad 0 \le x \le l_3$$

The first three normalized mode shapes are illustrated in the following figure:

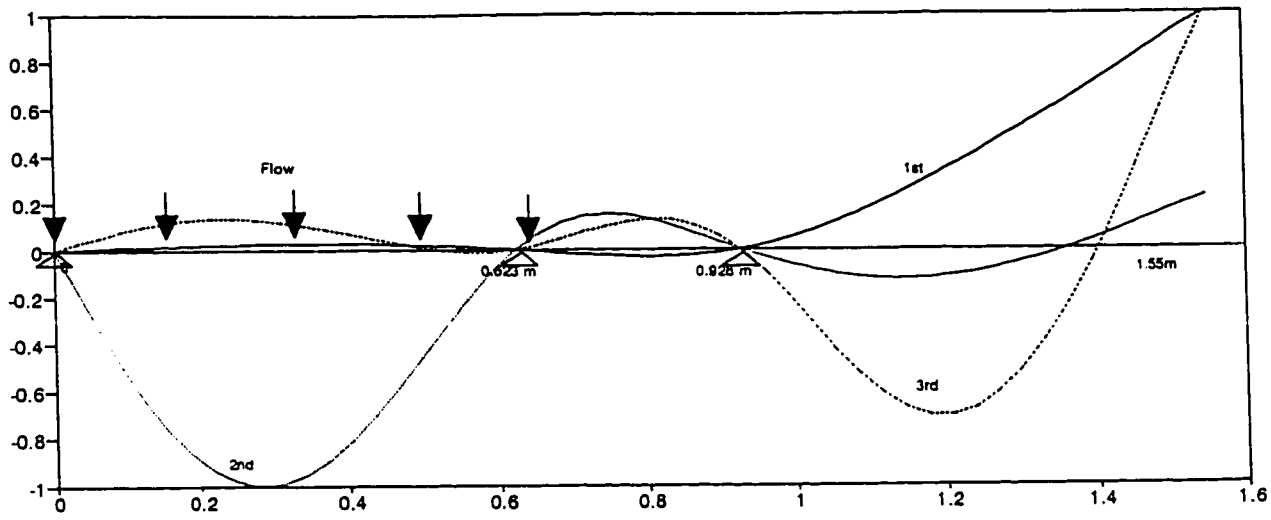

Figure 3.4 The first three normalized mode shapes

The energy fraction S_i at the third span is calculated by:

$$S_{i3} = \frac{\int_0^{l_3} \varphi^2{}_i(x)dx}{\int_0^{l_1+l_2+l_3} \varphi^2{}_i(x)dx} = \frac{\int_0^{l_3} u^2{}_{i3}(x)dx}{\int_0^{l_1} u^2{}_{i1}(x)dx + \int_0^{l_2} u^2{}_{i2}(x)dx + \int_0^{l_3} u^2{}_{i3}(x)dx}$$

The comparison between the present and Weaver & Parrondo's results are summarized in Table 3.1.

Table 3.1 The comparison of results

Mode	f_i (hz) [W&P]	**f_i (hz)** (present)	S_{i3} [W&P]	S_{i3} (present)
1	17.5	**17.59**	1.24×10^{-3}	**1.2×10^{-3}**
2	80.1	**80.94**	0.971	**0.9667**
3	118.2	**118.96**	0.025	**0.0257**

As seen in the table, the present calculation of natural frequency and mode shape agree well with previous results, determined by the finite element method. The analytical method was used in the following experimental study.

3.3 The Effects of Flow Location on S_i for a Single Span Tube

The numerator in the definition equation of S_i is an integration of mode shape along the cross flow tube section. Thus, the flow location has a significant effect on the value of S_i. The effect of flow location on S_i is further examined on a single span tube with respect to different support configurations. The tube is subjected to partial flow L_1/L. Here, only S_i of the first mode shape is computed. The higher mode results are presented in next section.

3.3.1 Both Ends are Simply Supported

The mode shape is defined as

$$\varphi(x) = \sin(\pi x/L)$$

a. flow at the central portion L_1

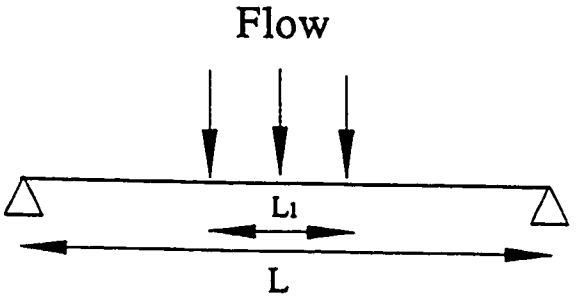

$$S_i(L_1/L) = \frac{\int_{(L-L_1)/2}^{(L+L_1)/2} \varphi^2(x)\,dx}{\int_0^L \varphi^2(x)\,dx} = \frac{L_1}{L} - \frac{1}{\pi}\sin\left(\frac{\pi L_1}{L}\right)$$

b. flow at the left end portion L_1

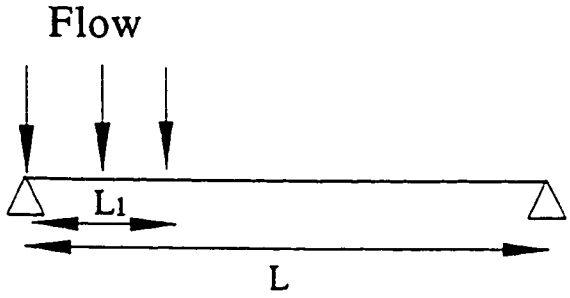

$$S_i(L_1/L) = \frac{\int_0^{L_1} \varphi^2(x)\,dx}{\int_0^{L} \varphi^2(x)\,dx} = \frac{L_1}{L} - \frac{1}{2\pi}\sin\left(\frac{2\pi L_1}{L}\right)$$

Because the critical reduced velocity is proportional to $1/S_i$, the results are plotted as $1/S_i$ versus admission ratio L_1/L, as shown in Figure 3.5. The larger is $1/S_i$, the larger the critical reduced velocity. As seen in the figure, $1/S_i$ for flow at the pinned end is always larger than that for flow at the center. However, with the increase of admission length ratio, the difference due to the flow location reduces significantly. Here, we assume a reasonable criterion based on the experiments conducted later: a 10% reduced velocity difference at the threshold is assumed negligible since this is within the experimental uncertainty. This corresponds to 21% $1/S_i$ ratio difference if $\alpha = 0.5$ in equation (2-1). Thus, in Figure 3.5, when L_1/L exceeds about 64%, the effect of flow location becomes negligible. This result indicates that a tube is more easily excited when the flow is located at the central portion of the tube than when the same flow is situated at the end portion of the tube as long as $L_1/L < 64\%$. This result is not

surprising, because the tube has the maximum deflection at the center in the first mode, which suggests that the least external work is required to produce a dynamic instability.

3.3.2 Both Ends are Fixed

The first mode shape is defined as

$$\varphi(x) = \frac{\cos(a_n L) - \cosh(a_n L)}{\sinh(a_n L) - \sin(a_n L)}[\sinh(a_n x) - \sin(a_n x)] + \cosh(a_n x) - \cos(a_n x)$$

$$a_n = (n+\frac{1}{2})\frac{\pi}{L} \qquad n=1,\ 2,\ \ldots$$

The mode shapes substituted into the S_i equation (2-5). Similar to the previous case, the analysis is symmetrical about the center. The results are shown in Figure 3.6. In this figure, $1/S_i$ is calculated for the flow located at the fixed end and the central portion of the tube respectively. The tube is much easier to excite when the flow is located at the center than at the fixed end. Using the same criterion defined in the previous section, the flow location effect disappears at admission ratio $L_1/L > 64\%$.

3.3.3 Left End is Fixed and Right End is Simply Supported

The first mode shape is defined as

$$\varphi(x) = \frac{\cos(a_n L) - \cosh(a_n L)}{\sinh(a_n L) - \sin(a_n L)}[\sinh(a_n x) - \sin(a_n x)] + \cosh(a_n x) - \cos(a_n x)$$

$$a_1 = (n+\frac{1}{4})\frac{\pi}{L} \qquad n=1,\ 2,\ \ldots$$

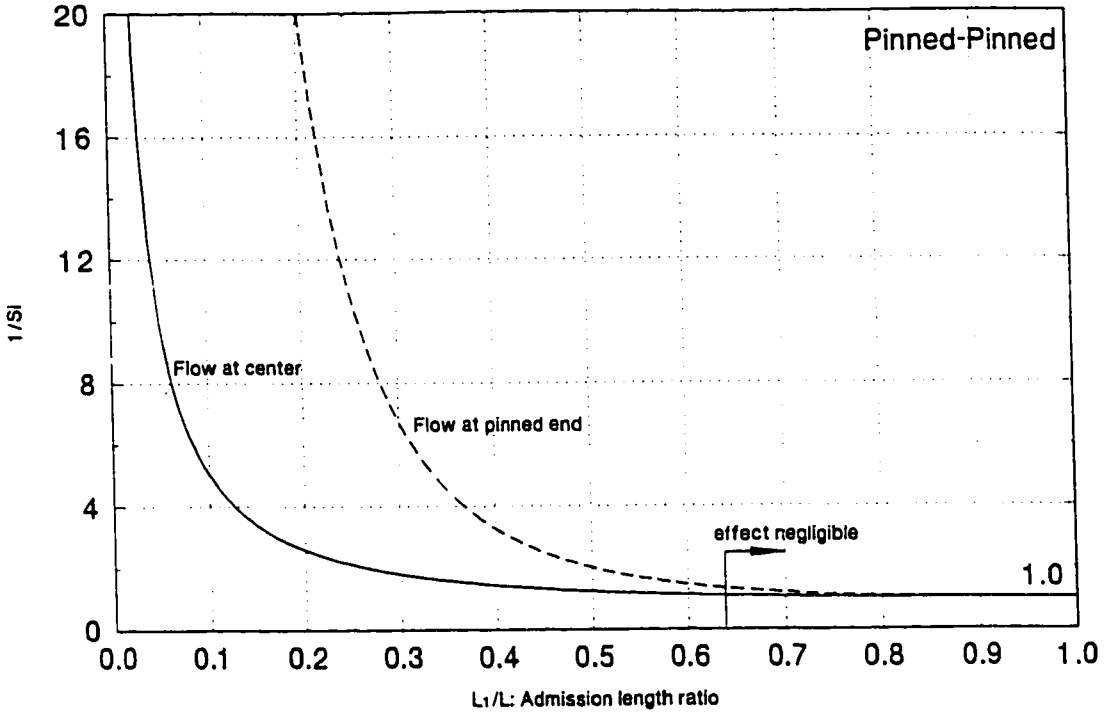

Figure 3.5 $1/S_i$ of simply supported - simply supported tube

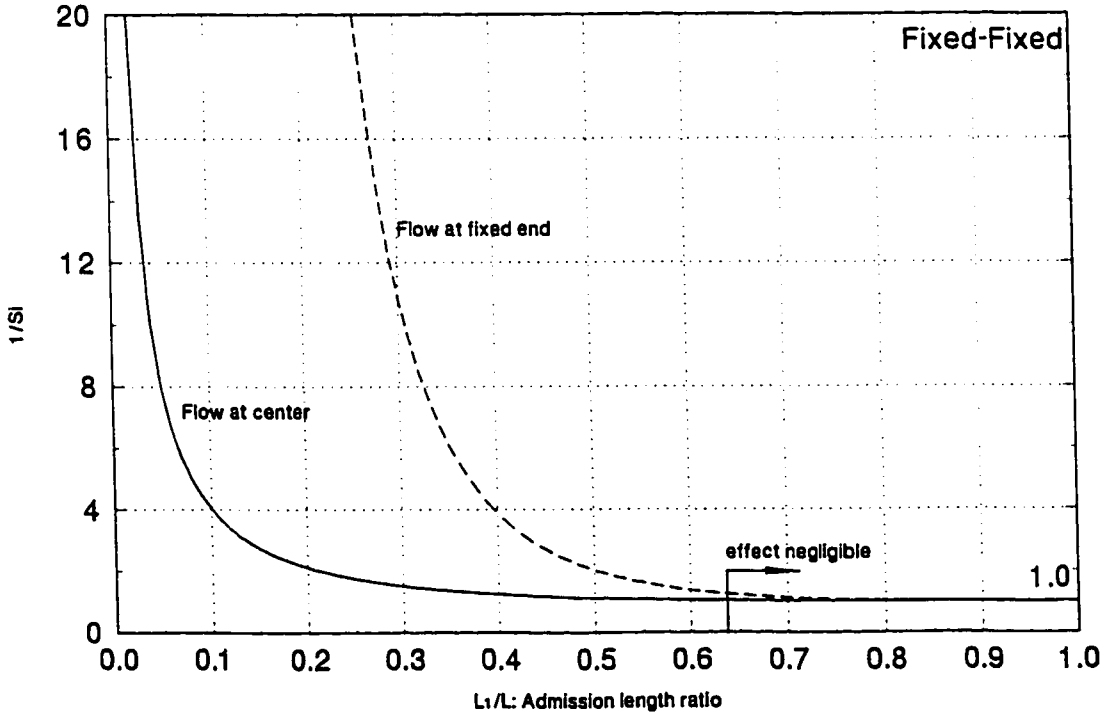

Figure 3.6 $1/S_i$ of fixed - fixed tube

The results are shown in Figure 3.7. In this figure, $1/S_i$ is calculated for the flow located at the fixed and pinned end, as well as in the center portion respectively. Not surprisingly, it is found that tube is easier to excite when the flow is located at the simply supported end than at the fixed end. Again, the critical velocity is the lowest when the flow is in the center. The difference between the flow at the center and at the pinned end disappears at $L_1/L > 52\%$. Based on the same criterion, the difference between the flow at the center and at the fixed end is negligible at $L_1/L > 70\%$.

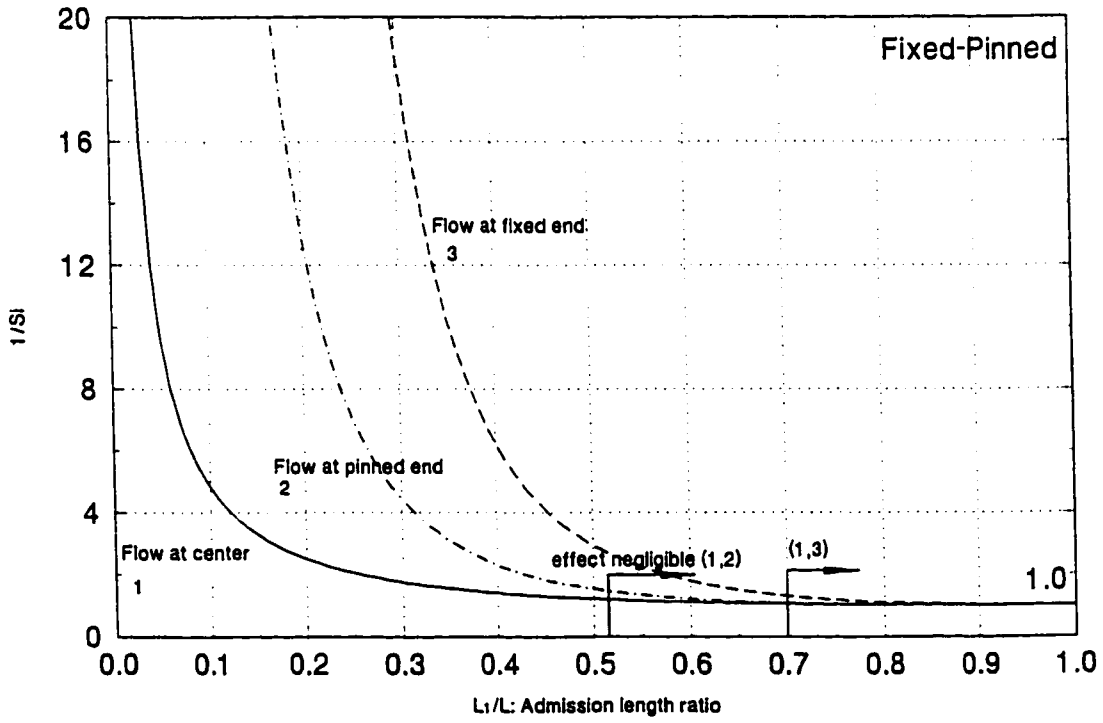

Figure 3.7 $1/S_i$ of fixed - simply supported tube

3.3.4 Cantilever Beam

The first mode shape is defined as

$$\varphi(x) = -\frac{\cos(a_n L) + \cosh(a_n L)}{\sin(a_n L) + \sinh(a_n L)}(\sinh(a_n x) - \sin(a_n x)) + \cosh(a_n x) - \cos(a_n x)$$

$$a_1 = 1.67\frac{\pi}{L}, \quad a_n = (n-\frac{1}{2})\frac{\pi}{L} \qquad n=2, 3, \ldots$$

The results are shown in Figure 3.8. In this case, the critical velocity of flow at the fixed end is significantly higher than that of flow at the center and free end. The difference among them is negligible at $L_1/L > 91\%$. Therefore, the effect of flow location for the cantilever support is stronger than other support configurations. For almost entire admission ratio, the effect of flow location can be "felt" by tubes.

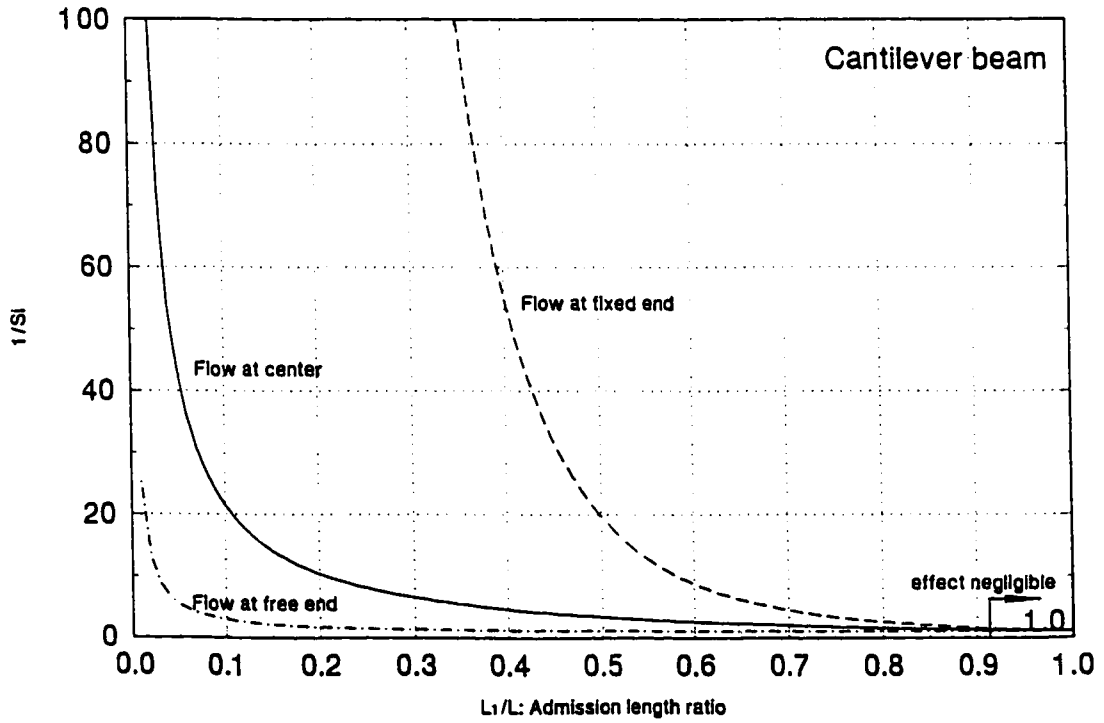

Figure 3.8 $1/S_i$ of cantilever tube

Since the current correlation [Weaver & Fitzpatrick, 1988] of Table 2.1 relates the critical reduced velocity to constants for a single span tube with full admission fluid flow, the first mode instability is always predicted. On the other hand, as seen in equation (2-8), S_i plays an important role in the prediction of partial admission tubes. Assuming the same damping, and added mass, we compare the critical velocity at two different vibration modes i and i+1. Using equation (2-8)

If $(1/S_i)_{i+1}{}^{\alpha} f_{i+1} < (1/S_i)_i{}^{\alpha} f_i$ i.e. $V_{i+1} < V_i$

the instability could occur at a higher mode. Hence, lower $1/S_i$ value may not necessarily imply lower critical velocity. Therefore, the $1/S_i$ values computed in this section are not conclusive with regards to the unstable mode. In the following section, a brief analysis is conducted on the possibility of higher instability modes by comparing the critical velocity of different modes on a single span tube with partial flow admission.

3.4 The First Excited Mode of a Single Span Tube with Partial Admission

Published results suggest that only the fundamental mode is excited on single span full admission tubes, regardless of tube supports. However, in the case of the partial admission, a higher mode could be excited first instead of the fundamental mode, depending on the flow location, admission ratio, and supports. From equations (2-4) and (2-5), the ratio of critical velocities can be obtained, assuming equal damping values and exponent $\alpha = 0.5$, for different modes.

$$\left(\frac{V_1}{V_i}\right)_{critical} = \frac{f_1}{f_i}\left(\frac{Si_i}{Si_1}\right)^{0.5} \qquad i = 2,3, \ldots$$

The results for the fixed-pinned supports are shown in Figure 3.9 for the ratio of the 1st

mode critical velocity to those of the 2nd and 3rd modes. L_1/L is the flow admission length ratio. Seen from the figures, the 2nd mode can only be excited prior to the 1st mode (i.e., $V_1/V_2 > 1$) when $L_1/L < 0.3$ and the flow location is close to the fixed end. Similarly, the 3rd mode can only be excited before the 1st mode for $L_1/L < 0.2$ and the flow location is close to the fixed end. The velocity ratio for other types of supports are shown in Figures 3.10 to 3.13, and a similar conclusion can be drawn from them.

For the pinned-pinned supports, Figure 3.10 shows that the 2nd mode cannot be excited before the 1st mode at any flow location. The 3rd mode can be excited before the 1st mode only at $L_1/L < 0.1$ when the flow is close to the pinned ends.

The results for the fixed-fixed supports are shown in Figure 3.11. The curves are similar to Figure 3.10. However, in this support configuration, the 2nd mode can be excited before the 1st mode when $L_1/L < 0.2$ and the flow location is close to the fixed ends. The same results apply to the comparison between the 1st and 3rd modes.

For the cantilever support, the results is shown in Figure 3.12. The higher modes can be easily excited before the 1st mode when the flow location is close to the fixed end.

By examining the mode shapes of a tube with different end supports, it is apparent that higher modes have a larger deflection close to the constrained supports (pinned, fixed), while the first mode has the largest deflection at or close to the middle (pinned-pinned, fixed-fixed, fixed-pinned). Therefore, flow at the end portion of the tube could excite higher modes. This theoretical result has been confirmed by experiments which will be discussed in Chapter 6. The calculation conducted here does not consider damping changes at different modes. Moreover, it assumes an exponent of 0.5 for $1/S_i$, which is questionable especially in liquid flow. Nevertheless, the general trend should remain similar.

Unfortunately, because of numerous combinations of span length ratio, the comparisons

for multi-span tubes are not as straightforward as the single span tubes. Each span-support configuration has to be computed individually.

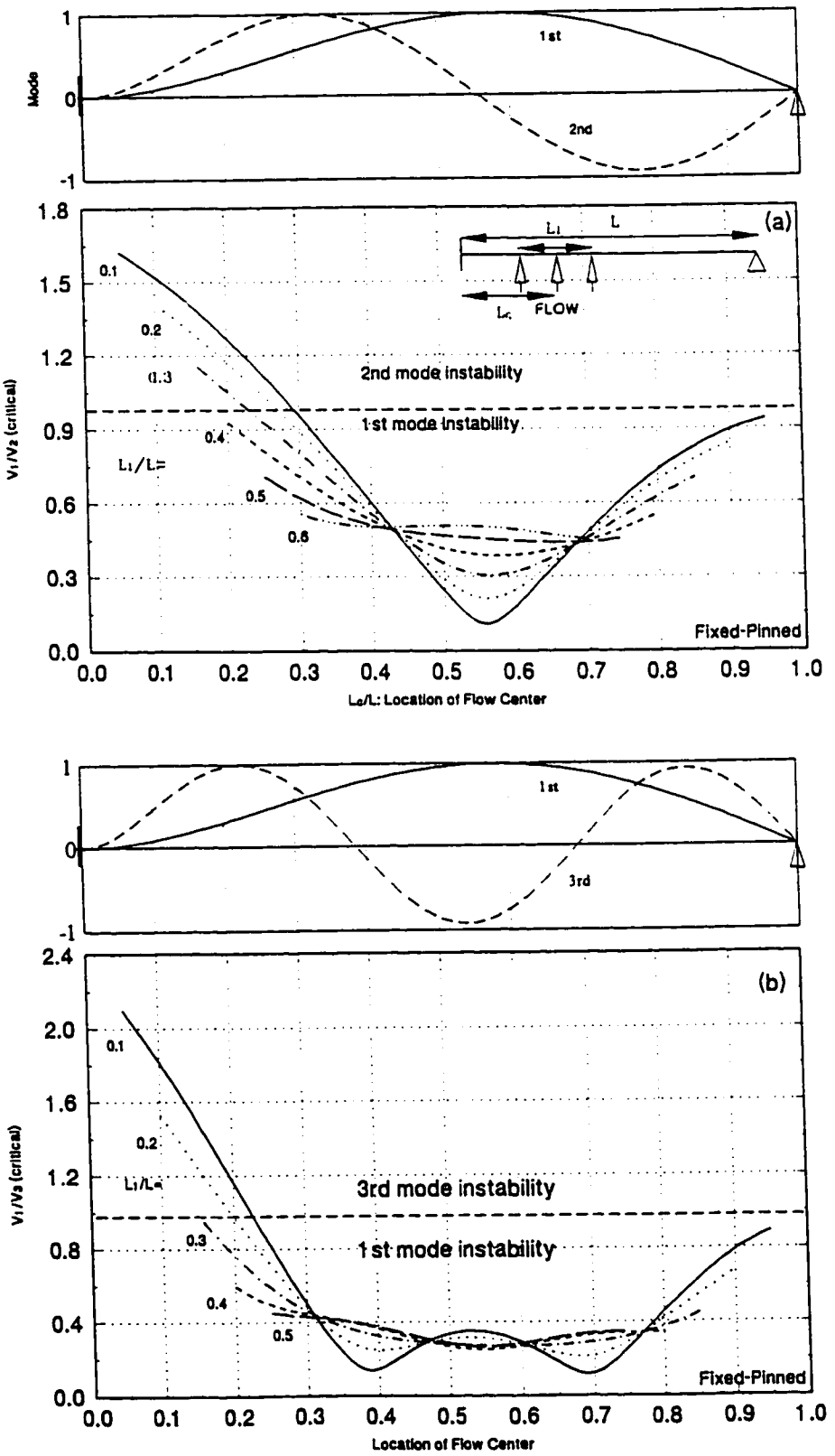

Figure 3.9 Critical velocity ratio of fixed - pinned tube (a). V_1/V_2, (b). V_1/V_3

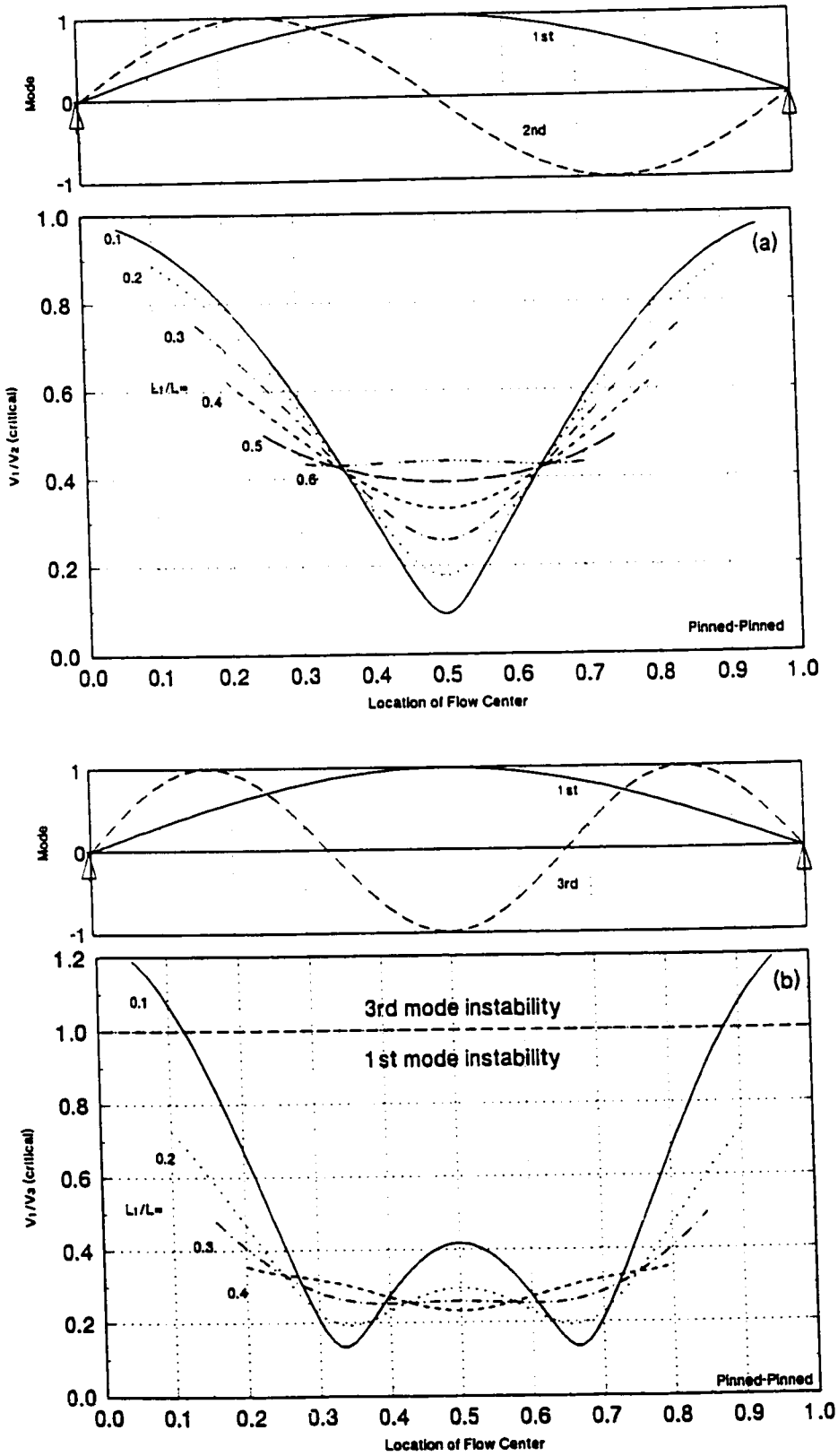

Figure 3.10 Critical velocity ratio of pinned - pinned tube (a). V_1/V_2, (b). V_1/V_3

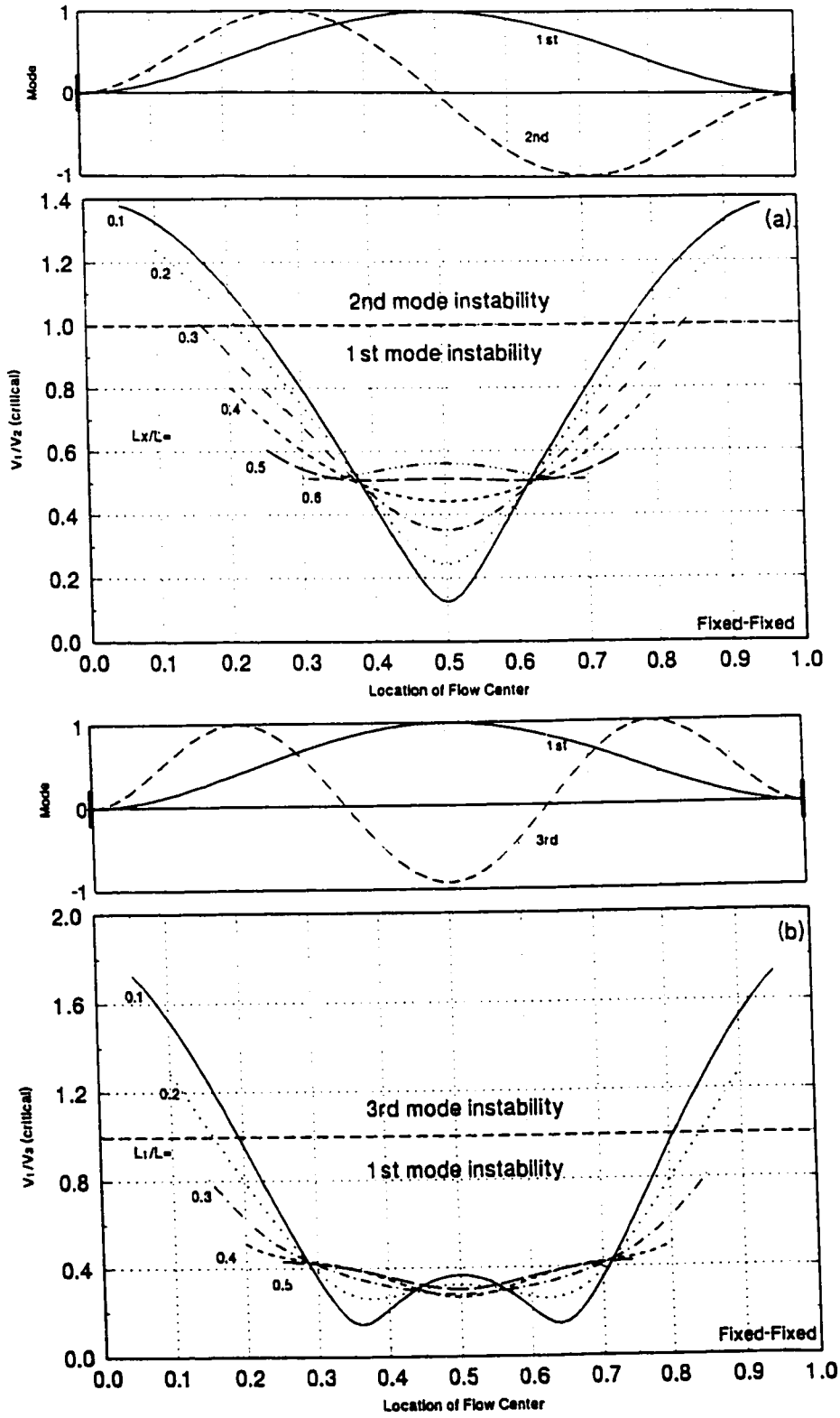

Figure 3.11 Critical velocity ratio of fixed - fixed tube (a). V_1/V_2 , (b). V_1/V_3

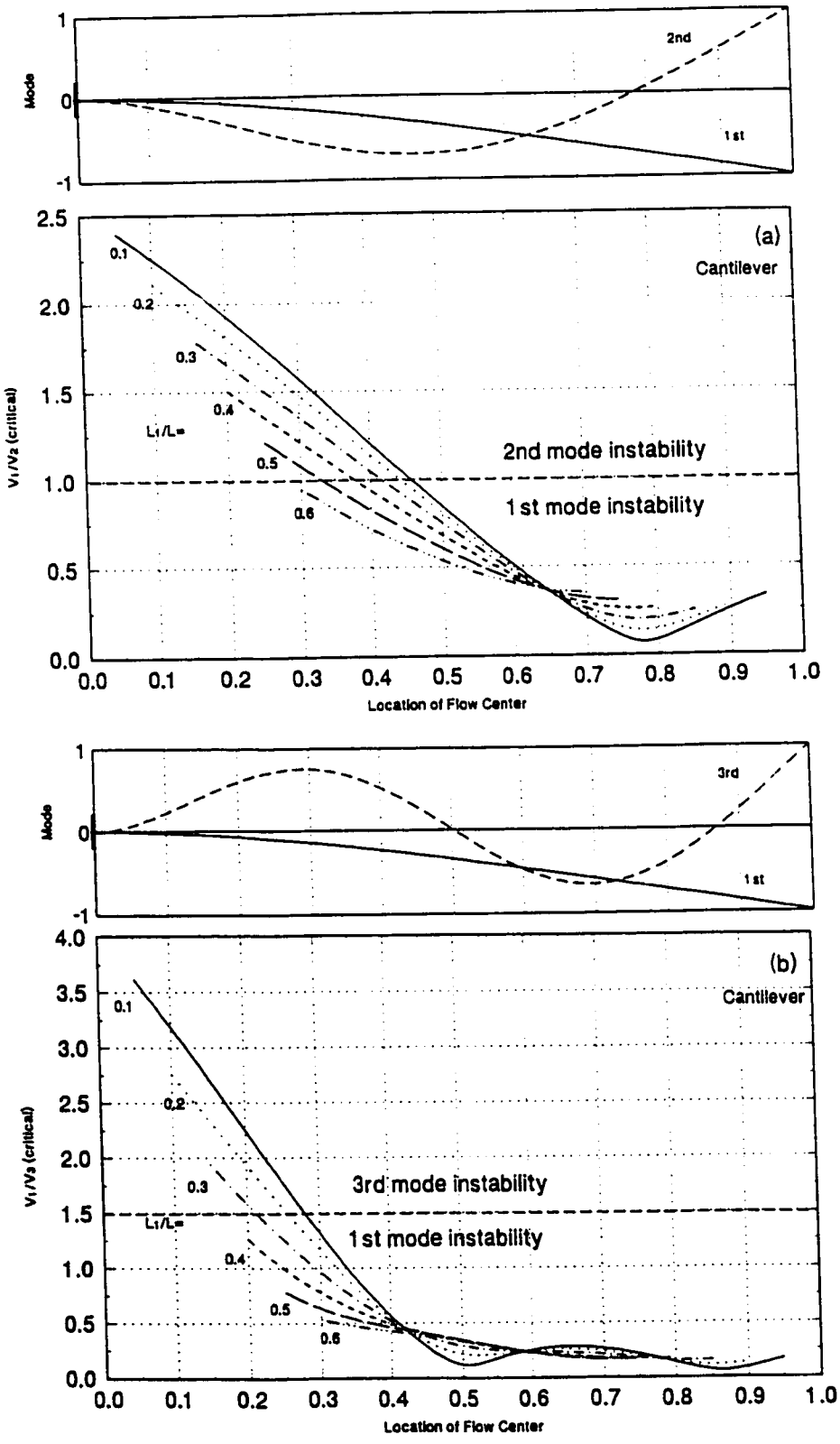

Figure 3.12 Critical velocity ratio of fixed - free tube (a). V_1/V_2, (b). V_1/V_3

CHAPTER 4

THE WATER TUNNEL AND TEST SECTION DESIGN AND CONSTRUCTION

4.1 The Existing Water Tunnel

The water tunnel used for this research is an existing facility which had been developed for previous research in flow-induced vibration. It is a closed-circuit type in which the water is continuously recirculated. The low-speed water tunnel schematic drawing is shown in Figure 4.1 (dimensions shown are the redesigned values). The pump (P) is a double suction Babcock and Wilcox centrifugal pump rated at 22.7 m^3/min for 33.5 m of head, which provides adequate capacity and head for the working range used in the present study.

The fluid leaving the pump passes through either the main line (0.304 m or 12" diameter) or the by-pass line (0.152 mm or 6" diameter), towards the first corner of the loop. Both are equipped with tuning vanes so that the flow has minimum losses and disturbances in these regions. The flow rate on both the main line and by-pass line are controlled by gate valves V1 and V2, respectively. The flow distribution and turbulence are improved by a wide angle transition section (T), settling chamber (S), contraction section (C1), and working section (W). Leaving the test section, the fluid passes through a rectangular section to a circular section (D) before it is directed towards the third turn. Through the third and fourth turns, the fluid is driven back to the pump.

4.2 The New Design of the Water Tunnel Part by Part

The original 305 x 305 mm water tunnel test section could not be used for the planned multi-span tube experiment. Hence, a new diffuser, settling chamber, contraction, test and

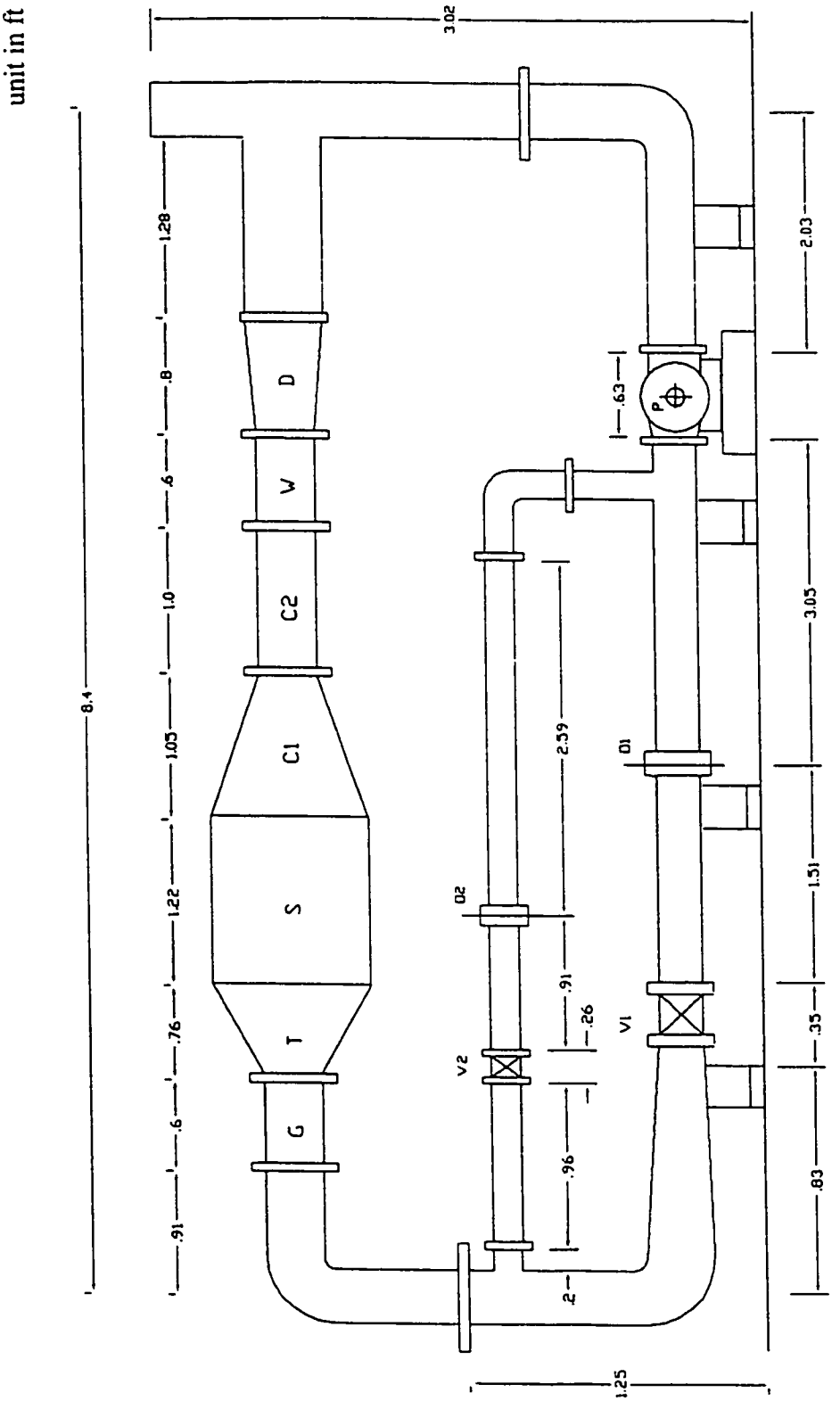

Figure 4.1 The schematic drawing of the water tunnel (redesigned, dimensions in meters)

transition section had to be designed and built.

4.2.1 Contraction Section

A contraction section placed upstream of the test section reduces the non-uniformities in the mean flow and suppresses the turbulent fluctuations by accelerating the flow. Only the longitudinal velocity fluctuations (u) are suppressed in absolute value. Lateral components are enhanced by the vortex stretching mechanism, but since the mean velocity is increased, the turbulence intensity becomes lower. Though the contraction ratio, Cr (entrance area/exit area), is mostly responsible for reducing non-uniformities, wall shape and contraction length are equally important to the successful design of a contraction section.

The non-uniformity reduction factor for the mean velocity and the turbulence intensity were derived theoretically for an asymmetrical contraction, with Cr >> 1, by Bradshaw & Pankhurst [1964], and are given as:

U-component mean velocity: $1/Cr^2$

V or W-component mean velocity: $1/Cr^{0.5}$

u-component rms intensity: $\{3(\ln 4Cr^3 - 1)\}^{0.5}/ 2Cr^2$

v or w-component rms intensity: $(3/Cr)^{0.5}/ 2Cr$

The design of a contraction cone centers on the production of a steady, uniform stream at its outlet, and the avoidance of flow separation. It is always possible to avoid the separation in the contraction by increasing its length, but this method results in an increase of tunnel length, construction cost and exit boundary layer thickness.

Since the reduction factor of non-uniformity of velocity distribution is proportional to 1/Cr, a large contraction ratio is advantageous. But a larger Cr may cause higher exit non-uniformities due to cross flow, possible problems of noise, and separation near the end. For a

small wind tunnel or water tunnel, the range of Cr is recommended as 6 to 9. In the present case, a contraction ratio Cr of 6 was chosen, which resulted in reduction factors of 2.8%, 40.8%, 5.8%, and 35.4%, respectively, for the four mean and fluctuating longitudinal and transverse components mentioned above. The exit dimensions of the contraction section were chosen based on the test section inlet dimensions. Then the contraction inlet dimensions were calculated by the pre-chosen contraction ratio Cr. A two dimensional contraction was adopted due to its better uniform velocity distribution and low construction cost.

The wall pressure coefficient is used to analyze the points where the wall velocity within the contraction is maximized at the exit and minimized at the inlet, respectively. They are defined by Morel [1977]

$$C_{pi} = 1 - \left(\frac{u_{min}}{u_{inlet}}\right)^2$$
$$C_{pe} = 1 - \left(\frac{u_{outlet}}{u_{max}}\right)^2 \qquad (4\text{-}1)$$

The parameters C_{pi} and C_{pe} should be minimized to avoid separation. Morel's calculation demonstrates that the values of 0.16 and 0.1, respectively, are proper upper bounds for the laminar inlet flow below which boundary layer separation is unlikely to occur.

For the current design, the particular values chosen for wall pressure coefficients were: $C_{pi} = 0.14$, and $C_{pe} = 0.0265$ (which leads to turbulence intensity less than 0.5% at the exit).

From Figure 4.2, the dimensionless parameters F_i and F_e can be obtained if the values of C_{pi} and C_{pe} are known. They are defined by Morel [1977]:

$$F_i = \frac{m-1}{m} X^{-2} \left(\frac{L}{H_1}\right)^{-3} \qquad (4\text{-}2)$$

$$F_e = \frac{m-1}{m} (1-X)^{-2} \left(\frac{L}{H_1}\right)^{-3} \qquad (4\text{-}3)$$

where: $m = H_1 / H_2$ inlet to outlet contraction section height ratio

X = contour shape parameter, L = contraction length

The sole contour shape parameter X is solved by equation (4-2) and (4-3):

$$X = (1 + \frac{1}{m}\sqrt{\frac{F_i}{F_e}})^{-1} \qquad (4\text{-}4)$$

The values of F_i and F_e and are 0.59 and 0.09, respectively, from Figure 4.2. The height ratio *m* is equal to the contraction ratio Cr of 6 due to the two dimensional geometry. Equation (4-4) gives X = 0.7. By substituting X back to equation (4-2) or (4-3) and solving the contraction length, we obtain L=1110 mm.

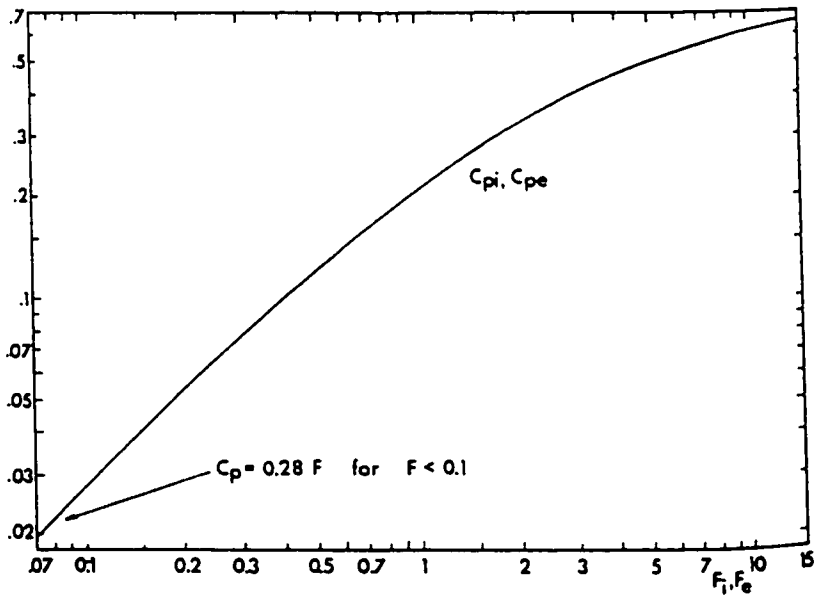

Figure 4.2 Dependence of C_{pi} and C_{pe} on the F_i and F_e respectively Morel [1977]

Then the wall contour coordinates (H,x) can be obtained from the following equations:

$$\frac{H - H_2}{H_1 - H_2} = 1 - \frac{1}{X^2}\frac{x^3}{L^3} \quad for \quad x/L \le X \tag{4-5}$$

and

$$\frac{H - H_2}{H_1 - H_2} = \frac{1}{(1 - X)^2}(1 - \frac{x}{L})^3 \quad for \quad x/L > X \tag{4-6}$$

which yields the final form of the contour equation:

$$\frac{H - H_1}{H_1 - H_2} = 1 - \frac{x^3}{0.7^2 \cdot 1110^3} \qquad x \le 777\ mm \tag{4-7}$$

$$\frac{H - H_2}{H_1 - H_2} = \frac{1}{0.3^2}(1 - \frac{x}{1110})^3 \qquad x \ge 777\ mm \tag{4-8}$$

Figure 4.3 shows the contraction section, made of 3.2 mm thick stainless steel. The total length is 1165 mm, including a 25 mm straight section at the inlet and outlet.

4.2.2 Wide Angle Diffuser

As discussed in the previous section, the uniformity of flow in a wind or water tunnel can be greatly improved by a contraction section with a large area ratio placed immediately upstream of the working section. Such a large area ratio requires the installation of a wide angle, short length diffuser. Diffuser with an equivalent cone angle greater than 6° is taken as a wide angle diffuser. For practical reasons wide angle diffuser is regarded as a means of reducing the length of a diffuser of given area ratio, rather than as a means of pressure recovery. Theoretically, when the axial velocity within the boundary layer decelerates more slowly than

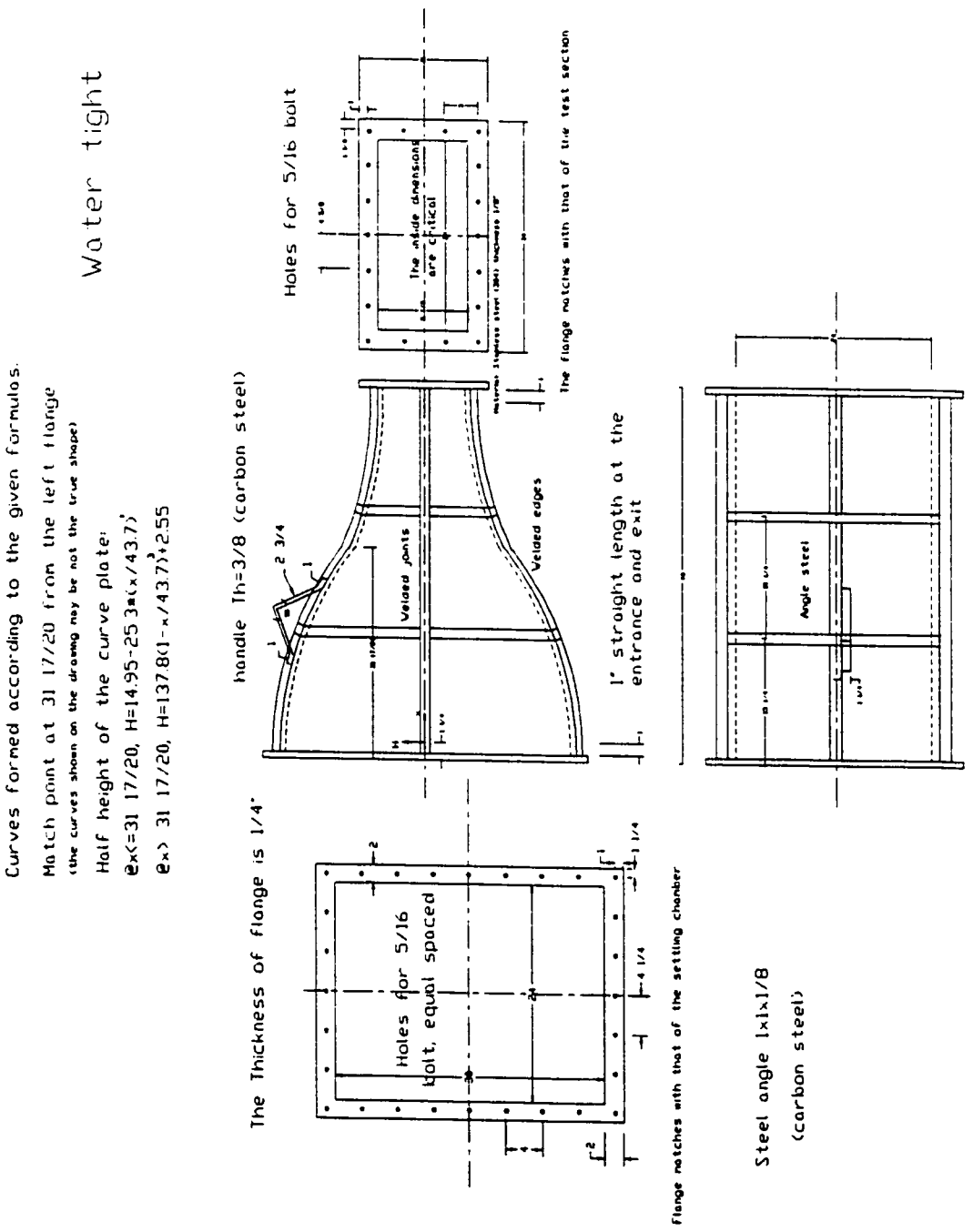

Figure 4.2 Drawing of the contraction section

1/3 the power of the axial distance, the boundary layer cannot exist without flow separation ($dU/dx \propto x^{-1/3}$). Separation control mechanisms such as screens, and split plates or vortex generators have to be employed.

There are four important parameters in wide angle diffuser design: area ratio AR, the diffuser angle 2θ, geometry and the type of separation control mechanism. If a screen is used, the number of screens, n, within the diffuser, and the pressure drop coefficient of each screen, K_s, are considered to be critical. Even though a curved wall is more effective, a straight-wall diffuser is chosen due to the construction difficulties of the former geometry. The divergence angle in both planes was kept approximately equal since the one with larger θ tends to separate earlier. The inlet dimensions were taken as the same size of the connecting pipe, which has a diameter of 360 mm. The outlet dimensions were dictated by the contraction ratio required in the contraction section. The inlet dimension of the contraction section is 760 x 610 mm with a Cr ratio of 6. Hence, the area ratio of the wide angle diffuser is 3.6 with a 360 x 360 mm inlet dimension. The length is chosen as 800 mm as a compromise between the angle and the length, which results in angles of $2\theta = 28°$, and $17.8°$ for the vertical and horizontal axes, respectively.

The most popular separation control mechanism is to install screens inside a diffuser despite their low efficiencies. In a wide angle diffuser it is better to use several screens of relatively small pressure drop coefficient K_s (less than 1.5) because increasing the K_s at one station has little effect on a station much further downstream. Although there are no fixed rules for choosing the screens, most of the designs in the past have been done with zero pressure recovery in slow speed tunnels. Thus, the number of screens and the pressure drop coefficients K_s are selected such that the pressure recovery in the diffuser is lost due to the screens. Over a hundred wide angle diffuser designs were analyzed by Mehta [1977]. The following figures give a guideline of the number of screens and the total value of K_s. In Figure 4.4, AR is plotted

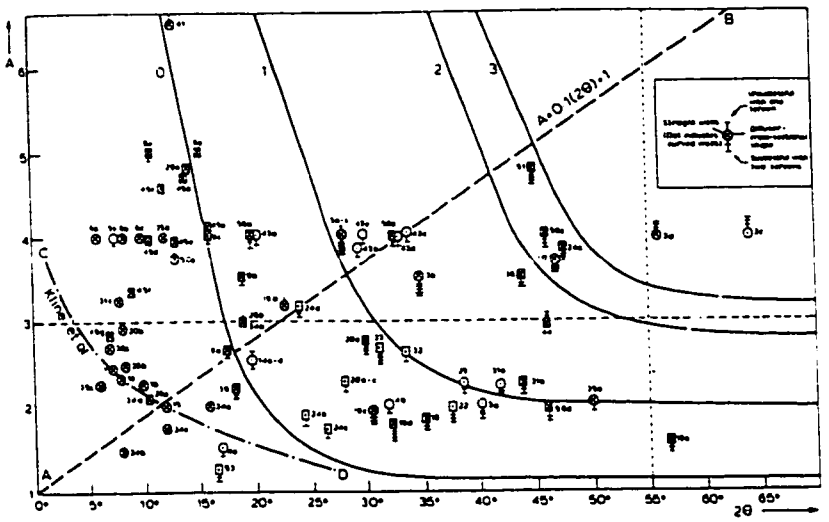

Figure 4.4 AR vs 2θ for diffusers with screens [Mehta, 1977]

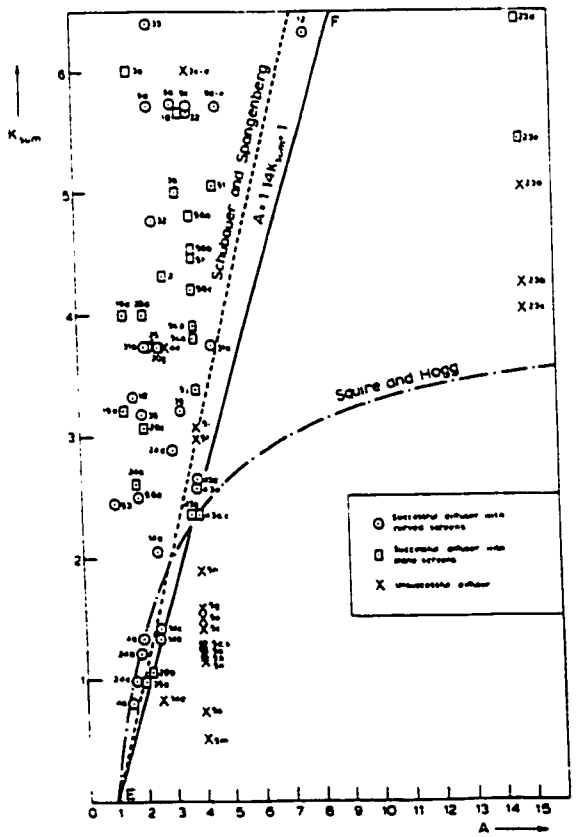

Figure 4.5 K_{sum} vs AR for diffuser with screens [Mehta, 1977]

against 2θ. The curves have a hyperbolic shape. With an angle of $2\theta = 28°$, 1 or 2 screens need to be installed. Figure 4.5 is a plot of the sum of the pressure coefficients of all of the screens. The straight line of $AR = 1.14\Sigma K_{sum} + 1.0$ gives the minimum required overall pressure drop coefficient. With an AR=3.6, the figure gives $\Sigma K_{sum} = 2.3$. Thus if two screens are chosen, $K_{s1,2} = 1.15\ (\Sigma K_{sum}/2)$.The pressure recovery coefficient is defined as

$$C_p = \frac{P_e - P_i}{1/2\rho U_i^2} \tag{4-9}$$

The ideal pressure recovery coefficient can be obtained by using Bernoulli's equation in terms of outlet and inlet areas

$$C_{pi} = 1 - \frac{A_i^2}{A_e^2} \tag{4-10}$$

Then, the efficiency η_d of the diffuser is given by

$$\eta_d = \frac{P_e - P_i}{\frac{1}{2}\rho(U_e^2 - U_i^2)} = \frac{C_p}{C_{pi}} \tag{4-11}$$

For zero static pressure recovery, the total required screen loss coefficient is

$$K_{sum} = C_p(\frac{A_e}{A_i})^2 \tag{4-12}$$

If more than one screen is used, which is usually the case, the pressure loss coefficient for any screen j is given by $C_p\,(A_{j+1}/A_j)^2$. This can be written in the terms of the diffuser coefficient η_d

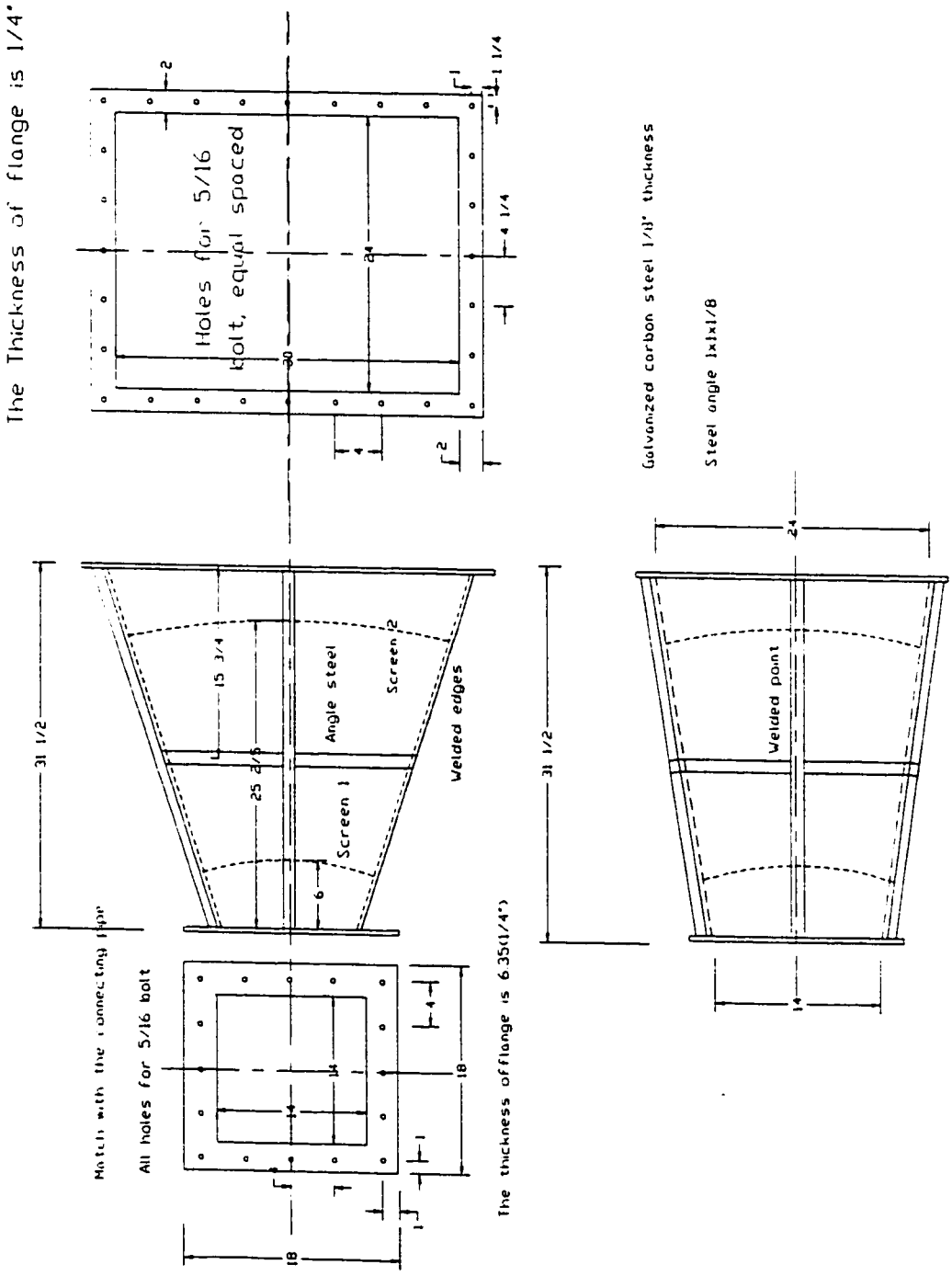

Figure 4.6 Drawing of the wide angle diffuser

and C_{pi} [Farell and Xia, 1990]

$$K_{sj} = \eta_d[(\frac{A_{j+1}}{A_j})^2 - 1] \qquad (4\text{-}13)$$

An efficiency η_d of 0.8, and C_p of 0.4 were assumed here. The position of the screens can be derived from equ. (4-13). In the table below, the screen position, area ratio and designed K_s are presented.

x (mm)	A (m x m)	A_{j+1}/A_j	K_s
100	406 x 432	1.38	1.13
333	686 x 559	2.18	1.13

4.2.3 Screens

Wind tunnel screens are normally made of metal wires interwoven to form square or rectangular meshes. Here, a stainless steel screen was selected to minimize the potential rust formation in the water tunnel. Screens make the flow velocity distribution more uniform by imposing a static pressure drop proportional to U^2 thus reducing the boundary layer thickness so that the ability to withstand the adverse pressure drop gradient is increased. A screen with $K_s \approx 2$ removes nearly all the variation in the longitudinal mean velocity. A screen also refracts the incidental flow towards the local normal direction and reduces the turbulence scale in the whole flow field. The parameters governing the wire gauze screen are the wire diameter d, and wire spacing l. With these two parameters, the open area ratio is calculated as $\beta = (1 - d/l)^2$. Screens with $\beta < 0.6$ should not be used since flow instability could result from a random coalition of jets.

If the Reynolds number based on the wire diameter is greater than 40, the wake behind

the wire will be turbulent. Therefore, screens generate both flow non-uniformity and turbulence, though both with much smaller scales compared to that of the incoming flow. Moreover, the small eddies are expected to decay rapidly.

Collar [1939] introduced the expression of screen pressure loss coefficient

$$K_s = C(Re)\frac{(1 - \beta)}{\beta^2} \tag{4-14}$$

C(Re) = 0.9 fits the experimental data very well when the velocity is less than 9 m/s.

The semi empirical screen deflection coefficient α is given by

$$\alpha = \frac{1.1}{\sqrt{1 + K_s}} \tag{4-15}$$

A 4 x 4 mesh stainless screen of d = 1.6 mm, and l = 6.35 mm is employed at every location. The corresponding parameters are

β	K_s	α
0.6	1.26	0.73

4.2.4 Honeycomb

Flow swirl and lateral mean velocity can be effectively removed by installing a honeycomb, but not by either screens or a contraction section. These non-uniformities are suppressed by honeycomb cells of a length l_c equivalent to about 5 to 10 cell diameters d_c. The design parameters of the honeycomb are l_c, d_c, and the number of cells. The cell size should be smaller than the smallest lateral eddy. The shape of the cells are usually unimportant except that they should be smooth and uniform. An aluminum hexcell honeycomb with the following parameters is used.

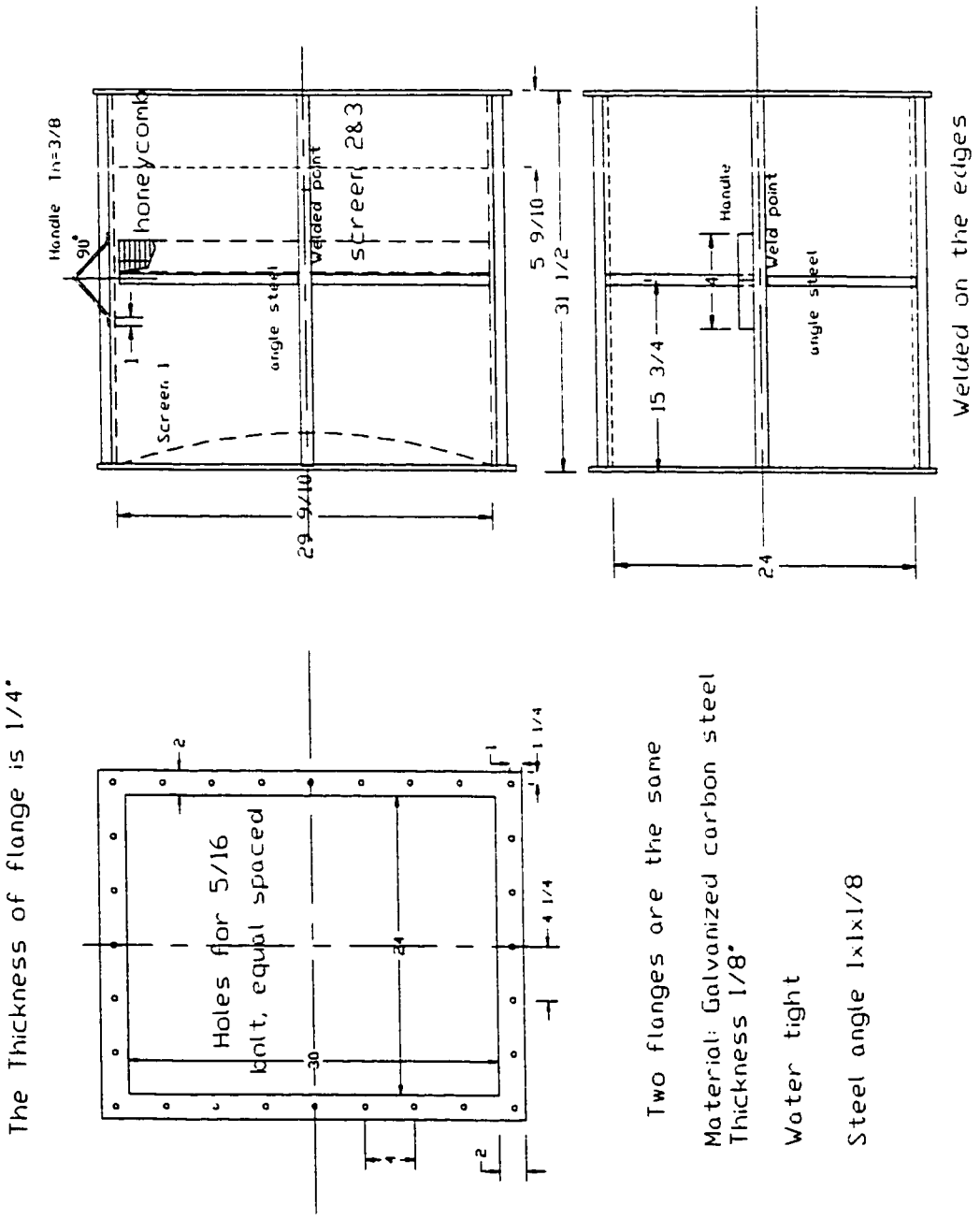

Figure 4.7 Drawing of the settling chamber

d_c mm	l_c mm	l_c/d_c	number of cells
4.76	50	10.5	20500

4.2.5 Settling Chamber

The settling chamber consists of a honeycomb and upstream and downstream screens. The cross section of the settling chamber is dictated by the wide angle diffuser and contraction cone. The straight walls are dominant in the selection of the geometry. The length of the settling chamber was chosen based on the number of screens and the required minimum spacing between the screens. Two screens were used in the chamber, one was installed upstream of the honeycomb, and one downstream. The optimum distance between the last screen and the contraction entry was also found to be about 0.2 of the cross section diameter [Mehta 1979]. Such a ratio also applied to the spacing between the honeycomb and the screens, both upstream and downstream. The locations of screens and honeycomb are as follows

Upstream screen (curved)	Honeycomb	Downstream screen (flat)
0 mm	400 mm	250 mm

4.3 The Mechanical Design of Test Section and Tube Bundles

4.3.1 Test Section Design Principles

The type of array used for the present study is a parallel triangular tube array with a pitch to diameter ratio of 1.48. One reason for selecting such an array is that it is a popular array, being widely used in contemporary design. Another reason is that the experimental results can be compared with the previous wind tunnel studies.

The width and depth of the tube array are very important in being able to simulate

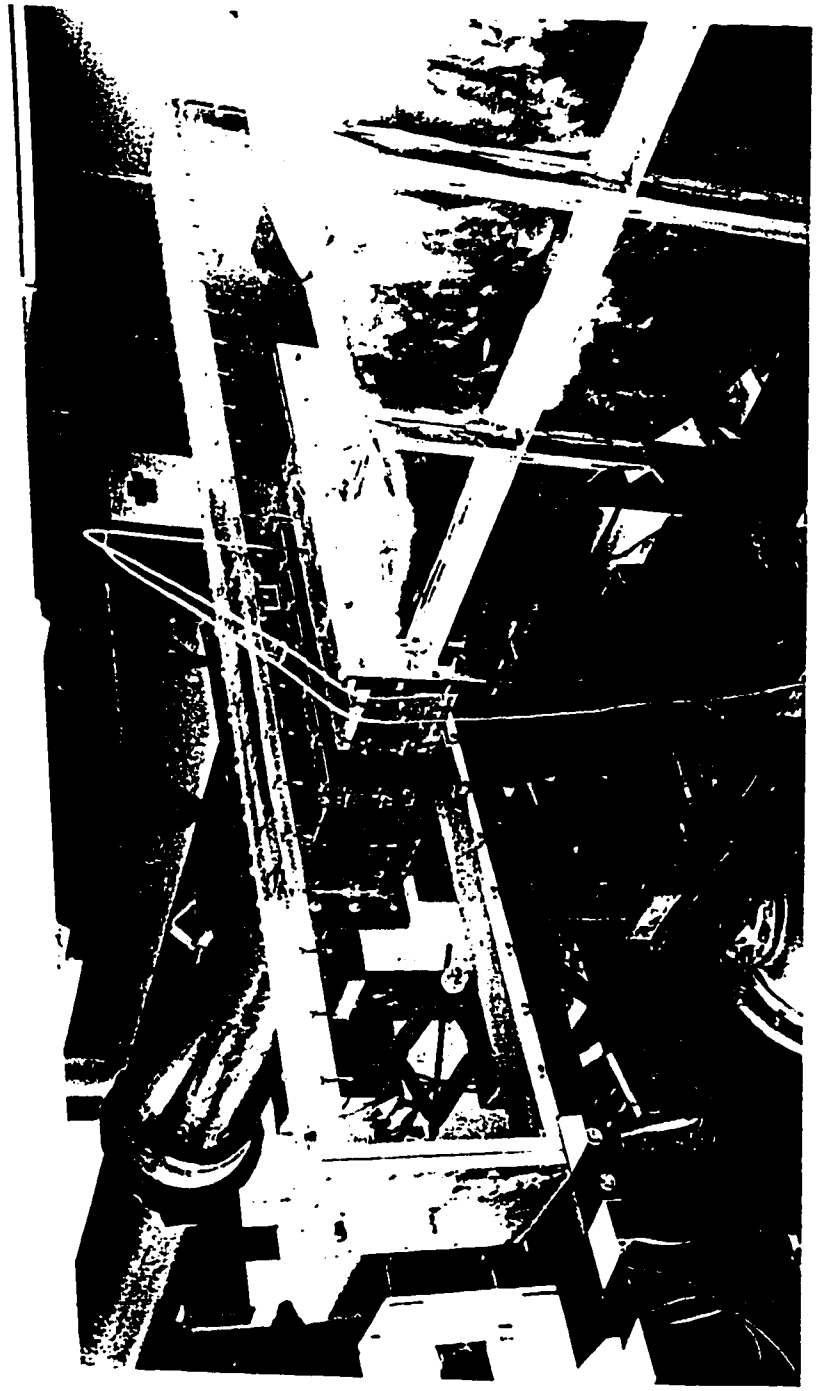

Figure 4.8 Photograph of test section, contraction section

correctly the various excitation mechanisms such as vorticity, turbulence, and fluidelastic instability. Experimental results reported in the literature [El Kashlan 1980, Grover 1977] indicate that the flow structure interaction behavior can be effectively simulated using a tube array at least seven rows deep.

It is also known that the fluid-structure interaction has an important effect on its own dynamical parameters and behavior, particularly on its natural frequencies. While this effect is negligible for bodies vibrating in air, it can be very important for structures vibrating in a liquid flow. The effect can be accounted for by adding an additional mass to the mass of the body and which is referred to as "fluid added mass". Parameters such as the amplitude and frequency of the structure's motion, shape, submergence, etc., can affect the added mass term. In the case of a staggered tube array in a liquid flow, energy is also transferred through the fluid between neighboring tubes, and is known as fluid coupling.

If proper dynamic simulation is to be achieved these phenomena should be adequately modeled. Chen et al. [1976] has shown that the coupling between a cylinder and other cylinders which are not immediately surrounding it, is negligible. This indicates that phenomena associated with the added mass effects in a tube bundle can be properly simulated with models that are only a few rows deep as long as the tubes surrounding the tube under study are also flexible.

The turbulent response amplitudes have a maximum value by the fifth or sixth tube row and do not change as further upstream rows are added. The third and fourth rows are critical for fluidelastic instability. Vorticity phenomena are most important in the upstream rows and at least five rows of tube are required to account for added mass effects. It is desirable to monitor the behavior of several tubes in the center of the tube bank. Therefore, it was decided to use seven rows in the present study. The test and contraction sections are shown in Figure 4.8.

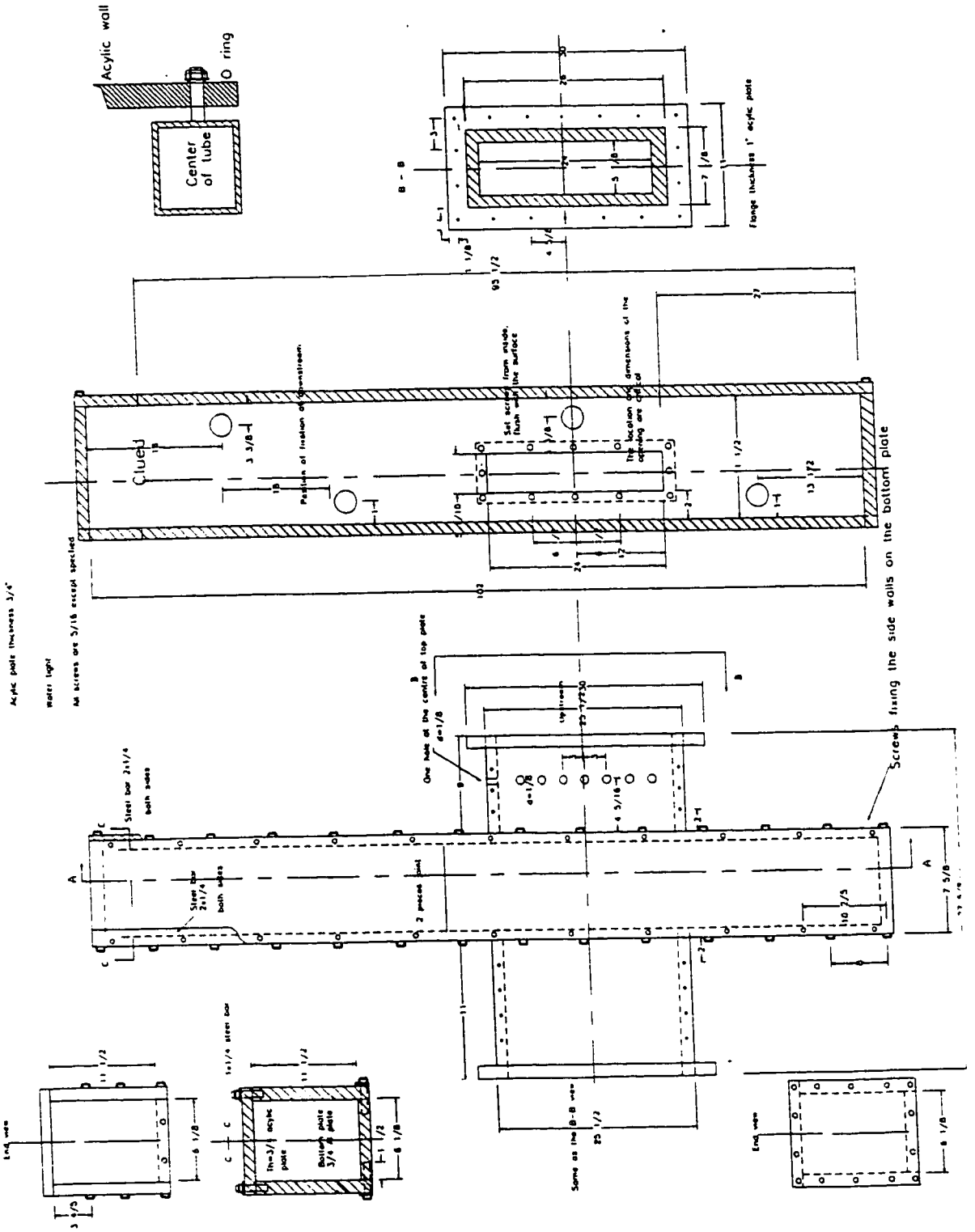

Figure 4.9 Detail drawing of the test section

4.3.2 The Acrylic Test Section

The acrylic test section (W) is positioned between the straight section (C2) and the downstream rectangular to circular transition section (D). Its total length is 699 mm in the direction of flow and it is built of 19 mm thick acrylic plates and an aluminum bottom plate as shown in Figure 4.9. which is used to provide a leak proof barrier for the tube bundles. The holes upstream are used in the measurement of the flow velocity by a pitot-static probe and in the measurement of turbulence characteristics by hot-film anemometers. In the design of the test section, the following configurations have been taken into consideration: single span with full flow admission; single span with partial flow admission, multi-span with partial flow admission. In addition, various types of support can be applied to the tube ends: clamped, simply supported (pinned), and free. All the intermediate supports consist of a support plate with clearance holes. Figure 4.10 is a sketch of flow-tube-support configuration for three tube spans in which the left ends of tubes were fixed and the right ends were free. In this case, the tubes are 6ft (1.83 m) long, with uniform flow across 2ft (0.610 m) of the span between the two intermediate supports. In any of the test cases, the flow admission length is always 2ft wide, the exit width of the contraction section.

4.3.3 The Tube and Support Assembly

A parallel triangular array with a pitch to diameter ratio of 1.48 was used, as shown in Figure 4.11. Only the central tube # 1 was instrumented with miniature-accelerometers. The array is seven rows deep, 7+2 (half tubes) columns wide. Two columns of half tubes are installed at the section side walls to reduce wall effects. Five columns of tubes at the center of the tube bank are mounted flexibly. The tube columns next to the half tubes are made of aluminum rods and are fixed solidly by screws to side supports. The tube parameters

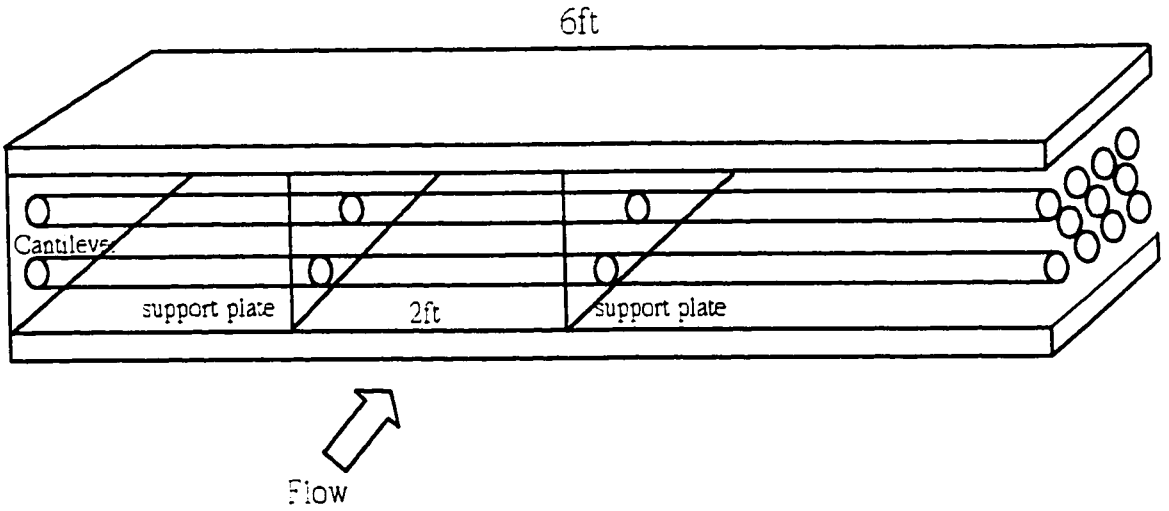

Figure 4.10 The sketch of flow, tubes and supports configuration

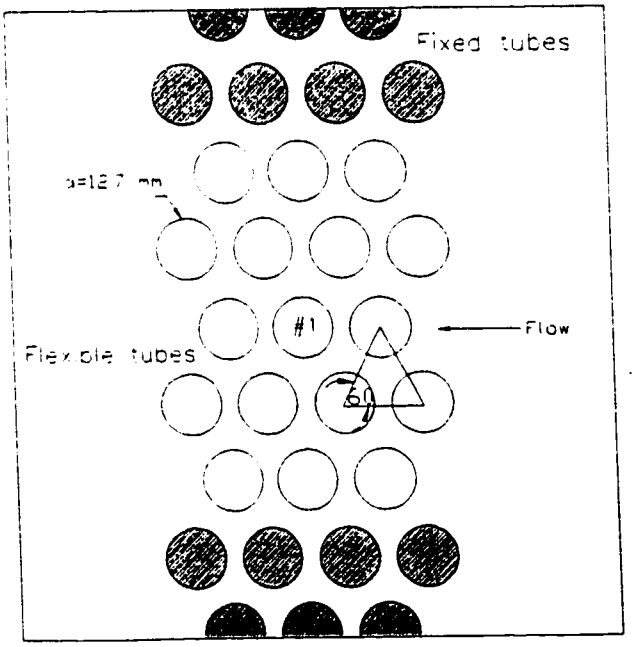

Figure 4.11 The parallel triangular tube array used in the experiment

are listed in the following table.

Material	OD (mm)	ID (mm)	E (Pa)	ρ (kg/m^3)	m (kg/m)
301 stainless steel	12.7	10.9	$197*10^9$	7970	0.2629

An aluminum frame was used to mount the test tubes and supports. The frame consists of four 51 x 51 x 3.2 mm square aluminum tubes welded at two ends. Three ∩ shape aluminum channels of 12.7 x 51 x 3.2 mm were used as the sliding track to allow the tube and support assembly to be moved and fixed at different locations along the frame. Two channels were welded to the two square aluminum tubes on the top, another one was welded between the two square tube at the bottom. An acrylic block, attached with half aluminum rods and intermediate support plates, can move along the frame. The arrangement of the frame is show in Figure 4.12, and the block is shown in Figure 4.13.

The details of the end supports (fixed and pinned) and the intermediate support are shown in Figure 4.14 and 4.15 respectively. The machined set-screws were designed to provide "pinned" supports. The 1/8" lock nuts were used to tighten the set screws to prevent the tube loosening as a result of vibration. At the fixed end, tubes were inserted into a 1" thick stainless plate, 1/8" set screws were used to tighten the brass caps mounted at the end of tubes. The arrangement of the miniature accelerometers is also shown in Figure 4.14. The tubes, the intermediate support and the end support photos are shown in Figure 4.16. The view of the whole assembly is shown in Figure 4.17. For the intermediate supports, the hole clearance is about 1.2% of the tube diameter. It is smaller than the typical clearance 3% of real heat exchangers. However, the purpose of this studyt is to investigate the fluidelastic mechanism itself rather than structural effects of supports. Unclear boundary conditions and significant tube impact due to large clearance may add more difficultiy and uncertaintiy to the study.

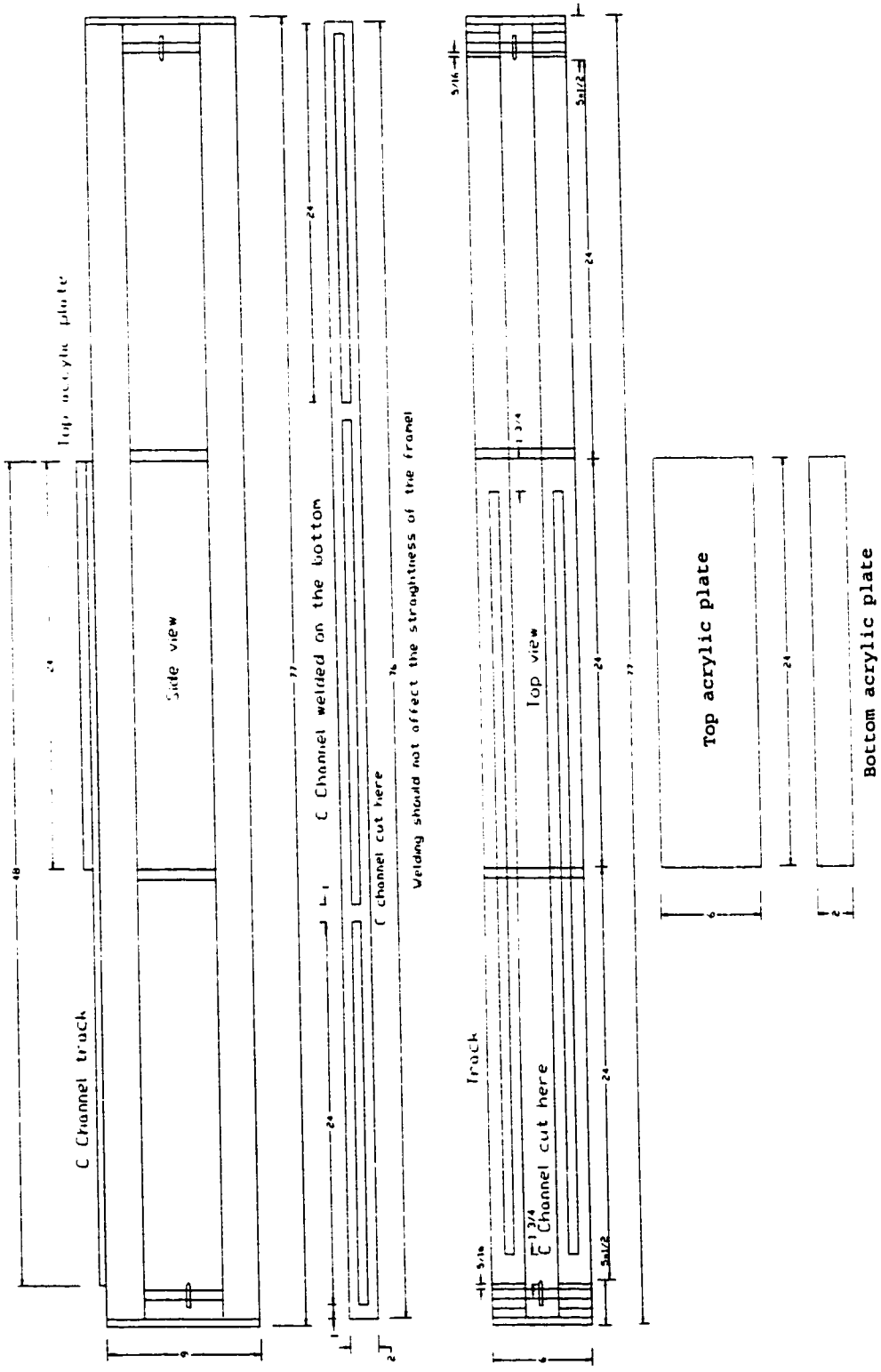

Figure 4.12 The arrangement of test frame

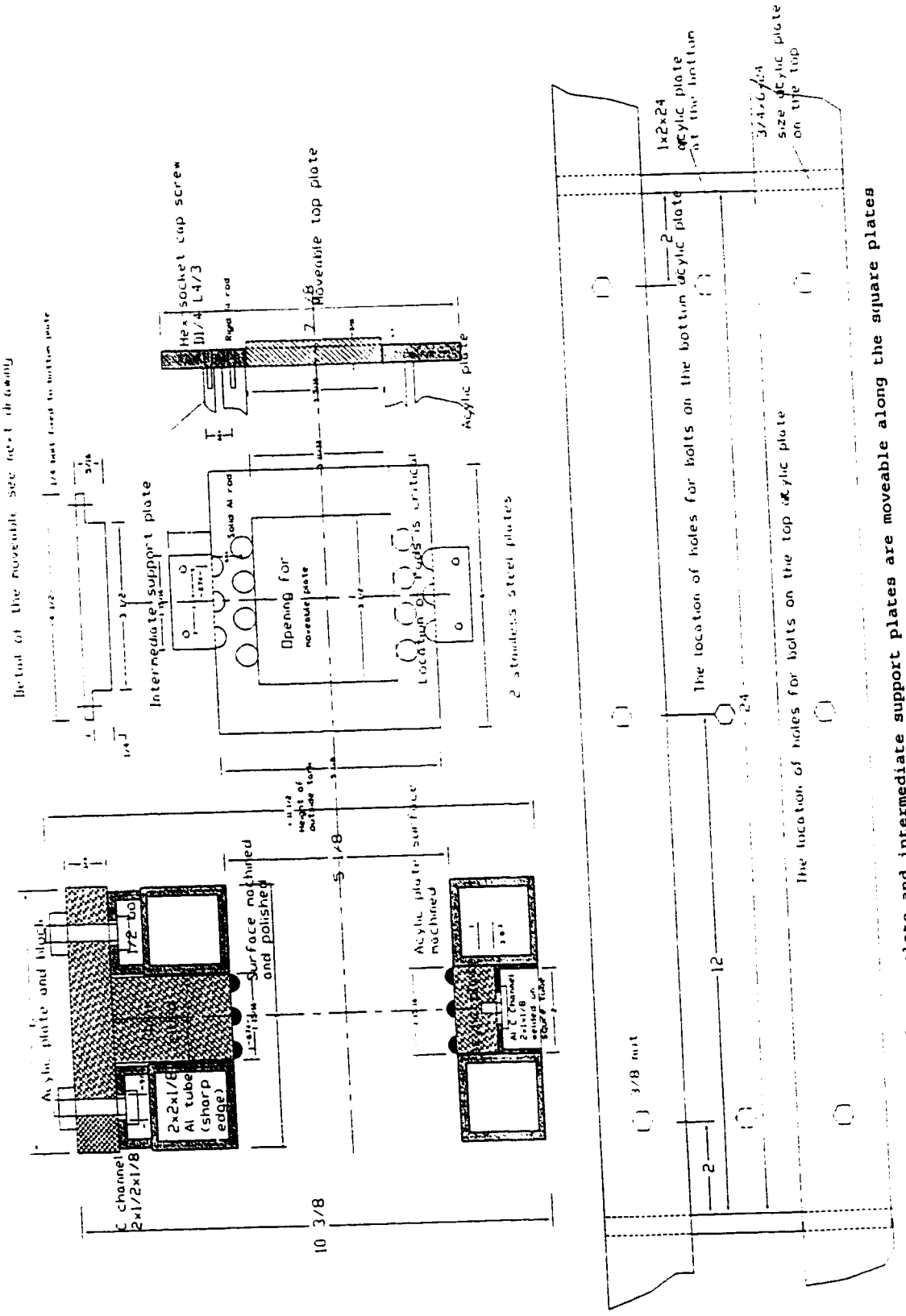

Figure 4.13 The test block subjected to the flow

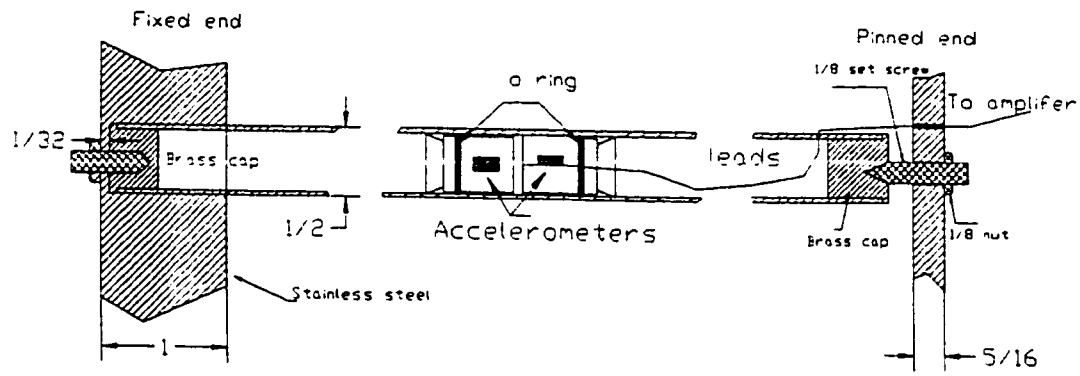

Figure 4.14 The detail of the fixed and pinned supports

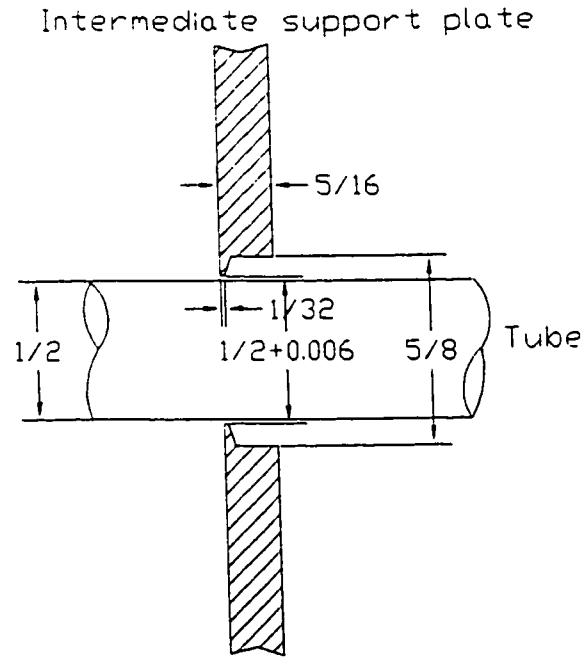

Figure 4.15 The detail of the intermediate support

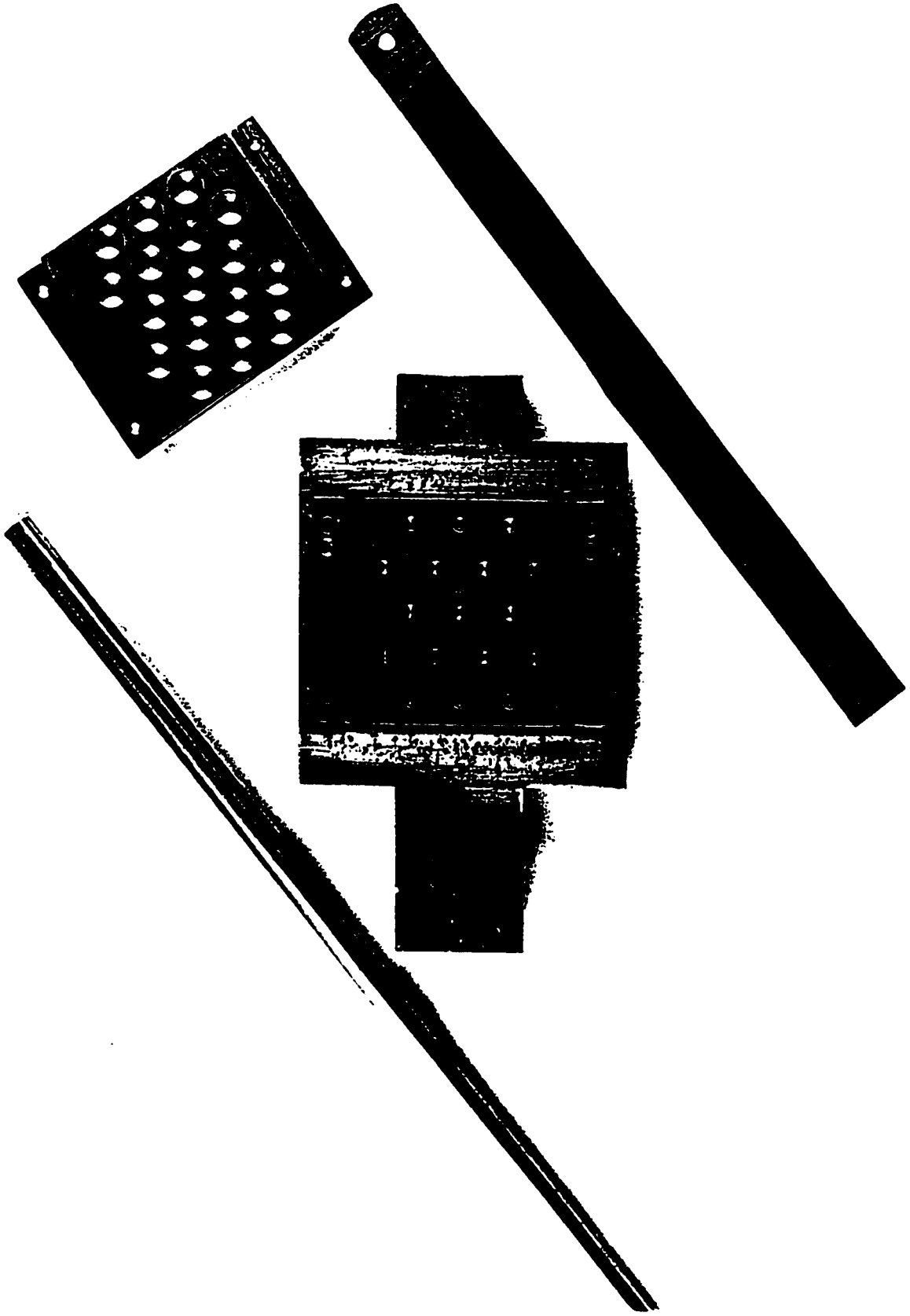

Figure 4.16 Photograph of pinned end support and intermediate support

CHAPTER 5

EXPERIMENTAL FACILITY, INSTRUMENTATION AND PROCEDURE

This chapter first details the various pieces of equipment used during the course of this research except for the water tunnel, which has already been discussed in the Chapter 4. Then, the experimental procedure is described. Finally, damping and added mass measurements are presented.

5.1 Experimental Facility and Instrumentation

The flow rate of the main and by-pass lines are controlled by gate valves V1 and V2 (see Figure 4.1), respectively. The 12" main line is capable of controlling flow velocities from 0.5 m/s to 4.7 m/s in the test section. The 6" by-pass line is capable of controlling flow velocities from zero to 0.9 m/s. In this research, only the by-pass line was used, as the flow velocity requirements were well below its maximum capability. It was noticed that once the velocity exceeds 2 m/s, the screens installed in the settling chamber start vibrating, accompanied by an enormous sound. To avoid screen assembly damage, it is recommended that the water tunnel not be operated in this velocity range for a long period.

The flow rate is determined through the use of an orifice plate, and a Brooks full-view by-pass rotameter. The unit on the 6 inch pipe line has a range from 100 to 1700 US gallons per minute (USGPM). The unit on the main line has a range from 500 to 6500 USGPM.

The by-pass Brooks full-view rotameter Type 1110-08-2C 1A, was calibrated with a pitot probe. The calibration curve is show in Appendix B. The pitch flow velocity is precise to better than ±0.008 m/s, The uncertainty analysis of the velocity measurement is detailed in

Appendix A. The upstream flow velocity was also measured using a pitot-static probe and a micro-manometer using carbon tetrachloride as the working fluid (S.G.=1.583).

Entran EGA-125-10D and EGA-125-25D miniature accelerometers were used in this research to monitor the tube motion. The pair of accelerometers was mounted orthogonally on a small carriage. The carriage is then inserted inside the tube, each accelerometer facing in the streamwise or transverse direction. The leads from the accelerometers pass through a small hole close to the end of the tube. The hole is carefully sealed by silicon sealant. Then the leads pass through a tube fitting from one end of the test section, which is also sealed by silicon. The accelerometer pair is connected to a multiple channel Vishay 2310 signal conditioner. The output of each signal conditioner was connected to a Hewlett-Packard 35670 dynamic analyzer, which has four channels. The analyzer has a function to integrate the acceleration spectrum so as to obtain the displacement spectrum. Hard copies of the response signals were obtained from a Hewlett-Packard 4P laser printer. The response signals were also capable of being stored in DOS formatted discs. The data on the discs can be transferred from SDF (Signal Dynamic Format) to ASCII data file by a SDFTOASC.EXE software program.

5.2 Experimental Procedure

The first step in the investigation of each tube array was the measurement of its natural frequencies and damping in air and still water. Given a small disturbance, the natural frequencies and damping can be obtained by measuring the amplitude decay of the tube response. To avoid modulations of adjacent tubes, both Weaver & Koroyannakis [1982] and Weaver & Yeung [1984] recommended that the damping value in still water should be obtained by keeping all the tubes rigid except the one being monitored. This procedure was followed in the present research.

After finishing the static test, the tube bundle and frame assembly were lifted to the side-stand attached to the test section. Then the assembly was moved into the test section. The length of the test tubes exposed to the flow was carefully adjusted so that it was in-line with the upstream acrylic opening (0.610 m). The assembly was secured by tightening screws on the test section downstream wall. Finally, the side end plate was closed, and sealed by an O ring. Silicon sealant was applied to the fitting where the leads of the accelerometers come out of the test section. Not until at least 24 hours later, when the sealing becomes effective, can the loop be filled with water. The vents on the top of the test section and at the setting chamber were opened to let air out of the loop.

When the system was ready for testing, various pieces of equipment, as outlined in the previous section, were conveniently arranged near the test section. Data was then recorded and plotted. Plotting the data allowed the comparison of trends in the response spectrum to the tube behavior, as viewed through sides of the test section.

The first step in the tube response investigation was to start the motor, and allow the cooling water to reach approximately 70°C. During the investigation, only the 6" gate valve was used to throttle the flow. The motor speed was maintained at roughly 1400 rpm.

Previous experiments [El Kashlan, 1980], as well as the present research, have shown that a hysteresis can occur in the tube response behavior. That is, the tube response pattern obtained when the flow velocity is increased from a lower flow velocity is different to that obtained when the flow velocity is decreased from a higher flow velocity if the latter is above the stability threshold. As the former path defines the stability threshold more clearly and this is the commonly accepted methodology used for generating data in the literature, all investigations in this study recorded the tube response as a function of increasing flow velocity.

The tube response investigations were all started at a flow velocity of $V_u = 0.08$ m/s or

lower depending on the tube support arrangements. At least 10 minutes were allowed for the flow to reach a steady state for every velocity increment. When there was no significant fluctuation in flow rate, the START key on the HP analyzer was pushed to begin collecting data. From previous experiments, as well as from the results of the present investigation, it was shown that 100 sample averages were more than sufficient to give repeatable values for the amplitude response behavior. The sampling frequency was set large enough to prevent leakage. Typically, the frequency spans on the monitor were 100 or 200 Hz depending on the test case. The sampling frequency was 2.56 times the frequency span. The number frequency resolution lines between the upper and lower frequency band was 800. At the end of the averaging cycle, the data was stored on a floppy disk for later analysis. Hard copies of the response spectra were also printed.

When the averaging cycles for both channels were completed, the flow velocity was incremented about 20 USGPM (0.016 m/s) or less and the measurement for the tube response was repeated. The tube response investigation was terminated when it was felt that a further increment of flow velocity would produce tube-to-tube clashing.

A typical 100 sample averaged acceleration and its converted displacement frequency spectrum are shown in Figure 5.1. A band-width average function on the HP analyzer is used to calculate average rms displacement amplitude at peaks for each mode (each frequency) in the x or y direction

$$rms\ dis_{x,y} = \frac{1}{\Delta f}\sqrt{\sum_{\Delta f} A(f_i)^2}, \qquad \Delta f = 5Hz \tag{5-1}$$

The rms value obtained from equation (5-1) is the rms displacement where the accelerometers are located. The total displacement is the vectorial summation of the

displacement in the transverse (y) and streamwise (x) directions.

$$rms\ dis_{total} = \sqrt{rms\ dis_x^2 + rms\ dis_y^2} \tag{5-2}$$

which has to be converted to the maximum displacement of the tube span by the application of the mode shape function. Of course, each mode has to be processed separately.

$$rms\ dis_{max} = rms\ dis_{total} \frac{Max[\varphi(x)]}{\varphi(x)_{acc.}} = \frac{rms\ dis_{total}}{\varphi(x)_{acc.}} \tag{5-3}$$

where Max[ϕ(x)] is the maximum modal displacement, which is normalized to unity for the mode comparison. $\phi(x)_{acc.}$ is the relative displacement for a given mode where the accelerometer is located.

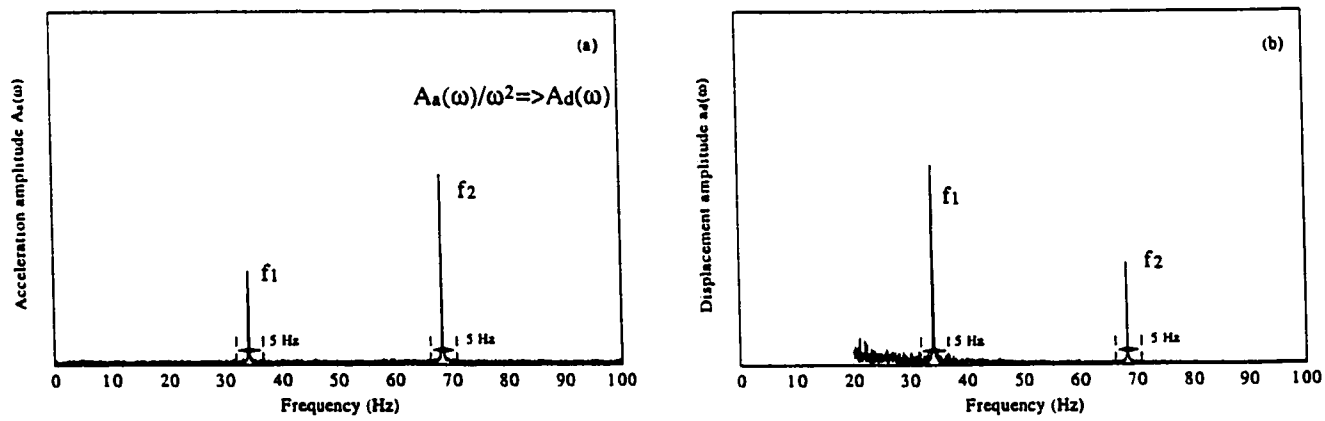

Figure 5.1 Typical frequency spectra of (a) acceleration and corresponding (b) displacement

5.3 Added-Mass and Damping Measurements

When a structural component vibrates in a viscous fluid, the presence of the fluid gives rise to a fluid reaction force which can be interpreted as the contribution of the added mass and added damping to the dynamic response of the components. A great amount of research has been conducted on the added mass and damping in heat exchanger tube bundles. Most of the work was done on single span tubes. In multi-span tube tests, the added mass coefficient may change with mode shape because each mode shape has its unique number of nodes and anti-nodes. Moreover, multiple mode frequency spikes and the coupling of neighboring tubes cause great difficulties and uncertainty in the measurements conducted on multi-span tube bundles. As far as damping is concerned, the multi-supports may raise the structural damping value, and such an increase may depend on mode shape. The possibility of looseness in the intermediate support plate adds another dimension of difficulty in the damping measurement.

5.3.1 Added-Mass Measurements

The added mass coefficient C_m is calculated using the expression

$$C_m = [(\frac{f_a}{f_w})^2 - 1]\frac{4m}{\rho \pi d^2} \tag{5-4}$$

where f_a and f_w are the natural frequencies measured in air and water, respectively, and m is the mass per unit length of tube without inclusion of the added mass. In the present experiments, m=0.2614 kg/m.

The difference in frequency measured in the transverse and streamwise directions was small, usually within 2-3%. Therefore, calculations were done using the frequency in the streamwise direction even though measurements had been conducted in both directions.

The added mass and damping tests were conducted in a large water tank. Initially, only one tube was submerged in still water. In order to obtain more comprehensive and reliable data, several measurements were taken by moving the intermediate support plates (location x, shown in Figure 5.2) while keeping the distance between the two intermediate supports the same (610 mm). Therefore, the natural frequencies of the tube varied with support location. Accelerometers were fixed 610 mm from the clamped end. Figure 5.2 shows the added mass coefficient measured from a single three-span flexible tube. As seen in the figure, the measurement was fairly consistent, and averaged $C_m = 0.99$, which is within experimental error to the theoretical value of 1.0 obtained using potential flow theory. The mode shape effects are negligible since there is no significant difference in C_m for the first four modes.

A tube bundle with seven flexible tubes was tested. The effects of coupling are obvious. Frequency spectra taken in air and water for one support location condition (x = 1155 mm, accelerometer at 610 mm) are displayed in Figure 5.3. Five frequency modes are clearly shown in the air measurement. Measurements in the streamwise and transverse directions are almost identical. The frequency spectrum obtained in water does not show an individual mode frequency but rather a band of mode frequencies with various peaks. In general, two dominant frequency peaks are related to each mode, which is due to the in-phase and out-phase coupling between the monitored tube and the other tubes. The difference between maximum and minimum frequencies increases with vibration mode. Chen [1977] predicted that there are $2n$ natural frequencies in a group of n tubes for each tube mode. The upper and lower frequencies are associated with the minimum and maximum added masses. From the present results, the intermediate frequencies between the upper and lower frequencies in the band are less significant.

The seven flexible-tube tests were also conducted with respect to several support

locations. The results are shown in Figure 5.4. In each mode, the existence of two frequencies f_{min} and f_{max} results in two added mass coefficients, corresponding to out-of-phase and in-phase coupling respectively. However, for the 1st mode, only a single dominant frequency was obtained except in one case. The separation of lower and upper bands are apparent in the 3rd and 4th modes. At higher modes, smaller displacement and an increasing number of nodes and anti-nodes may contribute to such results. The theoretically calculated results of the added mass coefficient by Chen [1977] are shown in Figure 5.5. At a pitch ratio of 1.47, the lower and upper C_m's are approximately 0.4 and 2.0 respectively for seven flexible tubes, which agrees with the present measurements fairly well.

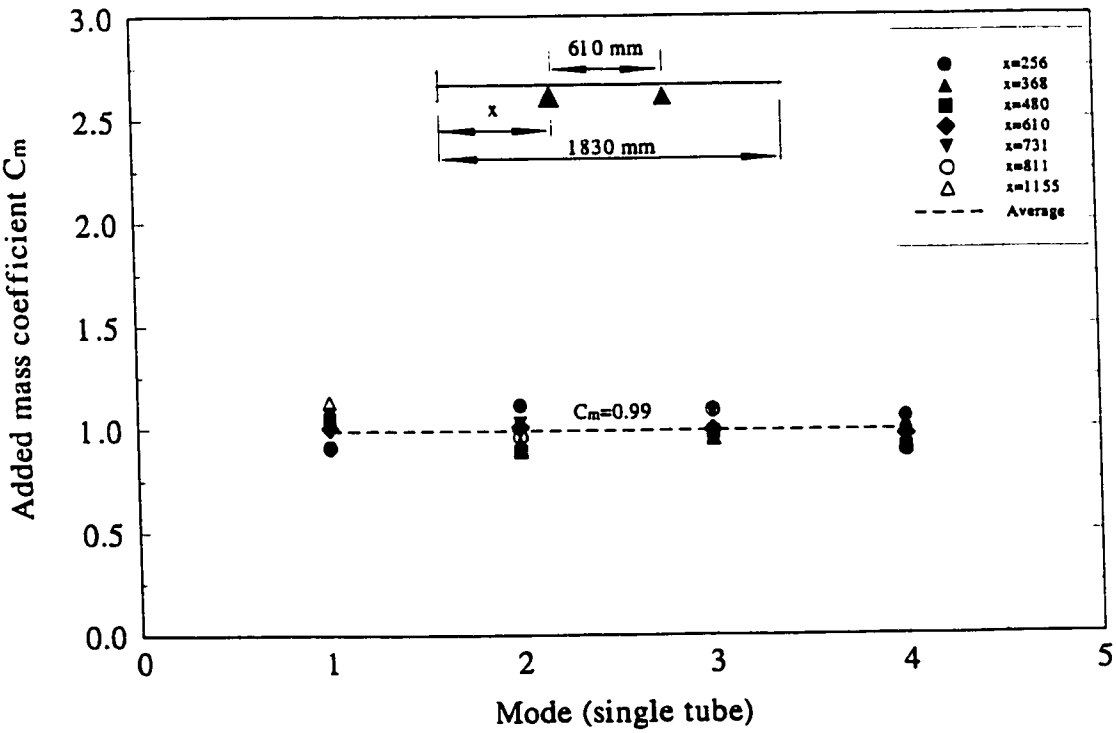

Figure 5.2 Added mass coefficient measured from a single flexible tube

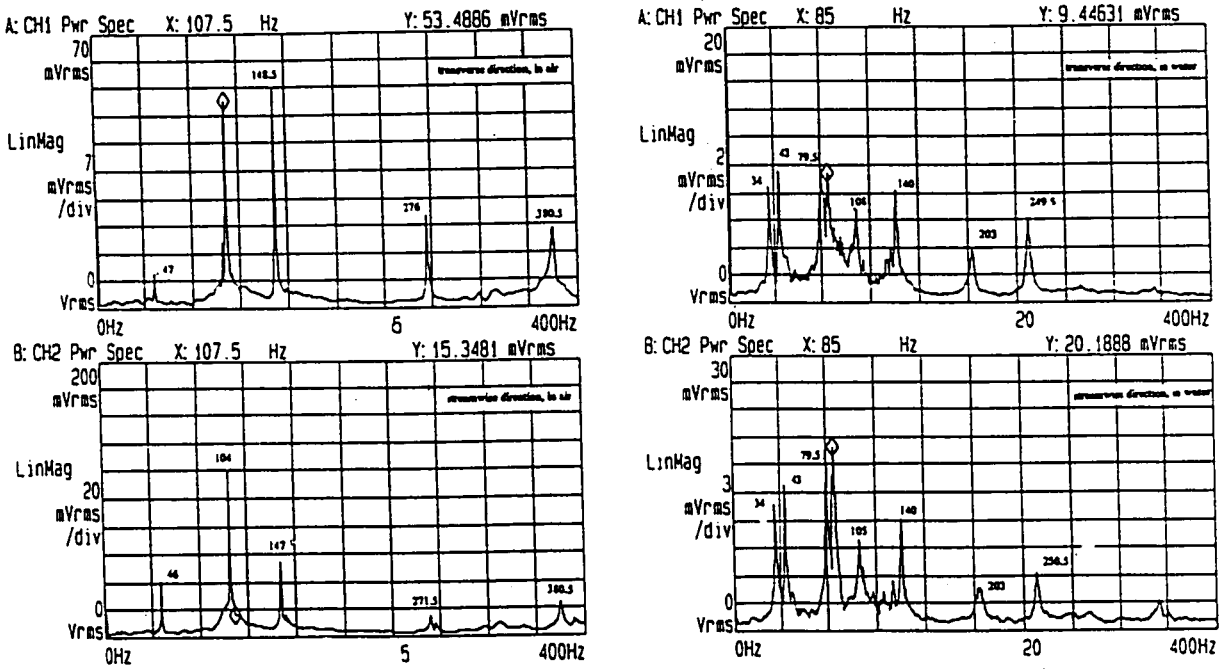

Figure 5.3 Frequency spectra measured in air and water at x = 1155 mm (7 flexible tubes)

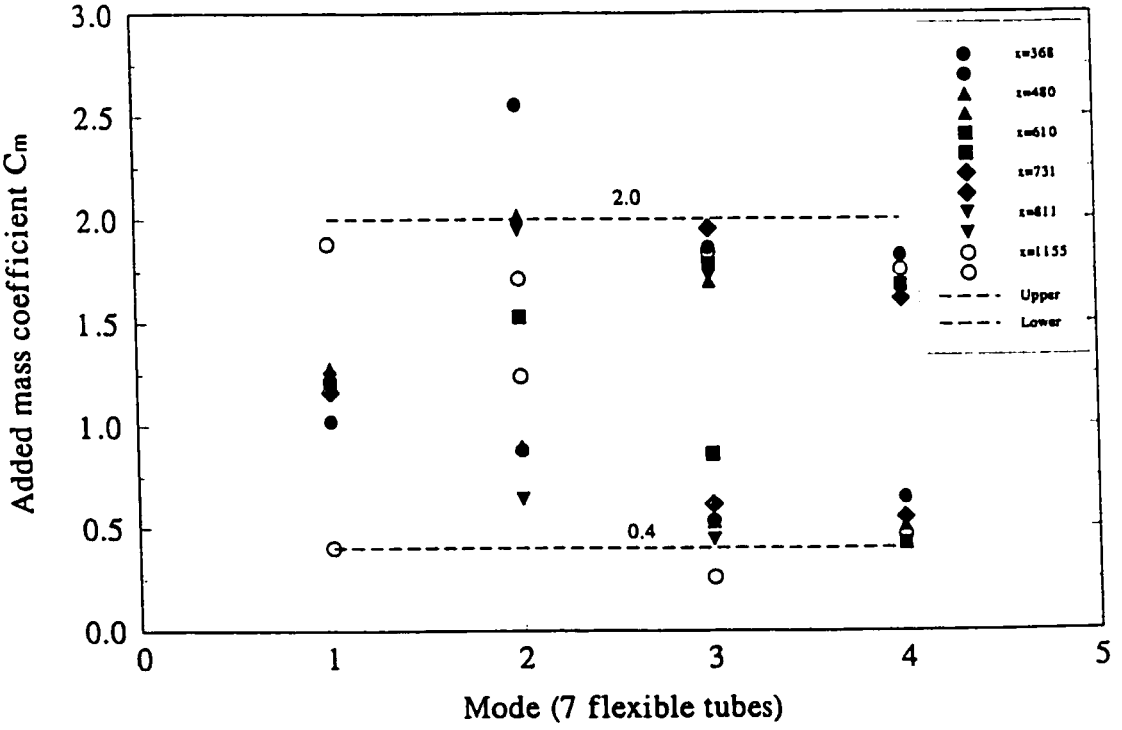

Figure 5.4 Added mass coefficient measured from a full flexible tube bundle

Table 5.1. Frequency measurement of 7 flexible tubes at x = 1155 mm

Mode	Frequency measured in air (Hz) f_a	Frequency measured in still water (Hz)		
		f_{min}	f_{max}	$f_{max} - f_{min}$
1	46.0	34.0	43.0	9.0
2	104.0	79.5	85.0	5.5
3	147.0	105.0	140.0	35.0
4	271.5	203.0	250.5	47.5
5	380.5	N/A	N/A	N/A

In equation (5-1), the reduction of frequency is entirely due to added mass, which is true while tubes are submerged in quiescent fluid. However, while tubes are subjected to cross flow, fluid stiffness may also contribute to the change in tube frequency. In general, the effects of fluid stiffness are expected to become significant only when the tube displacement becomes very large. If it is assumed the fluid stiffness is negligible, then the frequency shift in flowing fluid can be designated as being the result of an "apparent" added mass, because it is impossible to separate the effects of added mass and added stiffness. The comparison between apparent C_m calculated by frequency at instability to that measured in still water is shown in Figure 5.4. The test cases are those discussed in Chapter 6. All the cases are either in the 1st mode or 2nd mode since no higher instability modes have been observed. The difference in the effects of the apparent added mass in relation to quiescent as opposed to flowing water may be as high as 38% C_m at instability (such as case #2, #6), or almost negligible (such as case #19, #23). In the calculation of C_m in Chapter 6, the most dominant frequency at instability is used. Also, the individual value C_m is used instead of an averaged value since it appears meaningless to use an average value.

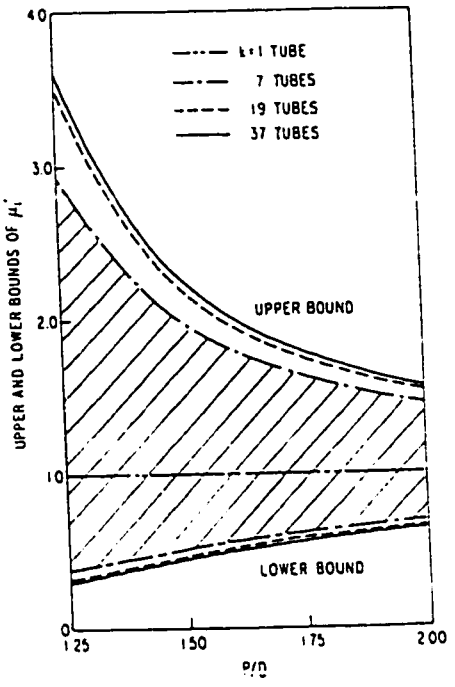

Figure 5.5 Upper and lower bounds of added mass coefficients [Chen, 1977]

It is worth noting that the effect of a negative fluid stiffness at instability due to the flowing fluid would reduce the frequency obtained at instability and, therefore, appears as an increased apparent added mass. This may account for the somewhat higher values of apparent added mass observed in Figure 5.4. However, there does not appear to be a clear trend in the data.

5.3.2 Damping Measurements

The mechanism which suppresses the vibration amplitude and/or causes it to steadily diminish in free vibration is called damping. In fluid flow, structures are subjected to several

forms of damping where more than one form may operate at once. Fluid damping is caused by energy transfer from an oscillating structure to the surrounding fluid and may be viscous or turbulent. Both types of damping are functions of flow velocity; viscous damping is proportional to the tube oscillating velocity while turbulent damping is proportional to the square of the tube oscillating velocity. Structural damping is caused by the internal friction in a solid material as it deforms during vibration. In the presence of support plates, damping caused by the interaction between tube and support became, in the present experiments, important and very complicated, as reviewed in Chapter 1.

The total damping can be measured by several methods, namely: the logarithmic decrement free decay method, the frequency bandwidth method, the magnification factor method and the phase angle method. The last two methods are not applicable due to the limitation of the present testing circumstances and tools available. The bandwidth method can be used to measure the total damping for in-flow situations. However, in single phase water flow, multiple close frequency peaks and unsteady motion may lead to unreliable results. Therefore, only the amplitude decay method was used to measure the total damping in air and still water. This method is also called the "pluck" method since it is conducted by plucking the system and capturing the displacement time history on an oscilloscope or other instrument. For lightly damped structures, such as tube bundles, the logarithmic decrement of damping δ, and damping ratio ξ, are related according to:

$$\delta = \frac{1}{N}\ln\frac{A_i}{A_{i+N}} \doteq 2\pi\xi \qquad (5\text{-}3)$$

During the test, non-measured tubes are fixed to prevent energy transfer to and from the measured tube. The signals were collected by the data acquisition board and processed by the

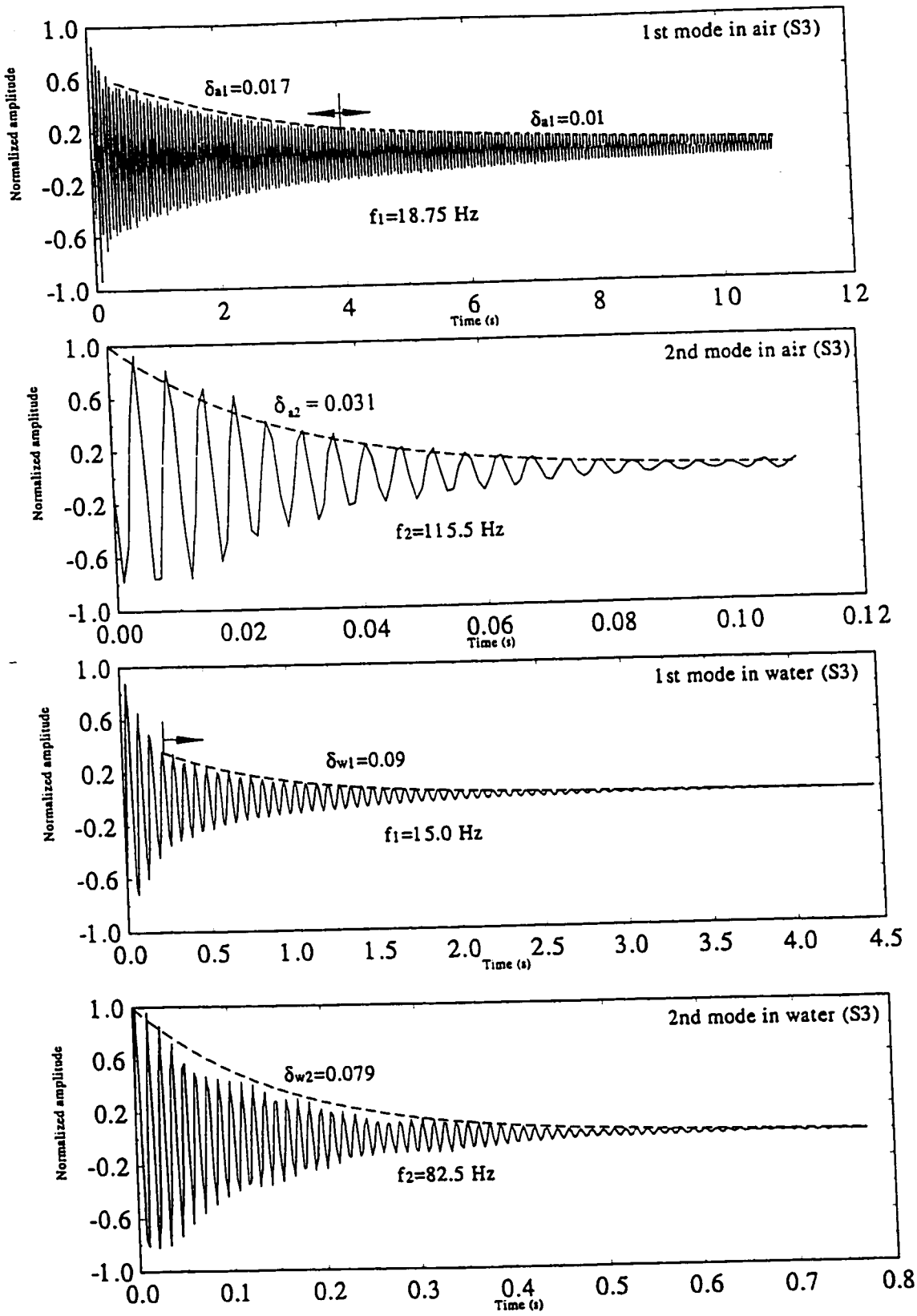

Figure 5.6 Typical damping traces in air and water (three-equal-span tube)

Globe software program. Since several modes could be excited at once, the damping measurement for each mode was conducted individually by hitting the highest deflection node location with reference to the mode shape figures. This led to the dominant motion of such a particular mode. In general, other modes still cannot be eliminated but only attenuated. In such a case, a band limited digital filter is applied to the frequency data to filter out unwanted frequencies, then converted back to the time domain. Since the resulting amplitude decay traces were not perfectly regular, a least-square curve fitting of the peaks over many cycles was used to obtain more reliable results. Typical decay traces and curve fitting are shown in Figure 5.6. In some cases, such as the last three figures, a single curve fitting, i.e. one damping value, matches most of the trace history fairly well. However, damping may change significantly with amplitude, such as in the first figure. In general, the first few peaks should be neglected due to high nonlinear damping at large amplitudes. Then a number of cycles (say 20, depending on the mode frequency) should be used to calculate the damping value because of their realistic amplitude compared with that at instability. In this study, five trials were completed for each tube-support arrangement, then the average was taken as the damping value used in later calculations. Great care was taken in the measurements. Nevertheless, the results are still scattered due to the complicated nature of the damping process. All damping values used in Chapter 6 are shown in Figure 5.7. There is no definite trend for the 1st and 2nd mode damping. In certain cases, it is impossible to calculate damping in the 2nd mode due to its weak and irregular trace. In such situations, 1st mode damping will be used instead. A similar result found by Pettigrew et al. [1986] is reproduced in Figure 5.8. These authors recommend an averaged value of $\xi = 1\%$, or $\delta = 0.06$, which is about the average value of all present measurements, but a lower bound on the damping values in water.

With regard to quiescent fluids, Blevins [1977] gave a formula to relate the 1st mode

viscous damping to higher mode viscous damping using the mode shape function

$$\frac{\delta_i}{\delta_1} = \frac{\int_0^L |\varphi_i(x)^3| dx}{\int_0^L |\varphi_1(x)^3| dx} \frac{\int_0^L \varphi_1(x)^2 dx}{\int_0^L \varphi_i(x)^2 dx} \qquad i=2,3... \qquad (5\text{-}4)$$

For a single span tube, the results are shown in Figure 5.9. In general, the ratio is less than 1.0 (not necessarily true for other configurations). With increasing mode number, the ratio becomes close to constant, though this occurs typically outside the range of practical interest. In addition, the above correction is obtained with the assumption of a small amplitude, and only by considering viscous damping. In the present study, the ratio of damping at different modes seems not to follow the above equation. The non-linear effects of multi-support tube configurations may well exceed the effects of fluid viscosity.

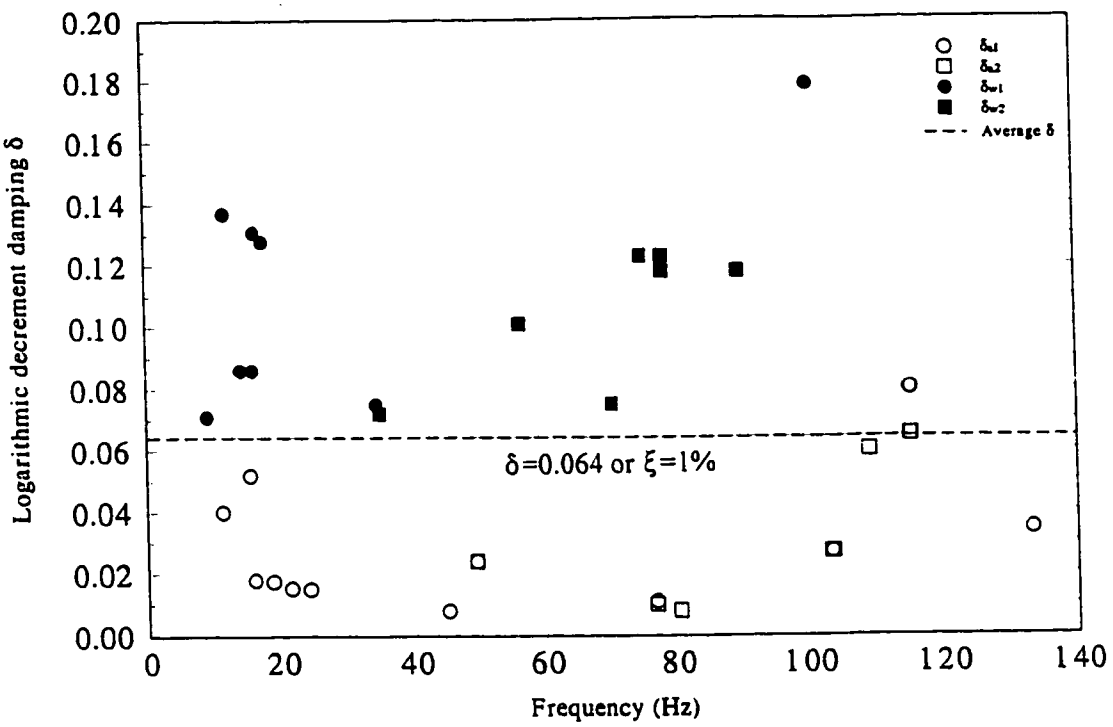

Figure 5.7 Damping values of all test cases conducted in Chapter 6

(open symbols are damping values measured in air, closed symbols are damping values measured in water, subscript 1 & 2 refer to mode number)

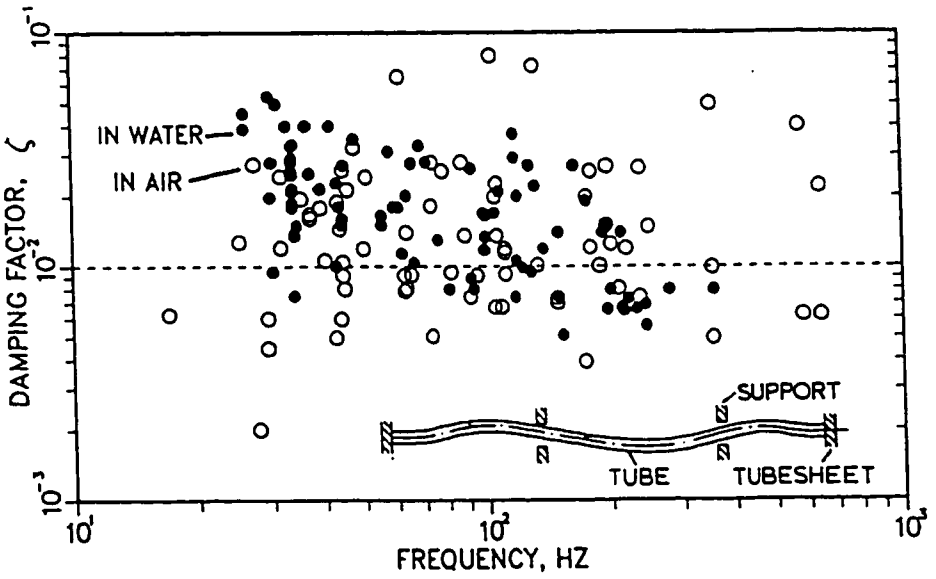

Figure 5.8 Damping of multi-span heat exchanger tube [Pettigrew et al., 1986a,b]

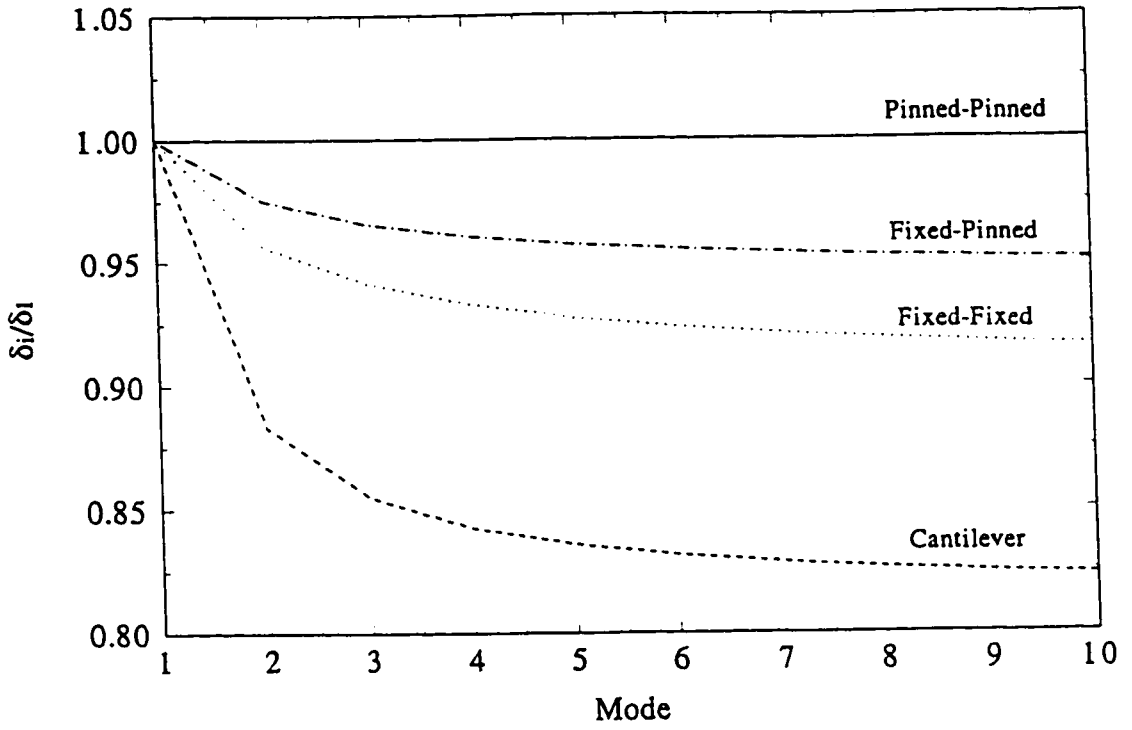

Figure 5.9 Viscous damping ratio of a single span tube, based on Blevins' theory [1977]

CHAPTER 6

EXPERIMENTAL RESULTS AND DISCUSSION

This chapter summarizes the experimental results recorded for single span, two-span and three-span test arrays. These results consist of tube response data and frequency spectra. The calculation of the reduced velocity and mass damping parameter, as well as the energy fraction factor, are also provided in order to reveal their correlations.

6.1 The Single Span Tube Bundle Test

Tests were conducted on the single span tube bundle array with full and partial admission. The results will be compared with Waring's [1986] wind tunnel test data with similar end supports.

6.1.1 Full Flow Admission

A flow induced vibration test was initially conducted on a single span (0.610 m long) tube bundle with full flow admission. Tubes were clamped at one end and pinned at the other. This datum case was to provide bench mark response characteristics for the whole test program. It is important that this experimental result should agree with the published data since the knowledge of the full admission field is relatively well established. The results will also provide a basis for interpreting the response characteristics of partial admission tests.

The streamwise, transverse and overall rms amplitudes for the instrumented tube are plotted against pitch velocity, as shown in Figure 6.1.1. This response curve, along with the corresponding frequency spectra, will be examined in detail to explain the flow-induced

mechanism of the tube response.

As the flow velocity is increased from zero, the overall amplitude increases gradually. This is associated with a gradual increase in both the streamwise and transverse response of the tube. The response spectra indicate that the motion changes from a multi-peak response at V_p = 0.49 m/s to a discrete response at about V_p = 1.8 m/s, as shown in Figures 6.1.2 and 6.1.1. Below 1.8 m/s, the tube response is very low and exhibits random characteristics, which are caused by turbulence buffeting. In Figure 6.1.1, the dominant and weak frequencies are denoted by solid and empty squares, respectively.

Beyond V_p = 2.0 m/s, the overall tube response begins to increase more rapidly, which is primarily due to the response in the transverse direction. But the overall response decreases to a local minimum value at about V_p = 2.6 m/s. The response frequency in this velocity interval

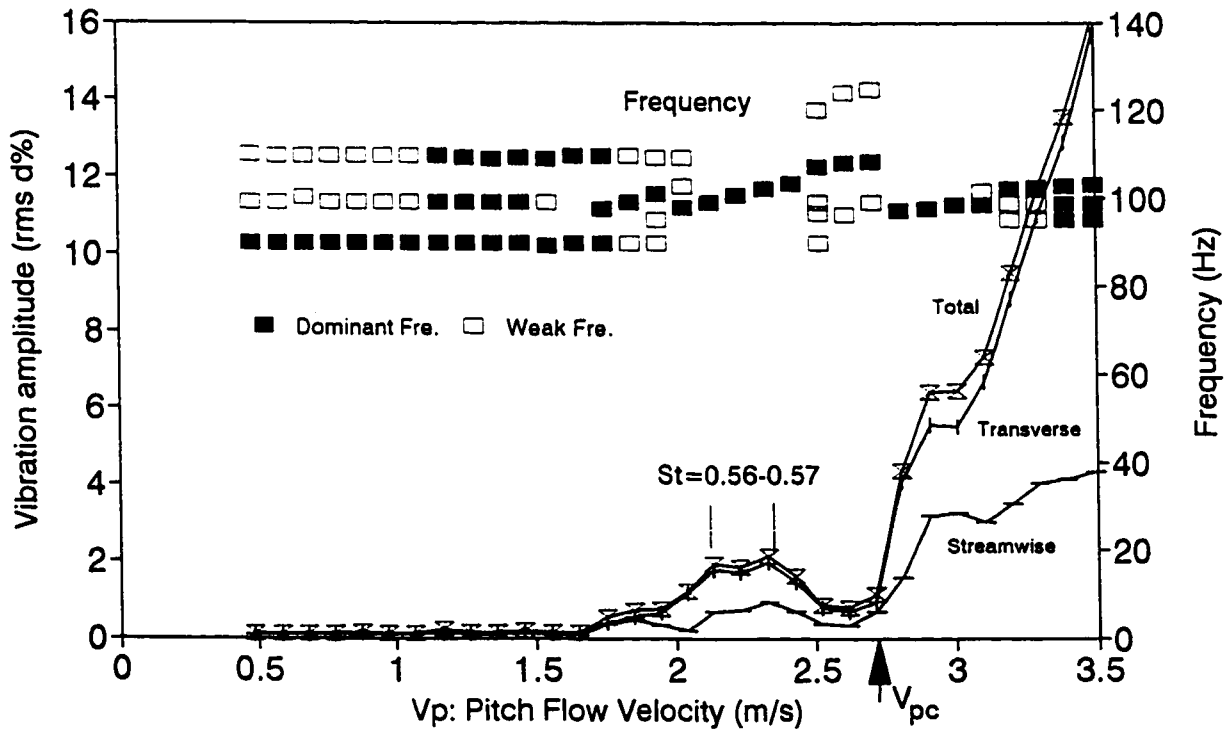

Figure 6.1.1 Tube response versus pitch velocity of single span full admission test

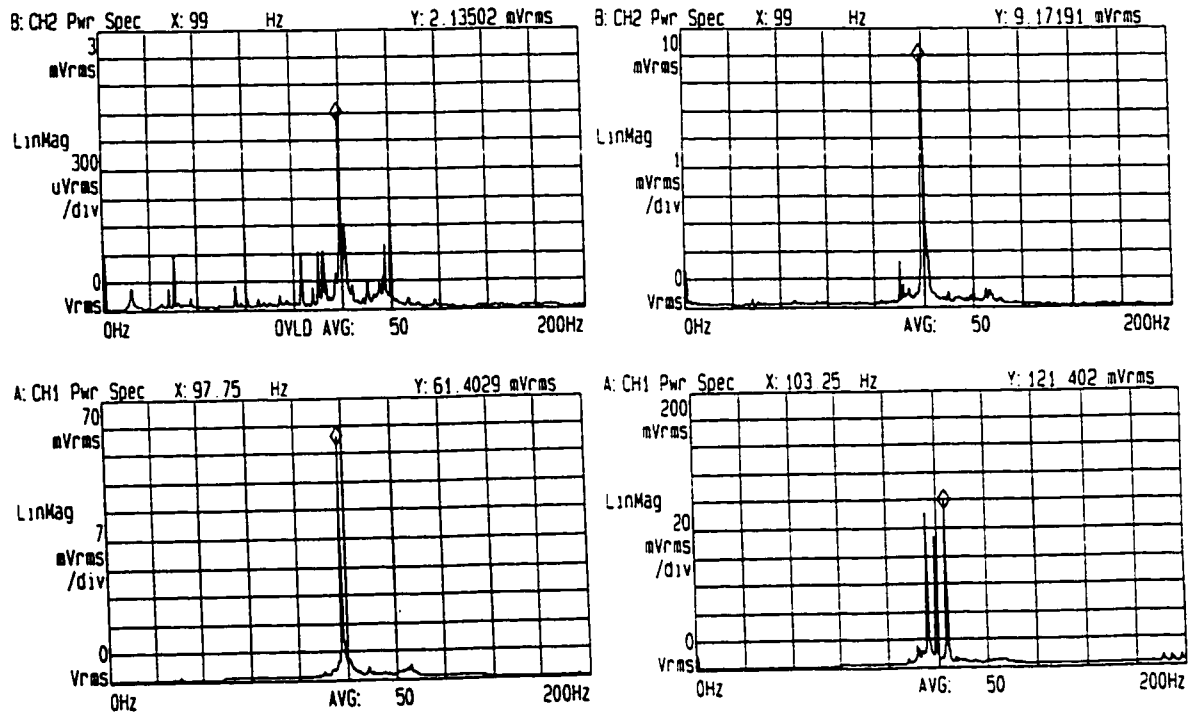

Figure 6.1.2 Tube response frequency spectrum at (a). $V_p = 0.49$ m/s; (b).$V_p = 1.84$ m/s, (c). $V_p = 2.9$ m/s; (d).$V_p = 3.3$ m/s.

range increases in a linear fashion with a single dominant peak. However, the line passing through these frequencies does not intercept the coordinate origin, which suggests that this is not a simple forced response at a vortex shedding frequency. A brief review of previous data is presented in the following sections to clarify the role of the vortex shedding mechanism in parallel triangular tube arrays.

Koroyannakis [1980], and Yeung and Weaver [1983, 1984] found no clear vortex

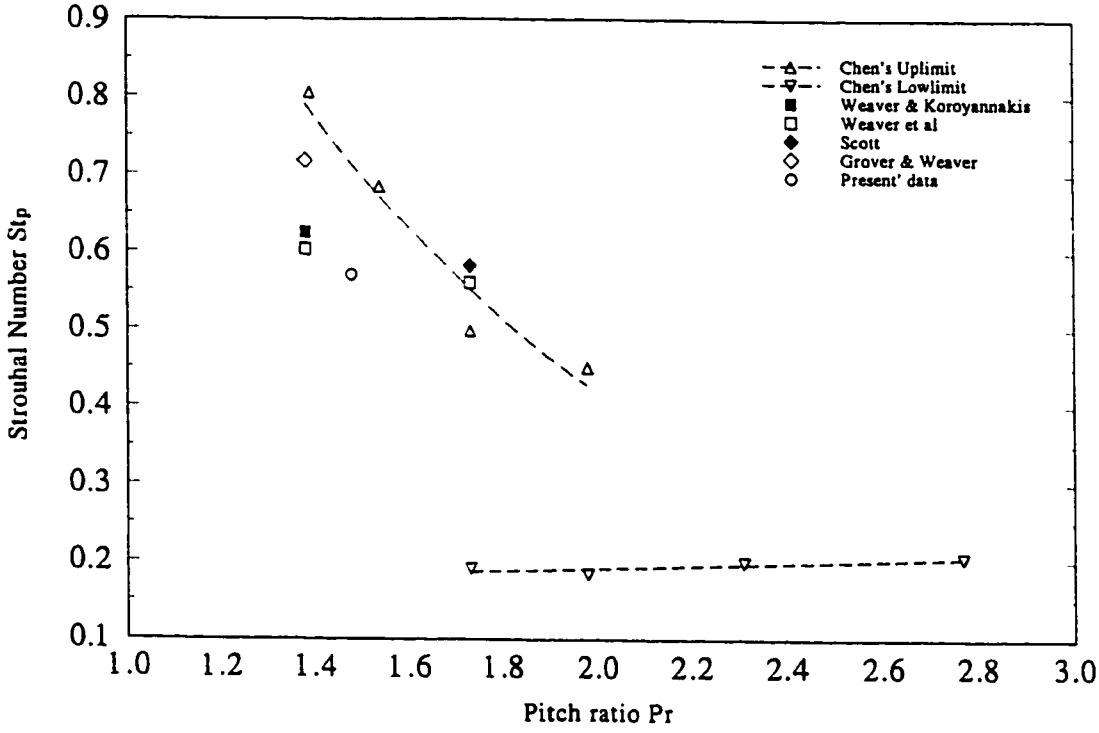

Figure 6.1.3 Strouhal number versus pitch ratio of parallel triangular tube array

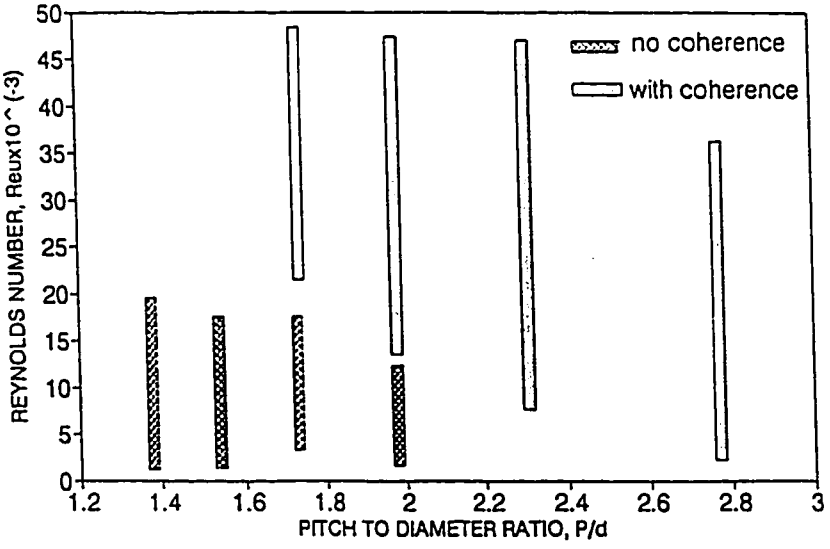

Figure 6.1.4 The coherence vs Reynolds number [Chen, 1993]

excitation present in their investigation of parallel triangular arrays in water with pitch ratios of 1.375 and 1.5, respectively. However, Weaver and Koroyannakis [1983] recorded evidence of a constant Strouhal number response in their study of the effects of asymmetric stiffness on a parallel array with Pr = 1.375. The reported Strouhal number was $St_p = 0.62$. Strouhal excitation has also been recorded from wind tunnel experiments on a parallel triangular array using hot wire measurements. Weaver et al [1986] measured a Strouhal number of $St_p = 0.60$ for Pr = 1.375, and $St_p = 0.36$ for Pr (P/d) = 1.73 in a wind tunnel test. For Pr = 1.73, Scott [1987] conducted a flexible tube array water test, and found $St_p = 0.58$. Grover and Weaver [1978] reported a value of $St_p = 0.72$ for Pr = 1.375 from a wind tunnel experiment. The most recent study of Strouhal periodicity on parallel triangular tube arrays was done by Chen [1993]. Rigid tube arrays with six pitch ratios were tested in a wind tunnel and the results are shown in Figure 6.1.3, together with the results mentioned above. The suspected vortex shedding data from the present study is also included. Chen further found that the periodicity coherence depends on both Reynolds number and pitch ratio, as shown in Figure 6.1.4. For Pr < 2.0, the Reynolds number has significant effects on vortex shedding. At low Re, vortex shedding is weak and has low coherence. These characteristics may be helpful in explaining the confusion regarding the existence of vortex shedding in the parallel triangular array, particularly in the small pitch ratio cases. In the present study, the maximum Re_u is about 11×10^3. Therefore, there is either no or only weak coherence in vortex shedding. In this Reynolds number regime, it is difficult both to find hard evidence of vortex shedding, and to distinguish vortex shedding from a possible region of secondary instability.

Interpolation of Chen's data gives $St_p = 0.74$ for the present tube array of Pr = 1.47. However, calculation in the range of $V_p = 2.13$ - 2.3 m/s in Figure 6.1.1 only gives $St_p = 0.56$ -0.57, which is about 20% smaller than Chen's data. The uncertainty of the present data prevent

arriving at a definite conclusion, as to whether the peak is caused by vortex shedding or a secondary instability, or the combination of both, the latter perhaps being more likely. Figure 6.1.1 also shows the response frequency, and the detailed displacement frequency spectra are given in Figure 6.1.5. The dominant frequency experiences two sudden changes at 2.0 and 2.7 m/s, which coincidentally, are the threshold velocity of the suspected secondary and the primary instability. This phenomenon further indicates that the debated secondary instability region may exist at least to a certain extent. Beyond $V_p = 2.72$ m/s, tube response increases dramatically and the tubes are considered to have become unstable. This velocity is defined as the threshold velocity, as denoted by the arrow symbol in Figure 6.1.1. At the onset of the instability, the frequency changes from several weak frequency peaks to a single dominant peak. Then this single frequency increases gradually with the increase of flow velocity. The

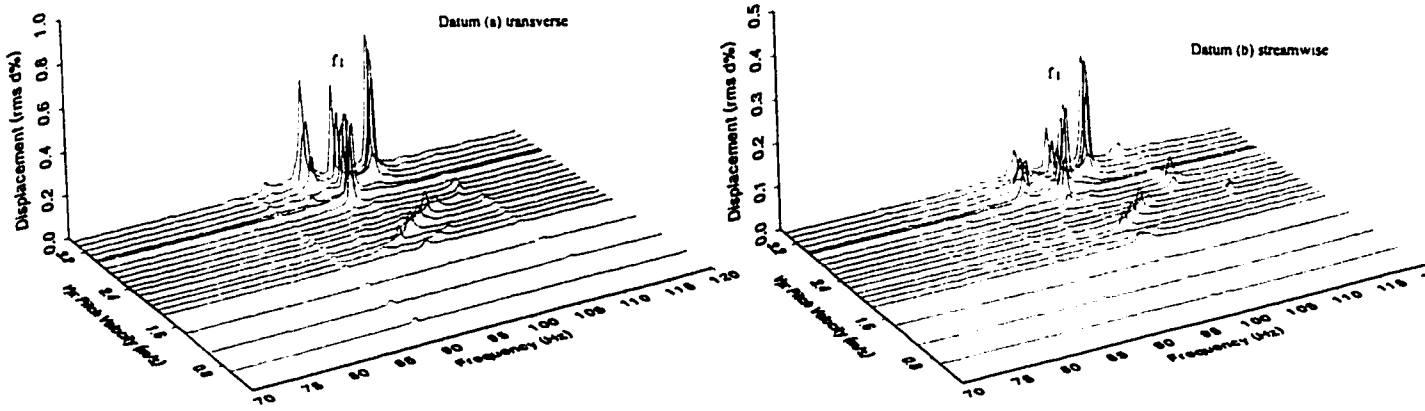

Figure 6.1.5 Tube frequency spectra (a). transverse (b). streamwise

frequency increase in the onset region was also observed by Feenstra [1993]. His flow visualization shows that the monitored tube vibrates out-of-phase with the neighboring tubes

before instability, while the tubes vibrate in-phase once instability has been established. Such in-phase motion reduces the added mass. However, the out-of-phase instability was also observed by the same author, just as it was in the present study. In most flow velocity regions, there are multiple frequency peaks appearing in the frequency spectrum. These frequency bands are typical for tubes oscillating in a liquid flow because of the strong coupling, as discussed by Chen [1983]. Very fine detuning may reduce the number of such coupled frequencies. In the present test, the tube natural frequency difference in air was less than 2%. It was found that the amplitude response versus velocity characteristics remained virtually unchanged whether the amplitude averaging calculation included such frequency side bands or not.

Beyond V_p = 3.30 m/s, three frequencies of equivalent strength appeared in the frequency spectra, Figure 6.1.2.(d). Such multiple peaks are likely caused by post-critical non-linear fluid forces and the looseness of the pinned supports. Below the threshold velocity, tube vibration amplitudes in the transverse and streamwise directions are of the same order except at the hump. After the onset of instability, the overall oscillation is dominated by transverse vibration.

The test data is summarized in Table 6.1.1. In the table, V_p = 2.14 (start of the small peak), 2.52 (end of the small peak) m/s, is where which the first response peak appears, and is included for the further analysis of the secondary instability undertaken later in this chapter. The critical velocities, calculated by Pettigrew & Taylor's, and Weaver & Fitizpatrick's criteria (for abbreviation, they are called Pettigrew's and Weaver's in the following sections) are also presented to evaluate if these criteria are conservative in the prediction of the instability.

$$\textit{Pettigrew's model:}\quad \frac{V_p}{fd} = 3.0\left(\frac{m\delta_w}{S_t\rho d^2}\right)^{0.5} \tag{6-1-1}$$

$$\textit{Weaver's model:}\quad \frac{V_p}{fd} = 4.8\left(\frac{m\delta_a}{S_t\rho d^2}\right)^{0.3},\ \textit{if}\ \frac{m\delta_a}{S_t\rho d^2} \geq 0.3 \tag{6-1-2}$$

$$\frac{V_p}{fd} = 1.0,\ \textit{if}\ \frac{m\delta_a}{S_t\rho d^2} \leq 0.3$$

As expected, both models predict a primary instability of the single span full admission case. The prediction by Weaver's model is more conservative that of Pettigrew's.

Table 6.1.1 Summary of single span tube test with full flow admission

Label	Mode	Frequency (Hz)		Damping δ		Threshold velocity (m/s) V_p				
		in air	in still water	in air	in water	secondary		final V_{pc}	Pettigrew	Weaver
1	1st		(unstable)			start	end			
		133.25	100.75 (108.25)	0.0343	0.1788	2.14	2.52	2.71±0.05	2.55	1.37

6.1.2 Partial Flow Admission

The next step was to extend the length of the tubes to measure the effects of partial admission on fluidelastic instability. The same diameter tubes of 1.83 m (6ft) length were used, such that the percentage of tube section subjected to cross flow was 33.3%, which remained unchanged despite the change of flow location in the following tests. Each test in this series was designated SP_i, which stands for single span partial admission test case *i*. Tube support conditions remain the same as in the datum case. The first three mode shapes and the location of the accelerometers are shown in Figure 6.1.6. Tube response at five flow locations was tested. The frequency and damping measurements were conducted prior to the flow tests. These values

were assumed to be constant in spite of the change of flow location.

Table 6.1.2 Summary of frequency and damping measurements for tubes used for S_i tests

Natural frequency (Hz)						Damping δ			
in air			in still water			in air		in still water	
1st	2nd	3rd	1st	2nd	3rd	1st	2nd	1st	2nd
15.5	49.5	103.25	12.0	35	94.5	0.052	0.024	0.137	0.072

6.1.2.1 SP1

Figure 6.1.7 shows the results of tube response versus pitch velocity for test SP1. In this and the following response figures, supplementary dotted lines are plotted to help identify the threshold velocity. The turbulence response at low flow velocity is approximated by a parabolic curve, which intersects with a straight line tangent to the unstable data at high velocity. The velocity where the two lines intersect may be taken as one definition of the critical velocity. However, in practice, the exact critical velocity is far from such an ideal situation. In general, a certain degree of uncertainty exists in defining the stability threshold. Figure 6.1.8 shows frequency spectra for transverse and streamwise directions. This figure clearly indicates that both the first and the second modes are excited. The published literature demonstrates that, primarily, the fundamental mode has to be excited for single span full admission tubes. For the partial admission case, it has been observed that higher modes can be excited depending on the location of the flow. The energy fraction, S_i, computation for fixed-pinned supports is carried out in Chapter 3.3. The critical velocity ratio for various modes are shown in Figure 3.9, which reveals that the higher mode can be excited first when the center of flow is close to the fixed end and partial admission is small. In the SP1 case, $L_x/L = 33.3\%$, location of the flow center X_c=

0.17, and thus $V_1/V_2 = 1.1 > 1.0$. Therefore, the 2nd mode should be excited prior to the 1st mode. In Figure 6.1.7, the tubes become apparently unstable in the 2nd mode at $V_p \approx 0.82$ m/s, while the 1st mode remains stable. The Strouhal number was calculated to determine whether the response could be caused by vortex shedding. As shown in the figure, $St_p = 0.48 - 0.37$ at the peak region, which is significantly lower than in Chen's data. Therefore, only the small peak at 0.61 m/s may be caused by vortex shedding. Still, it is interesting that the 2nd mode instability disappears beyond 1.2 m/s, then the amplitude increases again at 1.41 m/s, which is close to the onset velocity of the 1st mode instability. This phenomena suggests, once again, the existence of multiple unstable regions. The predictions by both models are conservative.

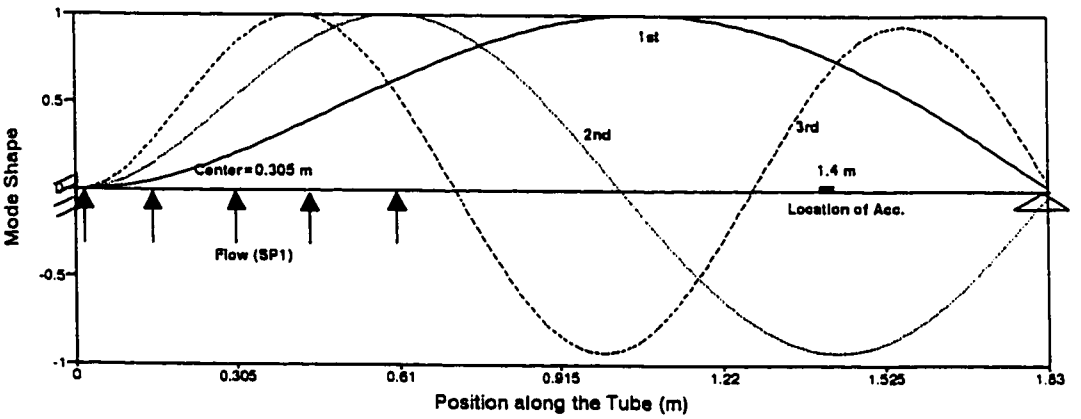

Figure 6.1.6 Mode shapes of single span partial admission flow (SP1 flow location)

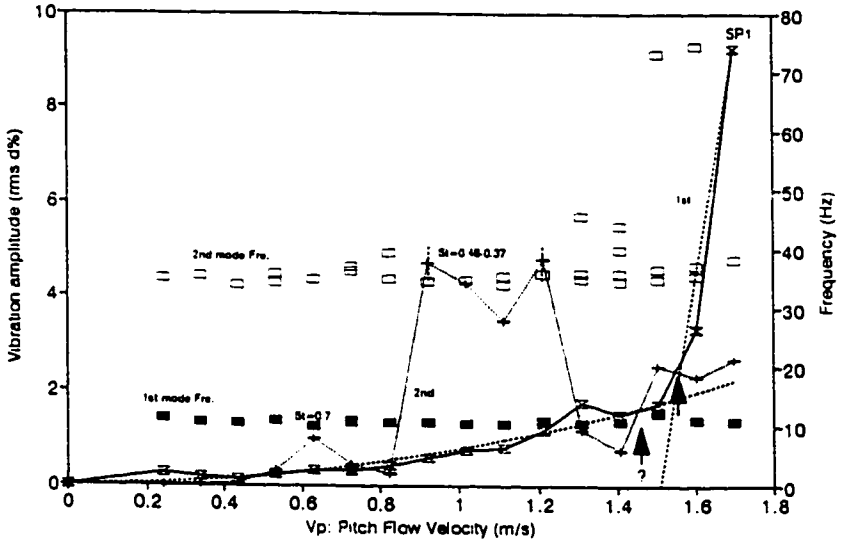

Figure 6.1.7 Tube response versus pitch velocity (SP1)

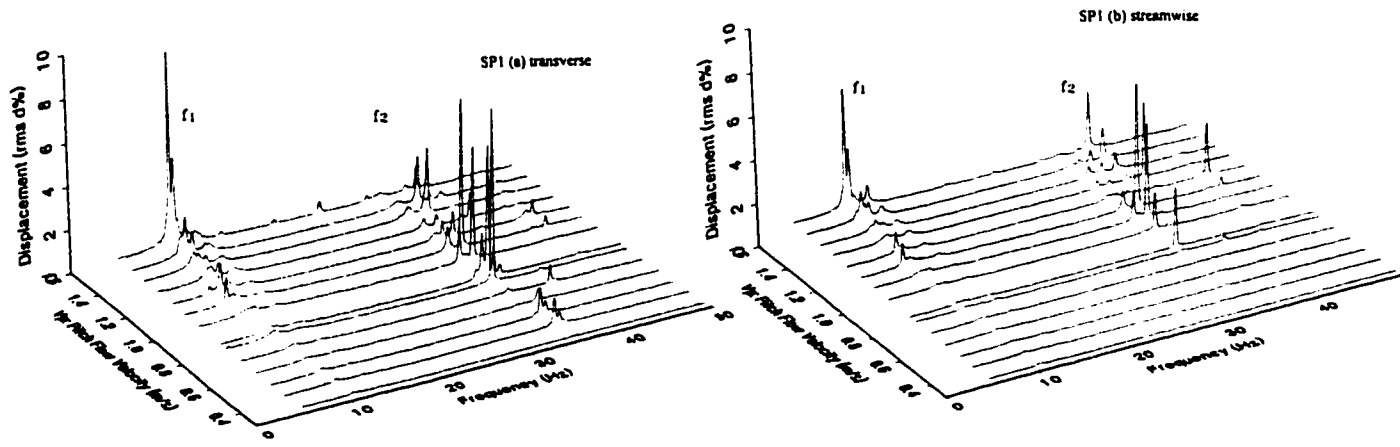

Figure 6.1.8 Tube response frequency spectra (SP1) (a) transverse, (b) streamwise

Table 6.1.3 Summary of SP1 test

Label	Mode	Frequency (Hz)	Energy fraction S_i	Critical velocity (m/s)				
				start	end	final V_{pc}	Pettigrew	Weaver
2	1st	10.875	0.0808			1.5±0.05	1.08	0.83
13	2nd	34.5	0.3137	0.83	1.31	1.41 ?	1.17	0.44

Weaver's criterion predicts correctly that the 2nd mode is the critical unstable mode while Pettigrew's criterion predicts that the 1st mode is critical. In the following tables, numbers printed in bold font represent nonconservative predictions.

6.1.2.2 SP3

In this test, the center of flow is at 0.61 m (X_c=0.33) away from the clamped support. From Figure 3.9, it is expected that the tubes should become unstable in the 1st mode because $V_1/V_2 < 1$. Figure 6.1.9 confirms this prediction. The frequency spectra given in Figure 6.1.10 indicate the 2nd mode response exists though it appears insignificant. Significant oscillation was only observed in the 1st mode. It is unlikely that the hump around 0.4 m/s is caused by vortex shedding, as the associated Strouhal number of 0.46-0.28 is too small. Beyond V_p = 0.53 m/s, the response increases sharply, and the tubes become unstable. It is not clear whether the 2nd mode instability occurs beyond V_p = 0.53 m/s, but it seems unlikely. The predictions for the 1st mode by both criteria are slightly nonconservative, but are within experimental error. The large amplitude in the 1st mode may excite, to some extent, 2nd mode response because of increased impacting at supports and perhaps high induced turbulence level. Therefore, it is difficult to conclude that the 2nd mode is an unstable mode, especially since its apparent critical velocity

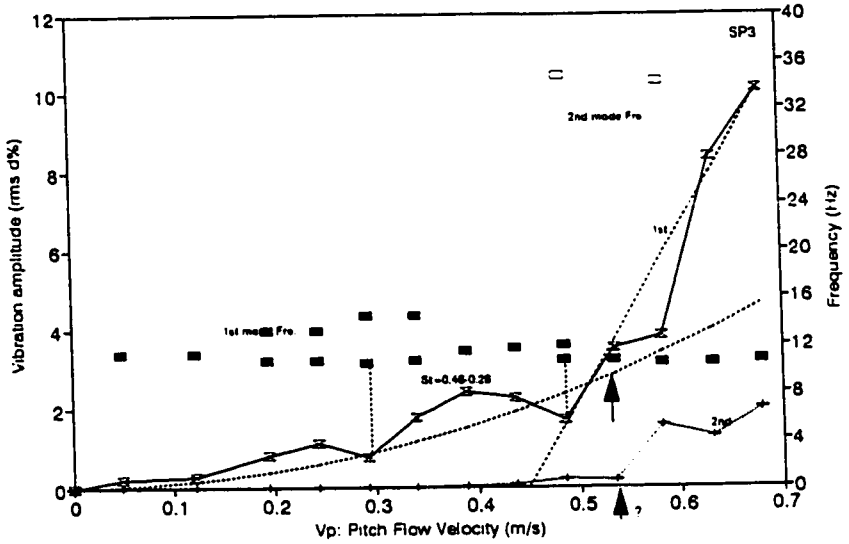

Figure 6.1.9 Tube response versus pitch velocity (SP3)

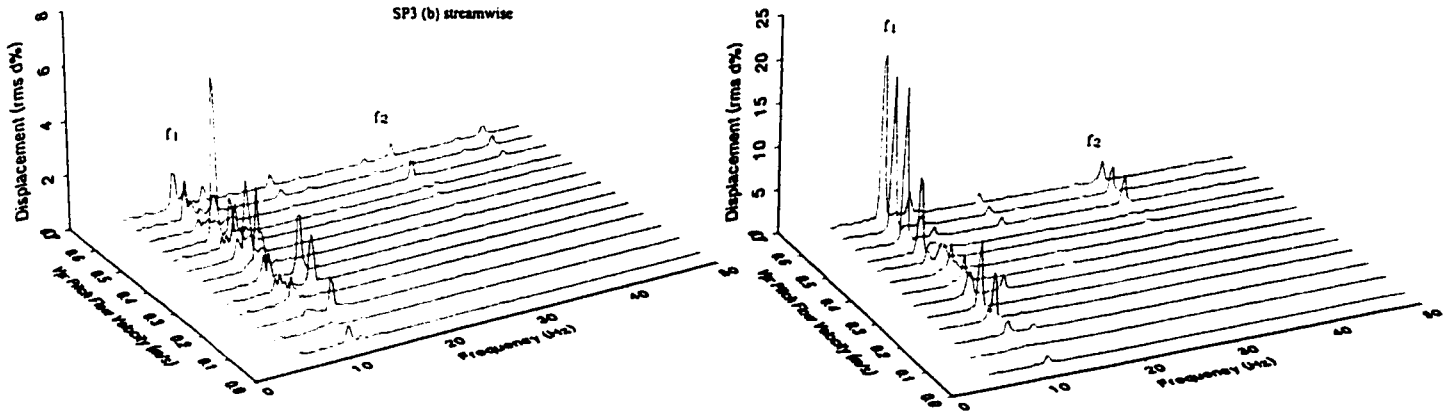

Figure 6.1.10 Tube response frequency spectra (SP3) (a) transverse, (b) streamwise

is so close to the 1st unstable mode, which has large response amplitude.

Table 6.1.4 Summary of SP3 test

Label	Mode	Frequency (Hz)	Energy fraction S_i	Critical velocity (m/s)				
				start	end	final V_{pc}	Pettigrew	Weaver
4	1st	10.75	0.3367	0.29	0.49	0.53±0.04	0.53	0.53
14	2nd	34.25	0.5236			0.53 ?	**0.90**	0.44

6.1.2.3 SP2

In this test, the center of the flow is at the center of the tube, 0.915 m (X_c=0.5) away from both supports. From the mode shape analysis, this is the section most vulnerable to be excited by an external force in the tube's 1st mode. In Figure 3.9, V_1/V_2 has a minimum value at X_c=0.5. Figure 6.1.11 shows the response curve. The frequency spectra are given in Figure 6.1.12. The peak around V_p = 0.28 m/s could be caused by vortex shedding because the associated St_p at the onset has a value of about 0.7 which is close to that found in Chen's data. Beyond V_p = 0.44 m/s, the instability occurs. Similar to the full admission test, the tubes vibrate primarily in the transverse direction. Both criteria predict correctly the 1st mode as the critical mode. The predictions by Pettigrew's criterion is close to the experimental value while Weaver's is quite conservative. However, the vibration amplitude exceeds 2% of tube diameter near a flow velocity of about 0.14 m/s.

Table 6.1.5 Summary of SP2 test

Label	Mode	Frequency (Hz)	Energy factor S_i	Critical velocity (m/s)				
				start	end	final V_{pc}	Pettigrew	Weaver
3	1st	10.25	0.628	0.12	0.34	0.44±0.01	0.39	0.14
14	2nd	34.25	0.285				1.53	0.46

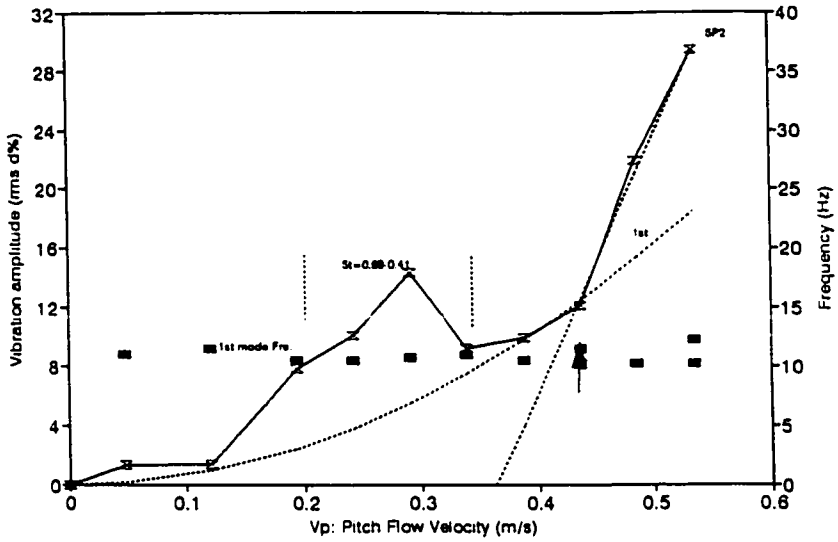

Figure 6.1.11 Tube response versus pitch velocity (SP2)

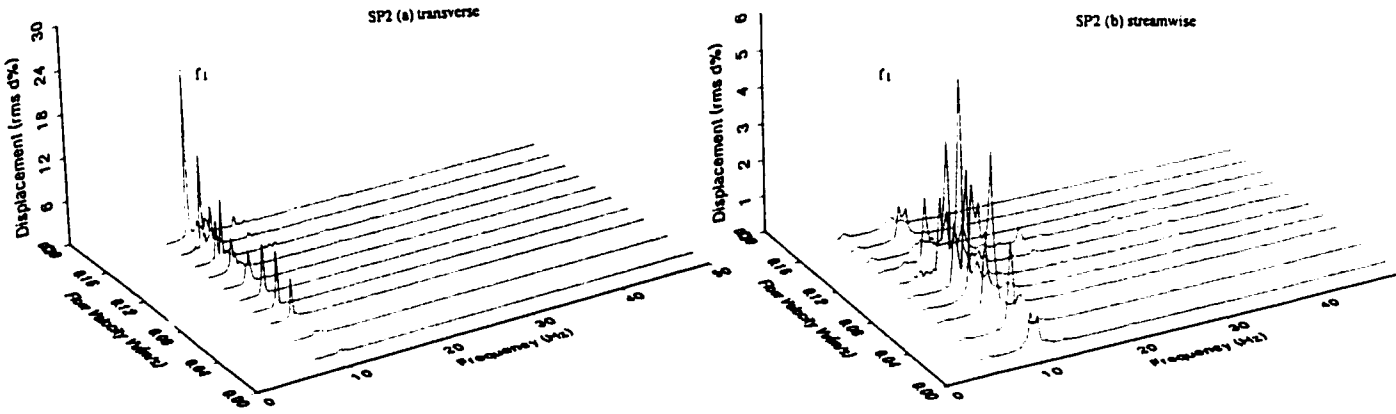

Figure 6.1.12 Tube response frequency spectra (SP2) (a) transverse, (b) streamwise

6.1.2.4 SP4

In this case, the center of flow is 1.193 m (X_c=0.65) away from the clamped support. Figure 6.1.13 presents the response characteristics. The frequency spectra are given in Figure 6.1.14. The stability threshold is clearly shown around V_p = 0.50 m/ s. The coupling between the monitored tube and the neighboring tubes may cause two frequencies to appear in the frequency spectra. The predictions by both criteria are conservative. No 2nd mode instability was observed, as predicted by both models. Similar to the SP2 case, only the 1st mode was observed.

Table 6.1.6 Summary of SP4 test

Label	Mode	Frequency (Hz)	Energy fraction S_i	Critical velocity (m/s)				
				start	end	final V_{pc}	Pettigrew	Weaver
5	1st	10.75	0.6305			0.50±0.02	0.39	0.14
	2nd	34.25	0.5236				1.25	0.53

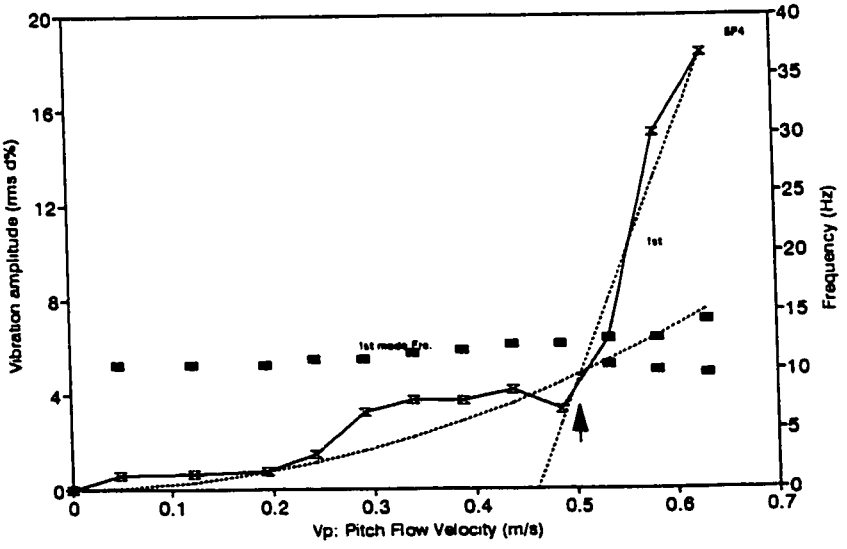

Figure 6.1.13 Tube response versus pitch velocity (SP4)

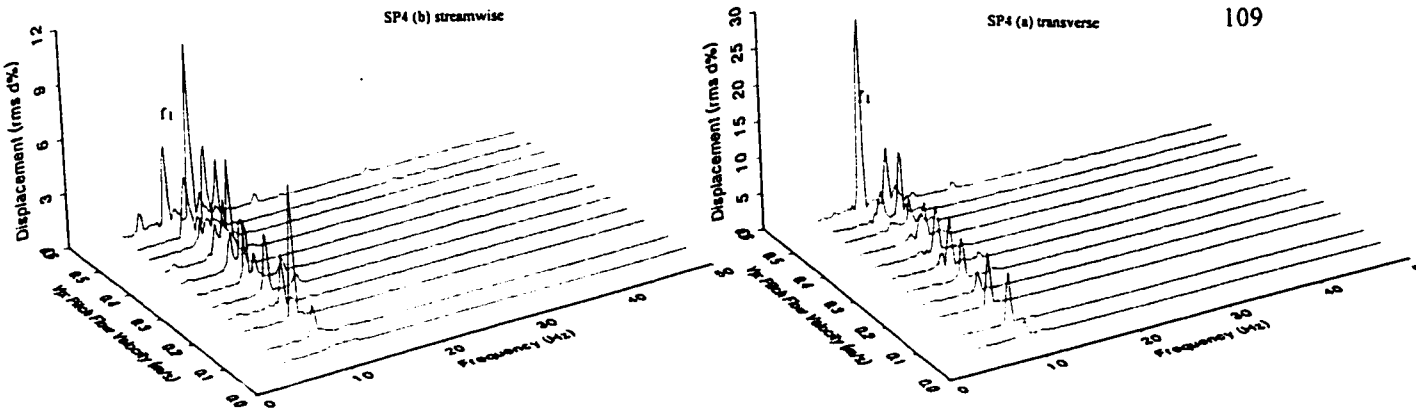

Figure 6.1.14 Tube response frequency spectra (SP4) (a) transverse, (b) streamwise

6.1.2.5 SP5

In this test, the center of the flow is 0.313 m (X_c=0.83) away from the pinned support. The response results are shown in Figure 6.1.15. The frequency spectra are presented in Figure 6.1.16. Both the 1st and 2nd mode are observed, but only the 1st mode oscillation is significant. There are no obvious effects of vortex shedding on the 1st mode. However, there is a low amplitude hump on the 2nd mode response. This may be caused by vortex shedding because St_p = 0.75-0.77. Beyond V_p = 0.75 m/s, the 1st mode instability occurs. At the same velocity, the 2nd mode vibration increases slowly. The predictions of the two models for the critical mode are different. Pettigrew's model correctly predicts the 1st mode as the least stable mode, while Weaver's model predicts the 2nd mode. It is not certain that the 2nd mode instability has actually occurred, because large response of the 1st mode may induce the 2nd mode vibration.

Table 6.1.6 Summary of SP5 test

Label	Mode	Frequency (Hz)	Energy fraction S_i	Critical velocity (m/s)				
				start	end	final V_{pc}	Pettigrew	Weaver
6	1st	10.25	0.3002			0.75-0.77	0.57	0.56
15	2nd	34.25	0.4057	0.58	0.68	0.73-0.82	**1.03**	0.43

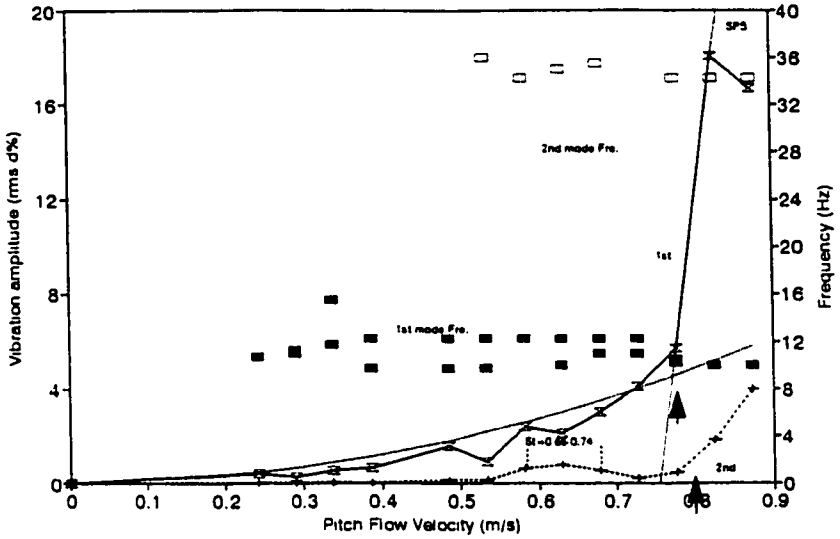

Figure 6.1.15 Tube response versus pitch velocity (SP5)

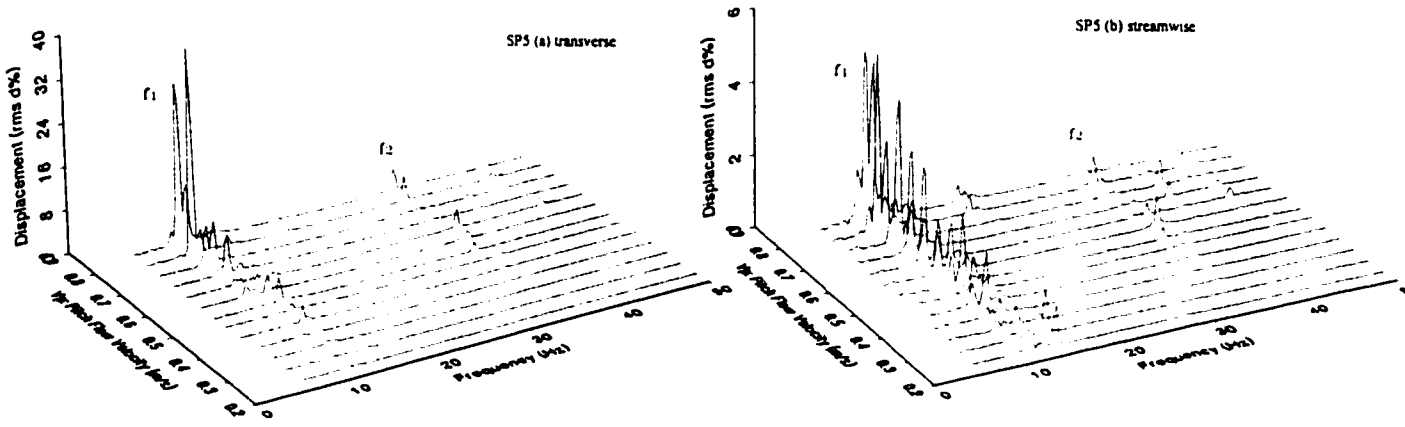

Figure 6.1.16 Tube response frequency spectra (SP5) (a) transverse, (b) streamwise

6.1.3 Summary of Single Span Partial Admission Tests

As discussed in Chapter 2, the S_i can be calculated theoretically by using the mode shape functions or experimentally by using the test data. In the present experiments, since the damping values for the full admission and partial admission tests are different, the experimental S_i has to be corrected by such values. From equations (2-4), (2-6) and (2-7)

$$\frac{1}{S_i} = \frac{\delta_{1_{Datum\ case}}}{\delta_{1_{Partial\ admission}}} \left[\frac{\left(\frac{V_p}{f_i d}\right)_{Partial\ admission}}{\left(\frac{V_p}{f_1 d}\right)_{Datum\ case}} \right]^{1/\alpha} \qquad (6\text{-}2)$$

Because damping in either water or air are used in different design guidelines, the S_i is corrected using both values, which are listed in Tables 6.1.1 and 6.1.2. The results for the single span partial admission tests are summarized in Figure 6.1.17. The lines in the figure represent the theoretical calculation results. Special attention should be directed to the comparison between the calculation by mode shape function and the experimental data corrected by damping in water, since the exponent $\alpha = 0.5$ in the S_i calculation and δ_w are the values paired together, as in Pettigrew's semi-empirical model. The trend of the experimental data and the theoretical calculation agrees fairly well, especially in the middle span of the tube. However, the theoretical prediction is overly conservative when the flow is located towards the ends of the tube span. On the other hand, the experimental data, corrected by air damping, agree with the theoretical calculation better along the whole span.

The experimental data obtained by Waring [1987] using a wind tunnel are also plotted for comparison. Her test was conducted with a pinned-pinned single span tube array. The dashed line represents the S_i calculated by the appropriate mode shape function. At the end of the tube span, the prediction is un-conservative, though slightly conservative in the middle. Hence, her results show the opposite trend in comparison with the present results. However, the range of her data between the middle and the end is much smaller, and the uncertainty is much larger, as indicated by her results from other admission length ratio tests. In the present study, although the same damping value is used in the five partial admission flow locations, it is expected that the actual damping in flow may depend somewhat on flow location.

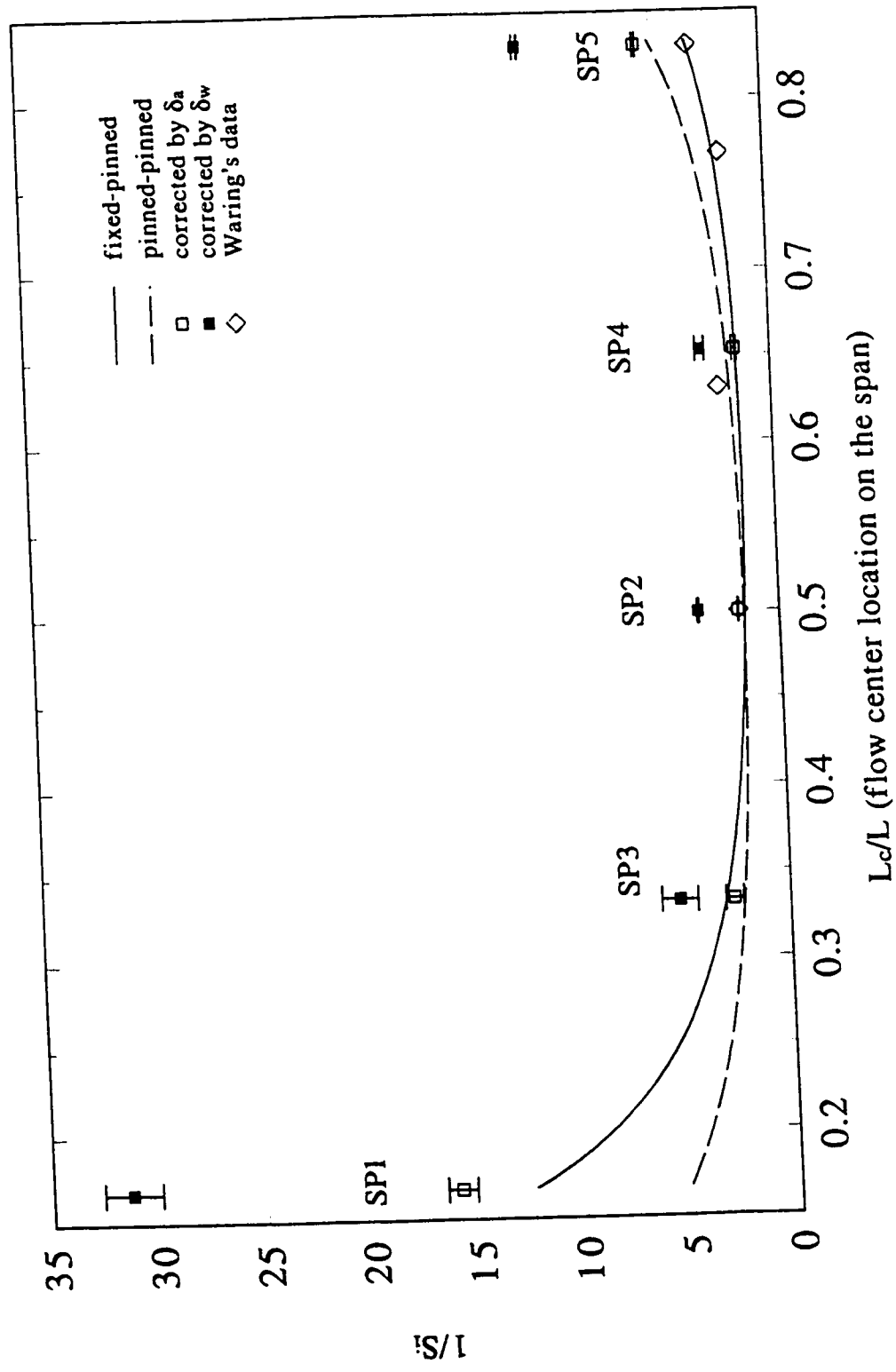

Figure 6.1.17 PAF of single span partial admission test

6.2 Two Spans with Partial Admission

This test series consists of two parts: equal and unequal span length.

6.2.1 Equal Span Tests

The 1.83m tube is divided into two spans of equal length. One end of the tube is fixed, the other is pinned, and a knife edge support plate is placed in the middle of the tube. The supports and first three mode shapes are shown in Figure 6.2.1. As seen in the figure, the first mode shape has deflections with opposite signs on each side of the central support plate. The work done by the fluid force, $W = \int_0^l f(x)\,\overline{\varphi(x)dx}$, could possibly be cancelled because of the sign change at each span. In this case, the tube should not become unstable when the flow is symmetrical about the central support plate. In the present study, because $\phi(x)$ is not a symmetrical function about the location of this support plate, the admission length on each side has to be calculated, using equation (6-3), to satisfy the above hypothesis. The total admission length is still 0.610 m as was used in the single span study.

$$Si_{left} = Si_{right}$$

$$\frac{\int_{x_1}^{0.915} \varphi_1^2(x)dx}{\int_0^{0.915} \varphi_1^2(x)dx + \int_{0.915}^{1.83} \varphi_2^2(x)dx} = \frac{\int_{0.915}^{x_1+0.610} \varphi_2^2(x)dx}{\int_0^{0.915} \varphi_1^2(x)dx + \int_{0.915}^{1.83} \varphi_2^2(x)dx} \qquad (6\text{-}3)$$

$$or \quad \int_{x_1}^{0.915} \varphi_1^2(x)dx = \int_{0.915}^{x_1+0.610} \varphi_2^2(x)dx$$

Here, x_1 is the location of flow left edge, $\phi_1(x)$, $\phi_2(x)$ are the mode shapes on the left and right side of the central support, respectively. It was found that $x_1 = 0.666$ m for the 1st mode. This location changes for each mode due to the different mode shape function. The verification test was done for the 1st mode because it has the simplest mode shape, which should lead to more convincing conclusions.

Prior to the flow test, the frequency and damping were measured in air and still water. The second mode damping could not be measured because of the weak and irregular decay signals, therefore the damping was assumed to be the same as that of the 1st mode. According to the previous measurements, the difference in damping between these two modes is usually not significant. Furthermore the weak signals of the 2nd mode may be due to higher 2nd mode damping, therefore, such an assumption can be considered reasonable and conservative.

Table 6.2.1 Summary of frequency and damping measurements for the two-span tests

Natural frequency (Hz)						Damping δ			
in air			in still water			in air		in still water	
1st	2nd	3rd	1st	2nd	3rd	1st	2nd	1st	2nd
45.0	80.5	168.5	34.5	70.5	127.0	0.008	0.008	0.075	0.075

A number of tests were done on the same tube - support configuration with different flow locations. The left edge flow locations and the first three mode shapes are shown in Figure 6.2.1 with N_i labels. The experimental results are summarized in Table 6.2.2, Figure 6.2.2 and 6.2.3. In the first test of N1, the left edge of the flow is at $x_1 = 0.666$ m, as previously calculated. The tube bundle becomes unstable in the 1st mode. The 2nd mode exists but has an insignificant amplitude and remains stable. Therefore the work done by the uniform flow across the tube on either side of the central support does not cancel itself but is additive. In fact, since the

fluidelastic force is proportional to the tube displacement $f(x) \propto \phi(x)$, the force and mode shape in the form of a work expression should be treated as scalars not vectors, i.e., $W \propto \int_0^l \varphi^2(x)dx$

The work is always additive along the tube span for any vibration mode.

Most predictions by both models are correct. In all of these cases, $MDE_a = m\delta_s/S_i\rho d^2 < 0.3$, thus predicted reduced velocity V_p/fd has a constant value of 1.0, according to Weaver's model, i.e., equation (6-1-2). Weaver's model is more conservative in this range than Pettigrew's model, the latter has a positive slope in the entire MDE range. In this experiment, S_i values cannot be obtained because the full admission test cannot be conducted due to the limited test section width. However, a comparison can be made by choosing one test case as a reference point. Since the damping and added mass values are the same for all test cases, the ratio of critical velocity to the reference case will give an indication of the energy fraction relationship. Test N2 is chosen as the reference case because it experiences both the 1st and 2nd mode instabilities. Thus, from equation (2-8), the ratio of critical velocity at location N2 to other locations is calculated by the following equation, with the assumption of the same damping and added mass at all locations. The assumption is reasonable since in each test, only the location of the tube bundle frame is adjusted inside the acrylic test section, while the end and intermediate supports are not moved.

$$\frac{V_{pr\,N1}}{V_{pr\,N2}} = \left(\frac{S_{i\,N2}}{S_{i\,N1}}\right)^{\alpha} \qquad (6\text{-}2)$$

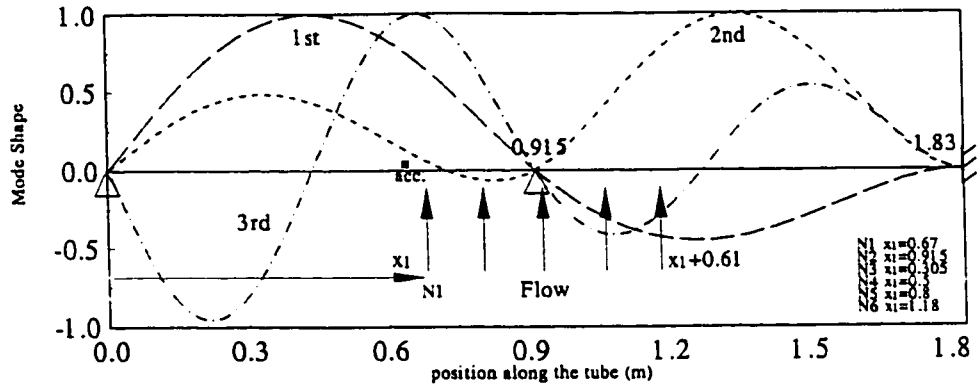

Figure 6.2.1 Flow location and the first three mode shapes of the two-span test series

Using this equation, the comparison between the experimental results (LHS) and the theoretical calculation (RHS) can be made directly. In addition, the exponent α can be determined by least-square curve fitting. The results are shown in Figure 6.2.4. Among the theoretical calculations, $\alpha = 0.5$ and 0.3 were used based on Pettigrew's and Weaver's models of equations (6-1-1) and (6-1-2). The variation of the 2nd mode curve is much larger than that of the 1st mode. There is no 2nd mode instability for N1, N4, and N3. The theoretical calculation has a maximum value in the 2nd mode at approximately at x= 0.25, where the 2nd mode instability is least likely to occur, since at this point, the flow is central on an section where the 2nd mode has very little displacement. The tests of N5, N2 and N6 exhibit the 2nd mode instability, which correspond to cases where the theory predicts 1st and 2nd mode instability at close to the same flow velocity. Figure 6.2.4 shows a number of interesting characteristics which tend to validate the theory. For $x < 0.4$, the second mode instability is predicted to occur at significantly greater velocities that the first mode, and no second mode instability was observed for cases N3, N4, and N1. For N2, N5 and N6, the second mode instability is predicted tc be critical by Pettigrew while Weaver predicts 1st mode critical. While the experiment shows the 1st mode to be

critical, the velocity for the 1st and 2nd modes are quite close.

Additionally, the trend of the predications for the critical velocity follows the trend of the experimental data quite well over the entire range of x. Finally, the results for critical velocity plotted this way are quite insensitive to the exponent α.

Table 6.2.2 Summary of two-span test

Test	x_1	Label	Mode	Frequency (Hz)	Energy fraction S_i	Critical velocity (m/s)				
						start	end	final V_{pc}	Pettigrew	Weaver
N1	0.67	47	1st	32.75	0.1542			2.9±0.01	1.61	0.42
N2	0.915	48	1st	33.0	0.1466			2.4±0.03	1.63	0.42
		53	2nd	65.0	0.7400	1.89	2.52	2.5±0.04	1.33	0.83
N3	0.305	49	1st	32.75	0.6597			1.0±0.02	0.78	0.42
N4	0.5	50	1st	36.75	0.3297			1.7±0.05	1.10	0.42
N5	0.8	51	1st	32.5	0.1304			3.0±0.02	1.76	0.41
		54	2nd	61.5	0.5437	2.31	2.99	3.0±0.02	1.66	0.78
N6	1.18	52	1st	34.5	0.1120			2.7±0.02	1.88	0.42
		55	2nd	66.5	0.7056			2.91±0.02	1.35	0.84

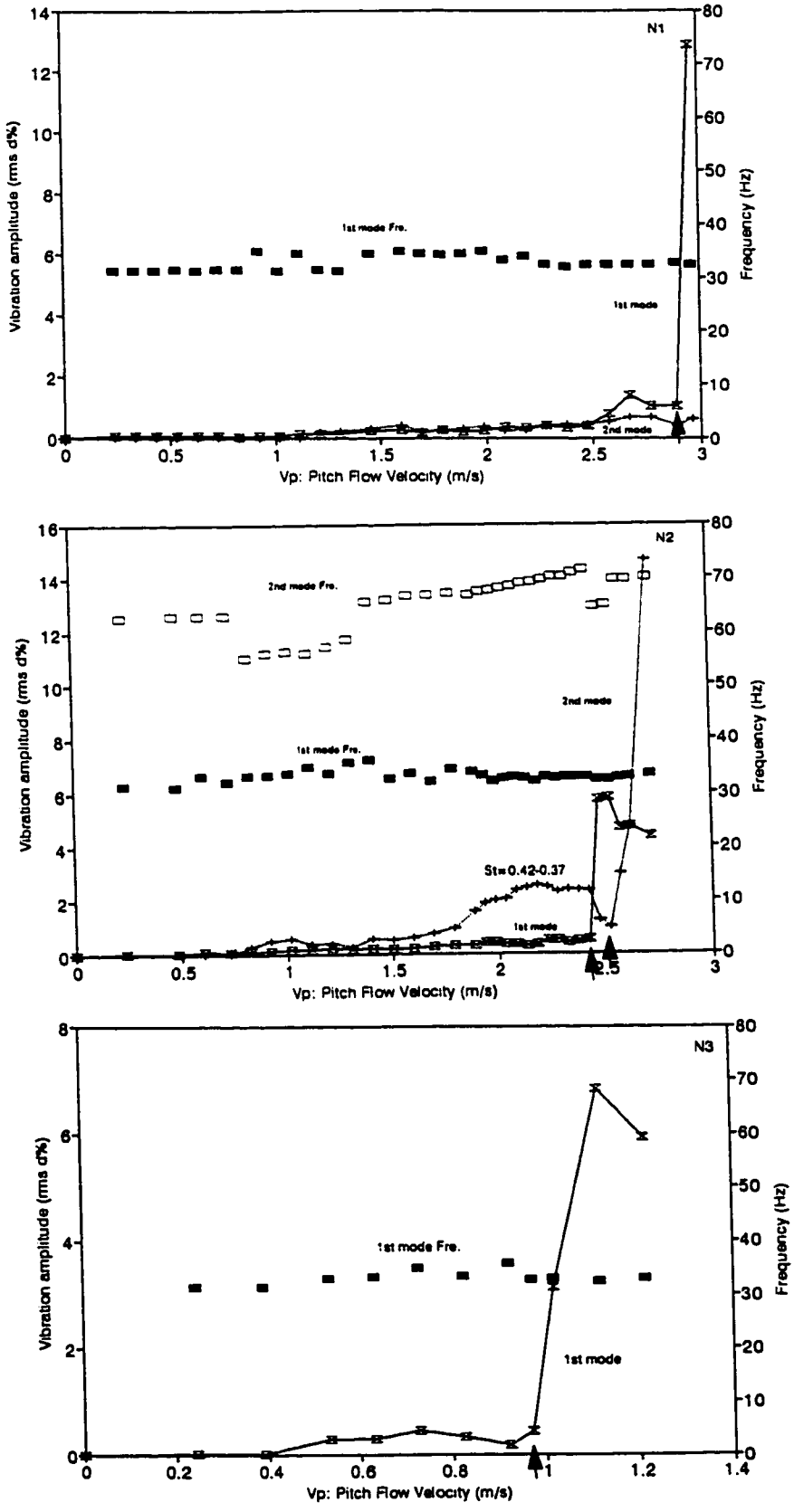

Figure 6.2.2 Tube response versus pitch velocity of two-span test (continuing)

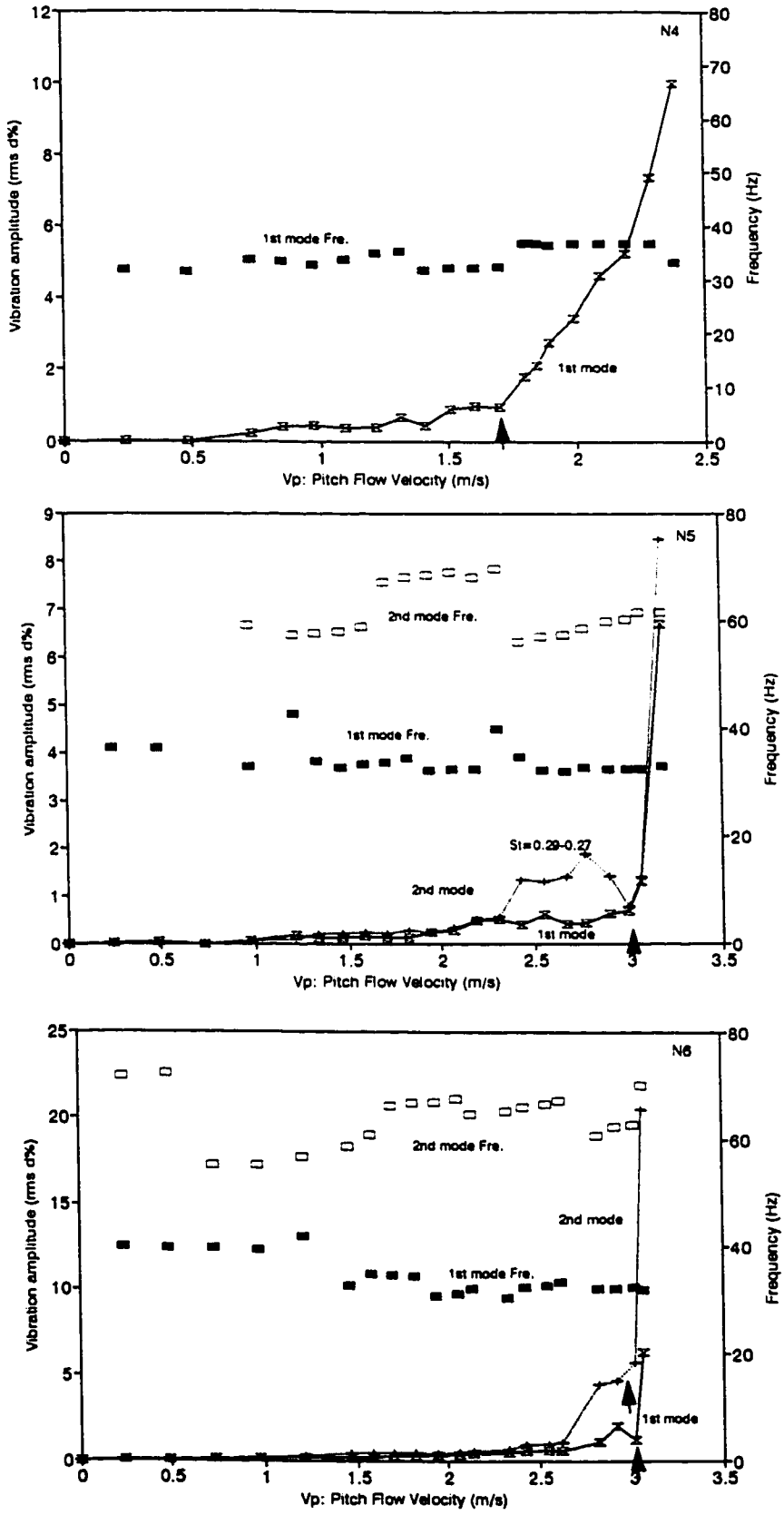

Figure 6.2.2 Tube response versus pitch velocity of two-span test

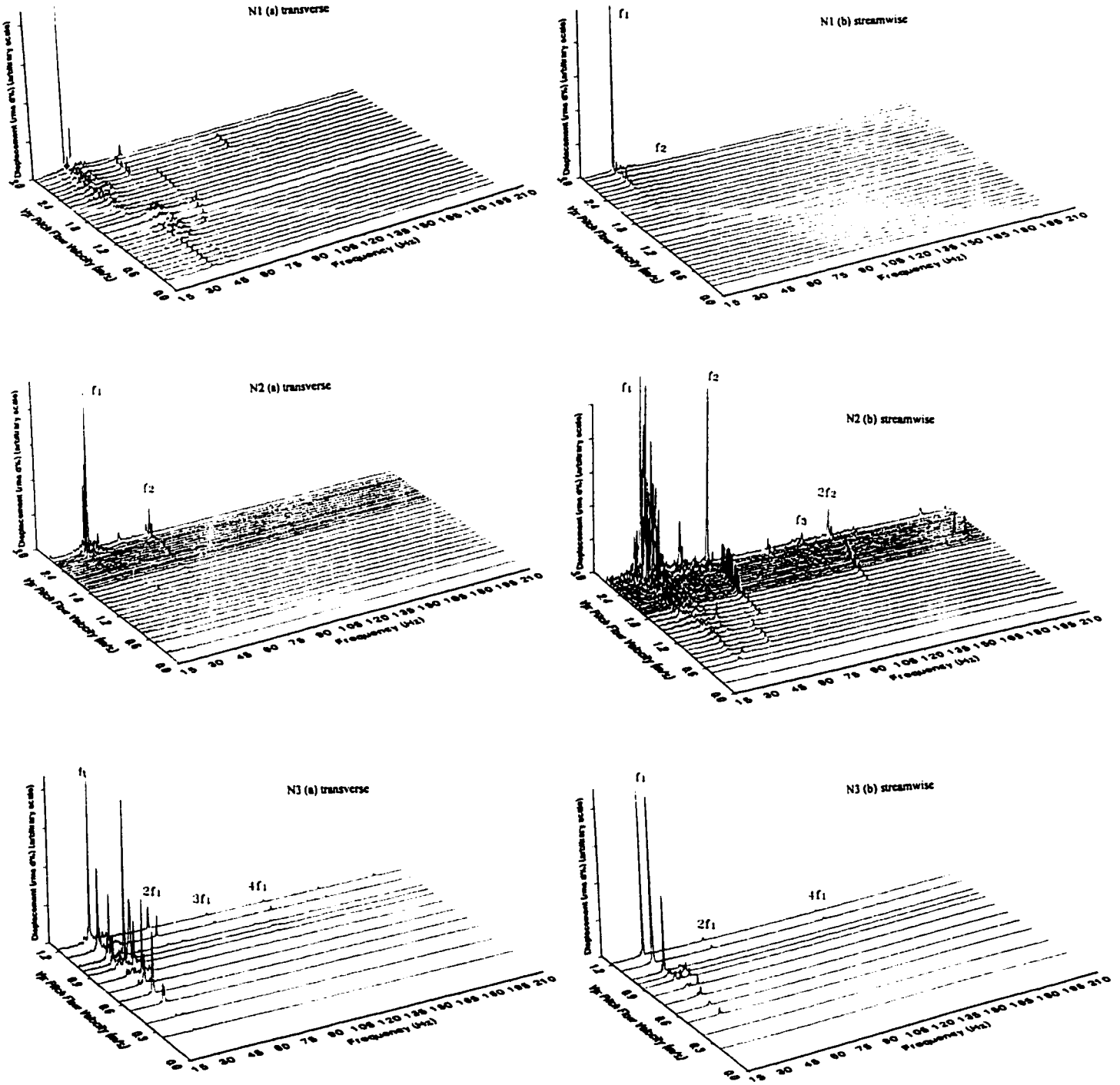

Figure 6.2.3 Tube response frequency spectra of two span test (a) transverse, (b) streamwise (continuing)

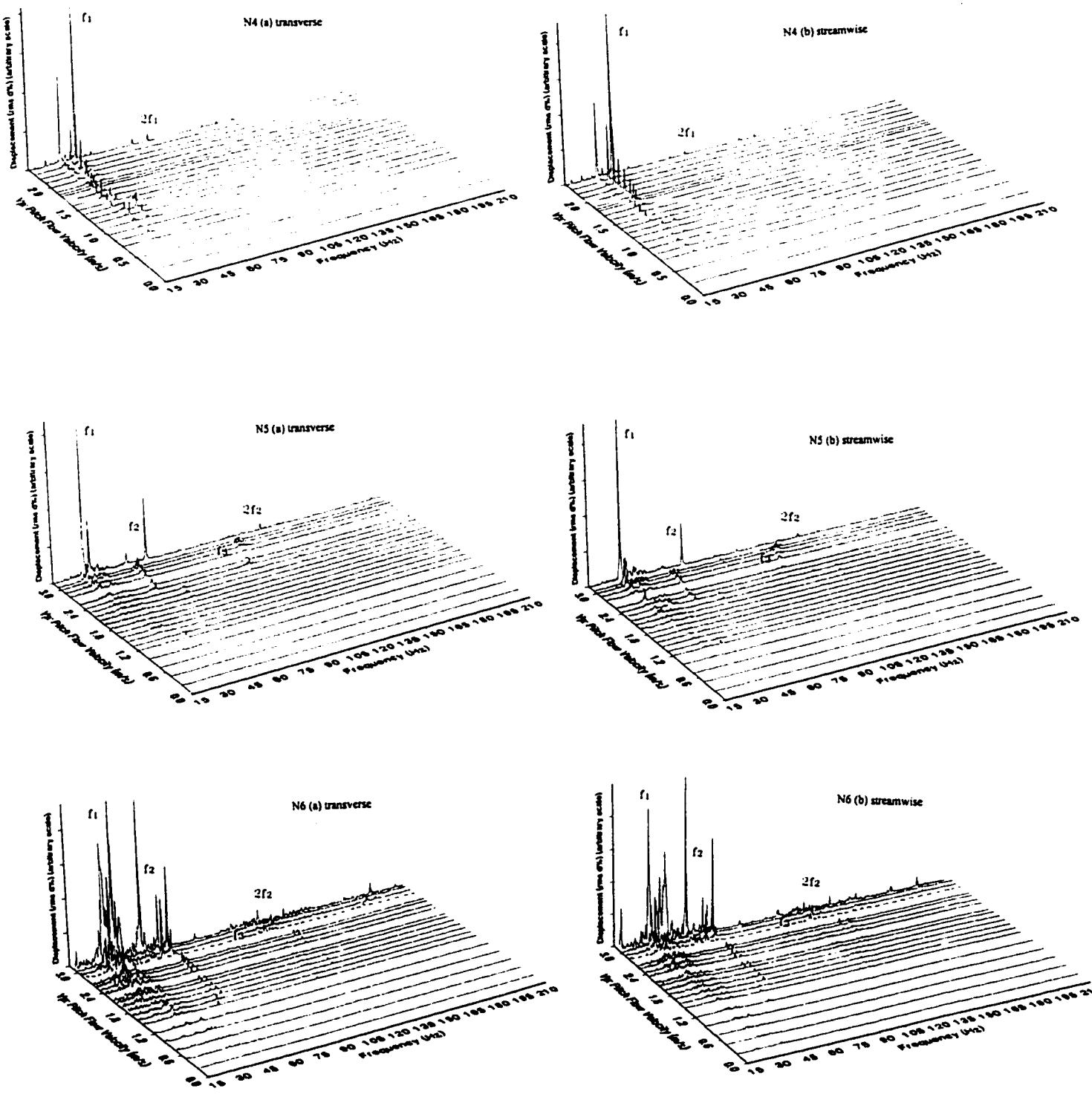

Figure 6.2.3 Tube response frequency spectra of two span test (a) transverse, (b) streamwise

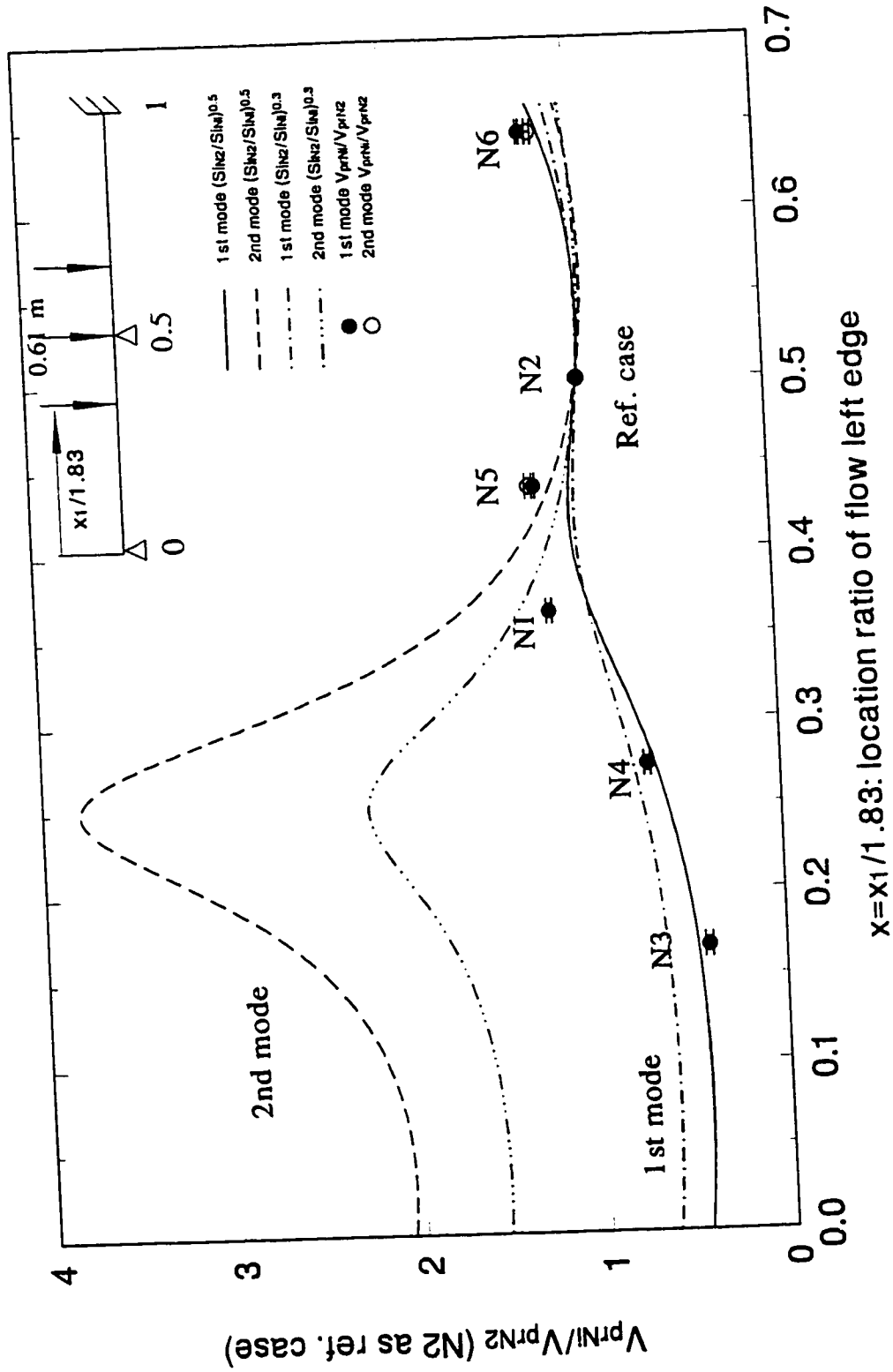

Figure 6.2.4 The comparison between theoretical calculation and experimental results

6.2.2 Two-Span Tubes with Unequal Length

A test was done on a two-unequal-span tube. The mode shapes and flow location are shown in Figure 6.2.5. The response and frequency spectra are presented in Figures 6.2.6 and 6.2.7. Once again, there is a peak near $V_p = 0.5$ m/s. $St_p = 0.5$ suggests that vortex shedding is unlikely to be the cause of this response peak. At $V_p = 0.78$ m/s, the 1st mode instability occurs. No 2nd mode was observed, as predicted by both criteria. The predictions for the 1st mode are conservative.

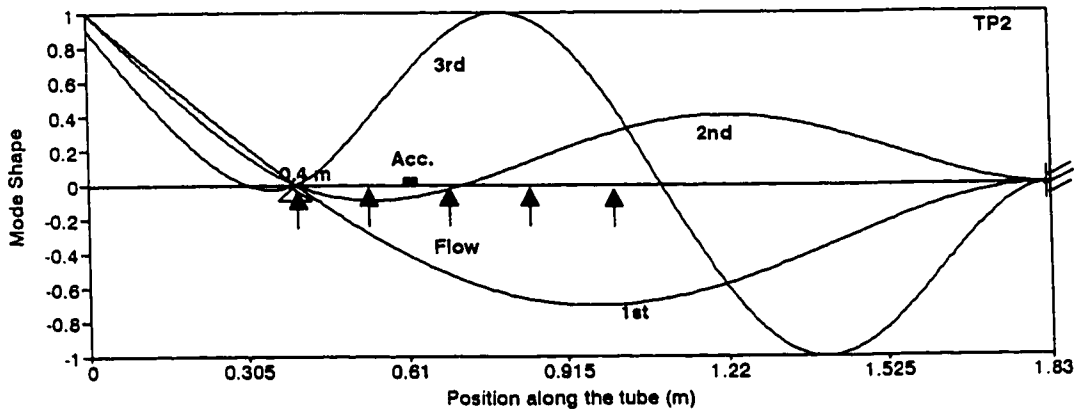

Figure 6.2.5 Mode shapes and flow location (TP2)

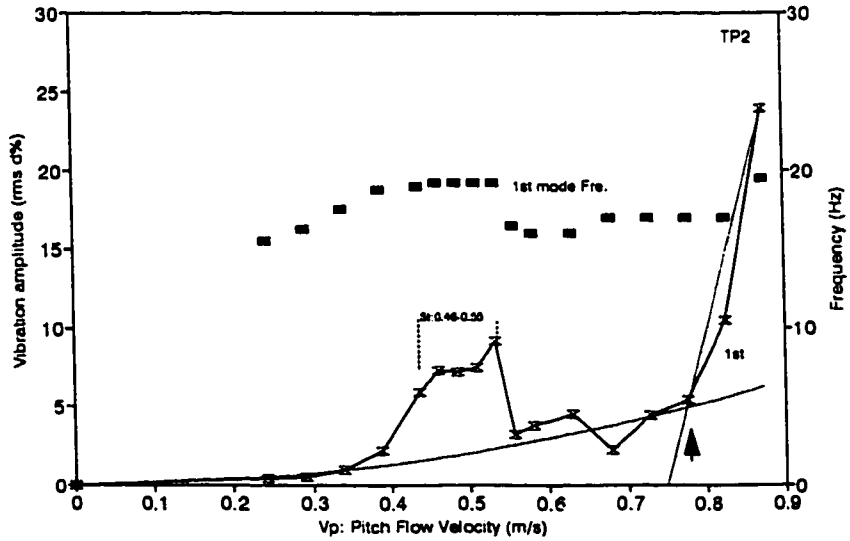

Figure 6.2.6 Tube response versus pitch velocity (TP2)

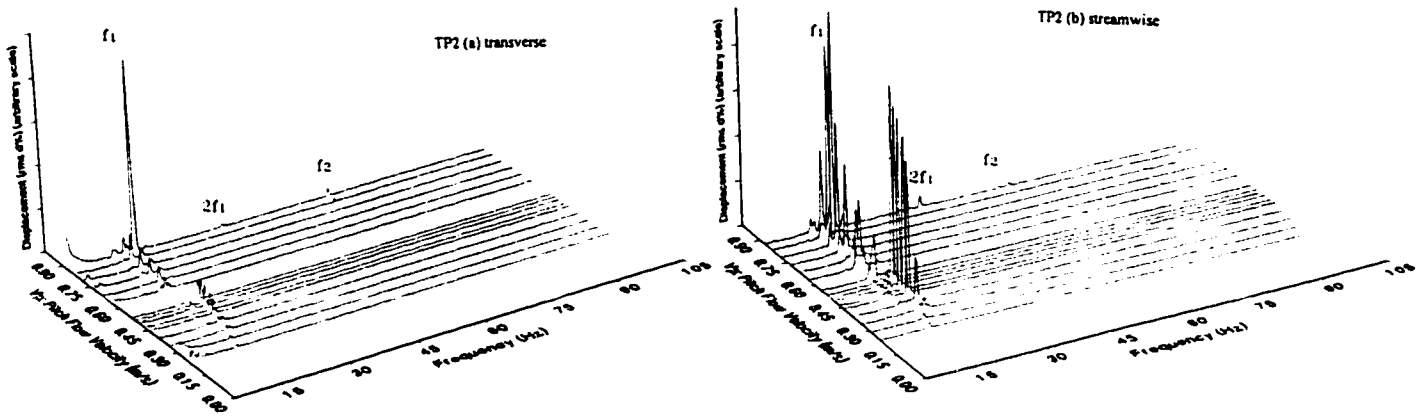

Figure 6.2.7 Tube displacement frequency spectra (TP2) (a). transverse (b). streamwise

Table 6.2.3 Summary of TP2 test

Label	Model	Frequency (Hz)	Energy fraction S_i	Critical velocity (m/s)				
				start	end	final V_{pc}	Pettigrew	Weaver
12	1st	17.0	0.3777	0.4	0.56	0.78±0.02	0.60	0.22
	2nd	66.0	0.4404				2.33	3.32

6.3 Three Spans Partial Admission Tests

Several tests were conducted on tubes with three spans. The comparison between frequency measurement and calculation indicates that the knife edge intermediate support plate represents a simple support. It is expected that damping increases with the increase in the number of supports. A few tests were also conducted on a single flexible tube in a rigid bundle.

6.3.1 Test of S3 with Equal Span Length

6.3.1.1 Full flexible tube bundle

Tubes of 1.83 m length were divided into three equal spans. Two support plates were placed in the locations of 0.61 m and 1.22 m from the fixed end, and the other end was set free. The first three mode shape functions and the location of the accelerometers are given in Figure 6.3.1. The full middle span was subjected to uniform freestream velocity. It is apparent that the 2nd mode has the largest deflection in the middle span. The accelerometers were located at 0.305 m from the free end, where all three modes have equivalent magnitude of displacement. Such an arrangement is necessary to maintain the accuracy of the maximum displacement calculation for all three modes. The response curve is shown in Figure 6.3.2, illustrating that only the first two modes were excited. Below V_p= 1.21 m/s, the displacement of both modes is very small but increases gradually, a behaviour which is apparently caused by random turbulence excitation. Beyond V_p= 1.21 m/s, the 1st mode amplitude increases only gradually, but the 2nd mode amplitude increases drastically, reaches a peak at V_p= 1.7 m/s, then reduces rapidly to a minimum value at V_p= 1.94 m/s. Beyond this velocity, the 2nd mode displacement starts, once again, to increase rapidly finally reaching the ultimate fluidelastic instability state. At V_p = 2.0 m/s, the 1st mode response increases drastically and becomes unstable. The Strouhal number, St_p = 0.63-0.58 of the first peak in the 2nd mode may be caused by vortex shedding, though we cannot exclude the possibility of a secondary fluidelastic

Table 6.3.1 Summary of S3 test

Label	Mode	Frequency (Hz)	Energy fraction S_i	Critical velocity (m/s)				
				start	end	final V_{pc}	Pettigrew	Weaver
7	1st	16.25	0.0126			2.03±0.02	**2.09**	1.38
16	2nd	87.0	0.6325	1.3	1.9	2.0±0.05	**2.49**	1.10

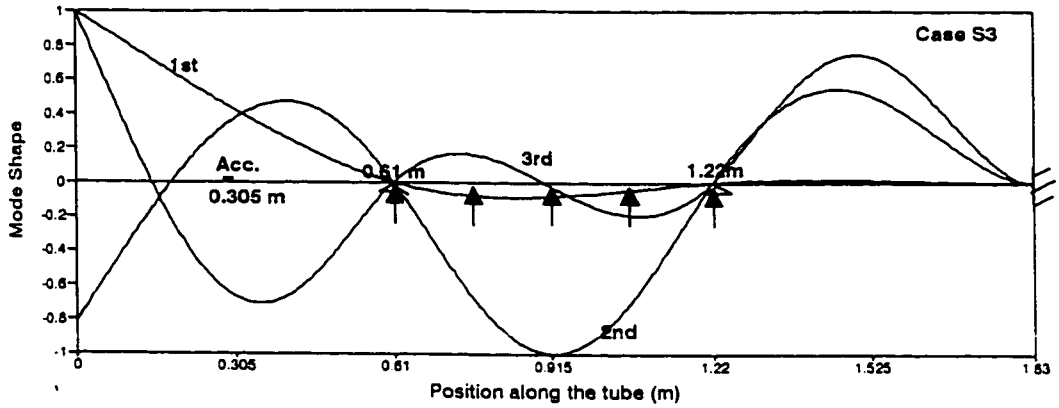

Figure 6.3.1 Mode shapes and flow location (S3)

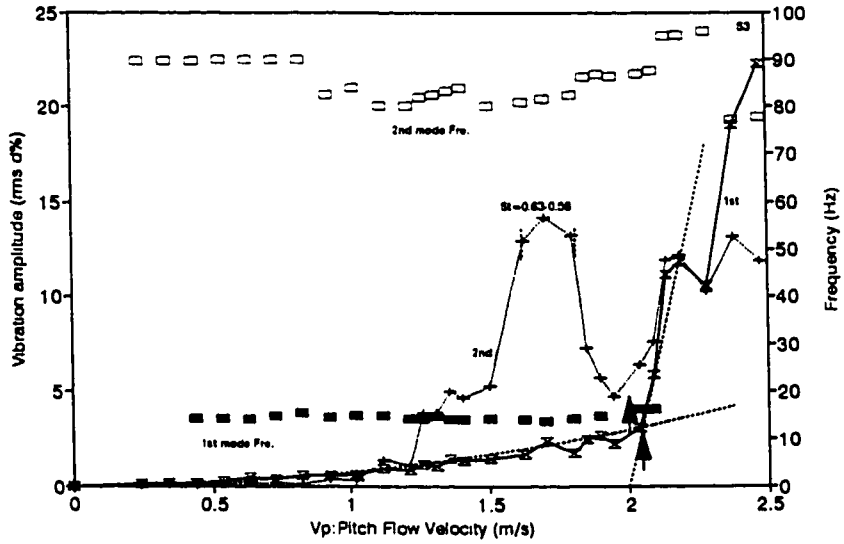

Figure 6.3.2 Tube response versus pitch velocity (S3)

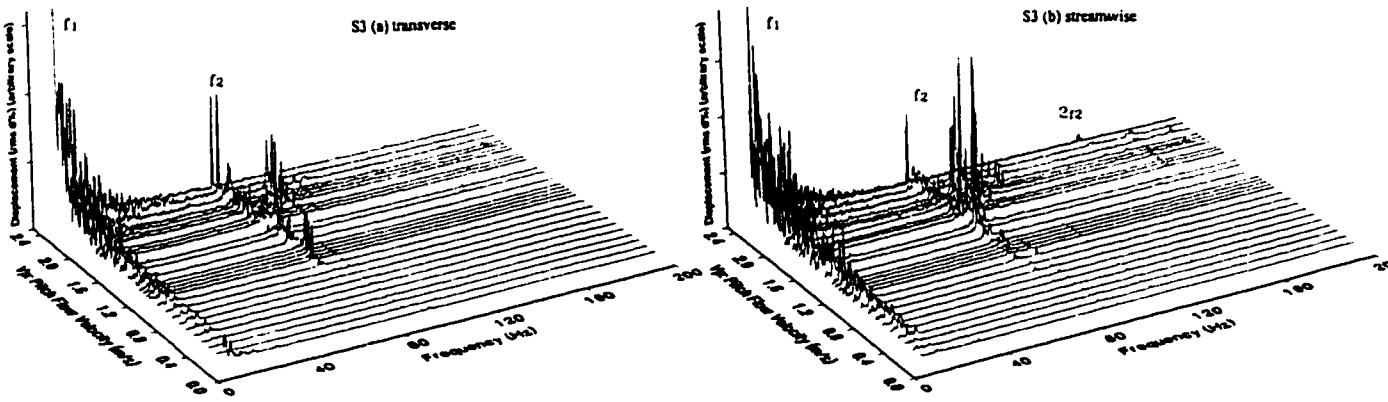

Figure 6.3.3 Tube displacement frequency spectra (S3) (a). transverse (b). streamwise

instability. The data is listed in Table 6.3.1. The predictions by Pettigrew's criterion are nonconservative for both modes, while by Weaver's criterion they are conservative. The Weaver model also correctly predicts the 2nd mode as the initial unstable mode.

6.3.1.2 Single Flexible Tube

In the low damping parameter region, fluidelastic instability is expected to be dominated by a fluid damping mechanism, in which relative tube displacement does not play an important role. A single flexible tube in a parallel triangular rigid tube bundle has been found to become unstable [Weaver, 1983]. A difference in the critical reduced velocity between a full flexible array and a single flexible tube was found to exist but was not significant. In general, the strong coupling between a monitored tube and its neighbouring tubes generates multiple peaks for a given tube mode. In the present study, more than one mode was found to be excited at the same velocity, and their frequencies could also be very close such that it was difficult to identify the correct peak for each mode. In addition, several single flexible tube tests, whose configurations were the same as the corresponding full flexible tube arrays, were conducted because it was easier to identify the vibration mode on the response spectrum due to the reduced coupling effects. The tube responses of the single flexible tube of test S3 are shown in Figure 6.3.4. The response amplitude is much smaller than that of the full flexible tube bundle. The first peak of the 2nd mode appears from V_p =1.5 to 1.8 m/s, then the response rises slowly until V_p = 2.23 m/s, where the amplitude starts to increase rapidly. The critical velocity for the 1st mode is not very clearly defined but is taken as V_p = 2.3 m/s, compared with V_p = 2.03 m/s of the full flexible bundle. The lack of tube coupling delays the critical velocities of both modes. The vortex shedding response (or secondary instability) is greatly reduced, which suggests the

importance of fluid coupling of tubes for this phenomenon. The critical velocity delay phenomenon is similar to the study of [Weaver and Yeung, 1984]. Again, predictions by Pettigrew's model are slightly unconservative, while Weaver's model is conservative and correctly predicts the least stable mode.

Table 6.3.2 Summary of S3 single flexible tube test

Label	Mode	Frequency (Hz)	Energy fraction S_i	Critical velocity (m/s)				
				start	end	final V_{pc}	Pettigrew	Weaver
8	1st	16.0	0.0126			2.45±0.05	2.38	1.37
17	2nd	90.75	0.6325	1.5	1.8	2.38±0.01	**2.40**	1.10

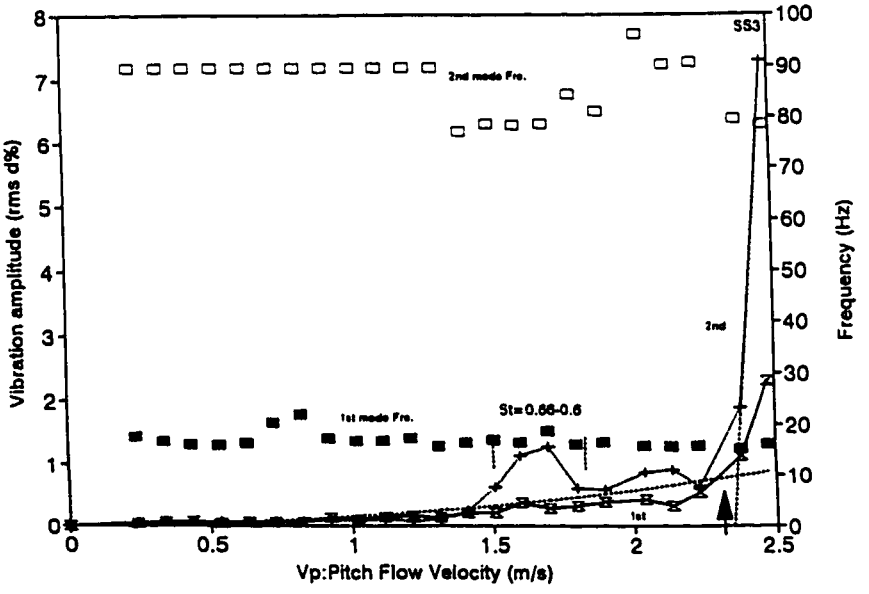

Figure 6.3.4 Tube versus pitch velocity (single flexible tube S3)

6.3.2 Test with Unequal Span Length (S4)

The span length and mode shape are seen in Figure 6.3.5. The 3rd mode has the largest deflection at the middle span. However, the 3rd mode dynamic response is small and does not become unstable, as seen in Figure 6.3.7. Only the first two modes become unstable, shown in Figure 6.3.6. In this test, the random turbulence response increases gradually but with relatively large amplitudes. There is a peak in the 2nd mode response at V_p = 1.41 to 1.7 m/s. The Strouhal number, St_p = 0.46 suggests that vortex shedding is unlikely to be the mechanism causing such a peak. The 1st mode becomes unstable at V_p = 1.89 m/s. The 2nd mode primary instability begins at V_p = 2.04 m/s, but the secondary instability occurs at V_p = 1.41 m/s, which is conservatively predicted by Weaver's criterion, as shown in Table 6.4.3.

Table 6.4.3 Summary of S4 test

Label	Mode	Frequency (Hz)		Energy	Critical velocity (m/s)				
		in air	unstable	fraction S_i	start	end	final V_{pc}	Pettigrew	Weaver
9	1st	11.25	9.75	0.0029			1.89±0.02	**2.49**	1.65
18	2nd	56.5	56.75	0.1059	1.41	1.7	2.04±0.03	**3.63**	0.72

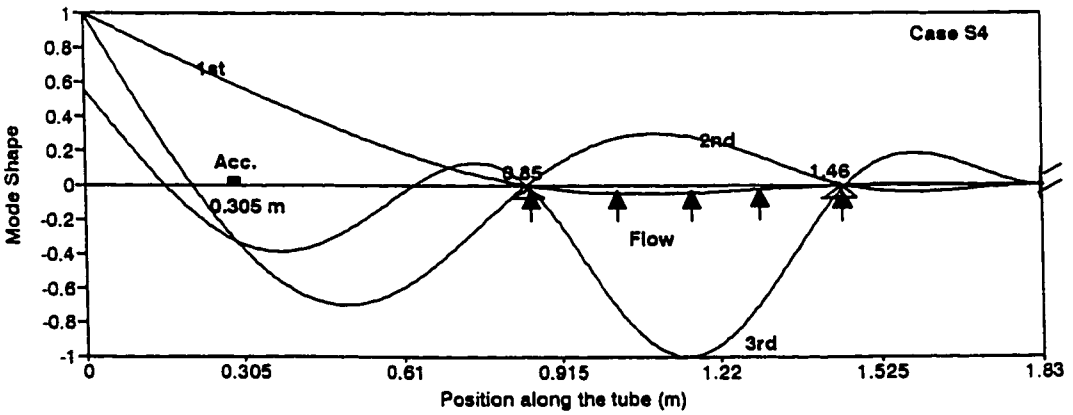

Figure 6.3.5 Mode shapes and flow location (S4)

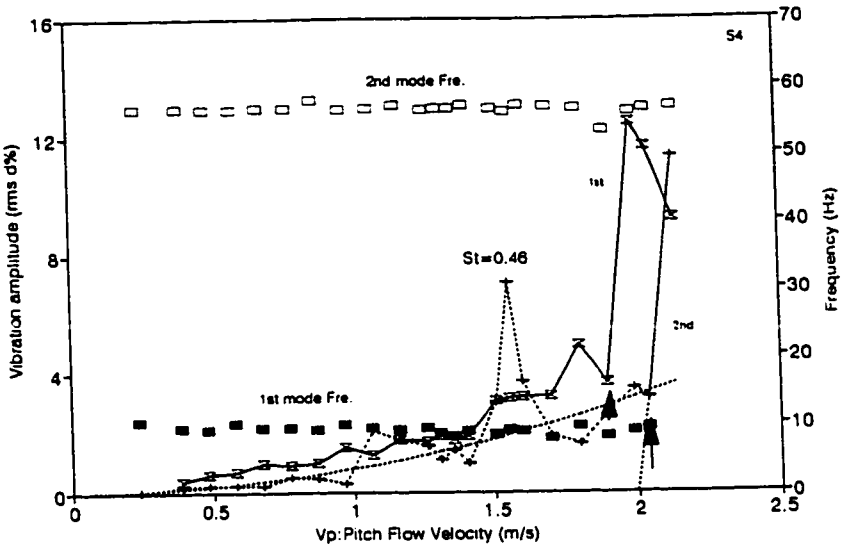

Figure 6.3.6 Tube response versus pitch velocity (S4)

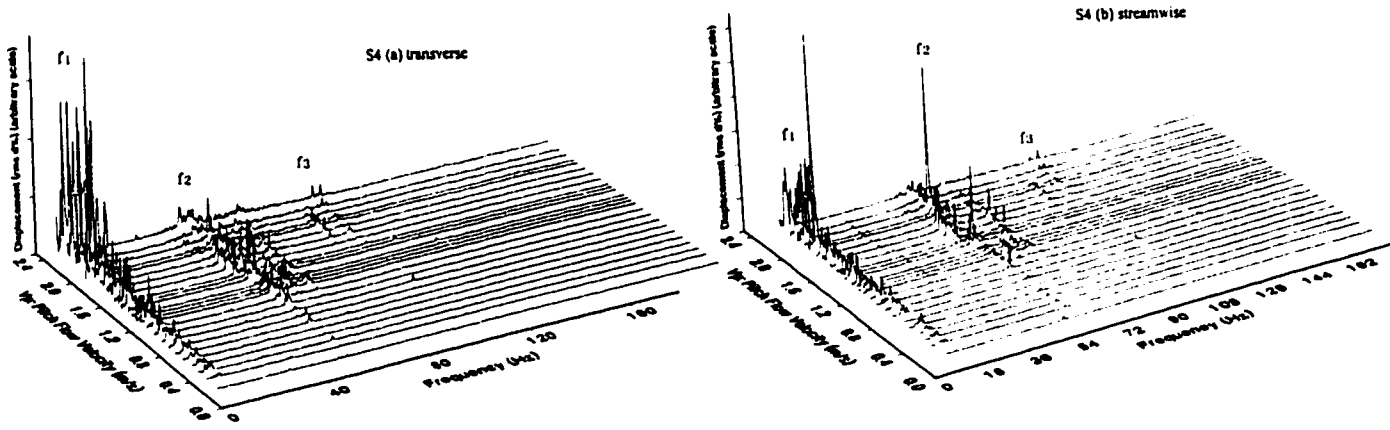

Figure 6.3.7 Displacement frequency spectra (S4) (a). transverse (b). streamwise

6.3.3 Test with Unequal Span Length (S5)

6.3.3.1 Full flexible tube bundle

The support locations are shown in Figure 6.3.8. It is expected that the 2nd mode will initially become unstable since it has the largest deflection in the middle span. The experiment verifies this prediction. The response and frequency spectra are shown in Figure 6.3.9 and 6.3.10 respectively. Only the 2nd mode response was observed. There is a peak between V_p = 1.02 to 1.89 m/s. Similar to previous cases, the Strouhal number is somewhat smaller than that expected for vortex shedding. The tube response increases dramatically at V_p = 2.3 m/s. There is a strong in-phase tube coupling prior to the onset of the instability, and the tube frequency drops from 90 Hz to 70 Hz. The prediction by both criteria are conservative, considering only the primary instability. Weaver's prediction is also conservative for the secondary instability which has amplitude of about 4% of tube diameter, see Table 6. 3.4.

Table 6.3.4 Summary of S5 test

Label	Mode	Frequency (Hz)		Energy	Critical velocity (m/s)				
		in air	unstable	fraction S_i	start	end	final V_{pc}	Pettigrew	Weaver
	1st	44.5		0.0394				3.94	3.74
19	2nd	103.5	91.0	0.6791	1.31	1.89	2.33±0.02	1.77	1.16

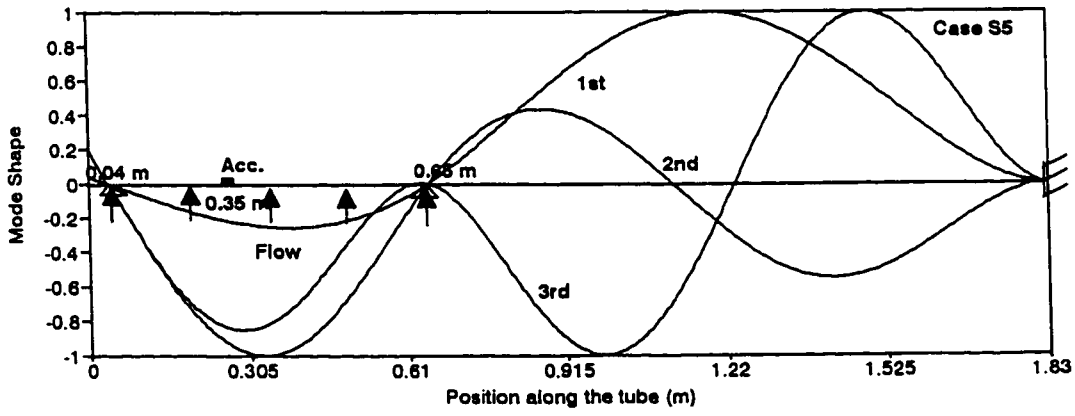

Figure 6.3.8 Mode shapes and flow location (S5)

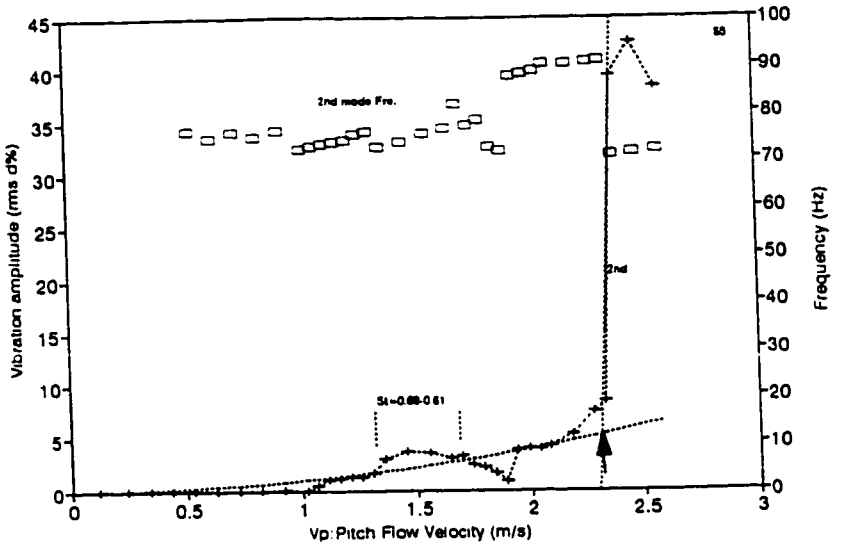

Figure 6.3.9 Tube response versus pitch velocity (S5)

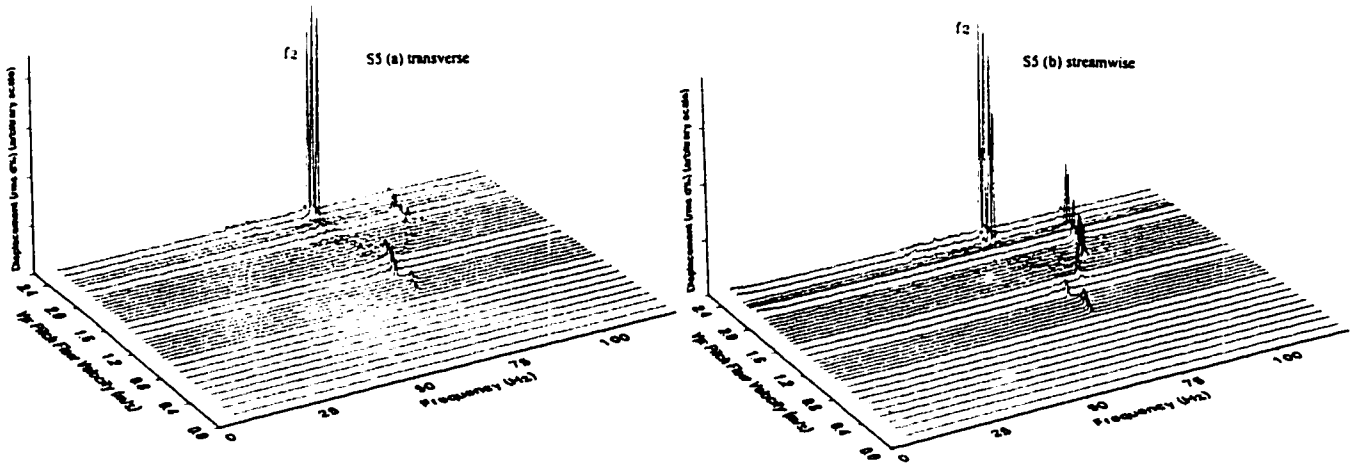

Figure 6.3.10 Displacement frequency spectra (S5) (a). transverse (b). streamwise

6.3.3.2 Single Flexible Tube

A single flexible tube investigation was also conducted on the S5 tube-support configuration. The response is shown in Figure 6.3.11. Similar to the full flexible tube array, only the 2nd mode is excited. The first peak appears between V_p = 1.21 to 1.99 m/s with St_p

= 0.68-0.57. The final critical velocity is around V_p = 2.33 m/s, where is the same as that for the fully flexible tube array, though with significant uncertainty. Predictions for the primary instability boundary by Weaver's model is conservative, while Pettigrew's prediction is slightly unconservative. Weaver's prediction is also conservative for the secondary instability which reaches a peak of nearly 10% tube diameter, see Table 6.3.5.

Table 6.3.5 Summary of S5 single flexible tube test

Label	Mode	Frequency (Hz)		Energy	Critical velocity (m/s)				
		in air	unstable	fraction S_i	start	end	final	Pettigrew	Weaver
	1st	44.5		0.0394				4.17	2.65
20	2nd	103.75	76.75	0.6791	1.21	1.99	2.1±0.1	**2.19**	0.97

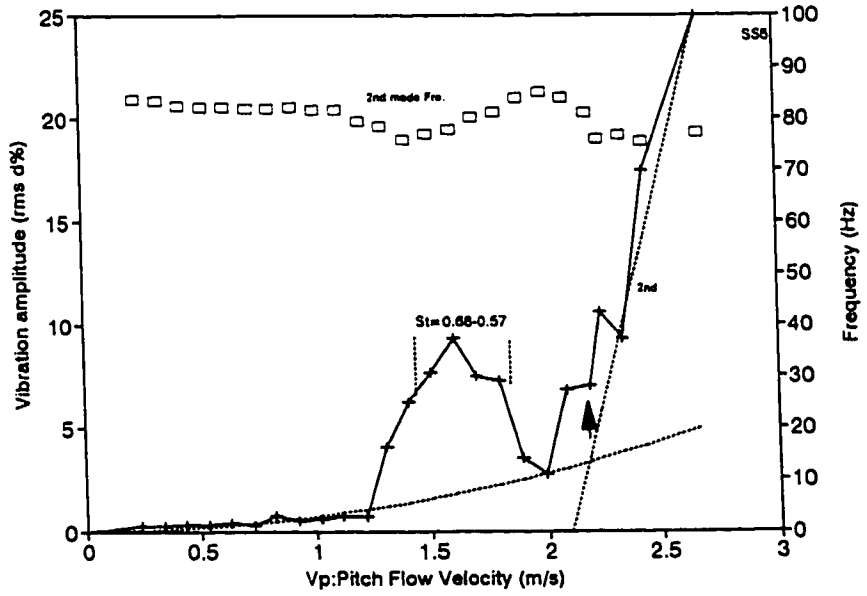

Figure 6.3.11 Tube response versus pitch velocity (S5 single flexible tube)

6.3.4 Test of S6 with Unequal Span Length

The support locations and mode shapes are shown in Figure 6.3.12. From the mode shapes, it seems that the 2nd or 3rd mode should become unstable initially. However, only the

1st and 2nd modes are excited, and they become unstable at almost the same velocity. As described in equation (3-17), the critical velocity ratios of the different modes is not only a function of the energy fraction, the magnitude of which can be judged from the mode shape figure, but is also a function of the mode frequency. A large deflection in one mode does not necessarily mean it is the unstable mode. In this case, because the frequency difference between the 1st and 2nd modes is so large that the 1st mode can still become unstable initially due to its low frequency. It is easy to perform the critical velocity ratio calculation for the single span, as shown in Figure 3.9 to 3.12. However, no systematic comparison can be made for multi-span tubes. Each tube-support configuration has to be calculated individually.

A peak in the 2nd mode at V_p = 1.45 m/s may be caused by vortex shedding because of Strouhal number St_p = 0.75. Critical velocities for both modes are almost the same, at V_p = 1.9 m/s. Only the predictions by Weaver's criterion are conservative, see Table 6.3.6.

Table 6.3.6 Summary of S6 test

Label	Mode	Frequency (Hz)		Energy	Critical velocity (m/s)				
		in air	unstable	fraction S_i	start	end	final V_{pc}	Pettigrew	Weaver
10	1st	24.25	17.0	0.0221			1.93±0.01	**2.96**	1.32
21	2nd	109.25	92.5	0.4612			1.93±0.01	**2.28**	1.17

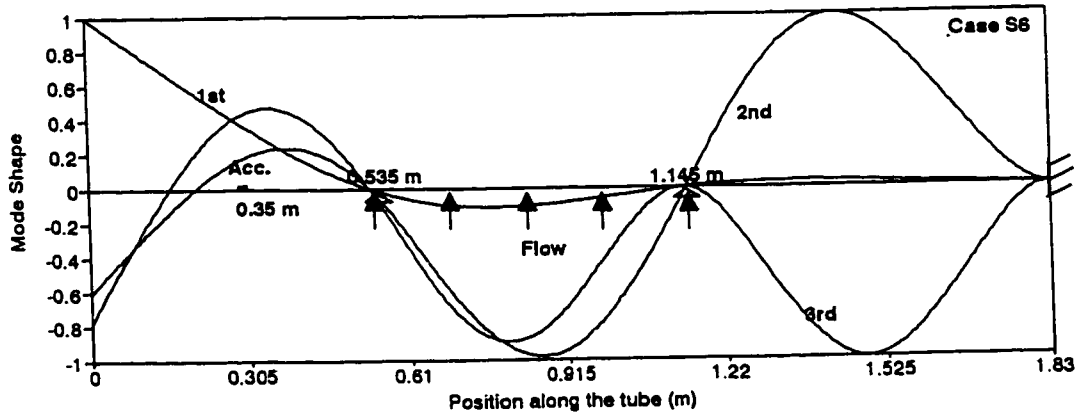

Figure 6.3.12 Mode shapes and flow location (S6)

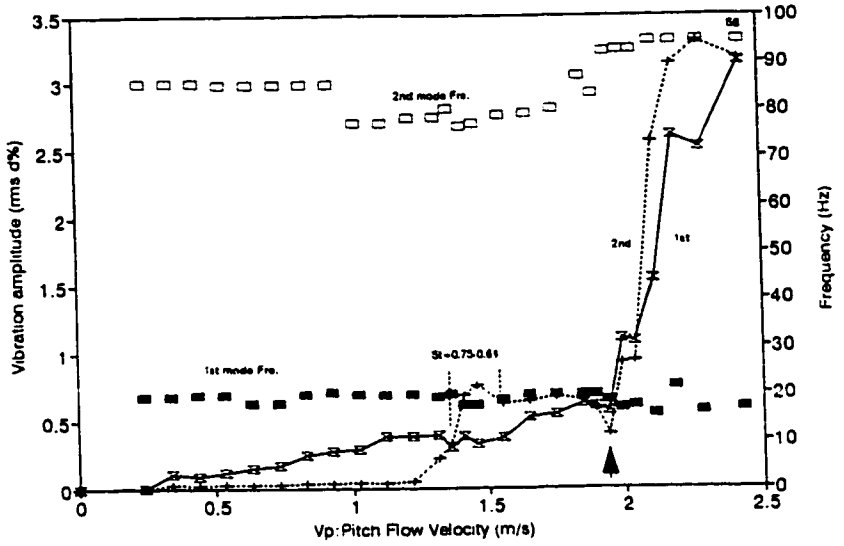

Figure 6.3.13 Tube response versus pitch velocity (S6)

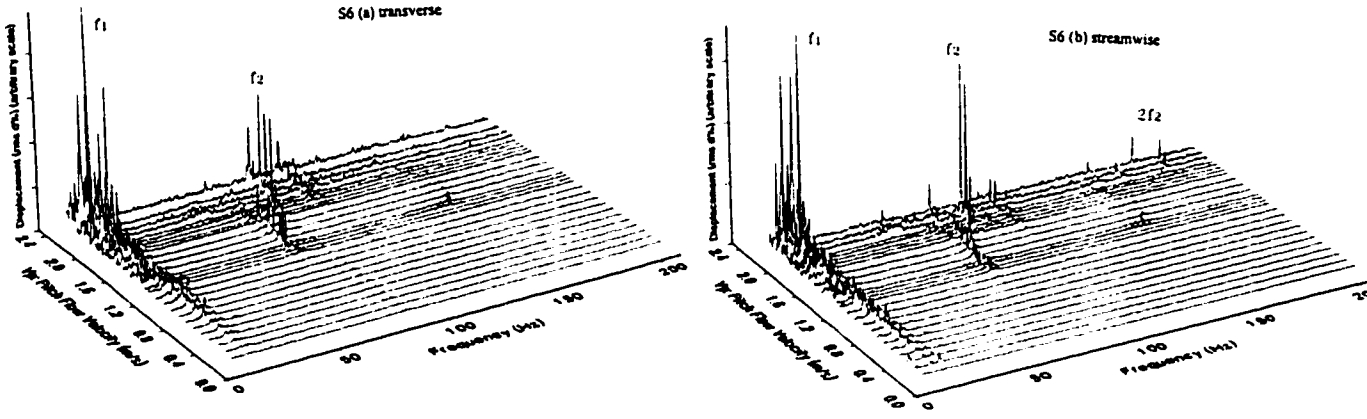

Figure 6.3.14 Displacement frequency spectra (a). transverse (b). streamwise (S6)

6.4 Summary of All Tests

In general, the fluidelastic instability map for uniform cross flow with full admission is a plot of reduced velocity versus mass damping parameter ($m\delta/\rho d^2$), is shown in Figure 2.4. In the case of partial admission, the mass-damping parameter has to be changed to a mass-damping-energy fraction parameter (MDE = $m\delta/\rho d^2 S_i$). As mentioned in Chapter 2, damping in air and still water are both commonly used in the stability analysis. Therefore, two different

Table 6.4.1 Summary of all tests

Test	Label	Mode	Frequency (Hz)		Damping δ		Energy fraction S_i	Critical velocity (m/s)			
			in air	unstable	in air	in water		secondary instability			final
								start (label)	end (label)	max dis.	V_{cr}
Datum	1	1st	133.3	108.25	0.0343	0.1788	1.0	2.14(23)	2.52(24)	2.1%	2.71±0.05
SP1	2	1st	49.5	36	0.052	0.137	0.0808				1.5±0.05
SP1	13	2nd	15.5	10.75	0.024	0.072	0.3137	0.83(25)	1.31(26)	4.5%	1.41?
SP2	3	1st	15.5	10.75	0.052	0.137	0.628	0.12(27)	0.34(28)	15%	0.44±0.01
SP3	4	1st	15.5	10.75	0.052	0.137	0.3367	0.29(29)	0.49(30)	2.5%	0.53±0.04
SP3	14	2nd	49.5	34.75	0.024	0.072	0.5236				0.53?
SP4	5	1st	15.5	10.75	0.052	0.137	0.6305				0.50±0.02
SP5	6	1st	15.5	10.75	0.052	0.137	0.3002				0.76±0.01
SP5	15	2nd	49.5	34.25	0.024	0.072	0.4057	0.57(31)	0.68(32)	1.0%	0.8±0.02
N1	47	1st	45	32.75	0.008	0.075	0.1542				2.89±0.01
N2	48	1st	45	33.0	0.008	0.075	0.1466				2.42±0.03
N2	53	2nd	80.5	65	0.008	0.075	0.7400	1.89(45)	2.52(46)	2.6%	2.52±0.04
N3	49	1st	45	32.75	0.008	0.075	0.6597				0.97±0.02
N4	50	1st	45	36.75	0.008	0.075	0.3297				1.70±0.05
N5	51	1st	45	32.5	0.008	0.075	0.1304				3.0±0.02
N5	54	2nd	80.5	61.5	0.008	0.075	0.5437	2.31(47)	2.99(48)	1.9%	3.0±0.02
N6	52	1st	45	34.5	0.008	0.075	0.1120				2.89±0.02
N6	55	2nd	80.5	66.5	0.008	0.075	0.7056				2.91±0.02
TP2	12	1st	21.5	17	0.0153	0.131	0.3777	0.4(43)	0.56(44)	9.0%	0.78±0.02
S3	7	1st	18.75	16.25	0.0175	0.086	0.0126				2.03±0.02
S3	16	2nd	115.25	87	0.065	0.118	0.6325	1.3(35)	1.9(36)		2.0±0.05
SS3	8	1st	18.75	16	0.0175	0.071	0.0126			15%	2.45±0.05
SS3	17	2nd	115.5	87	0.065	0.118	0.6325	1.5(33)	1.8(34)	1.6%	2.38±0.01
S4	9	1st	11.25	9.75	0.04	0.071	0.0029				1.89±0.02
S4	18	2nd	77	56.75	0.01	0.101	0.1059	1.41(37)	1.7(38)	7.5%	2.04±0.03
S5	19	2nd	103.5	91	0.027	0.123	0.6791	1.31(39)	1.89(40)	2.6%	2.33±0.02
SS5	20	2nd	103.75	76.75	0.027	0.123	0.6791	1.21(41)	1.99(42)	9.5%	2.1±0.1

S6	10	1st	24.25	17	0.015	0.128	0.0221				1.93±0.02
S6	21	2nd	109.2	92.5	0.06	0.118	0.4612			0.75%	1.93±0.02

MDE parameters will be presented: MDE_a and MDE_w in which damping in air (δ_a) and water (δ_w) are used respectively. In addition, damping measurements show that the damping value depends on the vibration mode, in both air and water.

The primary critical reduced velocity data are plotted in Figure 6.4.1 and 6.4.2 using MDE_w and MDE_a respectively. The reference number for each data point in the plots corresponds to the label number listed in previous tables.

6.4.1 Comparison with Existing Semi-Empirical Design Guidelines

The correlations proposed by Pettigrew & Taylor [1991] (equation 6-1-1) and Weaver & Fitzpatrick [1988] (equation 6-1-2) are also plotted in Figures 6.4.1 and 6.4.2 respectively. Pettigrew and Taylor use damping in water. On the other hand, Weaver and Fitzpatrick use damping in air. These correlations are the low boundary lines for a large number of test data found in the literature. Therefore, the conservativeness of a correlation can be justified by comparing the correlation line and test data obtained for a particular research goal. Of course, a certain margin is allowed, and the data must be both sufficient and reliable. In Figure 6.4.1, most of the first mode data (closed circles) are above Pettigrew's correlation, except for four data points, i.e., 7, 8, 9 and 10. However the majority of the second mode data points (open circles) are below the correlation curve. It seems that Pettigrew's correlation does not always give a conservative prediction, especially for the 2nd mode instability. In Figure 6.4.2, Weaver's correlation predicts conservatively not only the 1st but also the 2nd mode instability data.

From these two figures, it is apparent that the second mode instability has lower critical velocity boundary than that of the first mode. This phenomenon is further demonstrated in

Figure 6.4.3. In this figure, critical reduced velocity is plotted against energy fraction factor ($1/S_i$), instead of MDE, which excludes the uncertainty of the damping measurement. This figure will be helpful in revealing the effect of mode on critical reduced velocity, since S_i is only a function of mode shape and flow location. The figure indicates that the critical velocity of the second mode is somewhat lower than that of the first mode. The correlation of the first mode data is close to a straight line function in a log-log scale, but such a relation seems not to apply to the second mode data. Surprisingly, no 3rd mode instability with significant amplitude was found in this study. This agrees with Parrondo et al,'s data [1997], which is plotted in Figure 6.4.4 and 6.4.5. In that study, no instability mode higher than the second was found with an amplitude exceeding 2% of the tube diameter. Amidst this plotted data, the 3rd mode instability is included in spite of very small amplitudes. In the frequency spectrum analysis, especially using a logarithmic scale for the amplitude axis, higher mode frequency components are evident. The corresponding instability velocity can be found when plotting amplitude versus velocity. However, it is difficult to identify those components against the background noise, and the accuracy is low. In addition, it is arguable whether such a threshold velocity is really a critical velocity of fluidelastic instability. In practical applications, this small response is not likely to cause tube damage. In Parrondo et al's figures, multiple instability regions were identified by drawing curves through each data point. The data at the lower instability regions are mostly 2nd and 3rd mode data, and are related to small amplitudes (<0.3%d). However, this multiple instability phenomenon should not be overlooked. In Figures 6.4.6 and 6.4.7, the present secondary instability data (labels 25 to 48) listed in Table 6.4.1 are plotted together with Parrondo's data. The present data do not fit the secondary instability lines defined by Parrondo's data, although they are located in the same V_r - MDE_a region. The non-linear characteristics caused by the large vibration amplitude in the secondary instability of the present experiment

may contribute to such a discrepancy. The primary and secondary instability data are plotted in Figure 6.4.8 and 6.4.9. It is apparent that Pettigrew's model does not always correctly predict both primary and secondary instability velocities. On the other hand, Weaver's model consistently predicts conservatively all instability velocities.

6.4.2 Discussion of Existence of Secondary Fluidelastic Instability

Paidoussis et al, [1995] present a theoretical study by deriving unsteady forces from the Navier-Stokes equations. The quasi-unsteady model predicts no multiple unstable regions. Paidoussis et al also showed that damping and deviation of as little as 2% of a tube diameter from perfect array geometry can virtually eliminate the multiple instability regions, or only generate very small response peaks. Thus the authors argue that the multiple instability regions are "practically non-existent". The phenomenon suspected as the secondary instability is considered by the authors as vortex shedding. Vortex shedding and fluidelastic instability may overlap, especially in a liquid flow. However, they remain as two distinct excitation mechanisms.

As mentioned in the previous sections, the response peaks occurring prior to the ultimate fluidelastic instability may be caused either by the secondary instability or by vortex shedding. The response peak is usually smaller than the ultimate unstable response, but could be as high as 15% of the tube diameter, well in excess of the 2% limit set by the industry [Pettigrew and Taylor 1991]. Therefore, this kind of response and its mechanisms cannot be neglected in vibration analysis, as they have been up to the present. In order to identify the excitation mechanism of these peaks, their corresponding Strouhal numbers were calculated and plotted in Figure 6.4.10. Some of the data intersect Chen's high frequency line, but many of them have much lower values. In the present single span partial admission test (SP_i series), the natural

frequency for all tests is the same because of the unchanged support conditions. If the suspected peaks are caused by vortex shedding, they should occur at the same pitch velocity. But the corresponding velocity and Strouhal numbers are V_p = 0.8 - 1.3 m/s (St_p = 0.48-0.37) for SP1, V_p = 0.1 - 0.33 m/s (St_p = 0.69-0.41) for SP2, and V_p = 0.29 - 0.48 m/s (St_p = 0.46-0.28) for SP3. Such large differences in velocity and St_p in each case and the differences between the measured St_p and the St_p in the literature suggest that such amplitude response peaks may be not caused, at least solely, by vortex shedding. On the other hand, vortex shedding certainly is one of the possible excitation mechanisms. Several of the St_p are close to Chen's data, as shown in Figure 6.4.10. Therefore, at flow velocities below the stability threshold, no constant Strouhal number was observed. This suggests that the local response peaks may belong to an abnormal fluidelastic instability behaviour, i.e., a secondary instability. On the other hand, given the coincidence of some Strouhal numbers, one cannot overlook the possibility of the response being enhanced by some induced vorticity phenomena which would not otherwise have occurred at these Reynolds numbers. It is interesting that such a phenomenon has not been paid much attention in previous fluidelastic instability investigations in a liquid flow. The difficulty in identifying such a phenomenon may be attributed to the intricate response curves caused by coupled multiple peaks rather than by the absence of the phenomenon. It is too simplistic to attribute this kind of response to vortex shedding without further investigation and verification. Once a cylinder is in oscillation, vortices will always be shed from the cylinder, but it is difficult to determine whether the vortices cause such oscillation or vice versa. Price et al [1995] found that there is no vortex shedding from a rigid parallel triangular tube array with Pr = 1.375, though when one tube was set flexible, they found both vortex shedding and fluidelastic instability. In most flexible tube arrays, the interaction of secondary fluidelastic instability and vortex shedding in a liquid flow may exist. Further investigations should be conducted in a

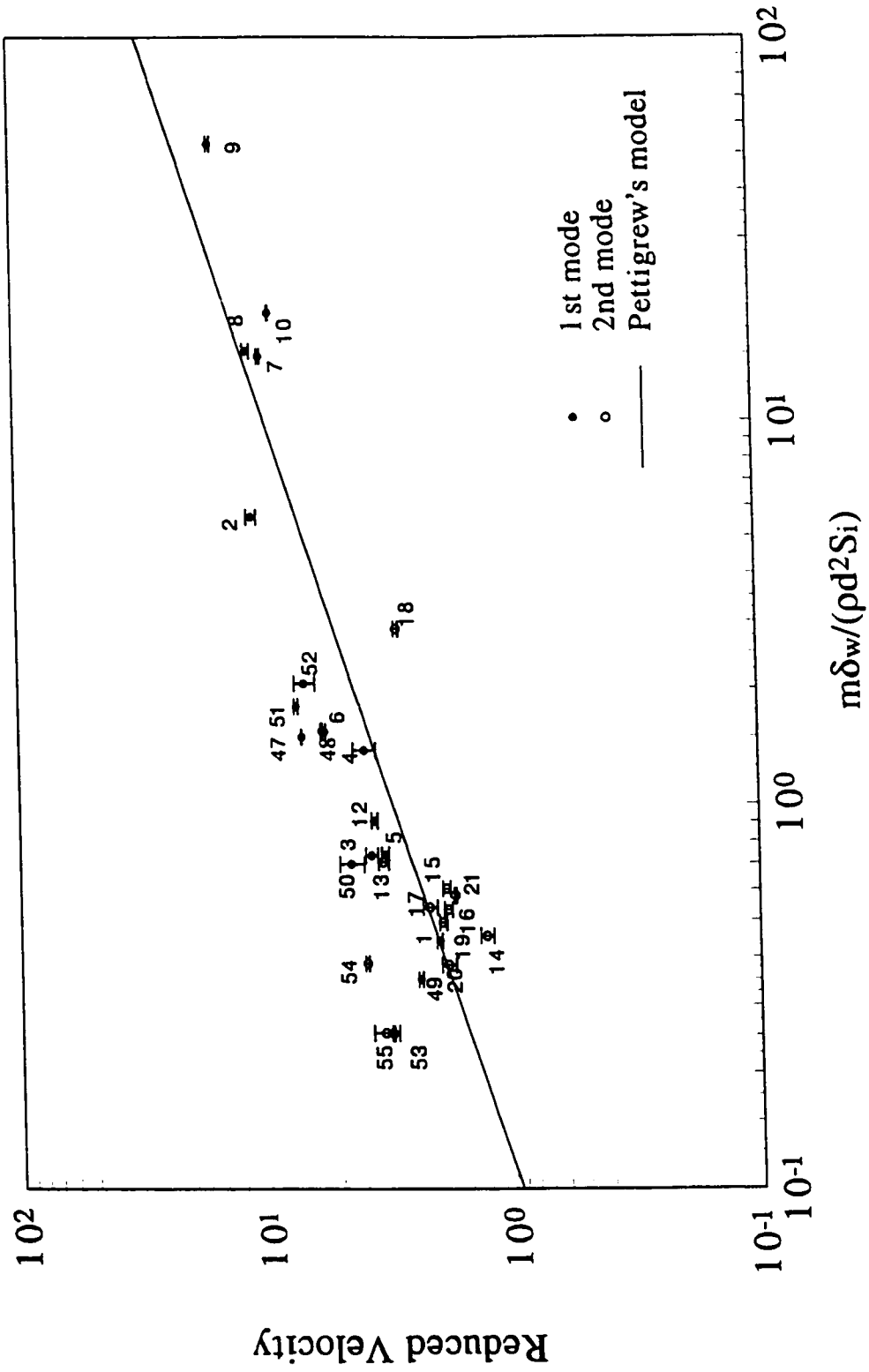

Figure 6.4.1 Critical reduced velocity versus mass-damping-energy-factor (MDE_w)

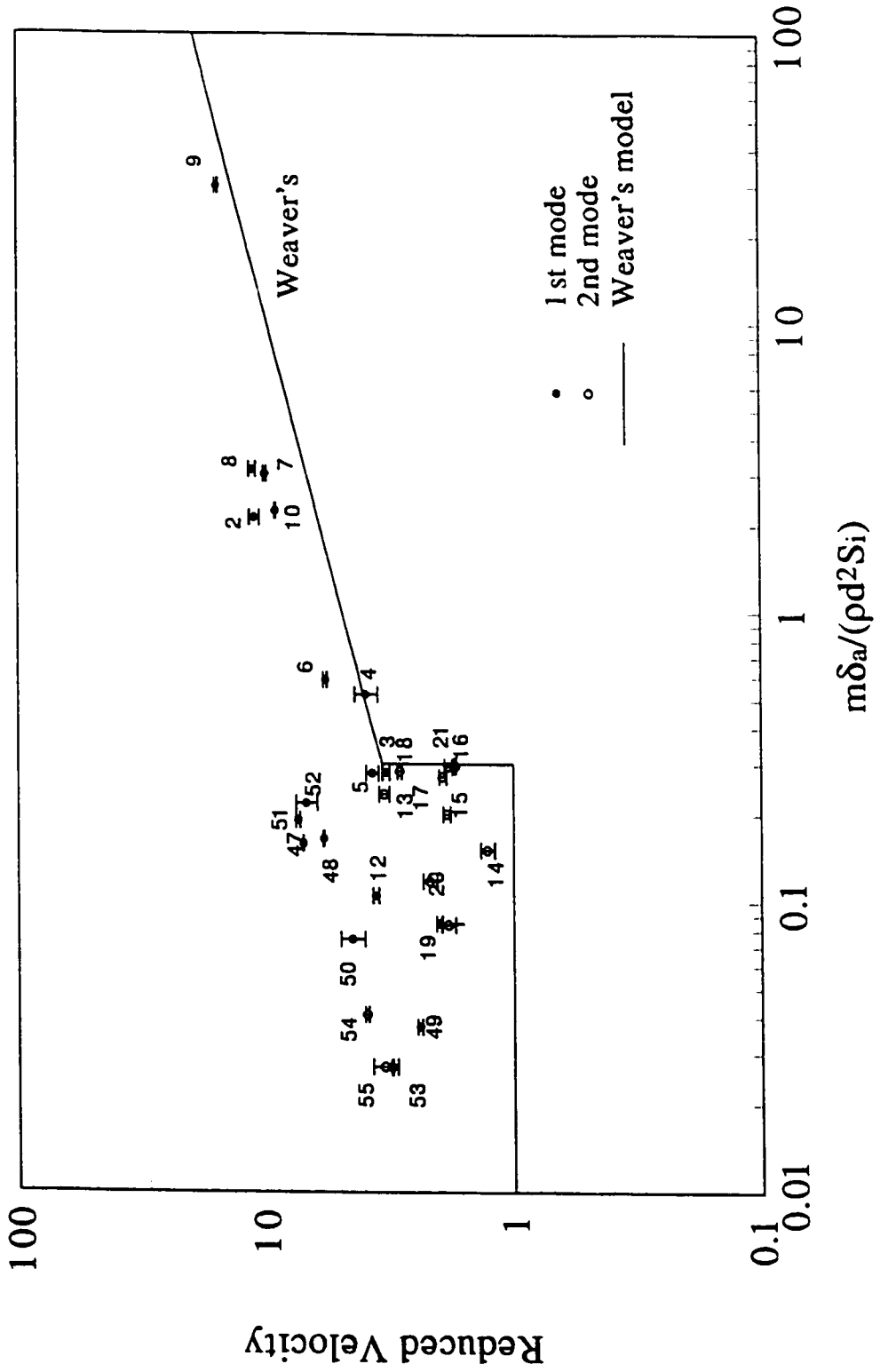

Figure 6.4.2 Critical reduced velocity versus mass-damping-energy-factor (MDE_a)

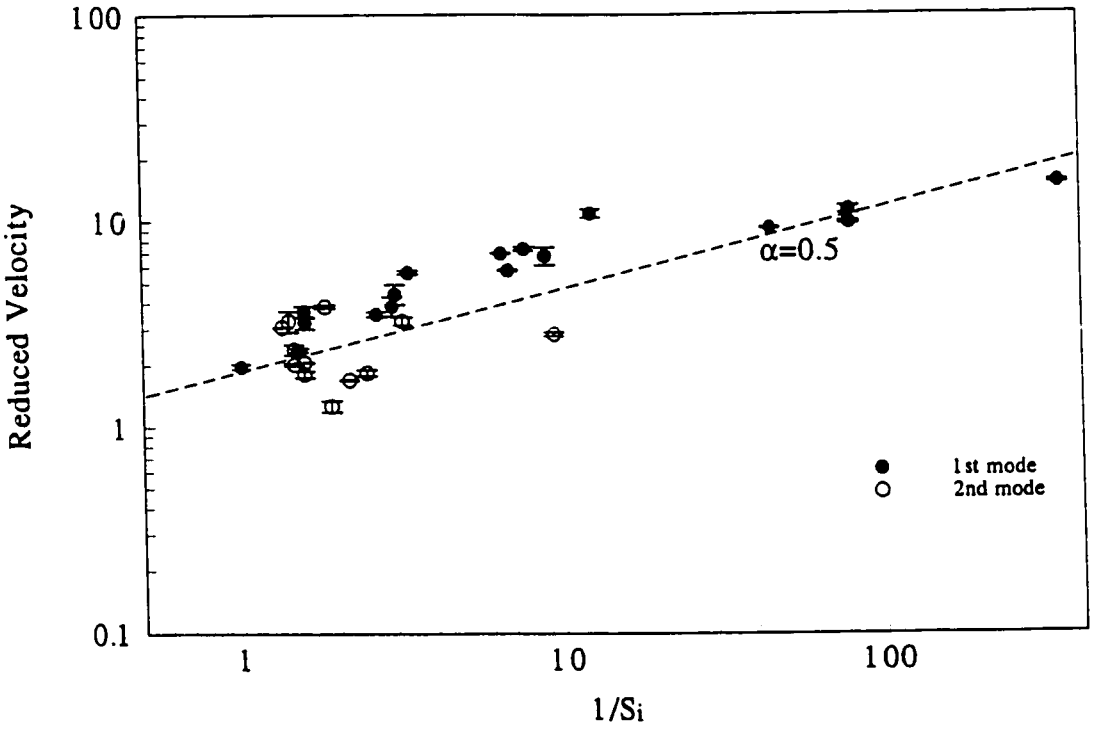

Figure 6.4.3 Critical reduced velocity versus energy fraction ($1/S_i$)

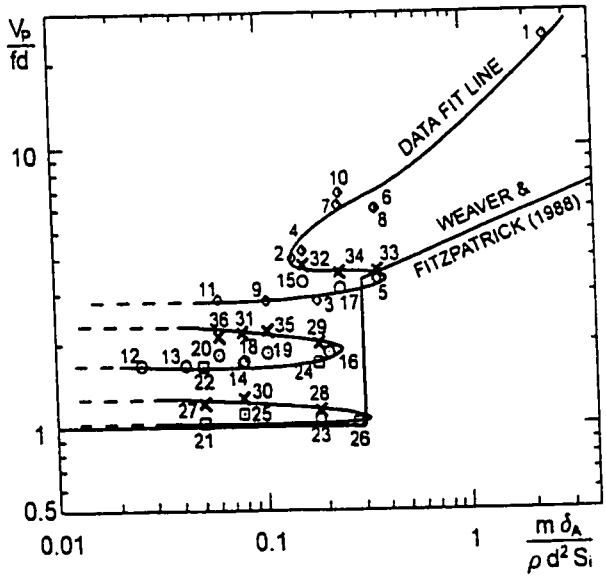

Figure 15 Stability map of the experimental data and comparison with the stability boundary of Weaver & Fitzpatrick (1988). Damping measured in air. ◇ data from group 1 of Table 2. ○ data from group 2 of Table 2. □ data from group 3 of Table 2. × data from group 4 of Table 2.

Figure 6.4.4 Critical reduced velocity versus mass-damping-energy-factor (MDE_s)

[Parrondo et al., 1997]

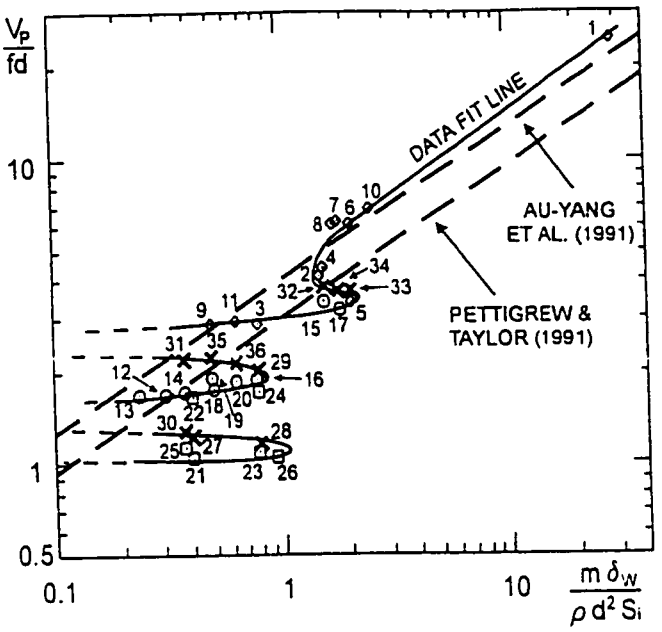

Figure 16 Stability map of the experimental data and comparison with the stability boundaries of Au-Yang *et al.* (1991) and Pettigrew & Taylor (1991) Damping measured in water. ◇ data from group 1 of Table 2. ○ data from group 2 of Table 2. □ data from group 3 of Table 2. × data from group 4 of Table 2.

Figure 6.4.5 Critical reduced velocity versus mass-damping-energy-factor (MDE_w)

[Parrondo et al., 1997]

specially designed test rig, which is able to separate these two mechanisms.

6.4.3 Conclusions of Experimental Results

Parrondo et al. [1997] found secondary instability phenomena using a two-span tube array. They also confirmed that Weaver and Fitzpatrick's correlation with addition of energy fraction predicts the critical velocity reasonably well for both the primary and secondary modes.

In the present study, a much improved test section was used. Different end and multiple intermediate supports were used to obtain a greater variety of flow conditions. From the different Strouhal numbers and the shape of the response peaks. It is apparent that the response peaks prior to the ultimate critical velocity are by no means a simple vortex shedding resonance

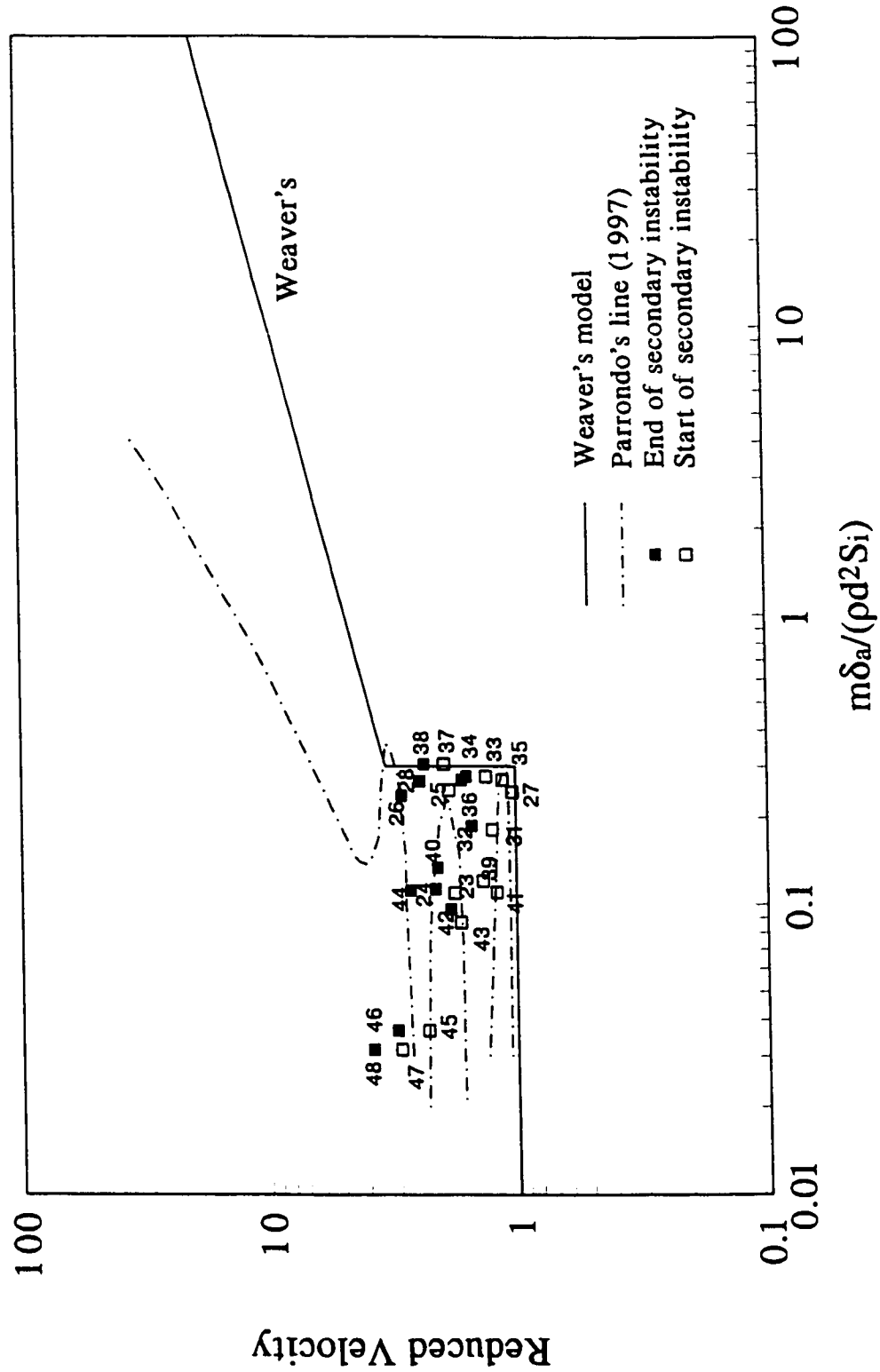

Figure 6.4.6 Secondary instability data of present results and Parrondo's (MDE_a)

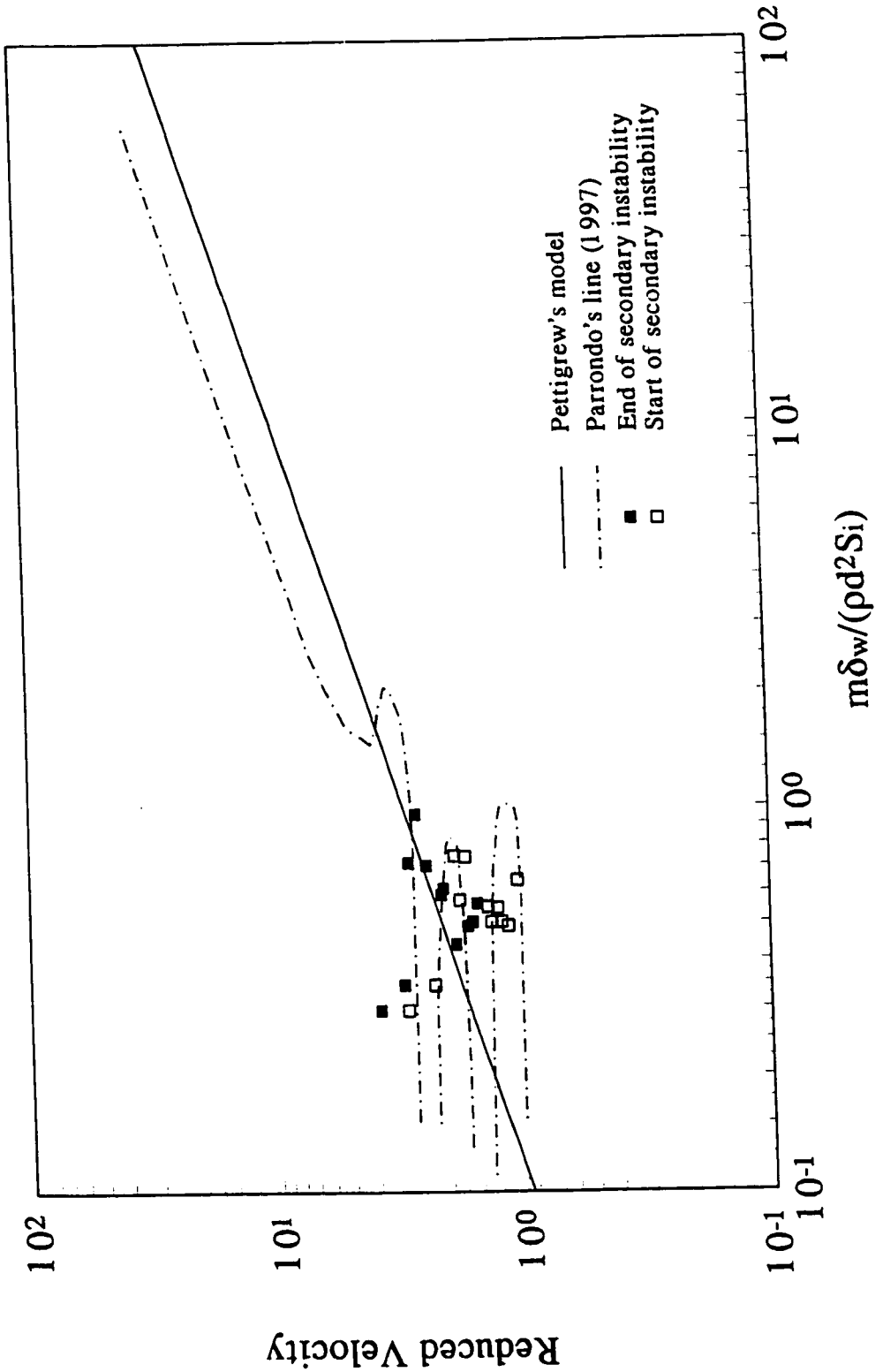

Figure 6.4.7 Secondary instability data of present results and Parrondo's (MDE_w)

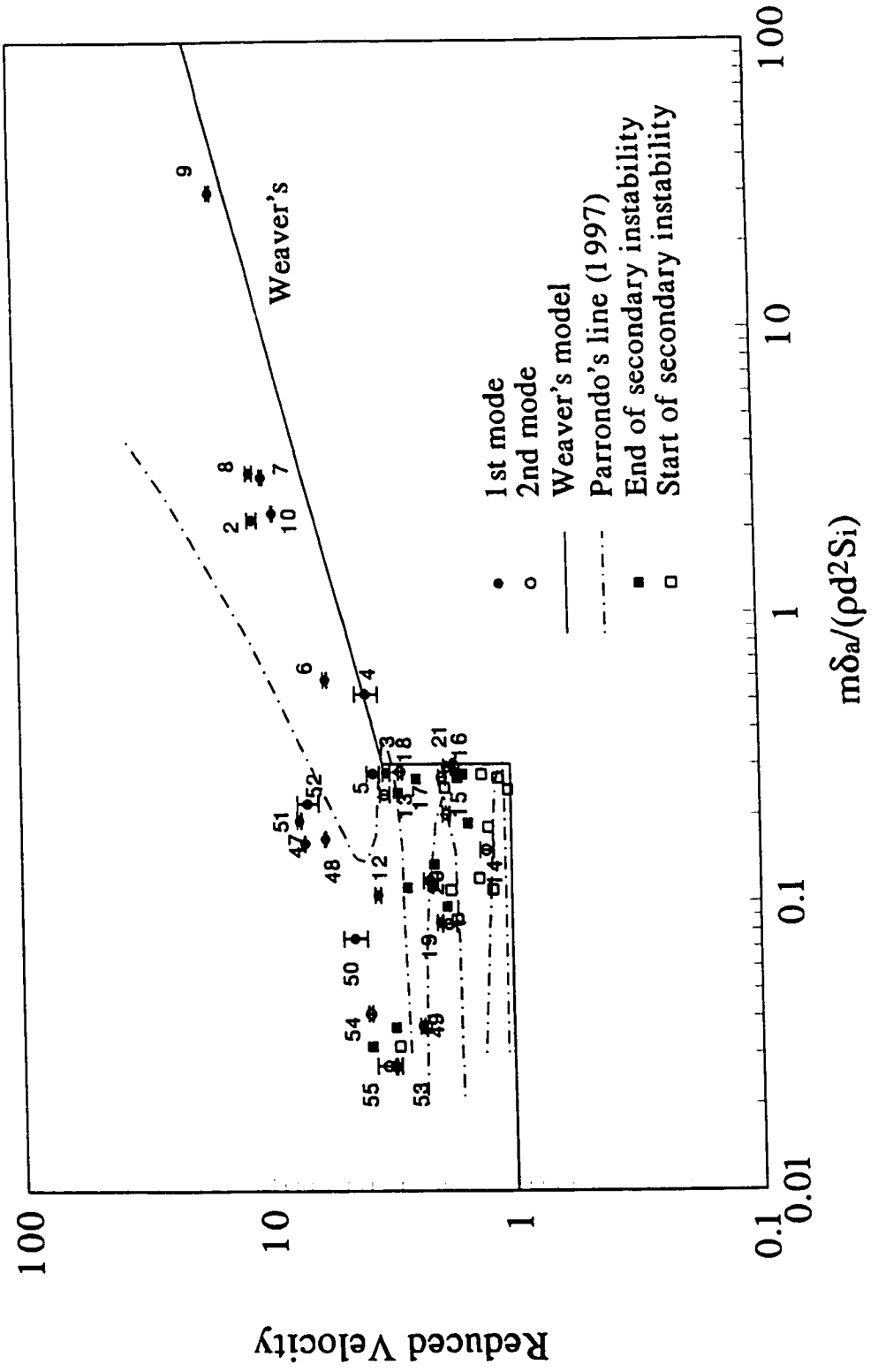

Figure 6.4.8 Critical reduced velocity versus MDE_a

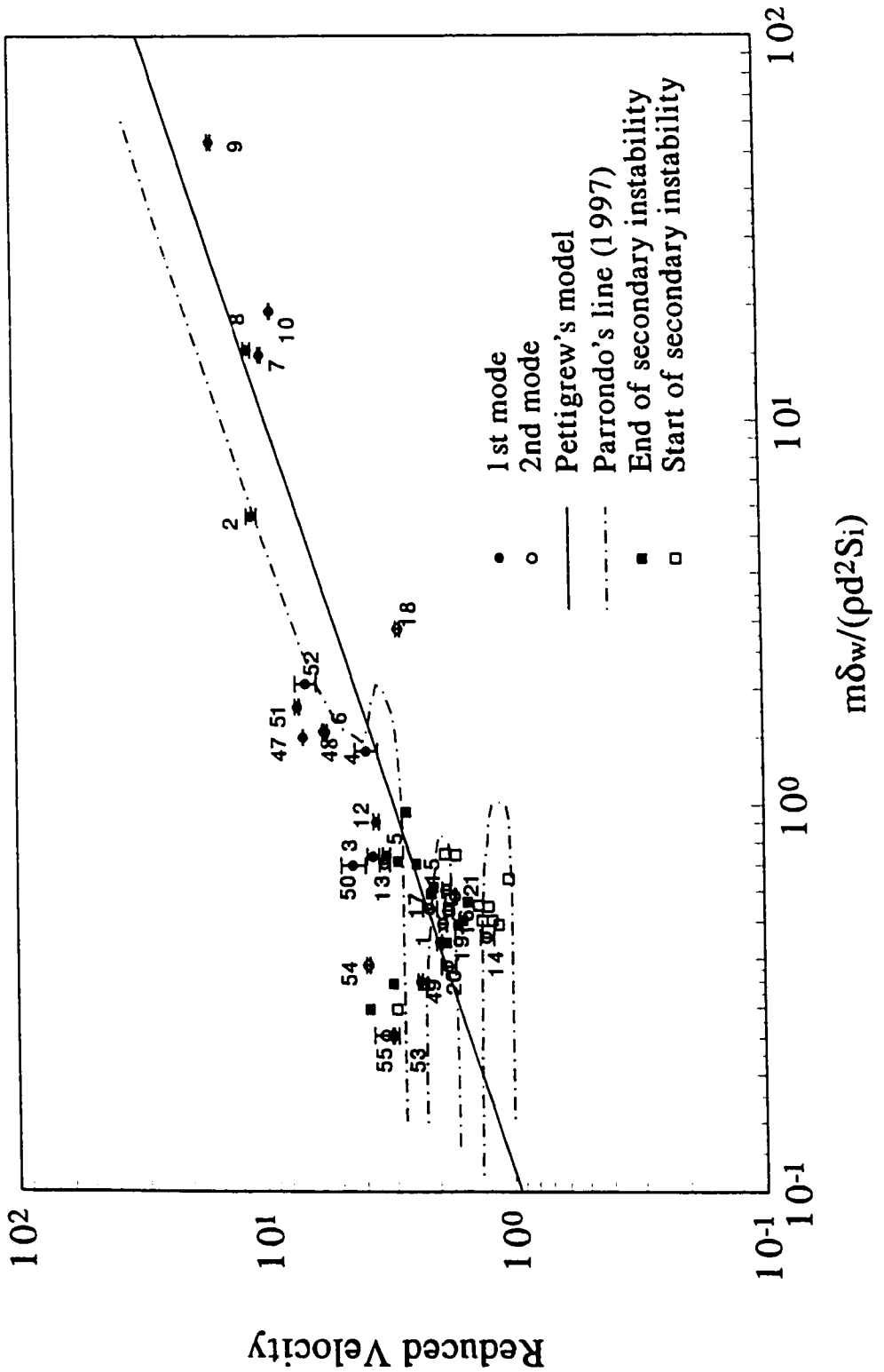

Figure 6.4.9 Critical reduced velocity versus MDE_w

phenomenon. In Parrondo et al. 's test, the secondary instabilities are primarily related to very small amplitudes, which is virtually insignificant from a practical point of view. Such small vibration response may be attributed to their simple test rig. The 2nd mode frequencies are typically larger than 200 Hz. The present experimental results show that significant response may occur at a practical frequency range for the 2nd mode. Higher than the 3rd mode, no significant amplitude was found. In addition, the large amplitudes of one mode may initiate the instability of the other modes, but usually the latter are associated with smaller amplitudes.

The present experimental results further confirm equation (6-1-2), i.e., Weaver & Fitzpatrick's correlation is able to conservatively predict the critical velocity. On the other hand, Pettigrew & Taylor's correlation does not always give conservative predictions or predict the correct mode. It is apparent from the present, as well Parrondo et al.'s results, that the reduced velocity for fluidelastic instability of multi-span flexible tube arrays with partial admission at small mass damping parameter, is independent of mass-damping-energy-factor.

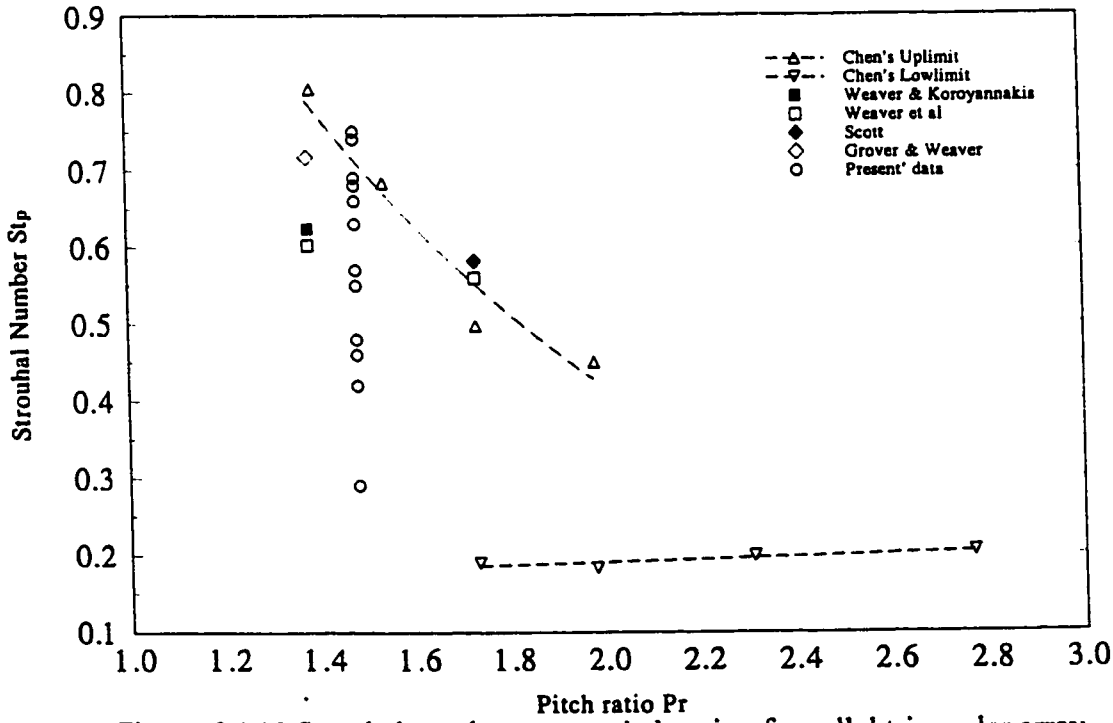

Figure 6.4.10 Strouhal number versus pitch ratio of parallel triangular array

CHAPTER 7

A FLUIDELASTIC INSTABILITY MODEL WITH AN EXTENSION TO FULLY FLEXIBLE MULTI-SPAN TUBE ARRAYS

7.1 Introduction

Fluidelastic instability design guidelines almost exclusively belong to the category of semi-empirical correlations, as mentioned in the previous chapters. In spite of substantial experimental data for various geometries and flow conditions, and a number of theoretical models, the mechanism of instability is not yet fully understood. To develop an accurate theoretical model remains a desirable objective. Numerous attempts have been reviewed in detail by Price [1995]. Typically , there are several types of theoretical models:

(1). Quasi-Static Models: Connors [1970], Blevins [1974].

The quasi-static model assumes that the fluidelastic instability is caused by relative displacement between tubes. Its ultimate expression is Connors' equation, written as the equation (1-1). This assumption has been proven inadequate by numerous studies, especially in liquid flow. However, Connor's equation still remains very popular in engineering applications because of its simple form, and is used loosely with different definitions of the parameters.

(2). Potential Flow Models: Dalton & Helfinstein [1971], Dalton [1980], Paidoussis et al. [1984].

These analyses neglect the wake region, and assume the flow is inviscid. A number of attempts have been made, but results are discouraging. It is apparent that potential flow theory is inadequate for the stability analysis of tube arrays in cross-flow.

(3). Unsteady Models: Tanaka & Takahara [1980, 1981], Chen [1983a, b].

Measured unsteady fluid force coefficients are used in cylinder motion equations. The results are in excellent agreement with the measured data for the same tube arrays. Unfortunately, many of the relevant fluid force coefficients must be measured for each array pattern and pitch ratio, as well as the reduced velocity range of interest. The theory is a significant theoretical advance since it reveals many important aspects of flow-structure interaction. However, the extreme requirements for experimental data have prevented it from becoming a practical design tool.

(4). Quasi-Steady Models: Price & Paidoussis [1982, 1984, 1986b].

In this type of model, the drag and lift coefficients are measured for stationary tubes at different displacement locations, and are assumed to be unaffected by tube motion, an assumption of the quasi-steady theory. This is known to be a good approximation at large reduced velocity (say, $U_r > 10$). The results agree reasonably well with the experimental data. This approach requires far less experimental input than the unsteady model.

(5). Semi-Analytical Model: Lever & Weaver [1982, 1986a, b], Yetsir & Weaver [1992, 1993a,b].

The unsteady continuity and momentum equations are used to derive the fluctuating fluid forced induced by tube motion. It is essentially an unsteady analytical model, requiring relatively little experimental input. The agreement of the model with experimental data appears quite good given the numerous approximations made. The objective of this chapter is to improve this model in several aspects, including its extension to multi-span tube arrays.

7.2 Yetisir and Weaver's Model

The theoretical model based on first principles was initially developed by Lever and

Weaver [1982, 1986]. Yetisir and Weaver [1993] extended it by introducing a disturbance decay function and multiple flexible tubes. Only a few details of Yetisir and Weaver's model that are relevant to the present modifications will be presented here.

There are four standard types of tube array geometry typically used in heat exchangers, as shown in Figure 7.1. The basic concept of this model is the same for all arrays. The differences in array geometry only affect the experimental parameters used in the model.

7.2.1 Basic Model Concept

The concept of "wavy wall" streamtubes is introduced in this model, as shown in Figure 7.2 for a parallel triangular array. The curvilinear coordinate s is used to represent the flow

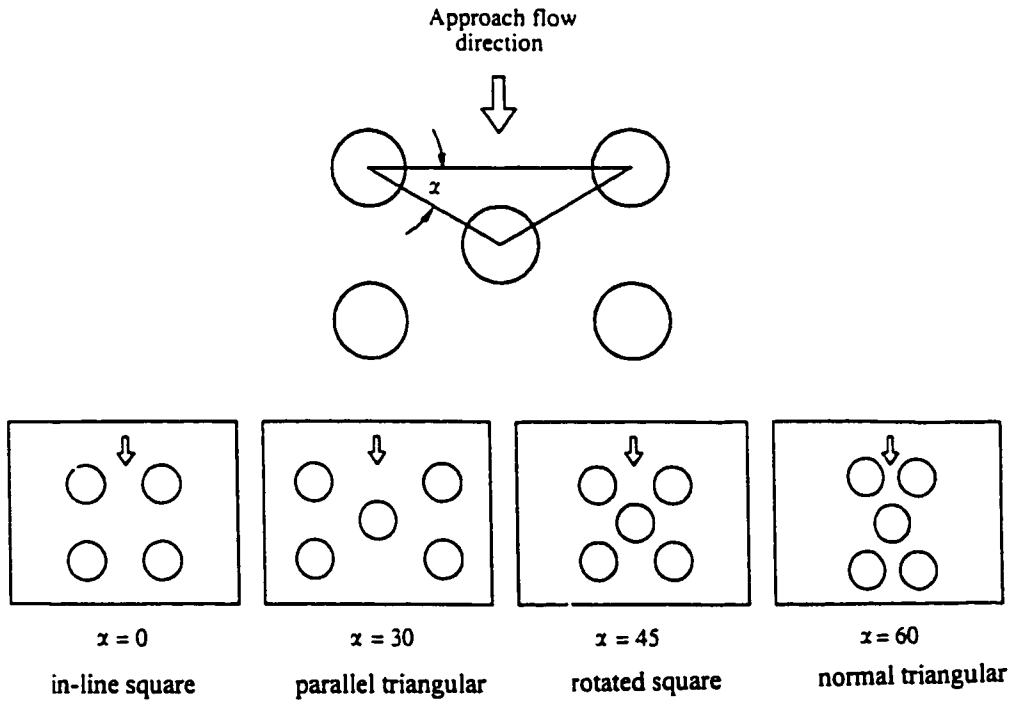

Figure 7.1 Four standard types of tube array geometry

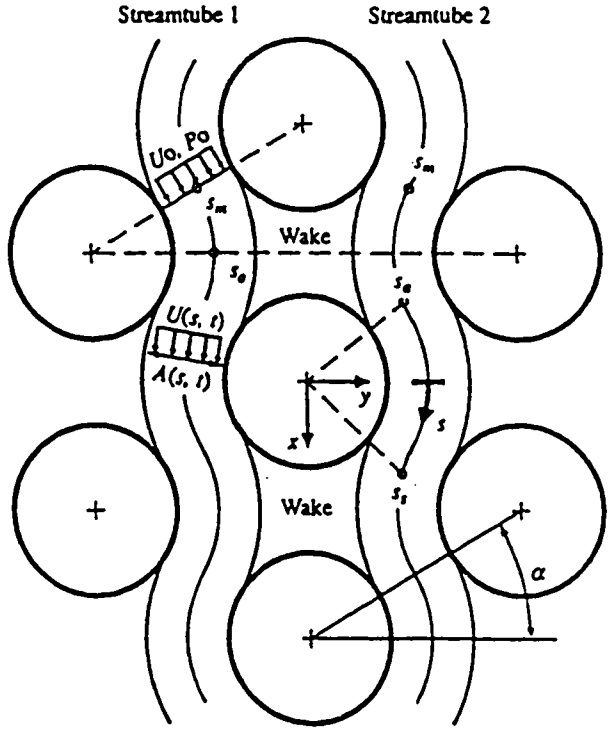

Figure 7.2 Streamtube pattern and curvilinear coordinate (Yetisir and Weaver, 1993)

path. The mean area of the streamtube is assumed to be constant over the entire length and is determined by the minimum gap area A_0 at location of $-s_1$

$$A_0 = \min(P\cos\alpha - d/2 \ , \ P - d) \tag{7-1}$$

The instantaneous streamtube area A(s,t) will change due to the tube vibration. A(s,t) consists of two terms: a mean component A_0, and a fluctuating component a(s,t)

$$A(s,t) = A_0 + a(s,t) \tag{7-2}$$

The same concept applies to velocity and pressure changes, which are caused by such area perturbations

$$U(s,t) = U_0 + u(s,t), \qquad P(s,t) = P_0 + p(s,t) \tag{7-3}$$

However, at a cross-section far enough upstream, say s_1, the perturbation will disappear and the velocity and pressure will be constant at values U_0 and P_0, respectively. The stream tube attaches to the flexible tube at $s = s_a$, and separates at $s = s_s$. And f(s) is an artificial decay function which takes account of the area perturbation decay from the flexible tube location to the upstream point. This will be discussed in detail later.

The effects of tube motion cannot be detected instantaneously by the entire tube array at each point of *s*, as would occur for an ideal incompressible fluid. Hence, a phase function $\phi(s)$ is introduced analytically to account for the delay in propagation of disturbances. Therefore, the upstream perturbation function a(s,t) can be expressed as

$$a(s,t) = a(s_m,t)f(s)e^{i\varphi(s)} \tag{7-4}$$

$a(s_m, t)$ is the area perturbation at the minimum gap. It is a function of tube geometry, which will be defined in the following section.

7.2.2 Continuity, Momentum and Pressure Forces

Applying the continuity equation along a streamtube

$$\frac{\partial}{\partial t}A(s,t) + \frac{\partial}{\partial s}[A(s,t)U(s,t)] = 0 \qquad (7\text{-}5)$$

Equations of (7-2) and (7-3) are substituted into (7-5), with the assumption of a harmonic disturbance frequency ω, this equation is then integrated along the coordinate s, from the entrance $s = s_i$ to exit $s = s_e$. Then eliminating steady-state and higher order terms and normalizing

$$\frac{1}{U_r}\frac{\omega}{\omega_n}\int_{s_i}^{s_e}\frac{\partial a^*(s^*,t^*)}{\partial t^*}ds^* + l_0^* A_0^*[u^*(s_e^*,t^*) - u^*(s_i^*,t^*)] + l_0^*[a^*(s_e^*,t^*) - a^*(s_i^*,t^*)] = 0 \qquad (7\text{-}6)$$

where $U_r = U_0/\omega_n l_0$ is the reduced velocity,

ω_n is the tube natural frequency in still fluid,

ω is the complex frequency of vibration

$l_o = 2s_1$ (s_1 is the distance from the vibrating tube to a point where the pressure disturbance is assumed negligible)

and $t^*=\omega t$, $a^*(s,t) = a(s,t)/d$, $l_0^* = l_0/d$, $A_0^* = A_0/d$, $u^*(s,t)=u(s,t)/U_0$, $s^*=s/d$, $p^*(s,t)=p(s,t)/P_0$

Following a similar procedure, the momentum equation can be written as

$$\frac{\omega}{\omega_n}l_0^* U_r\int_{s_i}^{s_e}\frac{\partial u^*(s^*,t^*)}{\partial t^*}ds^* + \frac{\omega}{\omega_n}\frac{l_0^*}{A_0^*}U_r\int_{s_i}^{s_e}\frac{\partial a^*(s^*,t)}{\partial t^*}ds^* + [2l_0^* u^*(s_i^*,t^*)+\frac{l_0^*}{A_0^*}a^*(s_i^*,t^*)]l_0^* U_r^2 + [2l_0^* u^*(s_e^*,t^*)+\frac{l_0^*}{A_0^*}a^*(s_e^*,t^*)]l_0^* U_r^2 = -p^*(s_i^*,t^*) - p^*(s_e^*,t^*) \qquad (7\text{-}7)$$

The pressure forces acting on the tube can be found by integrating the pressure term over the area of the flow attachment, $s_a^* \le s \le s_s^*$

$$F_x^* = \int_{s_a^*}^{s_s^*} p^*(s^*,t^*)\sin[\beta(s^*)]ds^*, \qquad F_y^* = \int_{s_a^*}^{s_s^*} p^*(s^*,t^*)\cos[\beta(s^*)]ds^* \tag{7-8}$$

where $\beta(s^*) = 2s^*/Pr$ is the angle of the normal vector on the flow attachment surface. (In Yetisir & Weaver's paper [1993], $\sin[\beta(s^*)]$ was mistakenly used for F_y^*, $\cos[\beta(s^*)]$ for F_x^*, which should affect the final result, at least quantitatively.)

The only parameters depending on experimental input are the attachment and separation points. Those data can be approximated from flow visualization studies of Weaver & Abd Rabbo [1985, 1986], and Scott [1987]. The four basic tube array patterns can be categorized into two groups:

Table 7.1 Experimental parameters used in the model calculation [Yetsir & Weaver, 1993]

Tube pattern		α	A_0^*	s_1^*	β_1	β_2
Group 1	In-line square	0°	Pr - 1	$Pr \cdot N_{row}$	10°	10°
	Parallel triangular	30°		$Pr \cdot \alpha \cdot N_{row}$	40°	10°
	Rotated square (Pr≤1.7)	45°			75°	15°
Group 2	Rotated square (Pr>1.7)	45°	Pr cos α-	$Pr(\alpha+\sin\alpha)/2 \cdot N_{row}$	85°	15°
	Rotated triangle	60°	0.5		85°	15°
$l_0^* = 2\,s_1^*$, $s_a^* = -\beta_1/2$, $s_s^* = \beta_2/2$, $N_{row} = 1.5$						

7.2.3 Equation of Motion

The flexible tube is assumed to have simple harmonic motion in two-degrees-of-freedom with the same natural frequency

$$\begin{aligned} m\ddot{x}+c\dot{x}+kx &= F_x a_1(s_m,t)+F_x a_2(s_m,t) \\ m\ddot{y}+c\dot{y}+ky &= F_y a_1(s_m,t)-F_y a_2(s_m,t) \end{aligned} \tag{7-9}$$

where $a_1(s_m, t)$ and $a_2(s_m, t)$ are the area perturbations of streamtubes 1 and 2 at the minimum gap, respectively. They are determined by the tube geometry. For Group 1 tube patterns

$$\begin{aligned} a_1(s_m,t) &= x(t)\sin\alpha - y(t)\cos\alpha \\ a_2(s_m,t) &= x(t)\sin\alpha + y(t)\cos\alpha \end{aligned} \tag{7-10}$$

For Group 2 tube arrays

$$a_1(s_m,t) = -\frac{1}{2}y(t), \qquad a_2(s_m,t) = \frac{1}{2}y(t) \tag{7-11}$$

A phase difference exists between x (streamwise) and y (transverse) directions. The solution can be described as

$$y(t) = Ye^{i\omega t}, \qquad x(t) = Xe^{(i\omega t+\psi)} \tag{7-12}$$

Based on Equation (7-12), the equations of motion in two directions are uncoupled and, therefore, the phase relation is irrelevant to the solution. The equations in both directions can be solved independently.

7.2.4 Characteristic Equation

Many studies have shown that instability normally occurs first in the transverse direction. The characteristic motion equation in the transverse direction can be obtained by substituting the appropriate terms into the second equation of (7-9)

$$\frac{m}{\rho d^2} = \frac{F_y^*(U_r, \frac{\omega}{\omega_n})}{1-(\frac{\omega}{\omega_n})^2+i\frac{\delta}{\pi}(\frac{\omega}{\omega_n})}, \qquad F_y^* = 2l_0^* U_r \cos\alpha F_y^*(s) = F_R^*(U_r, \frac{\omega}{\omega_n}) + iF_I^*(U_r, \frac{\omega}{\omega_n}) \tag{7-13}$$

where m is the tube mass per unit length including added mass, ρ is the fluid density, d is the tube diameter, δ is the logarithmic decrement of damping, and F_y is the total fluid force per unit length acting on the tube in the transverse direction, which is a function of frequency ratio and the reduced velocity, $U_r = U_0/(f_n d)$. The latter is related to the reduced pitch velocity, $U_f = U_p/(f_n d)$, by the following relationship.

$$U_r = \frac{U_p}{f_n d} \frac{1}{l_0^* A_0^*} \frac{\cos\alpha}{2\pi} (Pr-1) \tag{7-14}$$

where U_p is the pitch velocity. This relation is derived from the array geometry and flow continuity relationship between the minimum gap velocity, U_0, and the pitch velocity, U_p = [Pr/(Pr-1)]U_∞, where U_∞ is the free stream velocity.

In general, $\omega = \omega_R + \omega_I$. Here the real part, ω_R, represents the oscillation frequency, whereas the imaginary part, ω_I, represents the exponential decay or growth of the oscillation amplitude. There are two conditions which have meaningful physical explanations, depending on whether ω_I is negative or positive, respectively.

(1). $\omega_R \neq 0$, ω_I changes from "+" to "-", the tube changes from asymptotically stable to dynamically unstable.

(2). $\omega_R = 0$, $\omega_I < 0$, the tube becomes statically unstable (divergence).

A necessary condition for the transition to dynamic instability is that $\omega_R \neq 0$, and $\omega_I = 0$. This condition is used in the calculation in order to obtain a lowest reduced velocity U_f at given fluid and structure parameters, i.e., ω/ω_n, $m/\rho d^2$, and δ. However, it is rather difficult to conduct this procedure in Y-W model, because the fluid force is a complicated function of U_f, and can only be solved numerically. In practice, a reverse procedure may be performed. Since the fluid force has a real part and an imaginary part, the characteristic equation can be solved by separating the real and imaginary parts

$$\frac{\omega}{\omega_n} = -\frac{b}{2} + \left(\frac{b^2}{4} + 1\right)^{0.5}, \qquad b = \frac{\delta F_R}{\pi F_I}$$
$$\frac{m}{\rho d^2} = \frac{\pi F_I}{\delta \dfrac{\omega}{\omega_n}} \tag{7-15}$$

In the original Y-W model, an iteration procedure was applied to solve the frequency ratio, $\omega_r = \omega/\omega_n$, and the mass ratio, $m/\rho d^2$, at a given reduced velocity, U_f. Assuming a frequency ratio ω/ω_n, say 1.0, and a given U_f, we can compute first the fluid force F_y, then use equation (7-15) to solve $m/\rho d^2$ and ω/ω_n. If the latter is different from the original assumed value beyond a reasonable margin, the computation is repeated by updating the ω/ω_n value.

7.2.5 Phase and Decay Functions

An artificial decay function f(s*) is introduced to take account of the area perturbation

decay from the central tube. It has not been possible to determine this decay function experimentally. On the other hand, f(s*) should satisfy the following boundary conditions due to physical constraint:

$f(s^*) = 1.0$, at tube $s_a^* \le s \le s_s^*$, (no decay along tube contact region).

$f(s^*) = 0$, as $s^* \to \infty$, (negligible disturbance at large distance from tube).

The Y-W model proposed a decay function in the form

$$f(s^*) = \frac{1}{1 + Bs^{*n}} \qquad n = integer \ (=10) \tag{7-16}$$

Here, B is a constant obtained from boundary conditions.

In Y-W model, the time delay between the tube motion and the resulting fluid force was expressed by a phase function $\phi(s^*)$

$$\varphi(s^*) = \frac{1}{U_r} \frac{s^* - s_a^*}{s_1^* - s_a^*} \tag{7-17}$$

7.2.6 Equations of Motion for Multiple Flexible Tubes

The central and four neighboring tubes were considered by Y-W model in the calculation of the central tube instability, i.e., tubes 1 - 5 inclusive as shown in Figure 7.3. The fluid forces acting on each tube within the 5-flexible-tube-cell are found by superposition of the motion of each individual tube, and yield a 5 x 5 matrix relating the forces on the 5 flexible tubes to the displacement of those tubes. The matrix was expressed as:

$$\begin{Bmatrix} F_{y_1} \\ F_{y_2} \\ \{F_{y_3}\} \\ F_{y_4} \\ F_{y_5} \end{Bmatrix} = \begin{bmatrix} C_c & -C_u & -C_d & -C_u & -C_d \\ -C_d & C_c & 0 & 0 & 0 \\ -C_u & 0 & C_c & 0 & 0 \\ -C_d & 0 & 0 & C_c & 0 \\ -C_u & 0 & 0 & 0 & C_c \end{bmatrix} \begin{Bmatrix} y_1^{\cdot} \\ y_2^{\cdot} \\ \{y_3^{\cdot}\} \\ y_4^{\cdot} \\ y_5^{\cdot} \end{Bmatrix} \tag{7-18}$$

where C_y is the fluid force coefficient in y direction, which is calculated by equation (7-13). The subscripts y=u (upstream), c (central), d (downstream) represent the position of the vibrating tubes generating the force. A few assumptions are made to simplify the matrix and allow solution for F_{y1}, which is our prime interest.

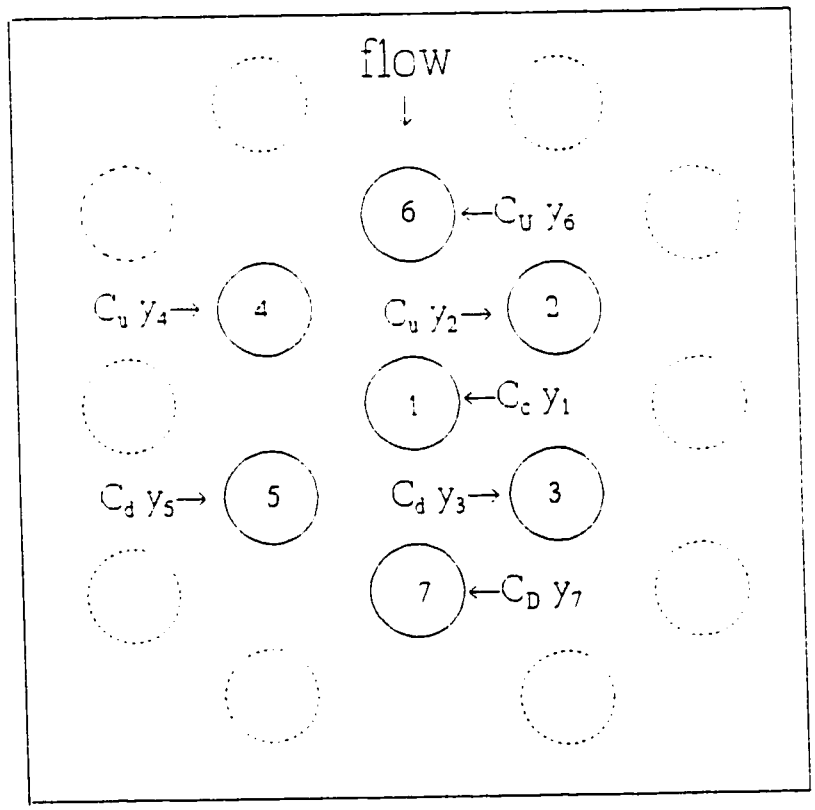

Figure 7.3 Forces acting on each tube due to the vibration of tube #1

(In Y-W's 5-tube-cell model, tubes #6 & #7 were not included in the analysis)

(1). The motion of the adjacent tubes in a row are equal in magnitude and are in-phase, i.e., $y_2^* = y_4^*$, $y_3^* = y_5^*$.

(2). There is a 180° phase difference between tubes in a row and the tubes two rows upstream and downstream. i.e. $y_3^* = -y_2^*$. This least stable mode leads to the lowest critical velocity [Price & Paidoussis, 1985].

Assuming $y_2^* = y_1^* \exp(i\psi)$, the constrained equation for the 5-tube-cell array is reduced to a single equation

$$F_{yl} = [C_c - 2(C_d - C_u)\exp(i\psi)]y_1^* \tag{7-19}$$

Equation (7-19) is used to calculate the stability threshold of the central flexible tube. The calculation procedure for the single flexible tube mentioned above applies.

Yetisir-Weaver's model overcomes some deficiencies of the previous Lever-Weaver model. The most significant improvements include, first, integration of the dynamic and static stabilities into one single model by introducing a decay function and frequency ratio, and, second, taking account of the effects of neighboring flexible tube motion. The calculations agree with experimental results reasonably well.

7.3 Extensions of Yetisir-Weaver's Model

Efforts have been made in this study to improve Y-W's model as follows.

7.3.1 An Explicit Form of the Instability Equation

While the Y-W model was an improvement over the L-W model, it has to be solved numerically, whereas, L-W's has the advantage of having an explicit instability expression.

Thus, the Y-W model is more difficult to use.

In the Y-W model, the decay function takes the form of equation (7-16). This makes it impossible to conduct an analytical integration of the continuity and momentum equations. Therefore, a simpler linear decay function is suggested here as

$$f(s) = \frac{s - s_1}{s_a - s_1}, \quad s_1 \le s \le s_a$$
$$f(s) = 1, \qquad s_a \le s \le s_s \tag{7-20}$$

For simplicity, the superscript "*" is neglected in the following sections. The original and modified decay functions satisfy the same boundary conditions and are both plotted in Figure 7.4. It will be shown later that the difference in final results is very small, but this new form enables us to obtain an analytical expression from the area perturbation function integrations.

Because the perturbation decay and time delay exist only in the path of the streamtube, two sets of area perturbation equations for the parallel triangular tube array are applied as

$$a_1(s,U_r) = f(s)e^{i\varphi(s,U_r)}\cos\alpha, \quad \varphi(s,U_r) = \varphi(U_r)\frac{s - s_a}{s_1 - s_a} \quad s_1 \le s \le s_a$$
$$a_2 = \cos\alpha, \quad f(s) = 1.0, \quad \varphi(s,U_r) = 0 \quad s_a \le s \le s_s \tag{7-21}$$

For other tube patterns, the equations are similar except for the $\cos\alpha$ term.

Equation (7-21) is substituted into the continuity equation (7-6) to find the unsteady flow velocity

$$
\begin{aligned}
u_1(s,U_r) &= \frac{1}{l_0 A_0}[l_0 a_1(s,U_r) + \frac{\omega_r i}{U_r}\int_{s_1}^{s} a_1(s,U_r)ds] \\
&= A_1[l_0 a_1(s,U_r) + \frac{\omega i}{U_r} A_2(s,U_r)], \qquad s_1 \le s \le s_a \\
u_2(s,U_r) &= -\frac{1}{l_0 A_0}\{l_0 a_1(s,U_r) + \frac{\omega_r i}{U_r}[\int_{s_1}^{s_a} a_1(s,U_r)ds + \int_{s_a}^{s} a_2 ds]\} \\
&= A_1\{l_0 a_1(s,U_r) + \frac{\omega_r i}{U_r}[A_2(s_a,U_r) + a_2(s-s_a)]\}, \qquad s_a \le s \le s_s
\end{aligned}
\tag{7-21}
$$

where A_1, A_2...are coefficients, most of them being functions of U_r, and listed in Appendix C.

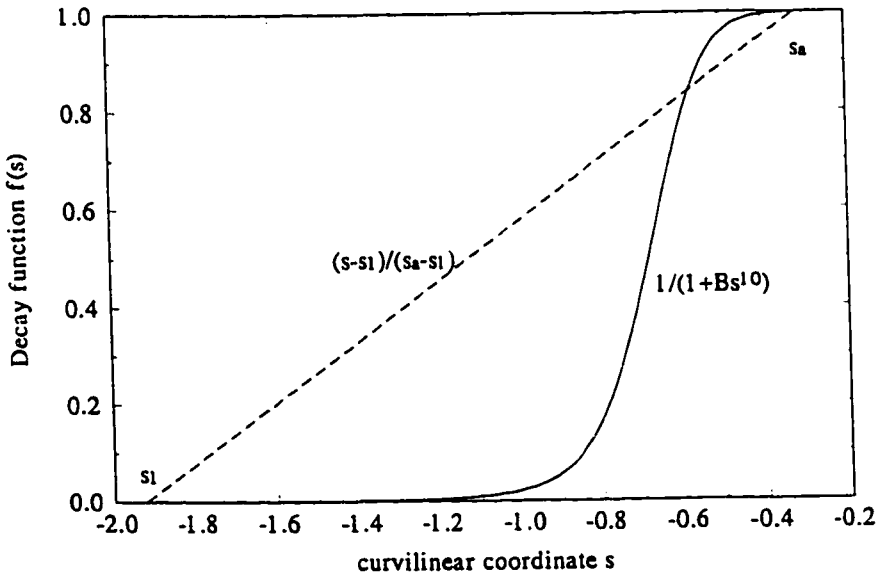

Figure 7.4 Area perturbation decay functions

Similarly, the unsteady pressure caused by tube motion is

$$p_2(s,U_r)=\omega_r l_0 U_r i[\int_{s_1}^{s_a} u_1(s,U_r)ds+\int_{s_a}^{s} u_2(s,U_r)ds]+\frac{l_0 U_r \omega_r i}{A_0}[\int_{s_1}^{s_a} a_1(s,U_r)ds+\int_{s_a}^{s} a_2 ds]$$
$$+[2l_0 u_2(s,U_r)+\frac{l_0}{A_0}a_2]l_0 U_r^2 \qquad s_a \le s \le s_s$$
$$=-\{\omega l_0 U_r i[B_1(U_r)+B_2(s,U_r)]+\frac{l_0 U_r \omega_r i}{A_0}B_3(s,U_r)+[2l_0 u_2(s,U_{r,s})+\frac{l_0}{A_0}a_2]U_r^2 l_0\} \tag{7-22}$$

The force acting on the tube is obtained by substituting equation (7-22) into (7-8)

$$F_y=-2l_0 U_r \cos\alpha \int_{s_a}^{s_s} p_2(s)\cos(\frac{2s}{Pr})ds \tag{7-23}$$
$$= -2l_0 U_r \cos\alpha[C_1(U_r)+C_2(U_r)+C_3(U_r)+C_4(U_r)+C_5(U_r)]$$

where C_1, C_2... are functions of U_r, and are listed in Appendix C.

The fluid force F_y is substituted into the characteristic equation (7-15) to solve the mass ratio $m\rho/d^2$ for a given U_r and damping δ. The above formulas have been derived for a parallel triangular array. For normal (rotated) triangular and rotated square (Pr >1.7), F_y has the same form, except that it is divided by $2\cos\alpha$, which is due to the different formula for the minimum gap perturbation area function $a(s_m,t)$ according to equations (7-10) and (7-11). Of course, other experimental parameters must be inserted according to Table 7.1.

The solution for a single flexible tube in a rigid parallel triangular tube array with Pr=1.47 is shown in Figure 7.5. The two different decay functions are used in the calculation while keeping other parameters the same. The difference between the two solutions is insignificant. Therefore, the linear decay function permits an explicit formula for instability

while giving essentially the same stability threshold.

7.3.2 The Inclusion of Upstream and Downstream Tubes

In Y-W model, five flexible tubes are included in each unit cell, which is sufficient for the in-line square tube array, and possibly also for the normal triangular and rotated square arrays. But for parallel triangular tube arrays, the downstream and especially upstream tube must have significant effects on the central tube because of their close proximity. The extended tube cell is shown in Figure 7.3 (including tubes #6 & #7). The forces acting on each tube can be written as

$$\begin{Bmatrix} F_{y_1} \\ F_{y_2} \\ F_{y_3} \\ F_{y_4} \\ F_{y_5} \\ F_{y_6} \\ F_{y_7} \end{Bmatrix} = \begin{bmatrix} C_c & -C_d & -C_u & -C_d & -C_u & C_U & C_D \\ -C_d & C_c & C_D & 0 & 0 & -C_u & 0 \\ -C_u & C_U & C_c & 0 & 0 & 0 & -C_d \\ -C_d & 0 & 0 & C_c & C_D & -C_u & 0 \\ -C_u & 0 & 0 & C_U & C_c & 0 & -C_d \\ C_D & -C_d & 0 & -C_d & 0 & C_c & 0 \\ C_U & 0 & -C_u & 0 & -C_u & 0 & C_c \end{bmatrix} \begin{Bmatrix} y_1^{\bullet} \\ y_2^{\bullet} \\ y_3^{\bullet} \\ y_4^{\bullet} \\ y_5^{\bullet} \\ y_6^{\bullet} \\ y_7^{\bullet} \end{Bmatrix} \qquad (7\text{-}24)$$

where subscripts "u, d" denote one row upstream and downstream tubes,

"c" denotes the central tube,

"U, D" denote two rows upstream and downstream tubes.

It is reasonable to assume the constraints of displacement of each tube in the tube cell are: $y_2^{\bullet} = y_4^{\bullet}$, $y_3^{\bullet} = y_5^{\bullet}$, $y_6^{\bullet} = y_7^{\bullet}$ and $y_2^{\bullet} = -y_3^{\bullet}$, based on the arguments made by Price and Paidoussis [1984]. Equation (7-24) can then be simplified to:

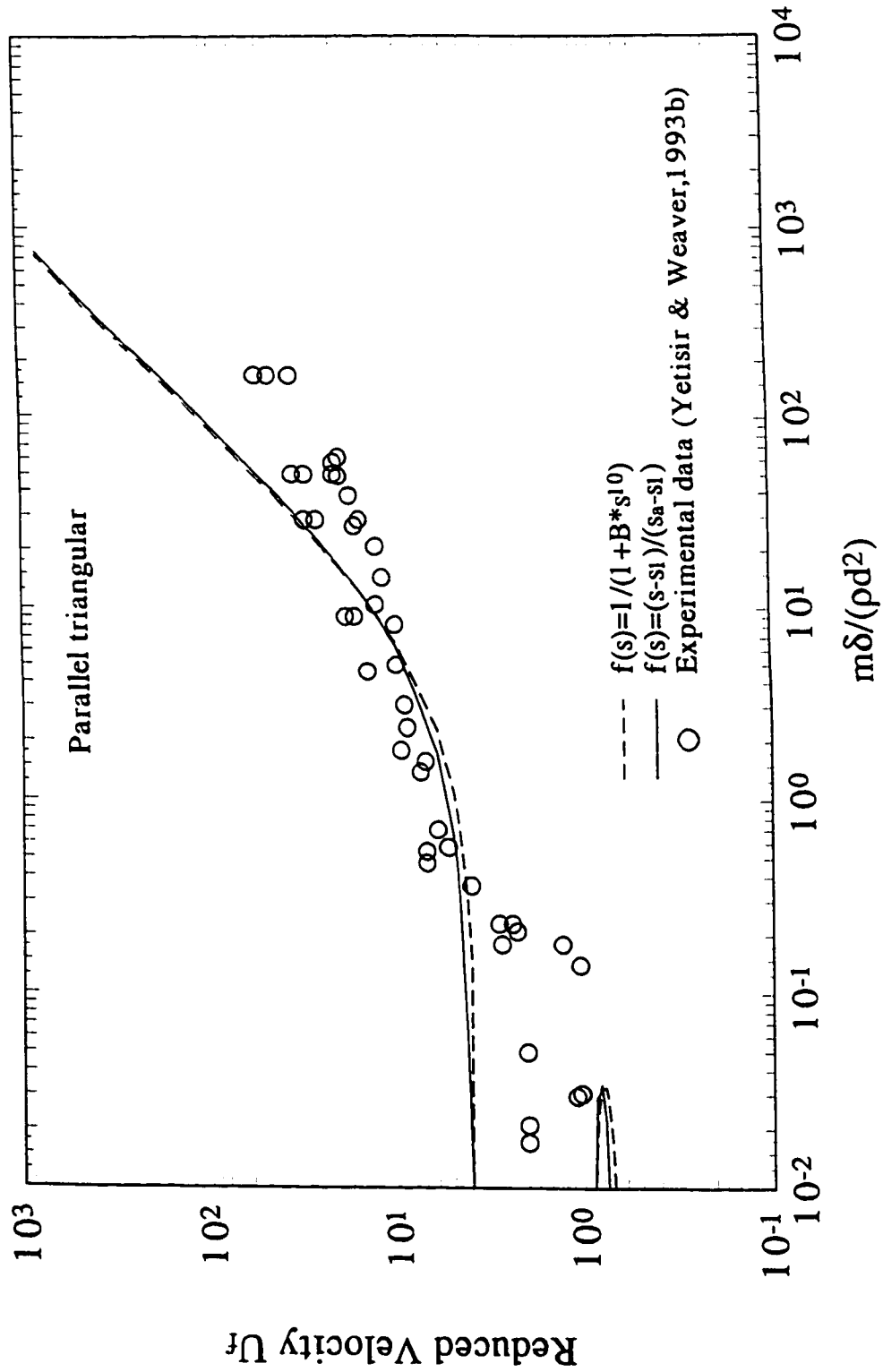

Figure 7.5 Stability prediction for a single flexible tube in a parallel triangular array, Pr=1.47

$$\begin{Bmatrix} F_{y_1} \\ F_{y_2} \\ F_{y_6} \end{Bmatrix} = \begin{bmatrix} C_c & -2(C_d-C_u) & C_D+C_U \\ -C_d & C_c-C_D & -C_u \\ C_D & -C_d & C_c \end{bmatrix} \begin{Bmatrix} y_1^* \\ y_2^* \\ y_6^* \end{Bmatrix} \tag{7-25}$$

y_1^* has a phase angle with y_2^* and y_6^*, i.e., $y_2^* = y_1^* \exp(i\psi_1)$, $y_6^* = y_1^* \exp(i\psi_2)$, respectively. Then the force acting on tube # 1 is

$$F_{y_1} = [C_c - 2(C_d - C_u)e^{i\psi_1} + (C_D + C_U)e^{i\psi_2}]y_1^* \tag{7-26}$$

By examining equation (7-15), the maximum value of the imaginary component of F_{y1} will give the minimum critical U_r, therefore the phase angles will be calculated by

$$\psi_1 = \tan^{-1}\frac{Re(C_d-C_u)}{Im(C_d-C_u)}, \quad \psi_2 = \tan^{-1}\frac{Re(C_D+C_U)}{Im(C_D+C_U)} \tag{7-27}$$

In Table 7.1, the distance from the central tube to where the pressure disturbance is assumed to be negligible, $s_1^* = 1.5N_{row}$. The inclusion of the two row upstream tube suggests the distance should be extended to $s_1^* = 2.5N_{row}$.

The results of the original 5-tube-cell and the modified 7-tube-cell calculations are shown in Figure 7.6, together with the experimental data referred in Yetisir and Weaver's papers [1993a,b]. Calculations were done in the transverse direction for a parallel triangular tube array with Pr = 1.47. The 5-tube-cell calculation has a slightly unconservative margin at many data points (there is a difference between the results of the present 5-tube-cell model and Y-W's 5-tube-cell results because that incorrect sinusoid functions were used in Y-W's calculation). The

7-tube-cell model's prediction is conservative for almost all the experimental data except for two data points at low mass damping parameters. At higher mass damping parameters, the curve fits the low data bound very well. In later analysis, it is shown that the curve also agrees well with Weaver's empirical correlation. It further confirms that in the stiffness-controlled range, the coupling between flexible tubes becomes more important. The stability predictions for both the transverse and streamwise directions respectively are shown in Figure 7.7. Over most of the mass damping parameter range, the boundary of the instability in the transverse direction is lower than that of the streamwise direction. Therefore, in the later analysis, only the instability in the transverse direction is investigated. In addition, it is interesting to notice that the multiple instability regions predicted by the 5-tube-cell disappear when using the 7-tube-cell model. In Figure 7.6, at $m\delta/\rho d^2 \approx 0.9$, there is a sudden drop of reduced velocity, similar to Weaver's empirical correlation at 0.3. This drop in reduced velocity is caused by the change of $-(C_d - C_u)$ and $C_D - C_U$ from the same sign to opposite ones, which suggests that the coupling mechanism could be different in the fluid-damping-controlled and fluid-stiffness-controlled ranges. The small lumps in the 7-tube-cell model and the multi-instability regions in the 5-tube-cell model in the low damping parameter range are caused by the unrealistically large value of the phase $\phi(U_r)$, which is discussed later. Such effects are much smaller if upstream and downstream tubes are included in the model.

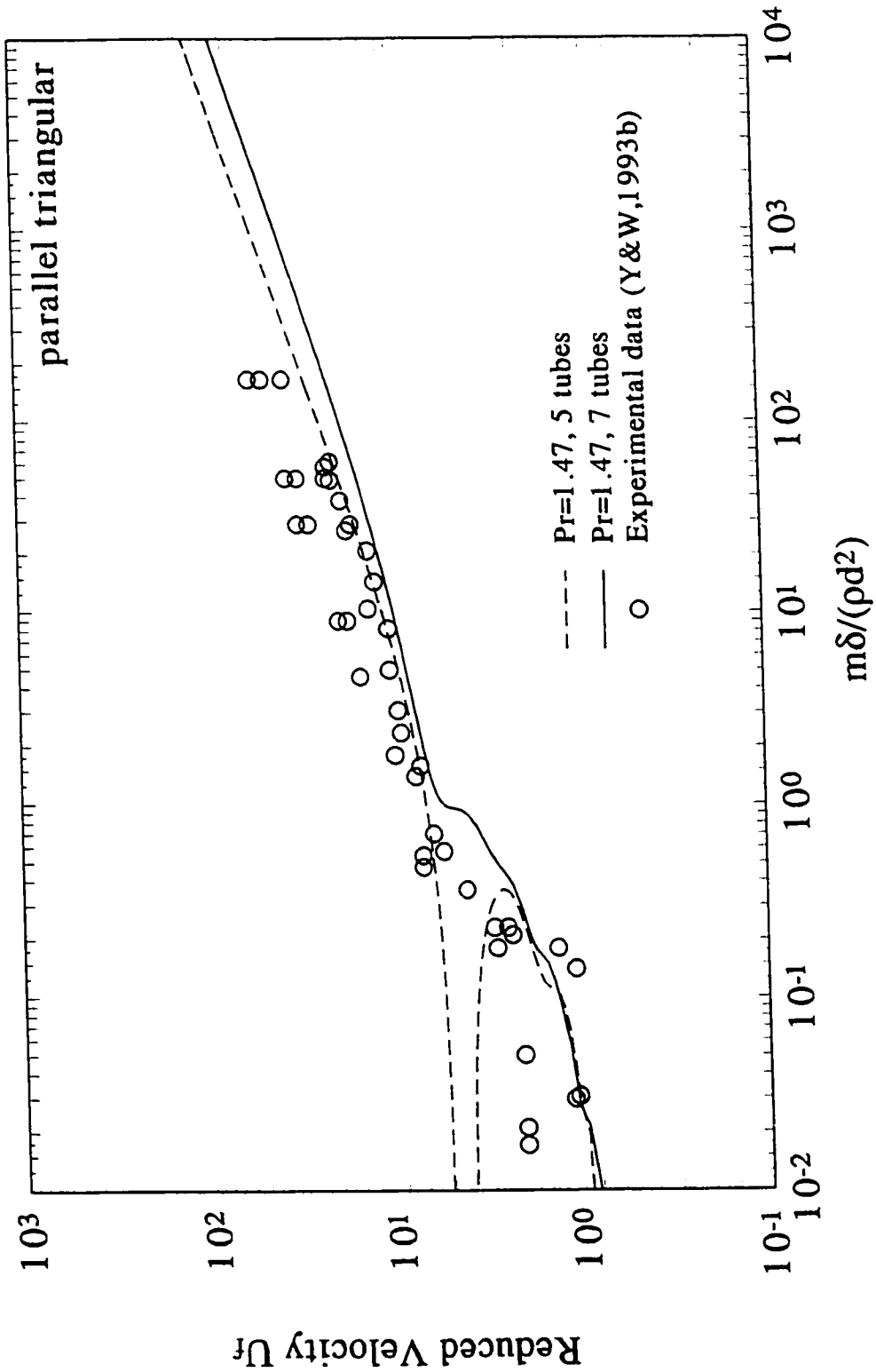

Figure 7.6 Stability prediction for parallel triangular tube array, Pr=1.47

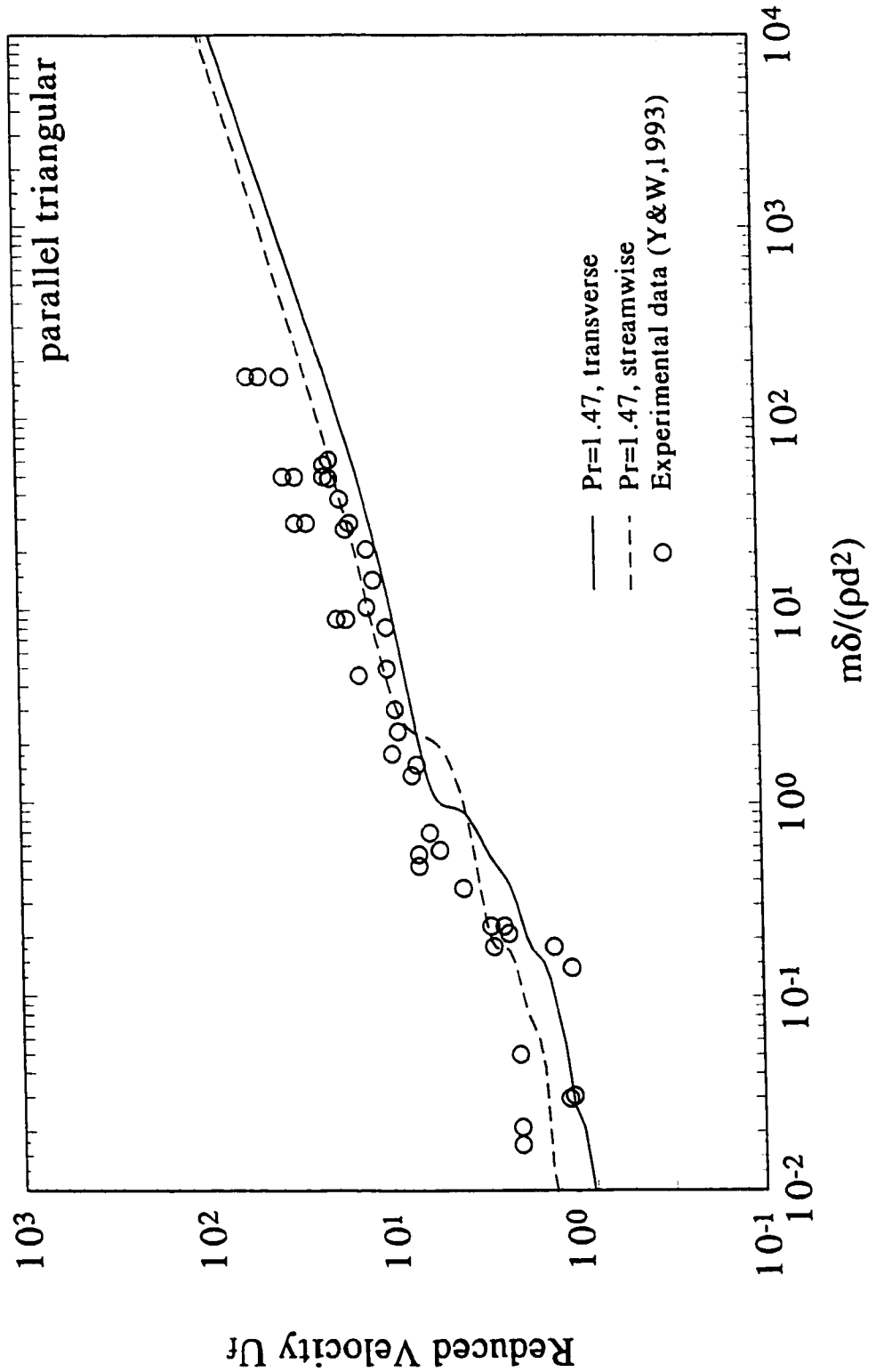

Figure 7.7 The comparison of stability predictions in transverse and streamwise directions, parallel triangular tube array Pr=1.47

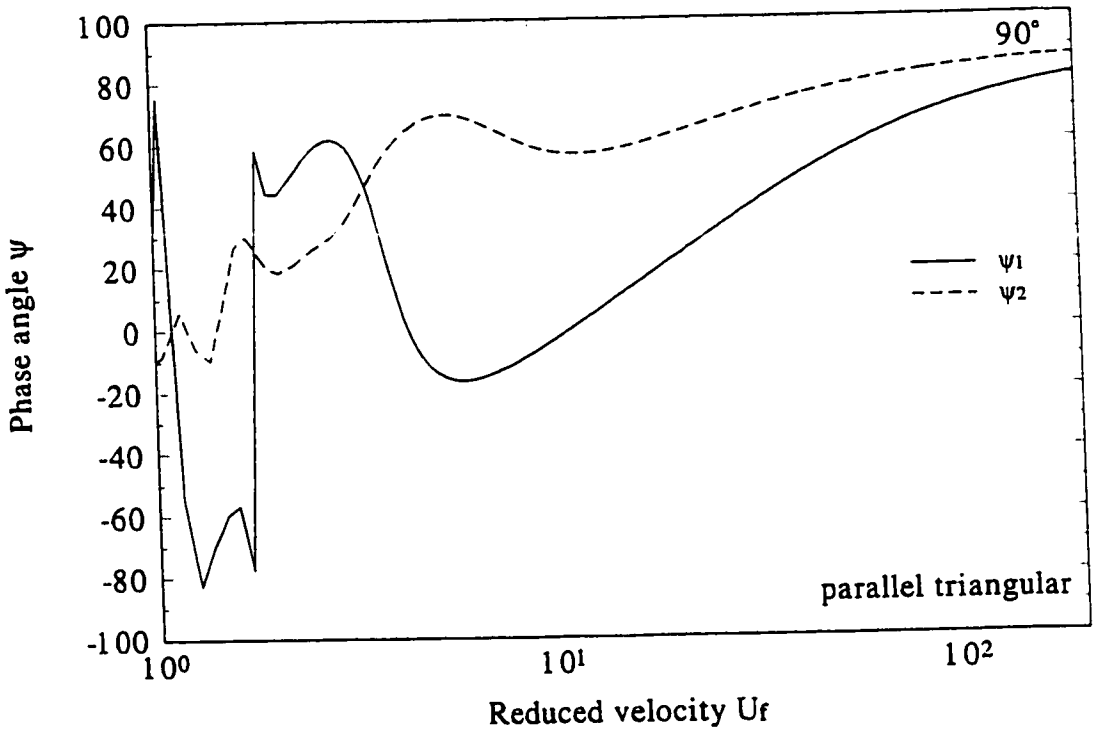

Figure 7.8 The relation of phase angle to reduced velocity U_f (parallel triangular, Pr=1.47)

The Figure 7.8 shows the change of phase angles ψ_1 and ψ_2 with U_f. At low U_f , the phase angles fluctuate between positive and negative values, again due to the large phase function value. With the increase of U_f, they both approach 90°.

The effects of pitch ratio are displayed in Figure 7.9 for the parallel triangular tube array. At low mass damping ratio, only the smallest pitch ratio (Pr = 1.2) tube array calculation has multiple instability regions. The critical reduced velocity increases with an increase in pitch ratio. With the increase of distance between the tubes, the interaction of the tubes tends to be reduced, which leads to higher critical reduced velocity. Weak coupling at the larger pitch ratio results in the single instability at the low mass damping ratios.

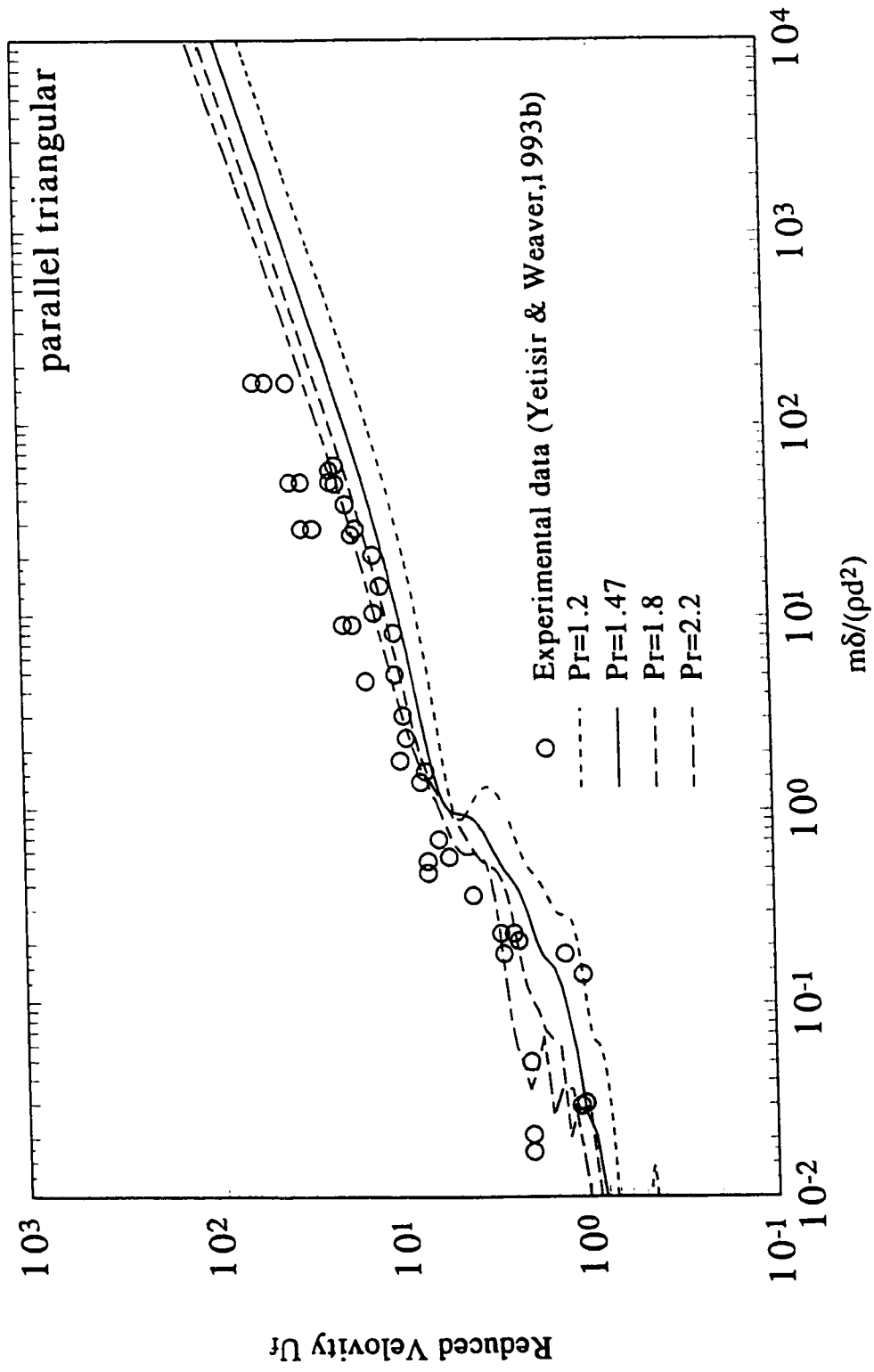

Figure 7.9 Effects of pitch ratio Pr on the stability (parallel triangular tube array)

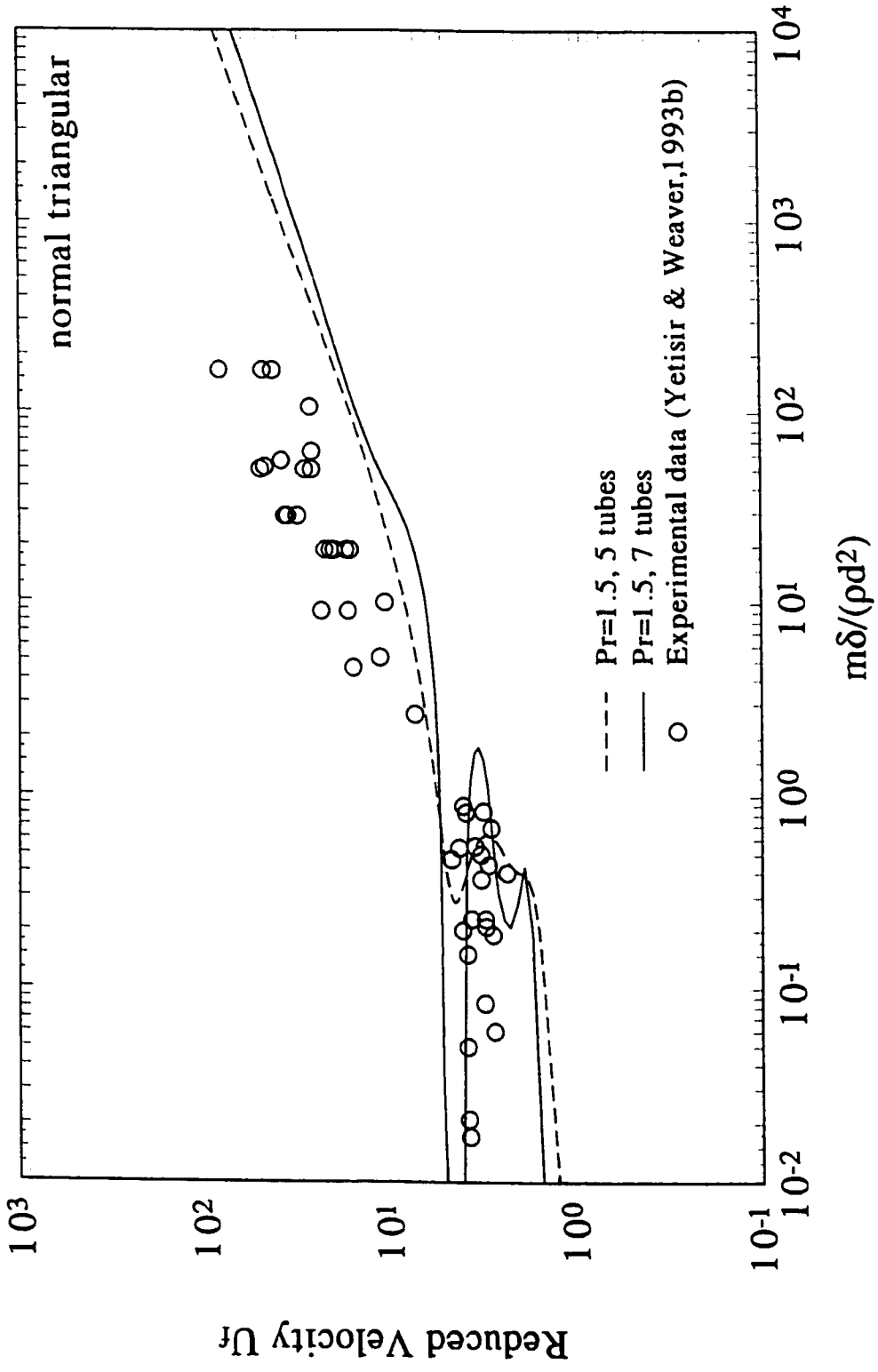

Figure 7.10 Stability prediction for normal triangular tube array, Pr=1.5

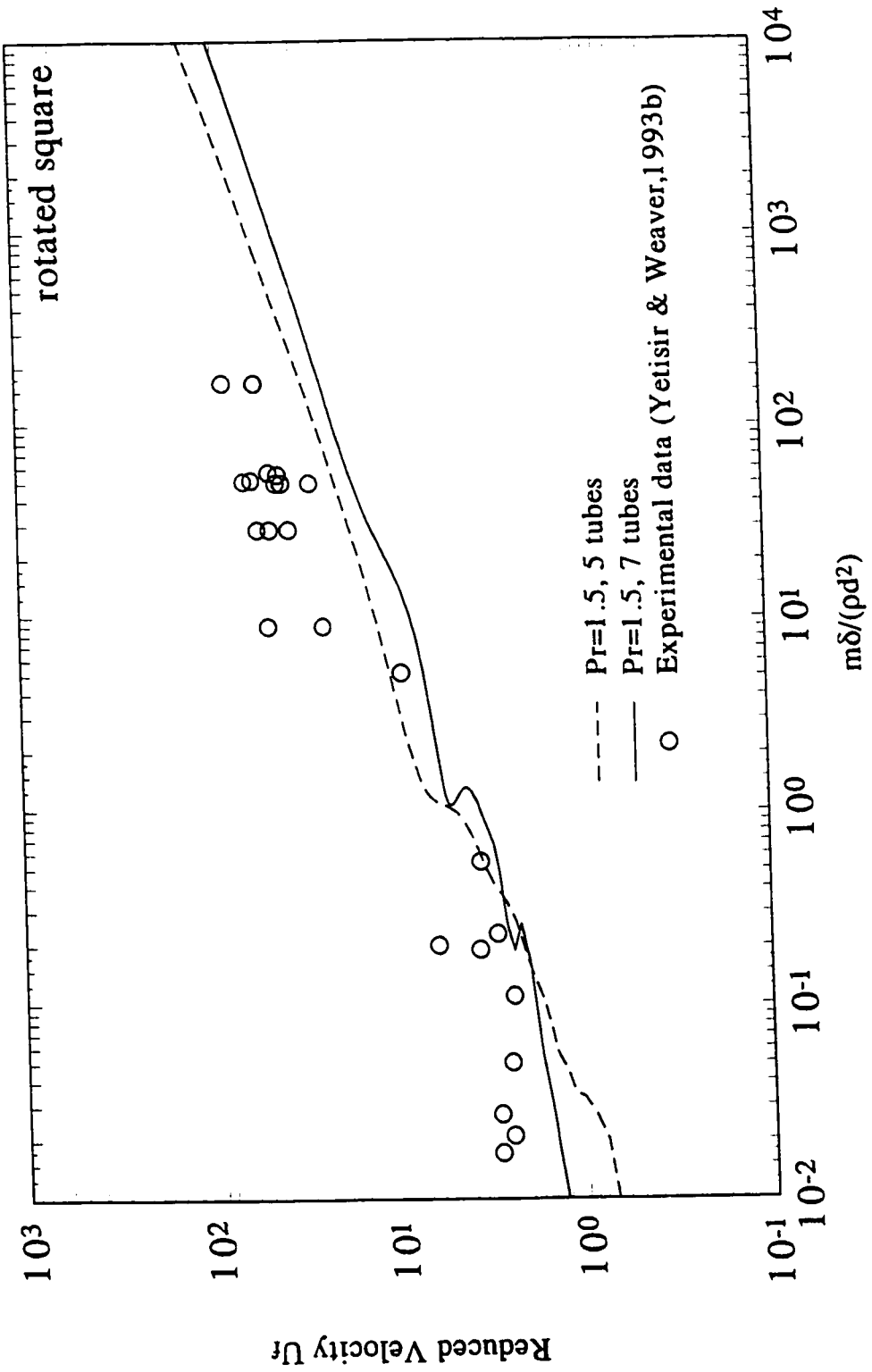

Figure 7.11 Stability prediction for rotated square tube array, Pr=1.5

The 7-tube-cell array model was also used to calculate the instability of the normal triangular and rotated square tube arrays. The results are shown in Figure 7.10 and 7.11, respectively. The inclusion of tubes two rows upstream and downstream in the mode does have some effects and appears to be slightly better at low mass damping parameter. As expected, because of the geometry of the these two types of tube array, the inclusion of tubes two rows upstream and downstream in the model may not be as important as for the parallel triangular tube arrays. Interestingly, the 7-tube-cell model reduces the stability threshold at high mass damping parameters while increases it at low mass damping parameters.

7.3.3 The Application to Multi-Span Tubes

In both L-W and Y-W models, the tubes, single or multiple, are considered as lumped masses. This is sufficient for full admission cross flow in single span tubes. However, as mentioned in previous chapters, modifications have to be made for the application of the model to multi-span and partial admission flow.

In a one-dimensional continuum, through normal coordinate transformation, the displacement of vibration v(x,t) can be expressed as a mode shape and time function

$$v(x,t) = \sum_{i=1}^{\infty} \varphi_i(x) y_i(t) \qquad (7\text{-}28)$$

By substitution of the displacement into the damped vibration equation with external force,

$$\sum_{i=1}^{\infty} m(x)\varphi_i(x)\ddot{y}_i(t) + \sum_{i=1}^{\infty} c(x)\varphi_i(x)\dot{y}_i(t) + \sum_{i=1}^{\infty} k(x)\varphi_i(x)y_i(t) = f(x,t) \qquad (7\text{-}29)$$

Multiplying by the mode shape function $\phi_i(x)$, integrating along the span length x, and applying

the orthogonality relationship together with the generalized mass and generalized forces leads to

$$M_n\ddot{y}_n(t) + c_n\int_0^L \varphi_n^2(x)dx\ \dot{y}_n(t) + \omega_n^2 M_n y_n(t) = F_n(t) \tag{7-30}$$

where the generalized mass

$$M_n = \int_0^L m(x)\varphi_n^2(x)dx \tag{7-31}$$

and the generalized force acting on the length of $l_1 \le x \le l_2$,

$$F_n(t) = \int_{l_1}^{l_2} \varphi_n(x) f(x,t)dx \tag{7-32}$$

If the mass is uniformly distributed along the span, the characteristic equation of equation (7-13) can be modified as

$$\frac{m\int_0^L \varphi^2{}_i(x)dx}{\rho d^2} = \frac{\overline{F}_y(U_r,\frac{\omega}{\omega_n})\int_{l_1}^{l_2} \varphi^2{}_i(x)dx}{1-(\frac{\omega}{\omega_n})^2+i\frac{\delta}{\pi}(\frac{\omega}{\omega_n})} \tag{7-33}$$

In the case of full admission, the integration of the force from l_1 to l_2 will be changed to 0 to L. Thus, the mode shape effects will be canceled from both sides of the equation. In the case of $\omega = \omega_n$, the equation (7-33) can be written as

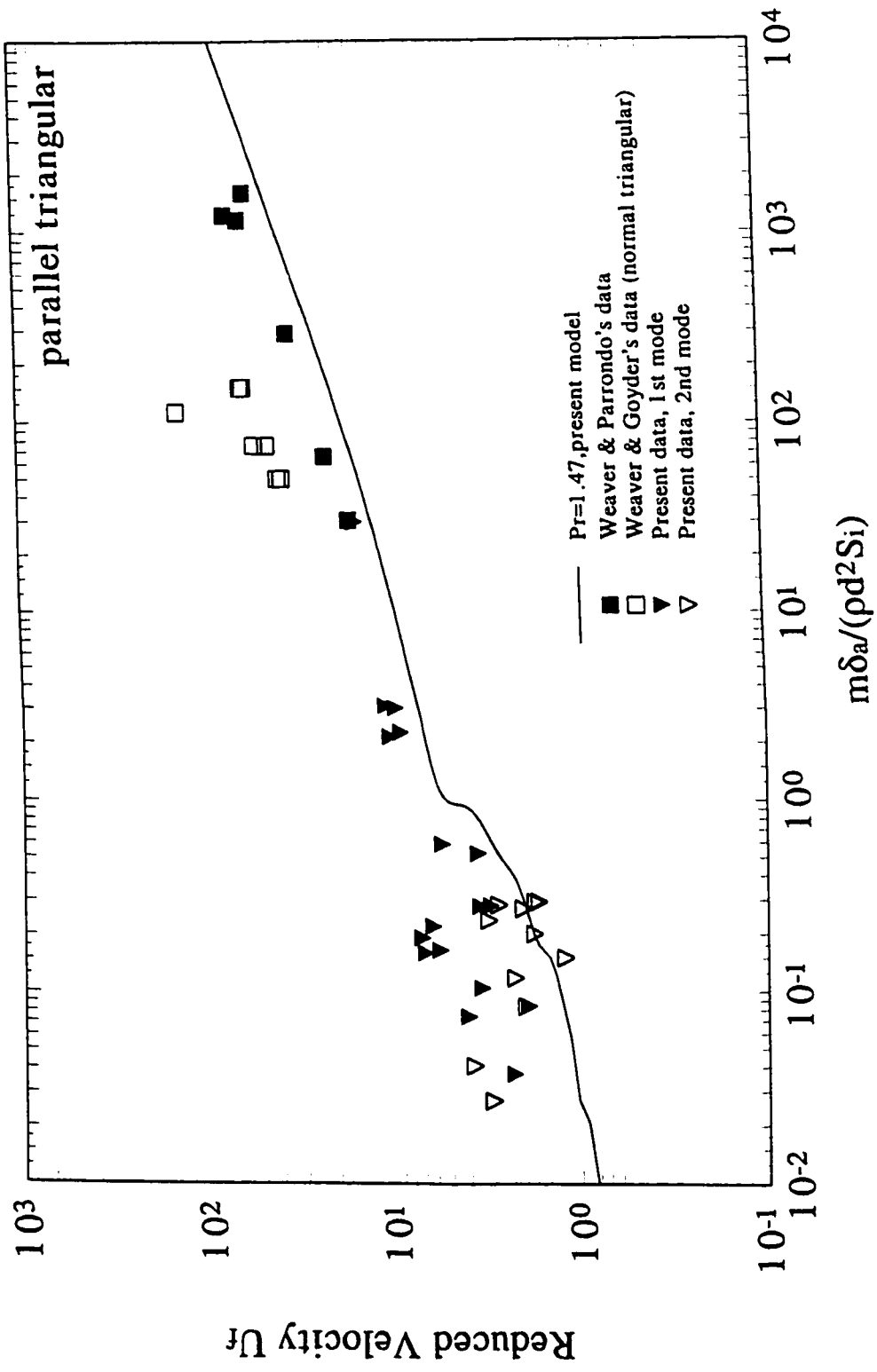

Figure 7.12 Stability prediction for multi-span parallel triangular tube array (Pr=1.47)

$$\frac{m\delta}{\rho d^2 S_i} = \pi Im(\overline{F}_y), \qquad where, \quad S_i = \frac{\int_{l_1}^{l_2} \varphi_i(x)^2 dx}{\int_0^L \varphi_i(x)^2 dx} \tag{7-34}$$

S_i is defined as the energy fraction factor, as mentioned in previous chapters. In general, $Im(F_y)$ is a polynomial function of reduced velocity U_f. At large mass damping parameters, the force function is proportional to the reduced velocity squared ($U_f = V_p/fd)^2$, thus, the equation is reduced to the modified Connor's equation.

The calculation of partial flow admission in the modified model only needs to take into account the effects of S_i. The stability curve is plotted as reduced velocity versus $m\delta/(\rho d^2 S_i)$. The comparison between the calculated and experimental results are shown in Figure 7.12 and Table 7.2. The predictions are conservative for most partial admission experimental data, except a few second mode points. One advantage of the present explicit expression for instability is that it enables us to solve for the critical reduced velocity at given mass damping ratio $m\delta/(\rho d^2)$, or mass damping energy factor $m\delta/(\rho d^2 S_i)$.

7.3.4 Effects of the Phase Function

In equation (7-21), the relation between phase angle and reduced velocity is expressed as $1/U_f$. Apparently, it is not reasonable that the phase lag is several cycles at low U_f.

Measurements done by Tanaka & Takahara [1980] are shown in Figure 7.13. Therefore, a new form of phase angle function was introduced based on this experimental data. It is interesting to note that the phase angle is of the order of zero for low values of reduced velocity and nearly 180° for high values of reduced velocity. The transition occurs around a value of

Table 7.2 The comparison of Weaver & Parrondo's test data [1991] and predictions by the present model

Case	$m\delta/(\rho d^2 S_t)$	Critical reduced velocity U_f	
		Measurement	Prediction
1	30.38	16.3	13.1
2	1602.0	55.9	44.1
3	1157.5	60.2	39.4
4	290.2	33.8	24.3
5	65.8	21.6	14.4
6	1227.6	71.2	40.3

V/fd ≈ 10, which is also about the value of reduced velocity at which the quasi-steady assumption becomes valid [Blevins, 1977]. While it is still artificial, at least this phase function now agrees in trend with experimental observations. It is written as

$$\varphi(U_r)=\frac{U_r^n}{1+U_r^n}\pi=\frac{aU_f^n}{1+aU_f^n}\pi, \qquad n=3 \text{ or higher integers}$$
$$a=\left[\frac{1}{l_0^* A_0^*}\frac{\cos\alpha}{2\pi}(Pr-1)\right]^n \tag{7-35}$$

Here, a is a constant from equation (7-14). The previous and proposed phase angle are both shown in Figure 7.14. The new phase function equals zero at low U_f and approaches π at higher U_f, similar to Figure 7.13. Calculations show that an increase of $n > 3$ has little effect on the stability calculation. This new phase function is substituted into the 7-cell-tube model, and results are shown in Figure 7.15. At high mass damping ratios, there is little difference between the two phase functions. However, only a single instability region is predicted by the new phase function. A large number of data at low mass damping ratio are not correctly

predicted by the model using the new phase function. It seems that a simple phase function is not sufficient to represent the complicated flow-structure interaction inside the tube bundles at low mass damping parameters. A more comprehensive approach should be made, such as [Paidoussis et al, 1996], which obtains the flow field parameters by solving the Navier-Stokes equations at low mass damping ratios.

7.3.5 The Comparison between the Theoretical Model, Semi-Empirical Model and Experimental Results of the Multi-Span Tube Arrays

As discussed in the previous chapter, Weaver and Fitzpatrick's semi-empirical model, i.e., equation (6-1-2),conservatively predicts all experimental critical reduced velocities of the present study and Parrondo et al's. Figure 7.16 shows the comparison between the present model, equation (7-33), and semi-empirical models. In this figure, because damping in air δ_a is used in defining the mass-damping-energy-factor MDE, the line representing Pettigrew's model does not apply for data points at small MDE_a range, say $MDE_a < 1$. For these data obtained in water tests, δ_w should be used, therefore, the MDE_w is much larger, those data points are shifted to right. Pettigrew's model is unconservative in this region, as concluded in Chapter 6. For the high MDE_a range, the slope of critical reduced velocity predicted by present 7-tube-cell model agrees well with Weaver and Fitzpatrick's semi-empirical model. Both of them predict the critical reduced velocity reasonably well not only for the full flow admission test data [Yetisir and Weaver, 1993], but also for the partial flow admission data (the rest of data points in the figure). There are several data points with small vibration amplitudes which fall below the theoretical model's prediction curve at small MDE_a. As mentioned in the previous section, the phase function used in the model for this range should be improved in the future.

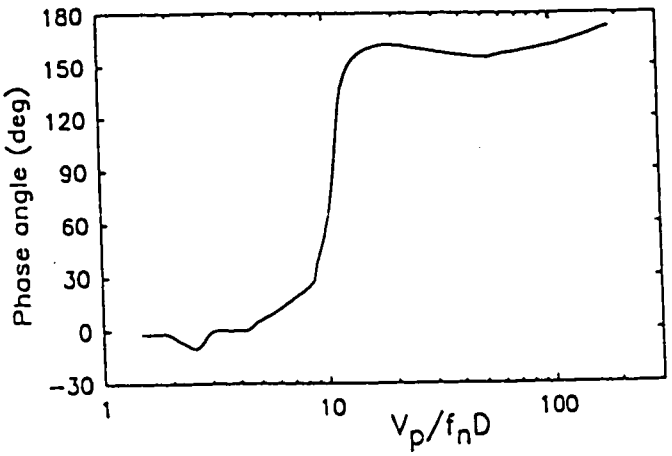

Figure 7.13 Phase angle between displacement and fluid force vs U_f [Tanaka & Takahara, 1980]

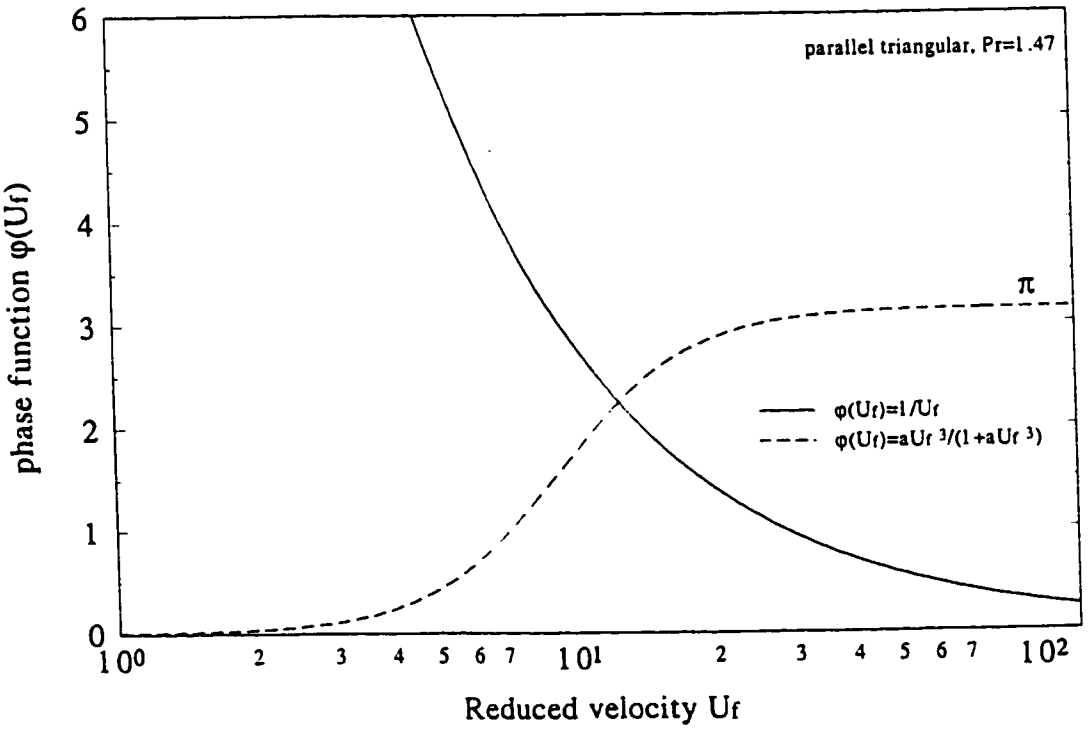

Figure 7.14 Original and proposed phase angle functions

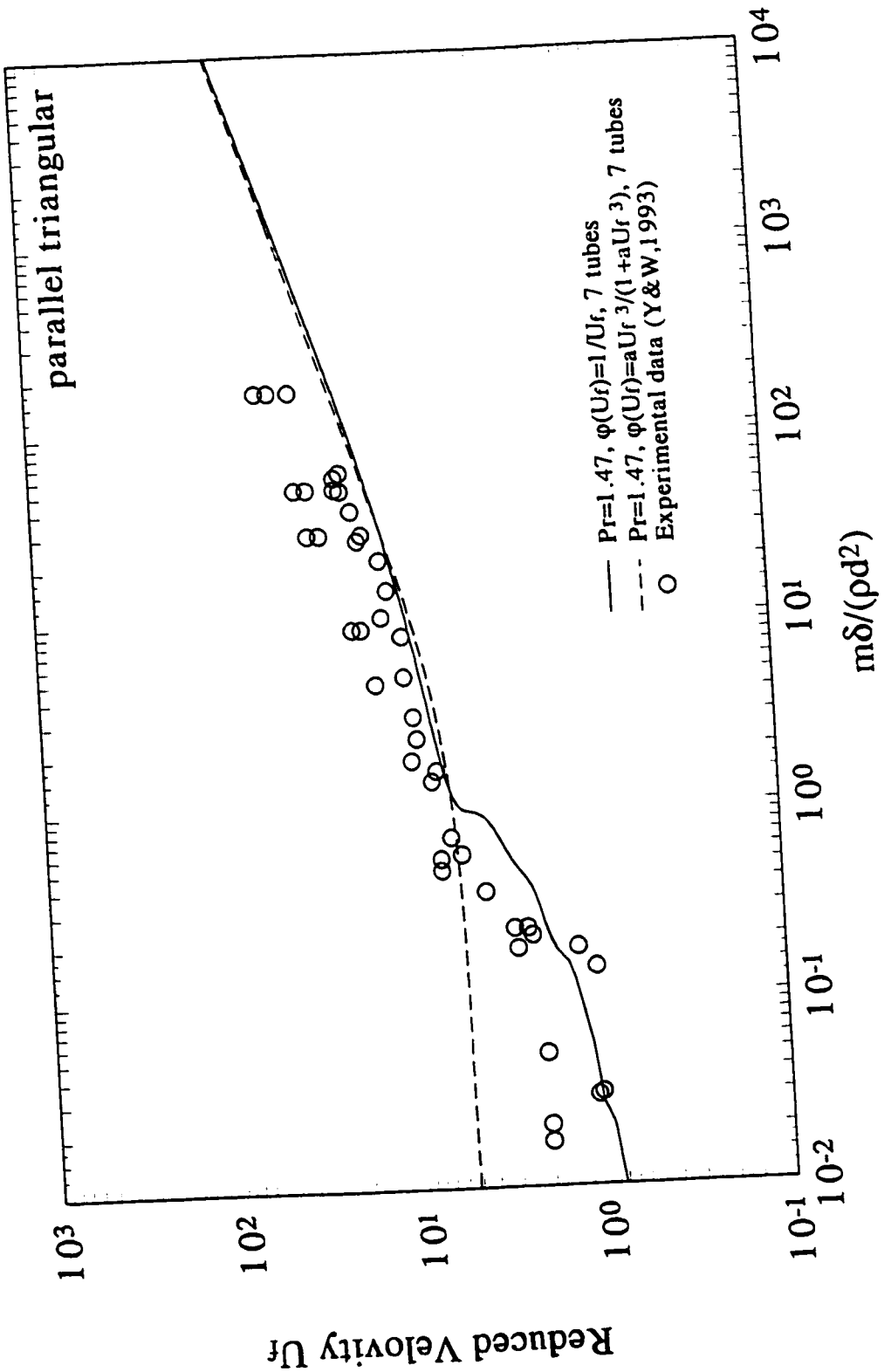

Figure 7.15 Stability predictions by using different phase functions

Figure 7.17 and 7.18 give the similar comparisons for normal triangular and rotated square tube arrays. In general, the present theoretical model and Weaver & Fitzpatrick semi-empirical model provide similar boundaries for the experimental data. Both of them show that in the low MDE_a range, the critical reduced velocity becomes independent of MDE_a. On the other hand, the theoretical model tends to be overly conservative in the high MDE_a range.

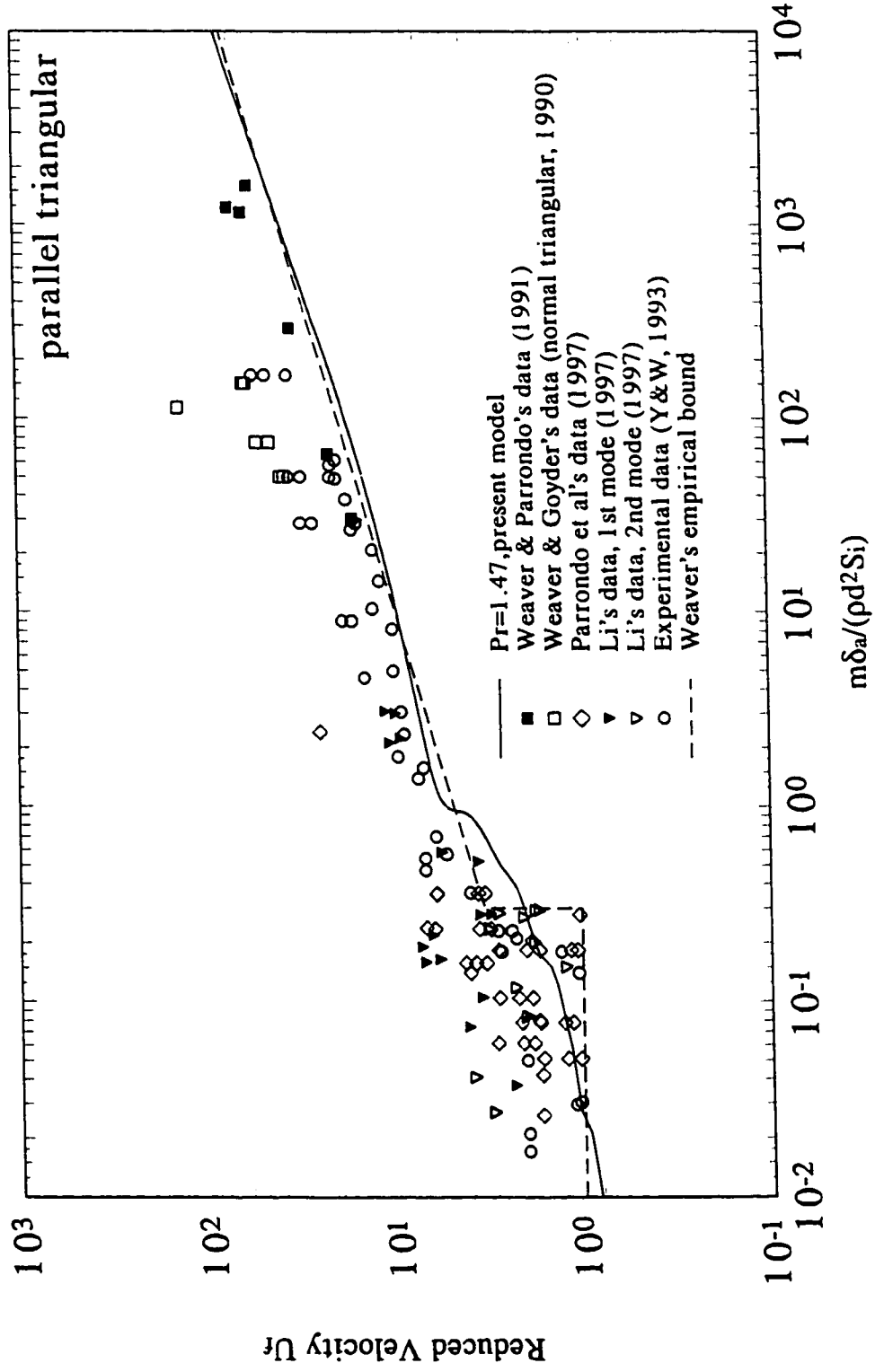

Figure 7.16 The comparison between theoretical, semi-empirical models and experimental data for parallel triangular tube

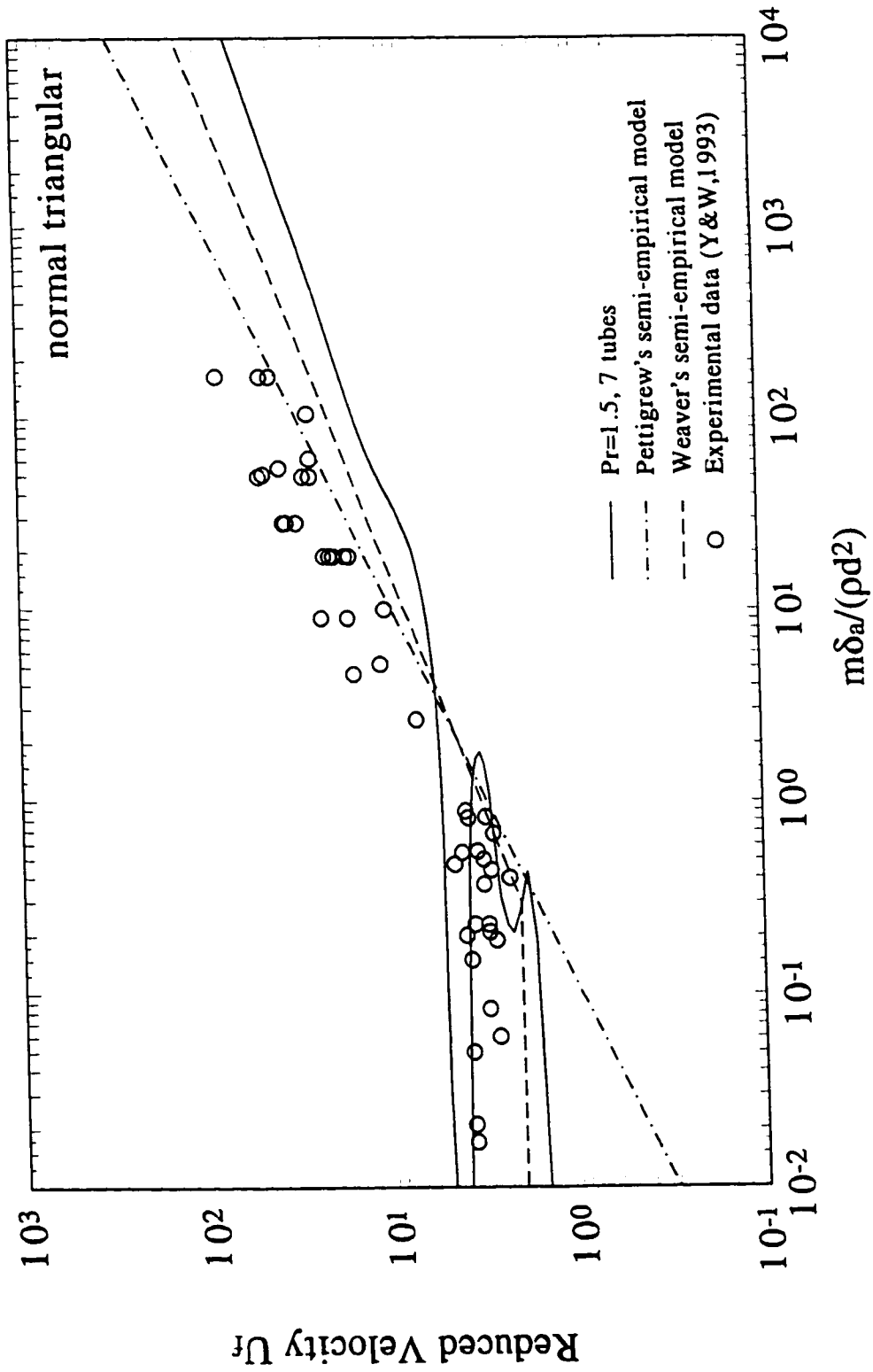

Figure 7.17 The comparison between theoretical, semi-empirical models and experimental data for normal triangular tube

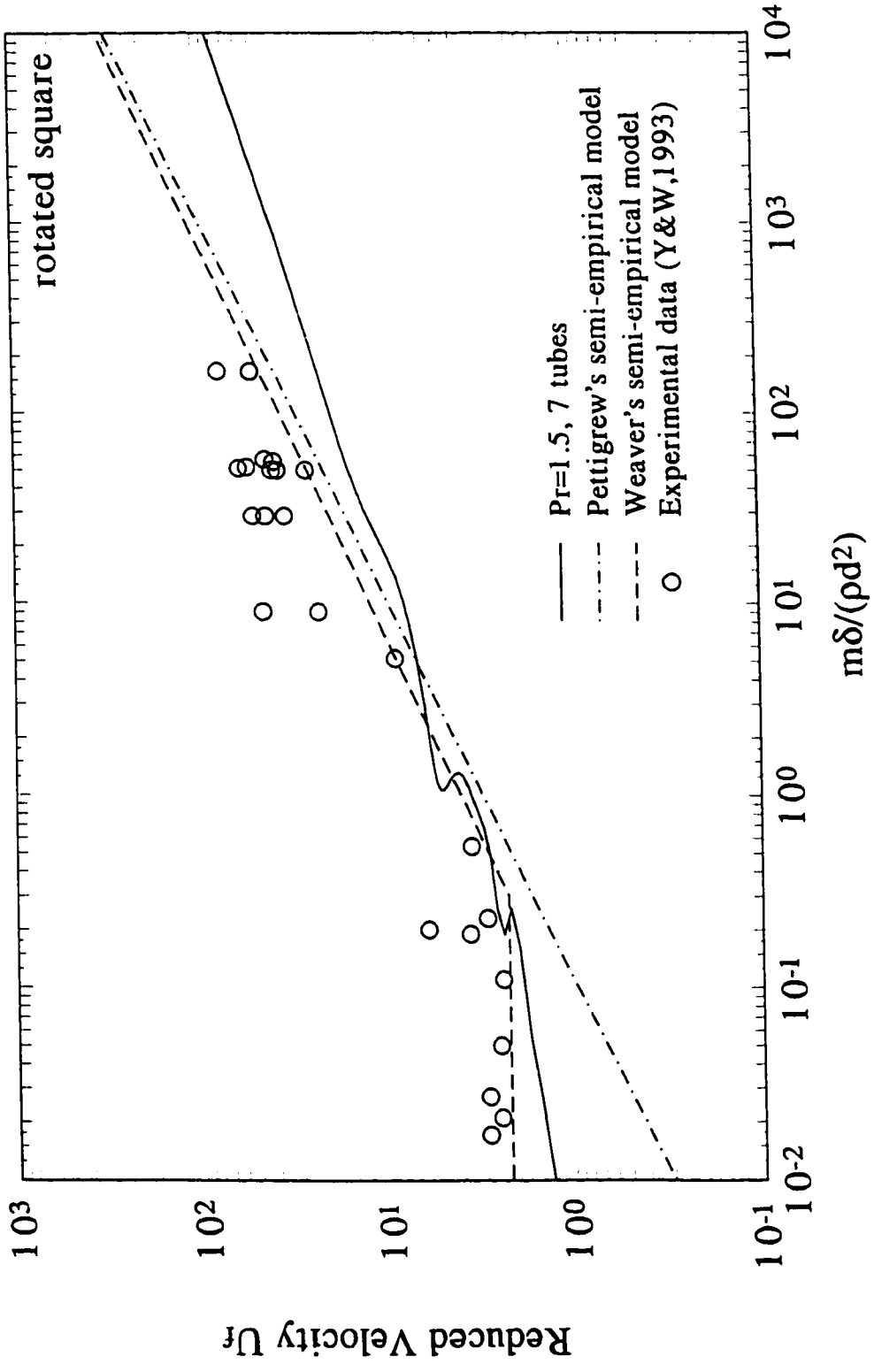

Figure 7.18 The comparison between theoretical, semi-empirical models and experimental data for rotated square tube

CHAPTER 8

CONCLUSIONS AND RECOMMENDATIONS

8.1 Conclusions

Flow induced vibration is a serious issue in the design and operation of steam generators and heat exchangers. The problem includes both long term fretting wear caused by turbulence buffeting and periodic vortex shedding, and short term destructive resonance caused by fluidelastic instability. In order to understand the nature of these phenomena so as to be able to avoid or control them, a great deal of research has been conducted in the past decades. Significant progress has been made but some fundamental questions have yet to be solved. Among them, are two important subjects: the validity of existing semi-empirical fluidelastic instability design guidelines in multi-span tube arrays; and the theoretical modelling of fluidelastic instability in tube bundles. The overall objective of this research was to give improved vibration design guidelines for nuclear steam generators and heat exchangers.

A water tunnel test section was specially designed and built to look at the first subject. The parallel triangular tube array consisted of 17 flexible tubes, 0.5" in diameter. Different end supports were used; clamped, pinned and free. The knife-edge intermediate supports could be moved along the tube span, so that the flow could cross at any section of the span. Full and partial flow admissions were tested by using two different tube lengths. Two miniature accelerometers were mounted perpendicularly and inserted into a tube to measure the tube acceleration. The signal was recorded using a dynamic analyser and the tube displacement was computed from this data. Various tube-support configurations were tested, including single span full admission, single span partial admission, two spans, and three spans with partial flow

admission. By analysing the experimental data, the following conclusions are made:

1. Significant fluid coupling was observed in the full flexible tube bundle submerged in the quiescent-fluid once an impulse excitation was applied. The corresponding frequency spectrum has the broad band characteristics at each oscillating mode, in contrast to a singular peak for the single flexible tube. The added mass coefficient measured in the still water was significantly different from that computed in the instability state. The in- or out-of-phase coupling among neighbouring tubes at the instability changes the tube natural frequency. The upper bound of added mass, corresponding to the lowest oscillating frequency for each mode, should give a conservative estimation of critical velocity. It is suggested that the added mass coefficient measured at the instability for each individual test should be used in the corresponding experimental instability calculations in order to establish a reliable data bank.

2. Damping in air and still water were both measured prior to each dynamic test. An attempt at in-flow damping measurement was unsuccessful because the half-power band width method is not applicable to frequency response spectre which have multiple closely spaced frequencies. It was found that there was no definite trend between the damping value and oscillating mode.

3. The data of the partial admission test on a single span tube array agrees well with the theory though the theory is overly-conservative when the flow is close to the end support.

4. The two-span tests showed that the work done by flow is additive along the span, regardless of the tube deflection shape. It is not possible to arrange a tube-support configuration, by taking advantage of opposite mode shape directions at two sides of an intermediate support, to avoid the fluidelastic instability at sufficient flow velocity.

5. A theoretical study was carried out on a single span tube with different end supports. The results show that the initial unstable mode could be higher than the fundamental if the

admission ratio is small and the flow is located close to the end support. For the pinned-pinned tube span, the calculation shows that the initial unstable mode is always the fundamental mode regardless of the admission length ratio or flow location. This conclusion is confirmed by the previous experimental results. In general, if the admission length ratio is larger than about 40%, the initial unstable mode is always the first mode, independent of the flow location.

6. Response peaks were observed prior to the flow velocity required for the ultimate fluidelastic instability. The corresponding Strouhal numbers cover a large range and often do not agree with data from the literature. It seems that both vortex shedding and secondary instability occur for these arrays. These two mechanism often cannot be distinguished from one another and, indeed, may interact with and enhance each other.

7. Only the first and second instability modes manifested significant vibration amplitudes. Higher oscillating modes are usually associated with the lower vibration amplitudes. The potential damage caused by the higher modes due to their high kinetic energy is not recognized by current design guidelines.

8. The present and previous experimental data suggest that energy fraction is a representative parameter in nonuniform flow velocity distribution analysis. However, existing design guidelines do not always give conservative predictions for the critical velocity. The stability map in the low and high mass-damping-energy fraction parameter (MDE) show different trends. Thus, a constant coefficient, K, relating the reduced velocity to the MDE parameter is not adequate. This agrees with observation for full admission conditions. It was found that Weaver & Fitzpatrick's correlation, corrected for partial admission, provides a good lower bound for the experimental data in the literature as well as the present study. More importantly, it always gives conservative critical velocity predictions.

The second objective of this research was to develop a theoretical model to analyse the

fluidelastic instability in multi-span tube arrays. The advantages of an accurate theoretical model are two fold: the systematic analysis of the effects of individual parameters and a better understanding of the fluid-structure interaction mechanisms. The development of the model was based on Yetisir-Weaver's unsteady model, which employs the continuity and momentum equations in the curvilinear coordinate. Several improvements have been achieved in the new model:

1. In the modified model, an explicit stability equation is obtained by using a linear area disturbance decay function. Such an explicit form enables the model to become a convenient analytical tool.

2. The calculation by the present model confirms that the critical reduced velocity in the transverse direction is lower than that in the streamwise direction over most of the mass damping parameter range. Therefore, only the instability in the transverse direction needs to be analysed. However, in practice, the vibration in the two directions are coupled, and the actual tube motion may switch from one direction to the other in an irregular whirling pattern.

3. The inclusion of the tubes two rows upstream and downstream from a central tube tube improves the experimental agreements, especially for the parallel triangular tube array.

4. The multiple instability regions, caused by the unrealistically large phase angle, were eliminated for the parallel triangular tube array, except at very small pitch ratios. The theory agrees well with the experimental data. Good agreement was also obtained between the theoretical model and Weaver & Fitzpatrick's semi-empirical correlation for all the investigated tube arrays.

5. The velocity distribution and mode shape function were introduced into the model, thus permitting it to be used to calculate the critical reduced velocity for the multi-span tube arrays with partial admission. A comparison between theory and experimental data shows

reasonable agreement.

8.2 Recommendations

The vibration of heat exchanger tubes caused by liquid cross flow is a very complicated problem, which exists in many practical applications and which has profound economic and environmental impacts. Many excitation mechanisms are involved, including, turbulence buffeting, vortex shedding and fluidelastic instability. Both fluid dynamics and structural dynamics have to be applied to interpret and solve this problem. Unfortunately, though significant progress has been made, some fundamental issues have not yet been clarified. In the study of multi-span tubes, more dimensions of difficulty are added: velocity distribution, mode shape, tube-support interaction, etc. In this study, attempts to address these problems and progress towards them have been made. Nevertheless, many questions still remain to be answered by future work.

For instance, in order to verify the existence of secondary fluidelastic instability, the vortex shedding phenomenon has to be measured with great confidence or to be avoided by a proper design of the test rig. With a verified Strouhal number at a given pitch ratio for a defined tube array pattern, flow velocity and tube frequency have to be adjusted to avoid the lock-in phenomenon. If the elimination of the lock-in is not possible, which may be the case in most test conditions, the phenomenon has to be identified with regard to its response and frequency characteristics, as well as Strouhal number. Flow visualization is a useful technique in the study of vortex shedding, but it is limited to relatively low Reynolds numbers and by the lighting location. The lighting and camera can only be placed in the end of the tube span. This is suitable for cantilever supported tubes, but not for other types of support, such as multi-span tube arrays. Therefore, the applicability of other techniques has to be investigated, such as mounting

pressure transducers on the surface of the tube.

Previous studies, as well as the present one, show that higher mode instability is usually associated with the smaller vibration displacements. The amplitudes may be so small that it is not a factor in the analysis of tube clashing. However, since the vibration velocity $\dot{x}$ is proportional to the vibration frequency ω, i.e., $\dot{x} \propto x\,\omega$, the higher modes are associated with the higher vibration velocity. Thus small amplitude vibration may have significant kinetic energy which could cause fretting wear damage at the support locations. This aspect has to be further investigated and a new criterion for instability may have to be created.

The present and previous theoretical models are able to give reasonable predictions for the critical reduced velocity for the fluidelastic instability of tube arrays in the large mass damping parameter region. However, fundamental understanding is needed in the low mass damping ratio region, where the quasi-steady assumption is not valid. To advance the theoretical modelling, the nature of the phase lag needs to be better understood. Preferably, this should be based on fundamental considerations, such as the analysis of the Navier-Stokes equations.

REFERENCES

Abd-Rabbo, A. and Weaver, D.S. 1986 A flow visualization study of flow development in staggered tube array. *Journal of Sound and Vibration* **106**, pp. 241-256.

Au-Yang, M. K., Blevins, R. D., and Mulcahy, T. M. 1991 Flow-induced vibration analysis of tube bundles: A proposed section III appendix N non-mandatory code. *ASME Journal of Pressure Vessel Technology* **113**, pp. 257-267.

Au-Yang, M.K. 1993 *ASME Technology for the '90s*. Ed. Au-Yang, M.K. New York. pp.959-972.

Blevins, R.D. 1974 Fluidelastic whirling of a tube row. *ASME Journal of Pressure Technology* **96**, pp.263-267.

Blevins, D. R. 1977 *Flow-Induced Vibration.* Van Nostrand Reinhold, New York.

Blevins, R. D. 1979 Formulas for natural frequency and mode shape. *Van Nostrand Reinhold Company,* pp.134-147.

Blevins, R. D. 1984 Letter to the editor. *Journal of Sound and Vibration,* Vol.**97,** pp.641-644.

Bradshaw, P. and Pankhurst, R.C. 1964 The design of low speed tunnels, *Prog. Aerospace. Sci.* V.**5**, pp.1-69.

Chen, S. S., Wambsganss, M. W., & Jendrzejczyk, J. K. 1976 Added mass and damping of a vibrating rod in confined viscous fluids. *ASME Journal of Applied Mechanics.* **43.** pp.325-700.

Chen, S. S. 1978 Crossflow-induced vibrations of heat exchangers tube banks, *Nuclear Engineering and Design* **47**, pp.67-86.

Chen, S.S. & Jendrzejczyk, J. K. 1983 Stability of tube arrays in crossflow. *Nuclear Engineering and Design* **75,** pp.351-374.

Chen, S. S. 1983 Instability mechanisms and stability criteria of a group of cylinders subjected to cross flow. Part I: theory; Part II: Numerical results and discussions. *ASME Journal of Vibration, Acoustics, Stress and Reliability in Design* **105,** pp.51-58 and pp.253-260.

Chen, S. S. 1984 Guidelines for the instability flow velocity of tube arrays in crossflow.

Journal of Sound and Vibration, Vol.**93,** pp.439-455.

Chen, S.S. 1989 Some issues concerning fluidelastic instability of a group of circular cylinder in cross-flow. *ASME Journal of Pressure and Vessel Technology,* Vol. **111,** pp.507-518.

Chen, Y. 1993 Strouhal periodicity in parallel triangular tube arrays. *Master's Thesis,* Department of Mechanical Engineering, McMaster University.

Clough, R. W.1975 *Dynamics of Structures.* McGraw-Hall.

Connors, H. J. 1970 Fluidelastic vibration of tube array excited by cross flows. *ASME Flow Induced vibration in Heat Exchangers,* Ed. D. D. Reiff. New York. pp.42-56.

Connors, H. J. 1978 Fluidelastic vibration of heat exchanger tube array. *ASME Journal of Mechanical Design* **100**, pp.347-353.

Dalton, C. & Helfinstein, R.A. 1971 Potential flow past a group of circular cylinders. *ASME Journal of Basic Engineering* **93**, pp. 636-642.

Dalton, C. 1980 Inertia coefficients for riser configurations. *ASME Energy Technology Conference and Exhibition*, New Orleans, paper 80-Pet-21. New York.

El Kashlan, M. 1980 Tube row and damping parameter effects on tube-array stability. *Master's Thesis,* Department of Mechanical Engineering, McMaster University.

Farell, C. & Xia, L. 1990 A note on the design of screen-filled wind-angle diffusers. *Journal of Wind Engineering and Aerodynamics* **33**, pp.479 - 486.

Feenstra, P. 1993 Two phase flow-induced vibration in heat exchanger tube arrays: an experimental investigation. *Master's thesis*, Department of Mechanical Engineering, McMaster University.

Franklin, R. B. & Soper, B. M. H. 1977 An Investigation of fluidelastic instabilities in tube banks subjected to cross flow. HTFS Report AERE-R8708, HTFS RS 192, AERE Harwell and National Engineering Laboratory, U. K.

Gibert, R. J., Chabrerie, J. & Sagner, M. 1978 Vibration of tube arrays in transverse flow. *ASME Journal of Engineering for Power,* Vol. **103,** pp.358-366.

Grover, L. K. 1977 Cross Flow-induced vibration deep inside a closely packed tube-bank. *Ph.D. Thesis,* Department of Mechanical Engineering, McMaster University.

Grover, L. K. & Weaver, D. S. 1978 Cross-flow Induced vibration in a tube bank - turbulent buffeting and fluidelastic instability. *Journal of Sound and Vibration* **59**, pp.283-294.

Koroyannakis, D. 1980 Liquid cross-flow-induced vibrations of a tube array. *Master's Thesis*, Department of Mechanical Engineering, McMaster University.

Lever, J. H. & Weaver, D. S. 1982 A theoretical model for fluid -elastic instability in heat exchanger tube bundles. *ASME Journal of Pressure Vessel Technology* **104**, pp.375-410.

Lever, J. H. & Weaver, D. S. 1986 On the stability of heat exchanger tube bundles, Part I: Modified theoretical model; Part II: Numerical results and comparison with experiments. *Journal of Sound and Vibration*, **107**, pp.393-410.

Mehta, R. D. 1977 The design of low speed wind tunnels. *Prog. Aerospace Sci.* Vol. **18**, pp. 59-120.

Morel, T. 1977 Design of two-dimensional wind tunnel contractions. *ASME Journal of Fluid Engineering.* pp.371-379.

Païdoussis, M. P. 1980 Flow-induced vibrations in nuclear reactors and heat exchangers, *Practical Experience with Flow Induced Vibrations*, Naudascher & Rockwell (eds.), pp.1-81.

Païdoussis, M. P. 1981 Fluidelastic vibrations of cylinder in axial and cross flow: State of the art. *Journal of Sound an Vibration* **76**, pp.329-360.

Païdoussis, M. P. 1983 A review of flow-induced vibration in reactors and reactor components. *Nuclear Engineering and Design* **74**, pp.31-60.

Paidoussis, M.P, Mavriplis, D. & Price, S.J. 1984 A potential - flow theory for the dynamics of cylinder arrays in cross-flow. *Journal of Fluid Mechanics* **187**, pp.45-59.

Paidoussis, M.P. & Price , S.J. 1995 On the virtual nonexistence of multiple regions for some heat-exchanger arrays in crossflow. *Journal of Fluids Engineering* **118**, pp.103-109.

Parrondo, J., Weaver, D. S. & Santolaria, C. 1997 Fluidelastic instability in a tube array subjected to partial admission cross-flow, *Journal of Fluids and Structures* **11**, pp.159-181.

Pettigrew, M. J., Sylvester, Y. & Campagna, A. O. 1978 Vibration analysis of heat exchanger and steam generator designs. *Nuclear Engineering and Design* **48**, pp.97-115.

Pettigrew, M.J., Goyder, H.G.D., Qias, Z.L., and Axisa, F., 1986a Damping of multispan

heat exchanger tubes. I. In gases. *Flow-Induced Vibration.* New York, The American Society of Mechanical Engineers, ASME PVP-Vol 104, pp.81-88.

Pettigrew, M.J., Rogers, R. J., and Axisa, F., 1986b Damping of multispan heat exchanger tubes. II. In liquids. *Flow-Induced Vibration.* New York, The American Society of Mechanical Engineers, ASME PVP-Vol 104, pp.89-98.

Pettigrew, M.J., & Taylor, C.E. 1991 Fluidelastic instability of heat exchanger tube bundles: review and design recommendations. *ASME Journal of Pressure and Vessel Technology,* Vol. **112,** pp.242-256.

Price, S.J. & Paidoussis, M.P. 1982 A theoretical investigation of the parameters affecting the fluidelastic instability of a double row of cylinders subjected to cross-flow. In *Proceedings 3rd International Conference on Vibrations in Nuclear Plant*, Keswick, U.K, pp.107-119.

Price, S. J. & Paidoussis, M.P. 1984 An improved mathematical model for the stability of cylinder rows subject to cross-flow. *Journal of Sound and Vibration* **107**, pp.615-640.

Price, S.J. & Paidoussis, M.P. 1986b A single-flexible-cylinder analysis for the fluidelastic instability of an array of flexible cylinder in cross-flow. *ASME Journal of Fluids Engineering* **108**, pp.193-199.

Price, S. J. 1993 Theoretical models of fluidelastic instability for cylinder arrays subject to cross flows. *ASME Technology for the '90s*. Ed. Au-Yang, M.K. New York, pp.713-773.

Price, S.J. 1995 A review of theoretical models for fluidelastic instability of cylinder arrays in cross-flow. *Journal of Fluids and Structures* **9**, pp.463-518.

Price, S. J., Paidoussis, M. P. & Mark, B. 1995 Flow-visualization of the interstitial cross-flow through parallel triangular and rotated square arrays of cylinders. *Journal of Sound and Vibration* **181**, pp.85-98.

Robert, B. W. 1966 Low frequency aeroelastic vibrations in a cascade of circular cylinders. *I.Mech. E. Mechanical Engineering Science Monograph,* No.4.

Scott, P. 1987 Flow visualization of cross-flow-induced vibration in tube arrays. *Master's Thesis,* Department of Mechanical Engineering, McMaster University.

Southworth, P. J. & Zdravkovich, M. M. 1975 Cross-flow-induced vibrations of finite

tube banks in in-line arrangements *I,Mech.E. Journal of Mechanical Engineering Science* **17**, pp.190-198.

Timoshenko, S. 1955 Vibration Problems in Engineering. *D. Van Nostrand Company,* pp.342-345.

Tanaka, H. & Takahara, S. 1980 Unsteady fluid dynamic force on tube bundle and its dynamic effect on vibration. *ASME Flow-Induced Vibration of Power Plant Components*, (ed. M.K. Au-Yang), PVP-Vol, 41, New York, pp.77-92.

Tanaka, H., & Takahara, S. 1980 Unsteady fluid dynamic force on tube bundle and its dynamic effect in vibration. *International Conference on Flow-Induced Vibration in Fluid Engineering,* Reading, England, pp.233-254.

Tanaka, H. & Takahara, S. 1981 Fluidelastic vibration of tube array in cross flow. *Journal of Sound and Vibration* **77**, pp.19-37.

Tanaka, H., Takahara, S., & Ohta, K. 1982 Fluid - induced vibration of tube arrays with various pitch-to-diameter ratios. *Fluid-Induced Vibration of Cylindrical Structures, PVP* **73**, pp.43-56.

Waring, L. F. 1986 Fluidelastic instability of tube array; partial admission effects. *Master's Thesis,* Department of Mechanical Engineering, McMaster University.

Waring, L. F. & Weaver, D. S. 1988 Partial admission effects on the stability of a heat exchanger tube array. *ASME Journal of Pressure Vessel Technology* **119**, pp.194-198.

Weaver, D.S. & Lever, J. 1971 Tube frequency effects on cross flow induced vibrations in tube arrays. *Proceedings of the fifth Biennial Symposium on Turbulence,* University of Missouri-Rolla, Missouri, pp.323-331.

Weaver, D. S. & Grover, L. K. 1978 Cross-flow induced vibrations in a tube bank. *Journal of Sound and Vibration* **59**, pp.277-294.

Weaver, D. S. & El-Kashlan, M. 1981 The effect of damping and mass ratio of the stability of tube bank. *Journal of Sound and Vibration* **76**, pp.284-294.

Weaver, D. S. & Koroyannakis, D. 1983 Flow induced vibrations of heat exchanger U-tubes, a simulation to study the effects of asymmetric stiffness. *ASME Journal of Vibration, Acoustics, Stress and Reliability in Design* **105**, pp.67-75.

Weaver, D. S. & Yeung, H.C. 1984 The effect of tube mass on the flow induced response of various tube arrays in water. *Journal of Sound and Vibration*, Vol. **93**, pp.409-425.

Weaver, D.S. and Abd-Rabbo, A. 1985 A flow visualization study of a square array of tubes in water crossflow, *ASME Journal of Fluids Engineering* **107**, pp.354-363.

Weaver, D. S. & Fitzpatrick, J. A. 1988 A review of cross-flow induced vibrations in heat exchanger tube arrays. *Journal of Fluids and Structures* **2**, pp.73-93.

Weaver, D. S. & Goyder, H. G. D. 1990 An experimental study of fluidelastic instability in a 3 span tube array. *Journal of Fluids and Structures* **4**, pp.429-442.

Weaver, D. S. & Parrondo, J. 1991 Fluidelastic instability in multi-span heat exchanger tube arrays. *Journal of Fluids and Structures* **5**, pp.323-338.

Weaver, D. S. 1992 An introduction to flow induced vibrations. *Course notes*, McMaster University.

Weaver, D.S., Lian, H.Y. & Huang, X.Y. 1991 A study of vortex shedding in a normal triangular tube array. *Proc. I.Mech.E. Int. Conf. Flow Induced Vibration. I.Mech.E.* 1991-6, pp.511-516.

Yu, X. 1986 An analysis of tube failure in a U-tube bundle. *ASME symposium on flow induced vibrations*, PVP **104**, pp.187-192.

Yetisir, M. & Weaver, D.S. 1992 A theoretical study of fluid instability in a flexible array of tubes. *In ASME Proceedings Symposium on Flow-Induced Vibration and Noise, Vol. 2: Cross-Flow Induced Vibration of Cylinder Arrays* (eds M.P. Paidoussis, S.S.Chen & D.A. Steininger), New York, pp.69-87.

Yetisir, M. & Weaver, D. S. 1993 An unsteady theory for fluidelastic instability in an array of flexible tubes in cross-flow. Part I: theory. *Journal of Fluids and Structures* **7**, pp.751-766.

Yetisir, M. & Weaver, D. S. 1993 An unsteady theory for fluidelastic instability in an array of flexible tubes in cross-flow. Part II: results and comparison with experiments. *Journal of Fluids and Structures* **7**, pp.767-782.

Yeung, H. C. & Weaver, D. S. 1983 The effect of approach flow direction on the flow induced vibrations of a triangular tube array. *ASME Journal of Vibration, Acoustics, Stress and*

Reliability in Design **105,** pp.76-82.

APPENDIX A

EXPERIMENTAL UNCERTAINTY

The freestream velocity V_∞ measurement is based on the Bernoulli equation using the readings from a Pitot-static probe

$$V_\infty = \sqrt{\frac{2(\rho_2 - \rho_w)g\Delta h}{\rho_w}} \tag{A-1}$$

Here, ρ_2, ρ_w are the density of monometer liquid and water respectively and Δh is the height difference of liquid column in the manometer.

The uncertainty of a derived quantity is calculated using the method of Kline and McClintock [1953]. Each measured value is expressed as

$$m \pm w \tag{A-2}$$

where m is the mean value, and w is its associated uncertainty. For a derived quantity R, composed of *n* independent variables, V. The absolute uncertainty is

$$w_R = \sqrt{(\frac{\partial R}{\partial V_1}w_1)^2 + (\frac{\partial R}{\partial V_2}w_2)^2 + \ldots + (\frac{\partial R}{\partial V_n}w_n)^2} \tag{A-3}$$

Substituting equation (A-1) into (A-3), and neglecting the density changes.

$$\frac{w_{V_\infty}}{V_\infty} = \sqrt{(\frac{\partial V_\infty}{\partial \Delta h}w_{\Delta h})^2}/V_\infty = \frac{w_{\Delta h}}{2\Delta h} \tag{A-4}$$

The graduation of monometer is 5/10000". The liquid used in the manometer is carbon tetrachloride, with density $\rho_2 = 15570\ N/m^3$. The typical uncertainties are:

$w_{V_-}/V_- = 7.5\%$ for $V_- = 0.1$ m/s.

$w_{V_-}/V_- = 0.075\%$ for $V_- = 1.0$ m/s.

APPENDIX B

CALIBRATION OF THE ROTAMETER AND THE WATER TUNNEL

The orifice-rotameter and water tunnel test section were calibrated using a Pitot-static probe.

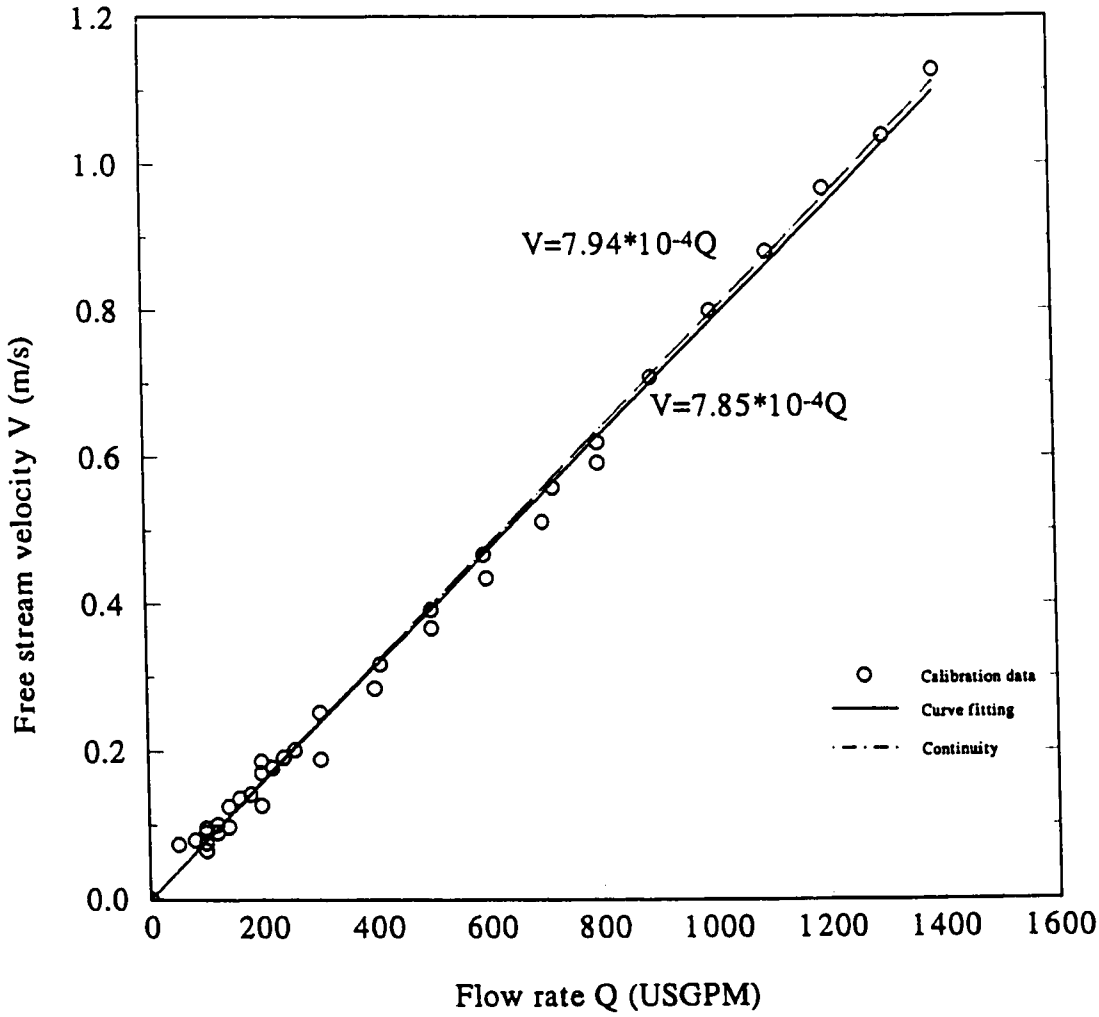

Figure B-1 Calibration of the rotameter

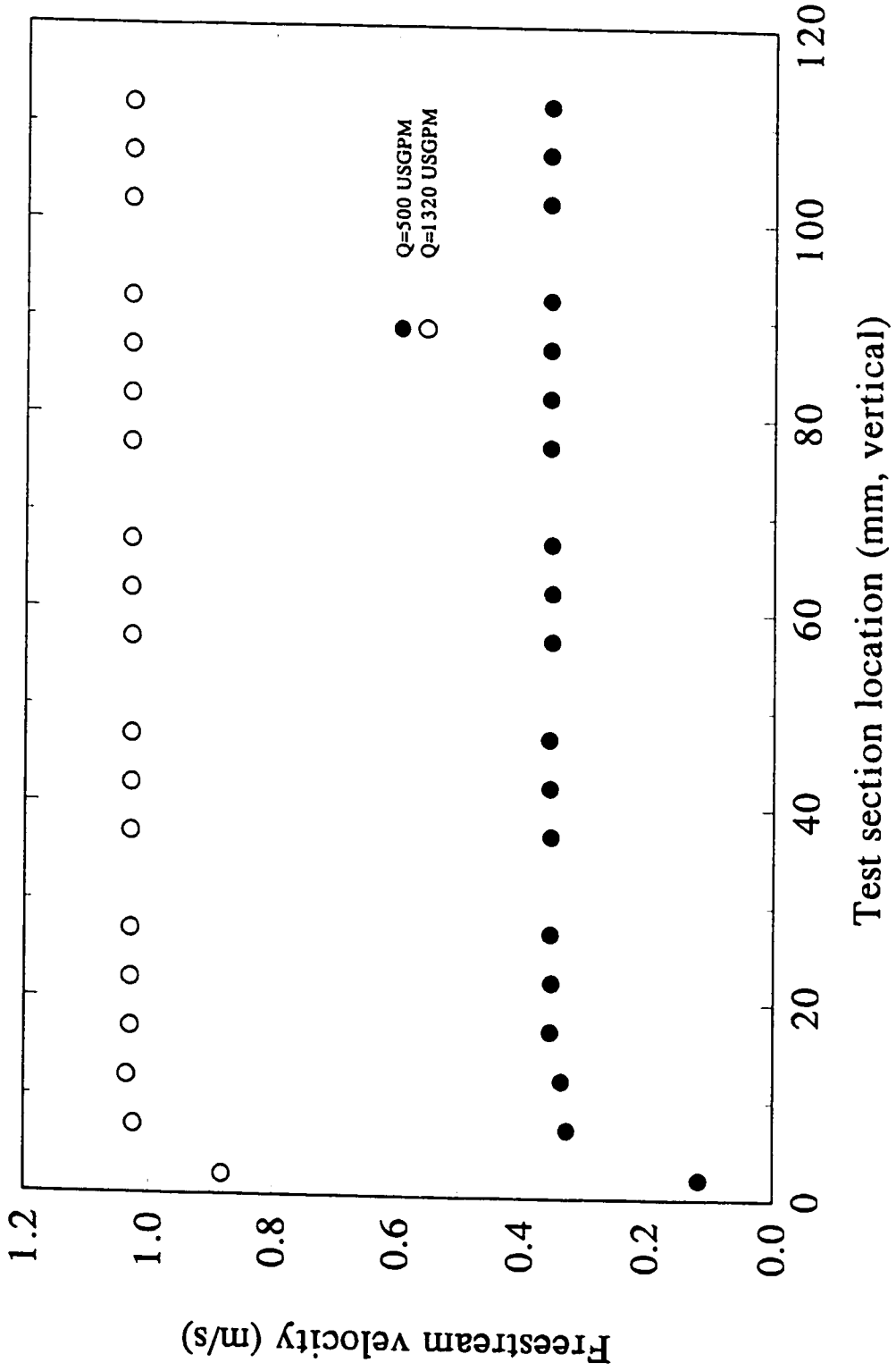

Figure B-2 Calibration of test section velocity profile in the vertical direction

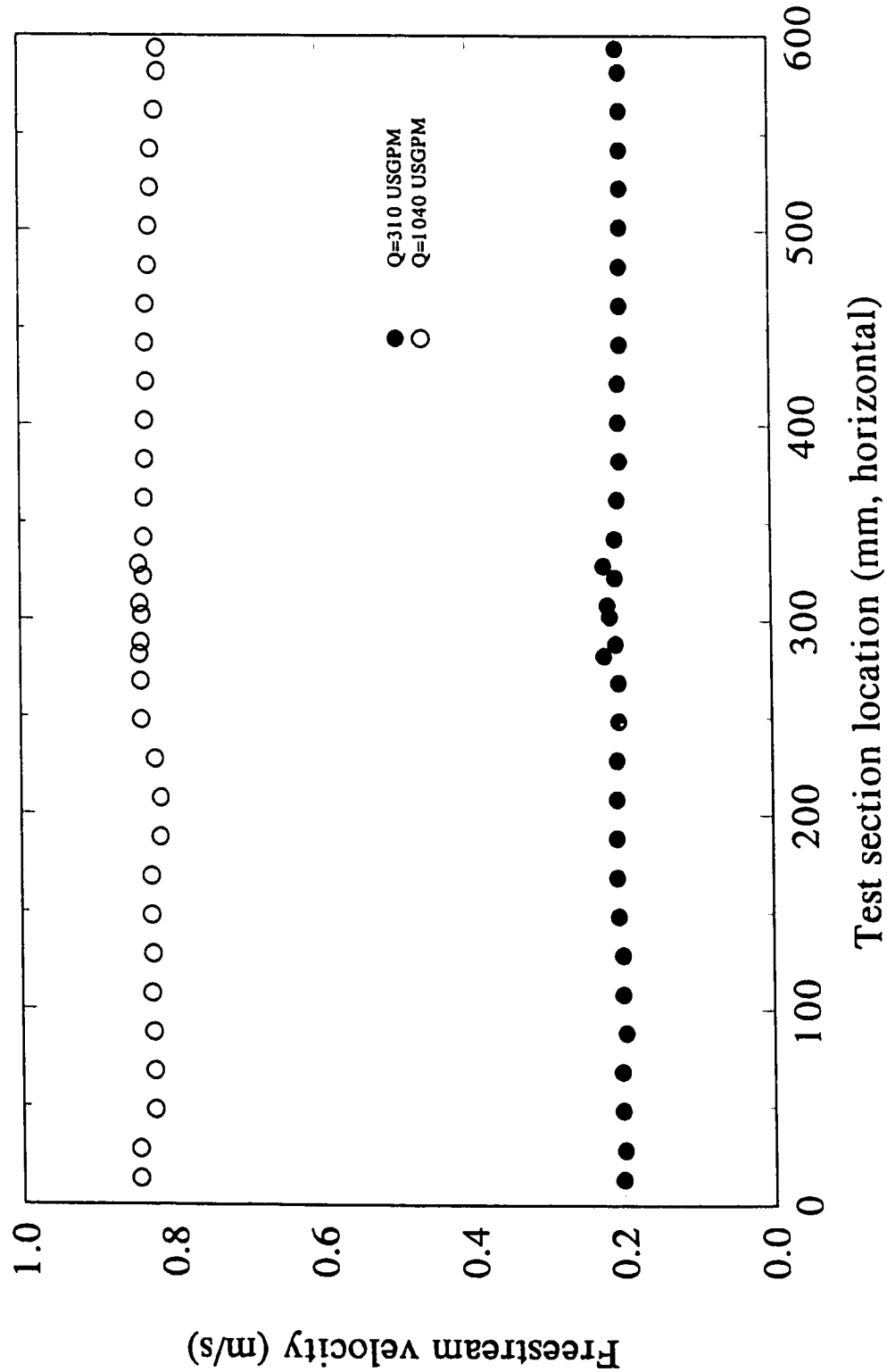

Figure B-3 Calibration of test section velocity profile in the horizontal direction

APPENDIX C

DERIVATION OF CRITICAL REDUCED VELOCITY OF FLUIDELASTIC INSTABILITY WITH THE CONSIDERATION OF MODE SHAPE AND FLOW VELOCITY DISTRIBUTION

The displacement of tube at mode n

$$u_n(x,\ t) = y_0\varphi_n(x)\sin\omega_n t\ = y_n(t)\varphi_n(x)$$
$$\textit{Hence} \qquad \dot{y}_n(t)\ = y_0\omega_n\cos\omega_n t \tag{C-1}$$

Thus

$$\sin\omega_n t\ = \frac{y_n(t)}{y_0}, \qquad \cos\omega_n t\ = \frac{\dot{y}_n(t)}{y_0\omega_n} \tag{C-2}$$

The fluid force can be written as

$$f(x,t)\ = f_0(x)\sin(\omega_n t\ +\ \theta_0)$$
$$= f_0(x)\sin\theta_0\cos\omega_n t\ +\ f_0(x)\cos\theta_0\sin\omega_n t \tag{C-3}$$

Substituting (C-2) into (C-3)

$$f(x,t) = f_0(x)\sin\theta_0\frac{\dot{y}_n}{y_0\omega_n}\ +\ f_0(x)\cos\theta_0\frac{y_n}{y_0} \tag{C-4}$$

The vibration equation with the generalized mass and generalized force in a normal-coordinate transformation is

$$M_n\ddot{y}_n(t) + c\int_0^l \varphi^2{}_n(x)dx\ \dot{y}_n(t) + \omega_n{}^2 M_n y_n(t) = F_n(t) \tag{C-5}$$

where

$$M_n = m\int_0^l \varphi^2{}_n(x)dx, \quad F_n(t) = \int_0^l \varphi_n(x) f(x,t)dx \tag{C-5-1}$$

Substituting (C-4) into (C-5-1)

$$F_n(t) = \int_0^l \varphi_n(x)[f_0(x)\sin\theta_0 \frac{\dot{y}(t)}{y_0\omega_n} + f_0(x)\cos\theta_0 \frac{y(t)}{y_0}]\ dx \tag{C-6}$$

Substituting (C-6) into (C-5)

$$\begin{aligned} M_n\ddot{y}_n(t) + [\ c\int_0^l \varphi^2{}_n(x)dx - \int_0^l \varphi_n(x)\frac{f_0(x)\sin\theta_0}{y_0\omega_n}\ dx]\dot{y}_n(t) \\ + [\omega_n{}^2 M_n - \int_0^l \varphi_n(x)\frac{f_0(x)\cos\theta_0}{y_0}\ dx]y_n(t) = 0 \end{aligned} \tag{C-7}$$

The stability threshold occurs at the total damping equal to zero, i.e.

$$c\int_0^l \varphi^2{}_n(x)dx - \int_0^l \varphi_n(x)\frac{f_0\sin\theta_0}{y_0\omega_n}\ dx = 0 \tag{C-8}$$

where

$$c = \frac{m\omega_n\delta}{\pi} \tag{C-8-1}$$

The fluid force can be expressed as

$$f_0(x) = \frac{1}{2}ky_0\rho U^2(x)\varphi(x) \tag{C-9}$$

where k is a constant, U(x) is the incoming flow velocity, which can be written as: $U(x)=U_\infty\psi(x)$. The phase angle $\theta_0 = 90°$, $\sin\theta_0=1$, i.e. the fluid force is in phase with fluid velocity. This implies $\omega/\omega_n = 1$.

Substituting (C-8-1) and (C-9) to (C-8), we obtain

$$\frac{m\omega_n\delta}{\pi}\int_0^l \varphi^2{}_n(x)dx = \int_0^l \varphi^2{}_n(x)\frac{\frac{1}{2}ky_0\rho U_\infty^2\psi^2(x)}{y_0\omega_n}\,dx$$

After simplifying the above equation

$$\frac{U_\infty^2}{\omega^2{}_n d^2}\frac{\int_0^l \varphi^2{}_n(x)\psi^2(x)\,dx}{\int_0^l \varphi^2{}_n(x)dx} = \frac{2}{\pi k}\left(\frac{m\delta}{\rho d^2}\right) \tag{C-10}$$

and $\omega_n = 2\pi f_n$, thus

$$\frac{U_\infty}{f_n d}\left[\frac{\int_0^l \varphi_n(x)\psi^2(x)\,dx}{\int_0^l \varphi^2{}_n(x)dx}\right]^{\frac{1}{2}} = 2\pi\left(\frac{2}{\pi k}\right)^{0.5}\left(\frac{m\delta}{\rho d^2}\right)^{0.5} = K\left(\frac{m\delta}{\rho d^2}\right)^{0.5} \qquad \text{(C-11)}$$

then effective velocity

$$U_{eff} = U_\infty\left[\frac{\int_0^l \varphi^2{}_n(x)\psi^2(x)\,dx}{\int_0^l \varphi^2{}_n(x)dx}\right]^{\frac{1}{2}} \qquad \text{(C-12)}$$

Thus

$$\frac{U_{eff}}{f_n d} = K\left(\frac{m\delta}{\rho d^2}\right)^{0.5} \qquad \text{(C-13)}$$

If velocity profile is uniform, i.e. $\psi(x) = 1$, then

$$\frac{U_\infty}{f_n d} = K\left(\frac{m\delta}{\rho d^2}\right)^{0.5} \qquad \text{(C-14)}$$

which is Connors' equation.

APPENDIX D

COEFFICIENTS IN CHAPTER 7

$$A_1=\frac{1}{l_0A_0}$$

$$A_2(s,U_r)=-i\frac{[(s\cdot s_1-s_1^2)\varphi_1(U_r)+i\cdot s_1^2]a_1(s,U_r)-i\cdot s_1^2a_1(s_1,Ur)}{(s_x-s_1)\cdot\varphi_1(U_r)}$$

$$A_3(s,U_r)=a_2(U_r)\cdot(s-s_x)$$

$$A_5(U_r)=i\frac{-a_1(U_r)\cdot s_1+a_1(U_r)\cdot s_1}{\varphi_1(U_r)}$$

$$A_6(s,U_r)=-i\frac{[s_x\varphi_1(U_r)\cdot s_1+i\cdot s_1^2]a_1(U_r)-[\varphi_1(U_r)+i]s_1^2a_1(U_r)}{\varphi_1(U_r)^2}$$

$$A_8(s,U_r)=a_2(U_r)(s-s_x)$$

$$A_9=\frac{P_r}{2}[\sin(2\frac{s_y}{P_r})-\sin(2\frac{s_x}{P_r})]$$

$$A_{10}=\frac{1}{4}\cos(2\frac{s_y}{P_r})P_r^2-\frac{1}{2}P_r(s_x-s_y)\sin(2\frac{s_y}{P_r})-\frac{1}{4}\cos(2\frac{s_x}{P_r})P_r^2$$

$$A_{11}=(-\frac{1}{4}P_r^3+\frac{1}{2}P_r^2s_x^2+\frac{1}{2}P_rs_y^2-P_rs_xs_y)\sin(2\frac{s_y}{P_r})+\frac{1}{2}P_r^2(s_y-s_x)\cos(2\frac{s_y}{P_r})+\frac{1}{4}\sin(2\frac{s_x}{P_r})P_r^3$$

$$A_{12}(U_r)=[\frac{1}{4}\cos(2\frac{s_y}{P_r})P_r^2-\frac{1}{2}P_r(s_y-s_x)\sin(2\frac{s_y}{P_r})-\frac{1}{4}\cos(2\frac{s_x}{P_r})P_r^2]a_2(U_r)$$

$$B_1(U_r,\omega_r)=A_1[l_0A_2(U_r)+\omega_r\frac{[-\varphi_1(U_r)+i]s_1^2A_5(U_r)+s_1\varphi_1(U_r)A_6(U_r)-s_1^2i\cdot(s_x-s_1)a_1(U_r)}{U_r(s_x-s_1)\varphi_1(U_r)^2}$$

$$B_2(s,U_r,\omega_r)=A_1\{l_0A_8(s,U_r)+\frac{i\omega_r}{U_r}[A_2(U_r)(s-s_x)+\frac{1}{2}a_2(U_r)(s-s_x)^2]\}$$

$$B_3(s,U_r,\omega_r)=A_2(U_r)+A_3(s,U_r)$$

$$C_1(U_r,\omega_r)=\omega_rl_0U_ri\cdot B_1(U_r,\omega_r)A_9$$

$$C_2(U_r,\omega_r)=\omega_rl_0U_riA_1\{l_0a_2(Ur)A_{10}+\frac{i\omega_r}{U_r}[A_2(U_r)A_{10}+\frac{1}{2}a_2(U_r)A_{11}]\}$$

$$C_3(U_r,\omega_r)=\frac{l_0U_r\omega_rj}{A_0}[A_2(U_r)A_9+A_{12}(U_r)]$$

$$C_4(U_r,\omega_r)=2A_1l_0^2U_r^2\{[l_0A_9a_2(U_r)+\frac{i\omega_r}{U_r}[A_2(U_r)A_9+A_{12}(U_r)]\}$$

$$C_5(U_r)=\frac{l_0^2U_r^2}{A_0}A_9a_2(U_r)$$